UCLA
UCLA Electronic Theses and Dissertations

Title
Exploration of Oligoaniline Synthesis and Applications in Supercapacitors

Permalink
https://escholarship.org/uc/item/8kz9b3f8

Author
Wang, Haosen

Publication Date
2019

Peer reviewed|Thesis/dissertation

eScholarship.org Powered by the California Digital Library
University of California

UNIVERSITY OF CALIFORNIA

Los Angeles

Exploration of Oligoaniline Synthesis and Applications in Supercapacitors

A dissertation submitted in partial satisfaction of the
requirements for the degree Doctor of Philosophy
in Chemistry

by

Haosen Wang

2019

© Copyright by

Haosen Wang

2019

ABSTRACT OF THE DISSERTATION

Exploration of Oligoaniline Synthesis and Applications in Supercapacitors

by

Haosen Wang
Doctor of Philosophy in Chemistry
University of California, Los Angeles, 2019
Professor Richard B. Kaner, Chair

Compared to rechargeable batteries, supercapacitors, also known as ultracapacitors or electrochemical capacitors demonstrate higher power and much greater cycle life. As the demand increases for energy storage devices with safe operations, high power ratings and long cycle life, supercapacitors have attracted much attention from both industry and academia. However, most commercial supercapacitors are carbon based, capable of storing only a fraction of the amount of charge that batteries do, limiting their applications to those that need short power bursts, but lower capacities. To enhance the energy density of supercapacitors, pseudocapacitance materials, such as transition metal oxides/hydroxides and conducting polymers, are introduced.

Polyaniline is a promising pseudocapacitance material with high conductivity, tunable morphology and high theoretical specific capacitance. Tetra-aniline (TANI) is the shortest

oligomer of PANI that demonstrates high conductivity and redox activities. Furthermore, the short chain length of TANI is believed to improve its resistance to chain breaking during cycling that undermines PANI's cycle stability. However, compared to PANI, research on the synthesis and supercapacitor applications of nanostructured TANI is relatively scarce. Therefore, the goal of this thesis is to develop methods to prepare TANI with various nanostructures and study the supercapacitor applications of TANI-based supercapacitors.

Chapter 2 presents a facile interfacial chemical synthesis to produce high purity TANI nanowires, while Chapter 3 is a study on the electrochemical deposition of TANI on different substrates using aniline dimer in organic-aqueous electrolyte solutions. Both methods are able to trigger nanostructure formation within TANI, and improve upon the pseudocapacitor performances of the TANI-based electrodes. Chapter 4 reports an original one-pot-one-step hydrothermal synthesis of reduced graphene oxide (rGO) - oligoaniline (OANI) nanocomposites. This process simultaneously reduces graphene oxide and deposits oligoaniline onto the rGO surfaces, inducing synergetic effects between the conducting oligomer and the carbon substrates. Chapter 5 presents an in-depth evaluation on the supercapacitor performances of TANI and its carbon nanocomposites. We composited TANI with 1D (carbon nanotubes), 2D (GO and rGO) and 3D (activated carbon) carbon materials to investigate how morphology and surface functional groups affect the supercapacitor performances of TANI-based electrodes.

The dissertation of Haosen Wang is approved.

Xiangfeng Duan

Yang Yang

Richard B. Kaner, Committee Chair

University of California, Los Angeles

2019

TABLE OF CONTENTS

LIST OF FIGURES

Chapter 1. Introduction

Chapter 2. One-step Interfacial Synthesis of Nanostructured Tetraaniline and its Applications in Electrochemical Energy Storage

Chapter 3. Electrochemical Deposition of Tetra-Aniline and Its Applications in Supercapacitor Electrodes

Chapter 4. Graphene/Oligoaniline Based Supercapacitors: Towards Conducting Polymer Materials with High Rate Charge Storage

Chapter 5. Evaluation of nanostructured Tetra-aniline and Tetra-aniline-carbon nanocomposites based supercapacitors

Chapter 6. Conclusions and Future work

LIST OF TABLES

ACKNOWLEDGEMENTS

As I am staring at the light at the end of the tunnel, I think it is quite appropriate to express my gratitude for those who made this journey possible. First, I would like to thank my advisor Professor Richard B. Kaner, for providing me with the opportunity and necessary means to do research under his guidance. Wise and kind, he has not only given me priceless advice and support with research projects to but also encouraged me to grow as a scientist (or an engineer, depending on how strict the definition is). I am really proud and grateful to be a Kanerite (or Kanerd).

I would also like to extend my appreciation to Dr. Maher F. El-Kady who was my research mentor. He introduced me to the supercapacitor research field and continued to help me along the way. I doubt I would be able to complete this chapter of my life without your mentorship. Thank you very much for your patience, kindness, and all the editing and technical support over the past few years!

Dr. Mengping Li and I joined the group in the same year, and we have been good friends ever since. Thank you for dragging me along all these years. Without your help, encouragements and companionship, my past few year would have been much less enjoyable. I will forever cherish our friendship and hope you all the best in life.

My gratitude also goes to the other supercapacitor subgroup members. Dr. Lisa Jiao-Jiao Wang and Dr. Jee Youn Hwang joined the group before me. They helped me greatly with laboratory techniques and general research discussions. It has been a pleasure to work alongside these two wonderful scientists. Dr. Yuanlong Shao stayed with our group for two years. I would like to thank him for all the insightful discussions and thoughtful comments.

During my years in the group, I have had the pleasure of mentoring a few undergraduate students: Mu-Hua Chen, Yunhui Xu, Runfang Hou, Ziwei Yu and Rui Wang. I sincerely appreciate all the assistance they had provided and hope that they succeed in whatever endeavors they choose to pursue in life.

I would also like to thank the entire Kaner group. In particular, I would like to thank Chenhao Ji and Shuangmei Xue for making my last year here pleasurable. I hope you lead a blissful life together as a couple. I would also like to thank Cheng-Wei Lin, Chris Turner, Matthew Kowal, Jialin Lei, Mackenzie Anderson, Chenxiang Wang, Xueying Chang, Ailun Huang and Shanlin Hu for their support and friendship. Thank you all for making this journey great!

I would also like to show my appreciations to a few important friends whom I shall not name. Thank you for being in my life and teaching me valuable life lessons. I hope you all lead wonderful lives.

Finally, I want to show my loving gratefulness and gratitude for my parents. Thank you for bring me onto this world and raising me up the way you did. Thank you for believing in me and being there for me when I most needed it. Even though I rarely say it, but I want you to know that I love you both very much.

Previous Publications and Contributions of Co-authors:

Chapter 2 is a version of Haosen Wang, Mu-Hua Chen, Yunhui Xu, Cheng-Wei Lin, Mengping Li, and Richard B. Kaner, "One-step Interfacial Synthesis of Nanostructured Tetraaniline and its Applications in Electrochemical Energy Storage". H.Wang conceived the experiments, performed most of the synthesis and characterizations, and wrote the manuscript. M.H. Chen and Y. Xu assisted with synthesis. C. W. Lin and M. Li helped with general discussions, data processing and manuscript revising. R. B. Kaner supervised the project and edited the manuscript. This manuscript will be submitted soon.

Chapter 3 is a version of Haosen Wang, Ziwei Yu, Cheng-Wei Lin and Richard B. Kaner, "Electrochemical Deposition of Tetra-Aniline and Its Applications in Supercapacitor Electrodes". H. Wang conceived the project and performed most of the experiments and characterizations. Z. Yu performed some synthesis and electrochemical characterizations. C. W. Lin provided insightful discussions and suggestions. R. B. Kaner supervised the project and edited the manuscript. This manuscript will be submitted soon.

Chapter 4 is a version of Haosen Wang, Ziwei Yu, Maher F. El-Kady, Mackenzie Anderson, Matthew D. Kowal, Mengping Li, and Richard B. Kaner, "Graphene/Oligoaniline Based Supercapacitors: Towards Conducting Polymer Materials with High Rate Charge Storage". H. Wang and Z. Yu conceived the project. H. Wang performed most of the synthesis and characterizations, and wrote the manuscript. Z. Yu performed some of the synthesis and characterizations. M. F. El-Kady provided technical support and manuscript editing. M. Anderson carried out XPS analysis and relevant data processing. M. D. Kowal provided the graphene oxide for synthesis and performed Raman IR spectroscopy analysis. M. Li assisted with data processing and interpretation, and provided some helpful discussions and comments. R. B. Kaner supervised

the project and edited the manuscript. The National Science Foundation CBET Grant 1337065, Nanotech Energy, Inc. and the Dr. Myung Ki Hong Endowed Chair in Materials Innovation (RBK) provided funding for this research. This manuscript has been published in *Energy Storage Materials* in 2019. I appreciate *Energy Storage Materials* for giving me the permission to reproduce the manuscript in this thesis.

Chapter 5 is a version of Haosen Wang, Rui Wang, and Richard B. Kaner, "Evaluation of nanostructured Tetra-aniline and Tetra-aniline-carbon nanocomposites based supercapacitors". H. Wang conceived the project, performed some synthesis and general characterizations, and wrote the manuscript. R. Wang performed most of the synthesis, electrochemical characterizations and data processing. R. B. Kaner supervised the project and edited the manuscript. This manuscript will be submitted soon.

VITA

2012	ACS Undergraduate Achievement Award in Inorganic Chemistry
2013	American Institute of Chemists Award
2013	Bachelor of Arts, Chemistry, Saint John's University, MN
2013-2015	Dean's Scholar Award, UCLA
2013-2018	Teaching Assistant, UCLA
2013-2018	Graduate Research Assistant, UCLA

PUBLICATIONS AND SELECTED PRESENTATIONS

H. Wang, Z. Yu, M. F. El-Kady, M. Anderson, M. D. Kowal, and R.B. Kaner, "Graphene/Oligoaniline Based Supercapacitors: Towards Conducting Polymer Materials with High Rate Charge Storage", *Energy Storage Mater*. (2019). doi:10.1016/J.ENSM.2019.02.019.

H. Wang, M.H. Chen, Y. Xu, C.W. Lin, M. Li, and R. B. Kaner, "One-step Interfacial Synthesis of Nanostructured Tetraaniline and its Applications in Electrochemical Energy Storage", *in-preparation*

H. Wang, Z. Yu, C.W. Lin and R. B. Kaner, "Electrochemical Deposition of Tetra-Aniline and Its Applications in Supercapacitor Electrodes", *in-preparation*

H. Wang, R. Wang, and R. B. Kaner, "Evaluation of nanostructured Tetra-aniline and Tetra-aniline-carbon nanocomposites based supercapacitors", *in-preparation*

M. Li, M. F. El-Kady, J. Y. Hwang, K. Marsh, **H. Wang**, M. Kowal, and R.B. Kaner, "Fabricating Hollow Co_3O_4/LSG composite for Higher Performance Supercapacitors", *Nano Res.* (2018) 11: 2836. https://doi.org/10.1007/s12274-017-1914-7

R.L. Li, CW. Lin, Y. Shao, FK. Yao, MD. Kowal, **H. Wang**, M. T. Yeung, SC. Huang, and R.B. Kaner, "Characterization of aniline tetramer by MALDI TOF mass spectrometry upon oxidative and reductive cycling", *Polymers, 2016,* 8(11), 401

Z Zhao, K Jia, JC Shaw, Z Zhu, W Wan, L Zhan, M. Li, **H. Wang**, X. Chen, Z. Li, S. Chen, Y. Zhou, R.B. Kaner and W. Cai "Synthesis of sub-millimeter Bi-/multi-layer graphene by designing a sandwiched structure using copper foils", *Applied Physics Letters*, 2016, 109, 123107

H. Wang, R. Hou, M. Li, M. F. El-Kady, and R. B. Kaner, Poster presentation on "Graphene-PEDOT-Platinum Tertiary Composite Material Based Catalyst for Hydrogen Evolution Reaction", Meeting Abstracts (MA2018-01 **2578**). The Electrochemical Society, May 15, 2018

R.B. Kaner, M.F. El-Kady, Y. Shao, J.Y. Hwang, L. Wang, M.Li, **H. Wang**, M. Kowal, W. Sun, S. Cho and R. Rizvi, (2016, April). Contributed Presentation on (invited) "Electrochemical Capacitors Based on Graphene", Meeting Abstracts (No. 6, p.565). The Electrochemical Society.

R.B. Kaner, M.F. El-Kady, L. Wang, J.Y. Hwang, Y. Shao, M.Li, **H, Wang**, J.M. Ko, M. Mousavi, Contributed Presentation on "Graphene-based supercapacitors," AMN7 Advanced Materials & Nanotechnology, Nelson, New Zealand, Feb. 8-12, 2015.

Chapter 1. Introduction

1.1. Current status of energy storage devices

With the rapid development of technology, electric appliances, from small portable devices like smart phones and laptop computers to large electric vehicles, have become increasingly ingrained in our modern way of life and have profoundly changed how we interact with the rest of the world. Because not all appliances can be cabled to a stationary power source all the time, and the technology and infrastructures for omnipresent wireless power supplies remain in development,[1,2] most electric devices currently require dedicated energy storage components. Batteries have been the most widely used power source for mobile devices due to their past satisfactory performances. However, recent years have seen batteries struggling to meet the ever-increasing power demand of smarter and more power-hungry portable devices, not to mention the pressures from the burgeoning field of high performance long range electric vehicles. The three main drawbacks currently hampering batteries are: 1) low power density that prevents fast charging or high power output, 2) heat generated during charging and discharging that causes overheating, thermal runaway and even explosions, and 3) mediocre cycle stability that limits the life expectancy of devices.

Fortunately, supercapacitors, also known as ultracapacitors or electrochemical capacitors, can improve upon these areas. Compared to batteries, supercapacitors demonstrate higher power density, low thermal heating and much longer cycle life, and have been commercially used in applications that require bursts of high power input/output or high fluctuations of current, such as regenerative braking, camera flashes, power tools, and even interfaces between loads and power grids.[3]

1.2. Basic designs and charge storage mechanisms of supercapacitors

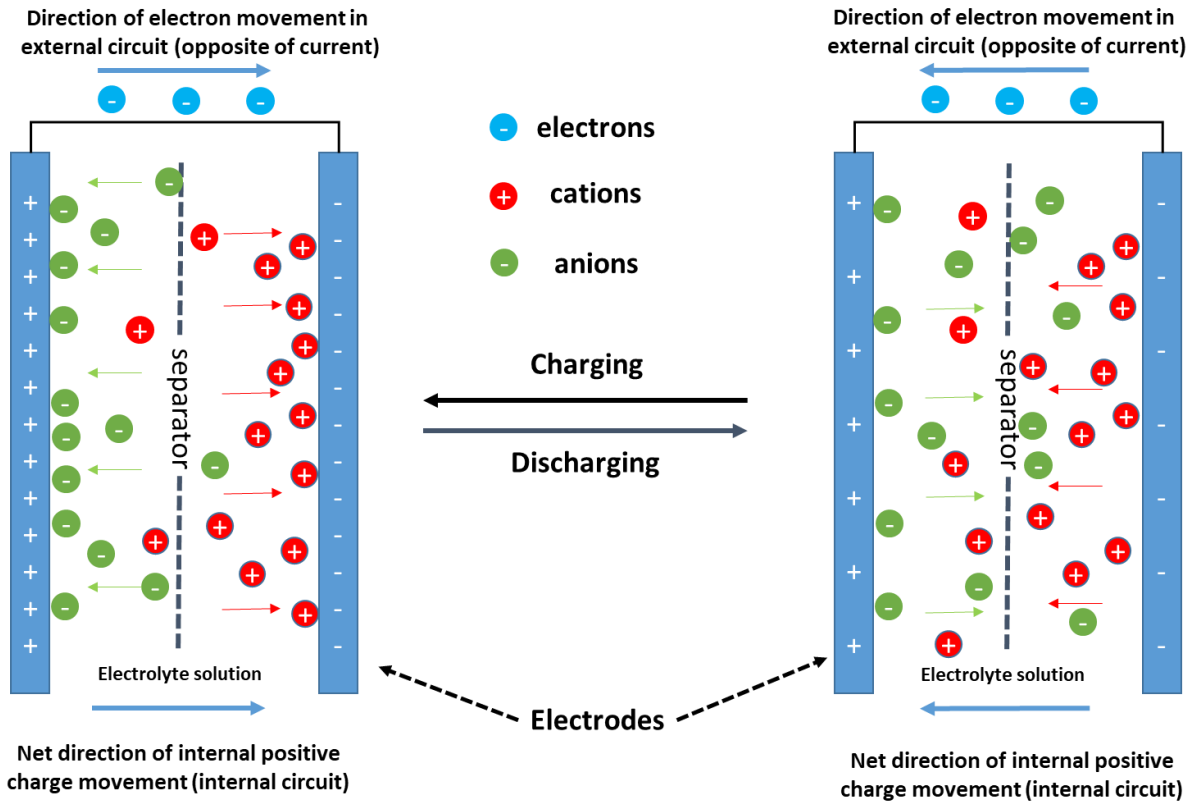

Figure 1.1 Schematic diagram of supercapacitor structure and working principle.

In terms of cell design, supercapacitors and batteries share many similarities. Both have two opposing electrodes connected to an external circuit through current collectors, an electrolyte solution providing ions to compensate for charge storage and an ion-permeable separator to prevent the short circuiting of the two electrodes, while maintaining internal ionic conductance. Figure 1.1 shows a diagram of the basic structures of a generic supercapacitor and its charging/discharging processes. During charging, a positive bias is applied to the positive electrode, pumping electrons from the negative electrode to the positive electrode through the external circuit, forming the external (negative) current. This external electric current causes the potential on the positive electrode to rise and accumulates net positive charges on the positive electrode surface, while the potential of the negative electrode decreases and net negative charges

accumulate on the negative electrode surface. The net charges on the electrodes in turn attract ions of opposite signs from the electrolyte solution to move close to the electrode surfaces, resulting in an internal ionic current and completing the circuit. The opposite process takes place during discharging, where the adsorbed ions diffuse away from the electrode surfaces, decreasing the potential difference between the positive and negative electrode, while electrons move from the negative electrode to the positive electrode through the external circuit. Note that the external electric current is equal in magnitude, but opposite in direction, to the internal ionic current.

Additionally, for a symmetric supercapacitor, the polarity of the electrodes can be reversed; however, an asymmetric supercapacitor does have designated cathodes and anodes for maximum performance. It is also worth mentioning that the entire device is equivalent to having two capacitors (one positive and one negative) connected in series; therefore, the relationship between total capacitance of the device and that of the individual electrodes is expressed by the following equation:

$$\frac{1}{C_T} = \frac{1}{C_{positive}} + \frac{1}{C_{negative}} \tag{1.1}$$

In Equation 1.1, C_T denotes the total capacitance of the capacitor, while $C_{positive}$ and $C_{negative}$ refer to the capacitance of the positive and negative electrodes, respectively. Given this relationship, capacitance matching for the two electrodes is of critical importance, as massively overloading on one electrode will result in the capacitance of the entire device being limited to that of the smaller electrode. In a symmetric device, the total capacitance of the device is equal to half the capacitance of each electrode.

There are two main charge storage mechanisms involved in the charge/discharge of supercapacitors: 1) electrostatic ion/charge adsorption on the interface between the electrode and electrolyte solution, and 2) Faradaic charge transfer through rapid reversible surface redox

reactions. A schematic diagram showing the difference between electrochemical double layer capacitance and pseudocapacitance is shown in Figure 1.2.[4]

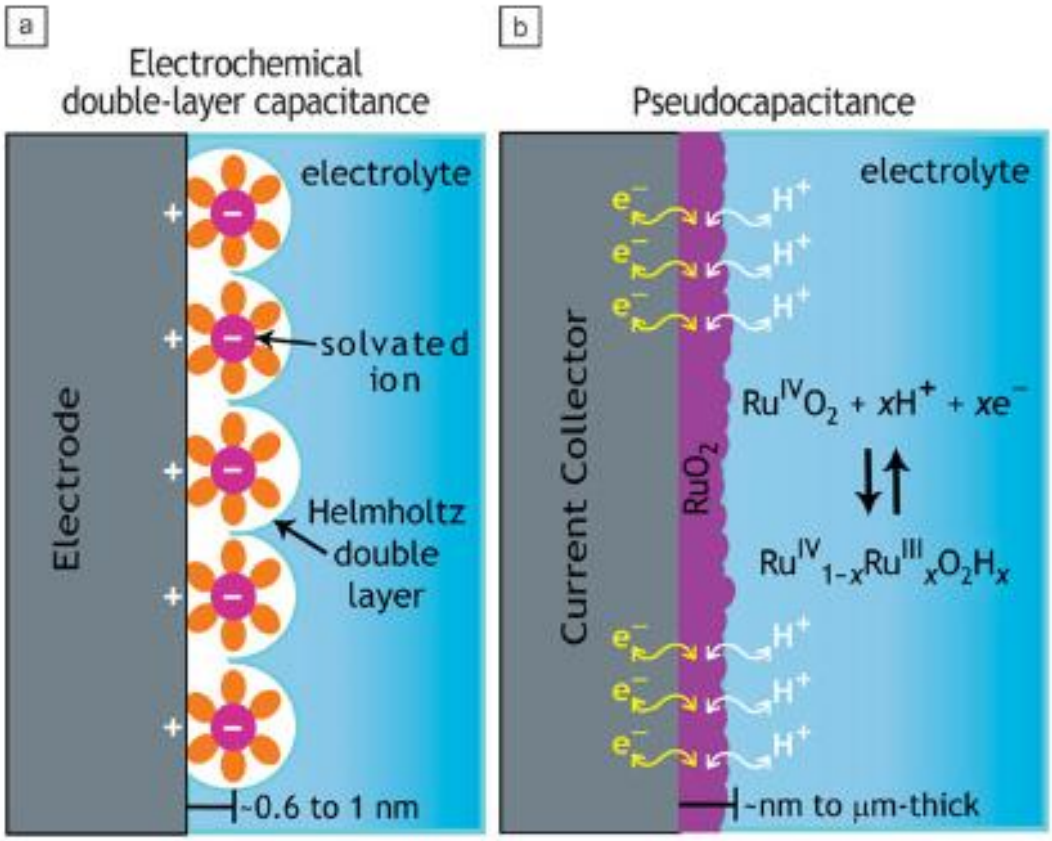

Figure 1.2 Schematic of charge storage via the process of either (a) Electrochemical double-layer capacitance (EDLC) or (b) pseudocapacitance.[4]

As shown in Figure 1.2a, net positive charges on the electrode electrostatically attract oppositely charge anions in the electrolyte solution, and the solvated ions accumulate on or near the electrode surface, forming the (inner and outer) Helmholtz double layer and a diffuse layer. In a typical EDLC with a low electrolyte concentration, the capacitance of the electrode is dominated by the Helmholtz double layer, whose capacitance can be expressed as follows:

$$\mathrm{C} = \frac{\varepsilon_r \varepsilon_0}{d} A \qquad (1.2)$$

where ε_r is the relative dielectric constant of the electrolyte in the supercapacitor and ε_0 is the permittivity of vacuum, d is the effective thickness of the electrochemical double layer, and A is the effective area of the electrode. The thickness of the double layer (d) is typically equivalent to the diameter of the solvent molecule, ~1.9 $\times 10^{-10}$ m for water, and most EDLC capacitors also have very high specific areas (A). These two factors combine to make EDLC supercapacitors demonstrate much higher specific capacitance than traditional capacitors.[5]

Another type of storage is pseudocapacitance, where the capacitance originates from fast and reversible Faradaic processes taking place near or within the electrode surface. There are several types of reversible or quasi-reversible redox reactions that can give rise to pseudocapacitance, such as underpotential deposition, lithium intercalation, bulk redox coupling reactions and redox reactions of conducting polymers. A good pseudocapacitance example, RuO_2, is shown in Figure 1.2b. Within the working potential window of RuO_2, Ru is able to transition through multiple oxidation states, from +2 to +6, accepting/donating protons from the electrolyte solution in the same process to balance charge. The capacitance that arises as a result of charge acceptance (q) and change in potential (V) is called pseudocapacitance (dq/dV). The behavior of pseudocapacitance is very similar to that of rechargeable batteries, but the pseudocapacitance materials typically have high surface and high ion conductance to allow for reversible reactions to happen primarily on the electrode surface (such that the kinetics are not diffusion-controlled like batteries).

The theoretical specific pseudocapacitance of a material is calculated by:

$$\mathrm{C} = \frac{n \times F}{M \times V} \tag{1.3}$$

where n is the average number of electrons transferred in the redox reaction, F is the Faraday constant, M is the molecular weight of the active material, and V is the working voltage window.

Based on this equation, each molecule of the pseudocapacitance material can donate or accept n charges to store energy, compared to the EDLC process where charges are adsorbed on electrode surfaces, allowing pseudocapacitors to have even higher energy density than EDLC capacitors.[6]

Depending on the major charge storage mechanism, supercapacitors can be categorized into three types: 1) electrochemical double layer capacitors (EDLC) that store charges electrostatically, 2) pseudocapacitors that store charges via surface redox reactions and 3) hybrid supercapacitors that combine both mechanisms. EDLC supercapacitors characteristically demonstrate long cycle life but relatively low energy density, while pseudocapacitors show improved specific capacitance but compromise on cycle stability. Hybrid supercapacitors are made of composite materials that can utilize both an electrochemical double layer and a Faradaic mechanism for charge storage, combining the strength of both EDLCs and pseudocapacitors. Figure 1.3 below shows the classification of these different types of supercapacitors and their representative electrode materials.[7]

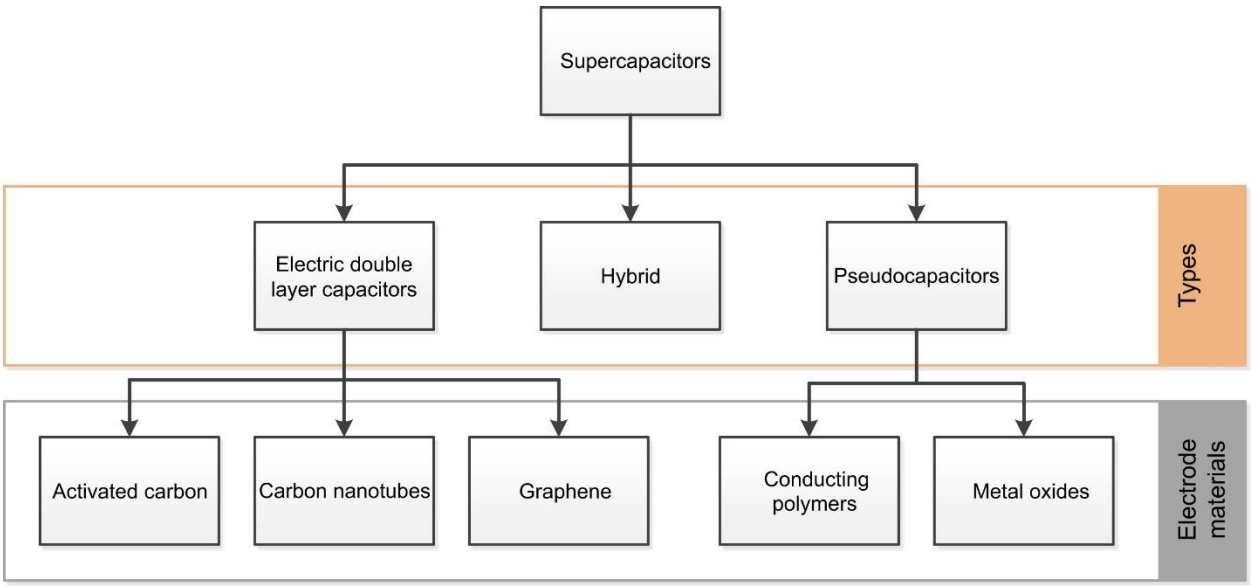

Figure 1.3 Classification of different supercapacitors. (Reproduced with permission.[7] Copyright 2016 Elsevier Ltd.)

1.3. Supercapacitor Performance Evaluation

1.3.1. Electrochemical characterization methods

To evaluate the performance of a supercapacitor, quite a few parameters need to be analyzed, among which are three essential ones: specific capacitance, operating voltage and equivalent series resistance (ESR). Figure 1.4 shows how these three core performance metrics are affected by various factors and how they in turn determine the final performance of a supercapacitor device.[8] As seen in Figure 1.4, factors like packing density, mass loading, electrode thickness and experimental setup can significantly affect the specific capacitance of a material. While the operating voltage of the material is determined by the electrolyte and cell configuration used (symmetric vs. asymmetric), the ESR is largely affected by the intrinsic resistance of the material, the current collectors, binder(s) and conductive additives, and even the fabrication techniques. These essential parameters then affects the energy density and power density of the supercapacitor, according to the following equations:

$$\mathrm{E} = \frac{1}{2}\mathrm{C}(V_1^2 - V_2^2) \tag{1.4}$$

$$\mathrm{P} = \frac{V^2}{4R_s} \tag{1.5}$$

In Equation 1.4, *C* is the capacitance of the device, and *E* is amount of energy that can be dispensed from the device (Wh) from its maximum operating voltage V_1 to the minimum operating voltage required by the application, V_2. This equation takes into consideration the fact that most appliances require a minimum working voltage and cannot discharge a supercapacitor to 0 V. To calculate the maximum energy, V_2 could be set to 0 V and *E* would be equal to the maximum energy. Equation 1.5 expresses the relationship between the maximum power output of the device

P (W) and its maximum working potential V and its equivalent series resistance R_s. The assumption of this equation is that the external load resistance is equal to R_s.

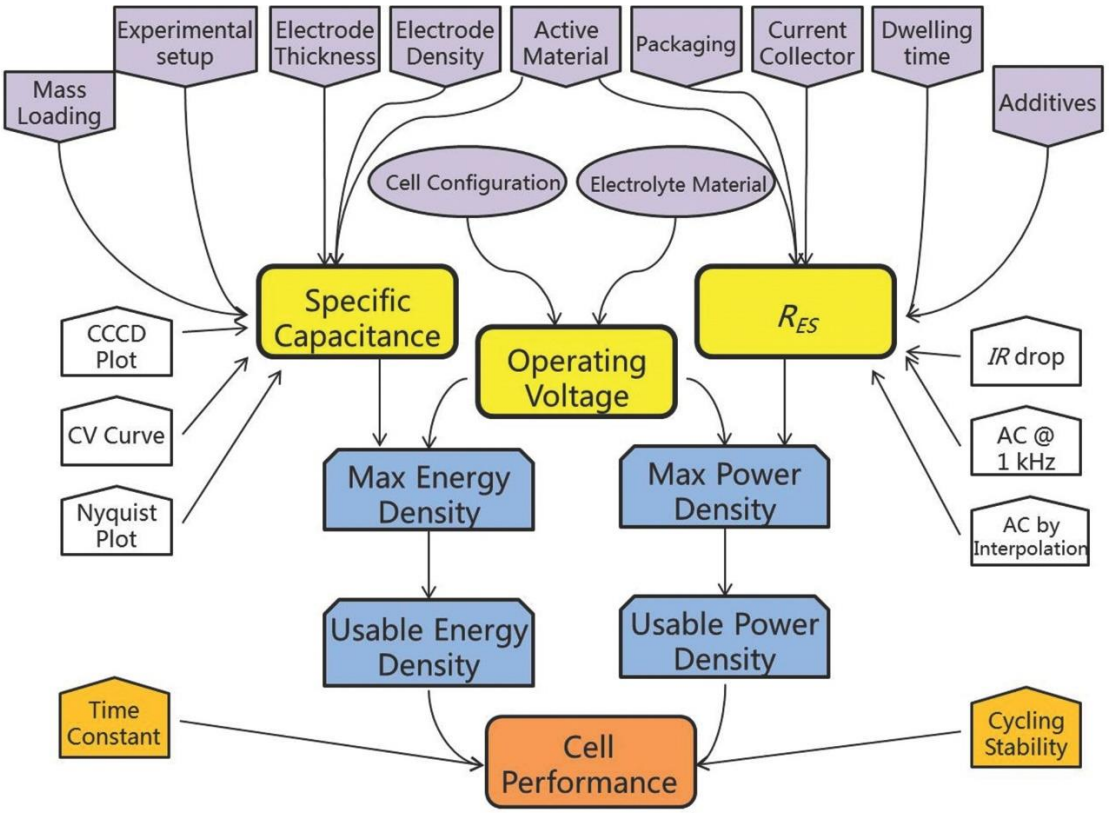

Figure 1.4 An illustration of key performance metrics, test methods, and major affecting factors for the evaluation of SCs. (Reproduced with permission.[8] Copyright 2015, WILEY-VCH)

To evaluate the performance metrics of a supercapacitor, three electrochemical characterization methods are employed: cyclic voltammetry (CV), galvanostatic constant current charge-discharge (CC), and electrochemical impedance spectroscopy (EIS).

Cyclic voltammetry applies a cyclic linearly changing potential sweep between the working electrode against the reference electrode (in a 3-electrode setup) or the negative electrode (in a 2-electrode setup) at fix scan rates, denoted by v. The range of scanned potential is the potential window. Plotting the potential of the working electrode against current or current density,

the 3-electrode cyclic voltammograms can reveal some important characteristics of the supercapacitor electrode. For instance, the CV plot of an EDLC electrode is close to rectangular, while that of a pseudocapacitor typically displays redox peaks. The curvature of the CV plots near the two ends of the potential window also shows the RC charging behavior of the supercapacitor, providing a qualitative indication of its ESR. CV is also a powerful tool to determine the optimal working window of a certain material in a specific electrolyte, as the breakdown of the material and/or electrolyte can be observed on the CV plot.

Galvanostatic constant current charge discharge (CC) applies a constant current, repeatedly charging and discharging the working electrode or the entire supercapacitor and generating a plot of time vs. potential. Given its similarity to the normal charging protocols of commercial supercapacitors, the CC method is regarded as the most accurate method to evaluate all three core parameters of the supercapacitor. It is also an efficient tool to study cycle stability of the supercapacitor.

Electrochemical impedance spectroscopy measures the impedance of a working electrode or a supercapacitor by applying a small amplitude alternating voltage, in a wide frequency range, near a certain potential against the reference electrode or the negative electrode. This effectively charges and discharges the device at or near the set potential, over a range of charging/discharging rates, revealing the frequency response of the device. The data of EIS are usually plotted in a Nyquist plot (real impedance vs. negative imaginary impedance) or a Bode plot (frequency vs. phase angle). While the Bode plot shows what type of response (capacitor, inductor, or resistor) the device shows in what frequency ranges, the Nyquist plot can be used to estimate the internal resistance, charge transfer resistance and ESR of the device.

1.3.2. Capacitance evaluation

As shown in Figure 1.3, all three methods can be used to evaluate the capacitance of a supercapacitor. Based on the discharge CV data, the capacitance can be calculated using the following equation:

$$C_{CV} = \frac{\int_{V_i}^{V_f} i dV}{(V_f - V_i) \times v} \tag{1.6}$$

where C_{cv} (F) is the capacitance determined based on CV, v is the scan rate (V/s), i is the instantaneous discharge current (A) read from the CV plot, V_f and V_i represent the upper and lower bound of the potential window (V), respectively. This equation effectively calculates the average discharge capacitance over the span of the entire potential window. To calculate the instantaneous capacitance, another equation should be used:

$$C_{ins} = \frac{i}{v} \tag{1.7}$$

where C_{ins} is the instantaneous capacitance (F), i is the current (A) read directly from the CV data, and v is the scan rate (V/s). This calculation shows instantaneous capacitance of the device at a given potential at a specific scan rate, and the C_{ins} can be plotted against potential to become an alternative representation of the CV plot.

To calculate the capacitance of a supercapacitor based on CC data, the following equation is used:

$$C_{cc} = \frac{i \times \Delta t}{\Delta V} \tag{1.8}$$

where C_{cc} is CC capacitance (F), i is the discharge current (A), Δt is the discharge time (s), and ΔV is the potential window of discharge (V). It is worthwhile to note that since an IR drop is

usually present in the CC curve, ΔV should be adjusted to exclude the loss of potential for more accurate results. This method again provides an average capacitance over the entire discharge potential window, and a more accurate method would be to take the slope of the CC curve.

The imaginary impedance from EIS data can also be utilized to derive the capacitance of a supercapacitor:[9]

$$C_{EIS} = \frac{-1}{2\pi f \times Im(Z)} \tag{1.9}$$

where C_{EIS} is the capacitance at a specific f frequency (Hz), and *Im(Z)* is the imaginary part of complex impedance at f frequency. The frequency is selected such that the device demonstrates a typical capacitor response, and the most commonly used frequency is the lowest frequency applied (0.01 Hz). Note that since EIS is performed at around a certain potential, the capacitance value might vary with the applied potential for non-EDLC capacitors.

1.3.3. Resistance evaluation

Another critical metric of a supercapacitor is the resistance components. A supercapacitor is treated as a system of capacitors connect in series to a resistor component, and the resistance is regarded as the equivalent series resistance (ESR). ESR is essentially a measure of the power performance of the supercapacitor. Note that ESR is only applicable to a device, and its counterpart for an electrode should be called uncompensated resistance.

ESR can be most accurately derived from the IR drop of a CC curve (with no resting period):

$$ESR = \frac{\Delta V_{IR}}{2 \times i} \tag{1.10}$$

where ΔV_{IR} is the change in potential between the maximum charging voltage and the maximum discharging voltage, and *i* is the applied constant current. The factor 2 is used to adjust for the fact that the maximum charging potential includes a $i \times ESR$ potential "rise" term, while the discharge potential also includes a $-i \times ESR$ potential drop term at its onset. Therefore, the measured ΔV_{IR} effectively is equal to $2 \times i \times ESR$. However, if the device was allowed to rest in between charge and discharge, the factor of 2 should be omitted.

The Nyquist plot from EIS data can provide more insight into the different resistance components of a supercapacitor. A supercapacitor Nyquist plot typically shows a semicircle in the high frequency range, followed by a 45° segment in the mid frequency range and a vertical line in the low frequency range. The semicircle is indicative of a charge transfer process, with the diameter as the charge transfer resistance. This semicircle is usually very small or even absent for an EDLC. The 45° segment corresponds to the ion diffusion process and its equivalent circuit element is called a Warburg impedance element. The vertical line in the low frequency range is representative of capacitance. The ESR is typically identified as the real component of the impedance data at 1 KHz. Another approach is to extrapolate the vertical part of the Nyquist plot and find its x-axis intercept.

1.4. Supercapacitors based on polyaniline/tetra-aniline

1.4.1. Polyaniline (PANI)

Even though polyaniline was discovered and reported in scientific literature in the 1860s,[10] it was historically used as a violet dye, called aniline black. It wasn't until more advanced electrochemical characterization methods were developed in the 20th century that interests in this conducting polymer were rekindled. Since the pioneering work of Alan MacDiarmid and coworkers,[11] PANI has become one of the most thoroughly studied conducting polymers due to its

tunable morphology, high conductivity, ease of synthesis, and redox properties. In the past few decades, with the development of supercapacitors, the pseudocapacitance application of PANI was explored rather extensively.[12]

Figure 1.5a shows the basic structures of polyaniline. PANI has three oxidation states: leucoemeraldine, emeraldine and pernigraniline, and each state has a doped and dedoped form, denoted by salt and base, respectively. PANI displays the highest conductivity in its emeraldine salt form. In terms of oxidation states, leucoemeraldine is the lowest, emeraldine is intermediate and pernigraniline is the highest oxidation state. The transition between two adjacent oxidation states involves 2 electrons per 4-moiety repeating unit, and these redox processes enable PANI-based electrodes to exhibit pseudocapacitance behavior (Figure 1.5b). On the CV curve, a/a' and c/c' redox peak pairs correspond to the transitions between leucoemeraldine to emeraldine and between emeraldine to pernigraniline, respectively. Depending on the properties of PANI electrodes and the electrolyte solutions, the peaks around 0.5 V vs. Ag/AgCl sometimes merge into one peak b/b', which is usually assigned to polymers with phenazine ring structures.[13] Zhang *et al.* studied PANI films in sulfuric acid and found two separate peaks in this region: Peaks b1/b1' is assigned to the benzoquinone to hydroquinone transition and b2/b2'is believed to be associated with the redox reactions of p-aminophenol and benzoquinonline.[14]

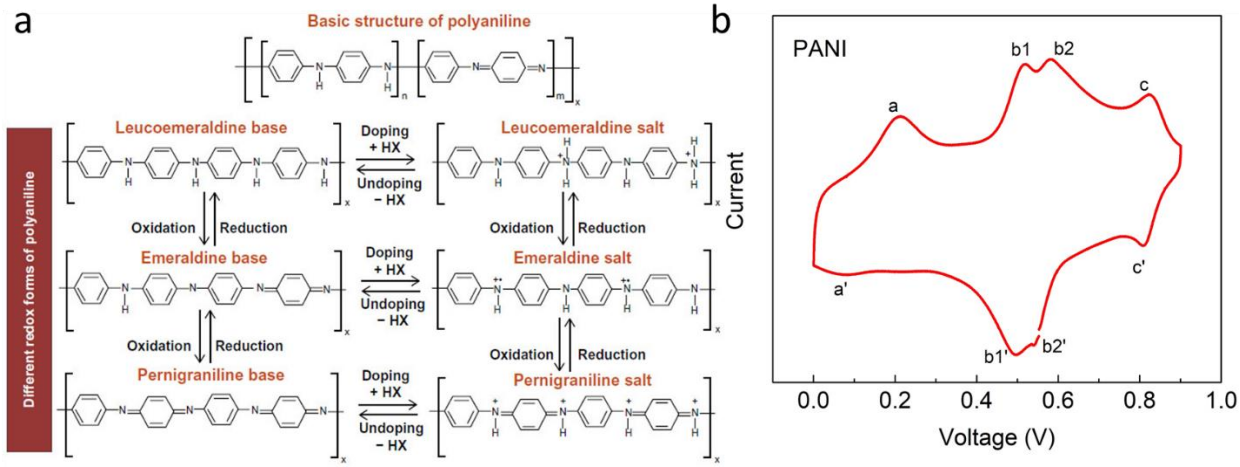

Figure 1.5 (a) Basic structure of PANI and different redox forms of PANI with its doped states (reproduced with permission.[15] Copyright 2015, Dove Medical Publishers, Ltd.) (b) Cyclic voltammogram of a PANI electrode in 1.0 M H2SO4 (20 mV/s).

Even though PANI is regarded as a pseudocapacitance material, its charge storage mechanism is not completely Faradaic, as PANI also has a non-negligible surface area that can store charge through electrostatic interactions. Therefore, in practice, PANI should be treated as a hybrid material with both EDLC and pseudocapacitance. The theoretical specific capacitance of polyaniline in aqueous acidic electrolyte was calculated by Li *et al.*, and the specific pseudocapacitance was found to be about 1700 F/g, while the EDLC contributes about 300 F/g, resulting in a combined 2000 F/g theoretical maximum specific capacitance. In this theoretical analysis, the authors assumed that each aniline moiety is able to contribute 1 electron over the potential window of 0.61 V, and the nanowire PANI electrostatically adsorbs ions in a similar fashion as vertically aligned carbon nanotubes. In real world applications, however, the 0.61 V potential window is too low, the number of charge transferred per unit is found to be lower than 1[16] and PANI nanowires are usually intertwined rather than being vertically aligned. Therefore the experimental specific capacitance of PANI is usually much lower.

Morphology is a very important factor in determining the electrochemical performance of PANI-based pseudocapacitors.[17,18] For instance, an interfacial polymerization method developed

by our group can produce PANI with very high aspect ratio nanowire morphology.[19] Utilizing this synthesis method, Guan and coworkers prepared PANI nanowire electrodes that show improved specific capacitance (548 F/g) and longer cycle life.[20] Electrochemical deposition methods can also synthesis nanostructured PANI, and Zhao *et al.* reported electrodeposition of 30 nm PANI nanowires on Ti/Si substrate that demonstrates 1142 F/g at 5 A/g current density.[21] An extreme case is reported by Kuila and coworkers, where an electrode of vertically oriented arrays of PANI 10 nm nanorods on ITO glass substrate shows very high specific capacitance of 3400 F/g.[22] However, this value was challenged by Peng *et al.* who claim that the specific capacitance is higher than the theoretical value.[23]

Although PANI exhibits much higher specific capacitance than EDLC capacitors, its cycle stability leaves much room for improvement. It is generally believed that the degradation of PANI results from both physical stress and chemical decomposition during cycling. As PANI is doped and de-doped during redox reactions, ions move in and out of its structures to balance the charge, causing volume changes and thus physical stress. Over time, the repeated physical stress compromises the physical integrity of the PANI electrode and causes capacity loss. In addition to physical degradation, PANI is also known to experience chemical decomposition at relatively high chemical potentials in both aqueous and organic electrolytes.[24,25] To mitigate these inherent drawbacks, many research groups have prepared hybrid composites of PANI and porous carbon materials that create synergetic effects between the carbon substrate and the conducting polymer, improving upon the cycle stability and overall electrochemical performances.[26–31]

1.4.2. Tetra-aniline (TANI)

Tetra-aniline or TANI, with 4 aniline moieties, is the smallest conjugated aniline oligomer that still demonstrates high conductivity and reversible redox properties. It is appealing because it has a very short chain length, which is believed to be less susceptible to volume change induced physical degradation. Figure 1.6a shows the basic structures and different oxidation states of TANI, while Figure 1.6b shows its characteristic cyclic voltammograms. Similar to PANI, TANI also has three oxidation states, and the transitions between adjacent oxidation states generate the two sets of peaks in the CVs. However, the potentials of the redox transitions of TANI are slightly different from those of PANI, likely due to the shortened chain length.[32]

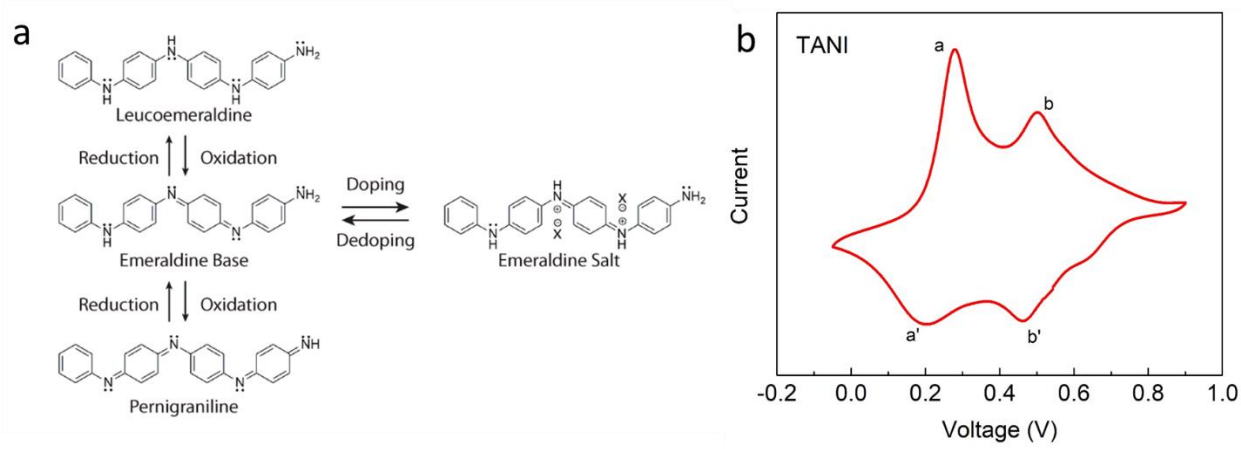

Figure 1.6 (a) Molecular structures exhibiting the redox chemistry and doping properties of aniline tetramer (Reproduced with permission.[33] Copyright 2016, MDPI AG, Basel, Switzerland) (b) cyclic voltammetry of a TANI electrode.

1.5. Objective and structure of this thesis

Compared to PANI, research on the synthesis and supercapacitor applications of nanostructured TANI is relatively scarce. Therefore, the goal of this thesis is to develop methods to prepare TANI with various morphologies and study the supercapacitor applications of TANI-based supercapacitors.

Chapter 1 is a brief introduction that discusses the fundamental working principles of supercapacitors and the electrochemical characterization methods employed to evaluate supercapacitor performances. Polyaniline/tetra-aniline and their applications in electrochemical energy storage are also briefly surveyed.

Chapter 2 presents an interfacial coupling reaction of aniline dimer that yields high purity nanostructured TANI. Traditional TANI synthesis usually results in globular morphology, and self-assembly of TANI into various nanostructures typically requires days to weeks. This one-step synthesis is quick, simple yet versatile. Various synthetic parameters are explored to study their effects on the molecular composition and morphology of the final product. The molecular weight of the product is found to be largely unaffected by most parameters, while the TANI morphology does depend on some key factors. In addition, the TANI nanowires demonstrate good supercapacitor performance with reasonably high specific capacitance (560 F/g at 10 mV/s), low equivalent series resistance and good rate capability.

Chapter 3 is a study on electrochemical deposition of TANI using aniline dimer in organic-aqueous electrolyte solutions. Cyclic voltammetry and pulse chronoamperometry were applied to electrodeposit aniline oligomers onto various substrates, and mass spectroscopy confirms the majority product of electrodeposition is TANI. Nanocomposites of TANI and activated carbon (AC) were prepared using electrodeposition methods, and their supercapacitor performances are

compared against TANI nanowire and TANI-AC physical mixture electrodes. The pulse deposited TANI-AC electrodes demonstrate much higher energy density than activated carbon electrodes and greatly improved cycle stability compared to TANI nanowires.

Chapter 4 reports a novel one-pot-one-step hydrothermal synthesis of rGO-OANI composite materials. In this study, aniline dimer is used to reduce graphene oxide (GO) while simultaneously forming oligoanilines (OANI) that homogeneously coat the surfaces of the reduced graphene oxide (rGO). SEM, FTIR, Raman, XRD, MALDI-TOF MS and XPS characterization methods confirmed the successful reduction of GO and the oligomerization of aniline dimer. The rGO-OANI composite materials exhibit significant synergetic effects between rGO and OANI, and demonstrate great specific capacity, rate capability and cycle stability.

Chapter 5 presents a detailed study on the supercapacitor performances of TANI and its carbon nanocomposites. TANI is composited with 1D (carbon nanotubes), 2D (GO and rGO) and 3D (activated carbon) carbon materials to analyze how morphology and surface functional groups affect the supercapacitor performances of TANI-based electrodes.

The last chapter (Chapter 6) is the conclusion of this thesis and suggests some directions for future work.

1.6. References

(1) Wei, X. C.; Li, E. P.; Guan, Y. L.; Chong, Y. H. *J. Electromagn. Waves Appl.* **2009**, *23* (7), 925–934.

(2) Sun, L.; Ma, D.; Tang, H. *Renew. Sustain. Energy Rev.* **2018**, *91* (December 2016), 490–503.

(3) Farhadi, M.; Mohammed, O. *2014 IEEE Ind. Appl. Soc. Annu. Meet.* **2014**, 1–8.

(4) Sugimoto, W.; Brousse, T.; Sassin, M. B.; Bélanger, D.; Crosnier, O.; Long, J. W. *MRS Bull.* **2011**, *36* (07), 513–522.

(5) Yu, A.; Chabot, V.; Zhang, J. In *Electrochemical Supercapacitors for Energy Storage and Dilivery: Fundamentals and Applications*; CRC Press, 2017; pp 37–98.

(6) Yu, A.; Chabot, V.; Zhang, J. In *Electrochemical Supercapacitors for Energy Storage and Dilivery: Fundamentals and Applications*; CRC Press, 2017; pp 99–134.

(7) González, A.; Goikolea, E.; Barrena, J. A.; Mysyk, R. *Renew. Sustain. Energy Rev.* **2016**, *58*, 1189–1206.

(8) Zhang, S.; Pan, N. *Adv. Energy Mater.* **2015**, *5* (6), 1–19.

(9) Kurzweil, P.; Chwistek, M.; Gallay, R. In *2nd European Symposium on Supercapacitors and Applications*; 2006; pp 1–23.

(10) H. Letheby, M.B., M.A., Ph.D., &c. *J. Chem. Soc.* **1862**, *15*, 161–163.

(11) Macdiarmid, A. G.; Chiang, J.-C.; Halpern, M.; Huang, W.-S.; Mu, S.-L.; Nanaxakkara, L. D.; Wu, S. W.; Yaniger, S. I. *Mol. Cryst. Liq. Cryst.* **1985**, *121* (1–4), 173–180.

(12) Eftekhari, A.; Li, L.; Yang, Y. *J. Power Sources* **2017**, *347*, 86–107.

(13) Geniès, E. M. .; Lapkowski, M.; Penneau, J. . *J. Electroanal. Chem. Interfacial Electrochem.* **1988**, *249* (1–2), 97–107.

(14) Zhang, A. Q.; Cui, C. Q.; Lee, J. Y. *Synth. Met.* **1995**, *72* (3), 217–223.

(15) Malhotra, B.; Dhand, C.; Lakshminarayanan, R.; Dwivedi, N.; Mishra, S.; Solanki, P.; Venkatesh, M.; Beuerman, R. W.; Ramakrishna, S. *Nanobiosensors Dis. Diagnosis* **2015**, *4*, 25.

(16) Peng, C.; Zhou, X.; Chen, G. Z.; Moggia, F.; Fages, F.; Brisset, H.; Roncali, J. *Chem. Commun.* **2008**, No. 48, 6606–6608.

(17) Jing, B.; Wang, X.; Zhou, L.; Kuang, H.; Wang, Q.; Cao, Q. *J. Appl. Polym. Sci.* **2013**, *130* (5), 3753–3758.

(18) Eftekhari, A.; Jafarkhani, P. *J. Electroanal. Chem.* **2014**, *717–718*, 110–118.

(19) Huang, J.; Kaner, R. B. *Angew. Chemie - Int. Ed.* **2004**, *43* (43), 5817–5821.

(20) Guan, H.; Fan, L. Z.; Zhang, H.; Qu, X. *Electrochim. Acta* **2010**, *56* (2), 964–968.

(21) Zhao, G. Y.; Li, H. L. *Microporous Mesoporous Mater.* **2008**, *110* (2–3), 590–594.

(22) Amarnath, C. A.; Hong, C. E.; Kim, N. H.; Ku, B. C.; Kuila, T.; Lee, J. H. *Carbon N. Y.* **2011**, *49* (11), 3497–3502.

(23) Peng, C.; Hu, D.; Chen, G. Z. *Chem. Commun.* **2011**, *47* (14), 4105.

(24) Kabumoto, A.; Shinozaki, K. *Synth. Met.* **1988**, *26*, 349–355.

(25) Mažeikienė, R.; Malinauskas, A. *Synth. Met.* **2001**, *123* (2), 349–354.

(26) Liu, X.; Shang, P.; Zhang, Y.; Wang, X.; Fan, Z.; Wang, B.; Zheng, Y. *J. Mater. Chem. A* **2014**, *2* (37), 15273–15278.

(27) Yan, J.; Yang, L.; Cui, M.; Wang, X.; Chee, K. J.; Nguyen, V. C.; Kumar, V.; Sumboja, A.; Wang, M.; Lee, P. S. *Adv. Energy Mater.* **2014**, *4* (18), 1–7.

(28) Moussa, M.; El-Kady, M. F.; Abdel-Azeim, S.; Kaner, R. B.; Majewski, P.; Ma, J. *Compos. Sci. Technol.* **2018**, *160*, 50–59.

(29) Zhang, K.; Zhang, L. L.; Zhao, X. S.; Wu, J. *Chem. Mater.* **2010**, *22* (4), 1392–1401.

(30) Wang, H.; Hao, Q.; Yang, X.; Lu, L.; Wang, X. *Electrochem. commun.* **2009**, *11* (6), 1158–1161.

(31) Wu, Q.; Xu, Y.; Yao, Z.; Liu, A.; Shi, G. *ACS Nano* **2010**, *4* (4), 1963–1970.

(32) Shacklette, L. W.; Wolf, J. F.; Gould, S.; Baughman, R. H. *J. Chem. Phys.* **1988**, *88* (6), 3955–3961.

(33) Li, R.; Lin, C.-W.; Shao, Y.; Chang, C.; Yao, F.-K.; Kowal, M.; Wang, H.; Yeung, M.; Huang, S.-C.; Kaner, R. *Polymers (Basel).* **2016**, *8* (11), 401.

Chapter 2. One-step Interfacial Synthesis of Nanostructured Tetraaniline and its Applications in Electrochemical Energy Storage

Abstract

Nanostructured tetra-aniline can now be synthesized via a simple, yet versatile one-step interfacial oxidation. Using select agents, aniline dimer can be oxidized to form high purity tetra-aniline (TANI) with nanowire, nanofiber, or nanosheet morphologies. The purity of the product is largely unaffected by parameters such as concentration, oxidizing agent to dimer ratio, types of oxidizing agents or dopants used. However, the morphology of TANI can be tuned by varying the concentration of the oxidizing agent. High aspect ratio nanowires of aniline dimer salt were also obtained through self-assembly across the organic-aqueous interface, shedding light on the origin of PANI's nanowire morphology. The TANI nanowires were found to exhibit good supercapacitor performance with reasonably high specific capacitance (560 F/g at 10 mV/s), low equivalent series resistance and good rate capability. Being a simplified model for polyaniline with comparable electrochemical properties, TANI is a useful material to help understand how polyaniline based supercapacitors degrade over prolonged cycling.

2.1. Introduction

Due to its electrical conductivity, tunable morphology, pseudo-capacitive properties, mechanical flexibility and low cost, PANI has received a great deal of attention since its rediscovery in the 1980s.[1] A tremendous amount of research has gone into exploring possible applications for PANI including chemical sensors,[2–4] electric actuators,[5] anticorrosive coatings,[6,7]

non-volatile memory,[8,9] electrochemical supercapacitors,[10,11] etc. Oligoanilines, especially phenyl-capped tetra-aniline (TANI), have also been investigated in recent years as they can serve as a simplified model for PANI.[12–16] One particularly active field is TANI based supercapacitors.[17,18] It is well known that nanostructured PANI could improve its electrochemical properties;[11] however, most TANI used in these supercapacitors are amorphous.

The traditional synthesis of TANI has usually resulted in amorphous products.[19] Our research group and others have attempted to shape amorphous TANI into various nanostructures post-synthesis,[12,15,16] but the processes are rather time consuming, often requiring days of self-assembly. Our group has also developed an interfacial oxidative polymerization method using aniline monomer and ammonium persulfate to synthesize PANI with a well-defined nanowire morphology.[20] However, to the best of our knowledge, no thorough investigation of interfacial oxidative polymerization of N-phenyl-p-phenylenediamine (aniline dimer) has been reported.

Herein, we describe a facile synthetic method to produce nanostructured TANI in just a single step. The products exhibit distinct nanowire/fiber/sheet structures with high purity and reasonably high yields. The electrochemical/pseudo-capacitive properties of TANI nanowires are explored, demonstrating the potential for nanostructured TANI to be used as supercapacitor electrode materials.

2.2. Results and Discussions

Aniline dimer is an interesting starting material, not only because it exhibits a lower reduction potential than aniline monomer,[21] thus allowing the use of milder oxidizing agents (e.g. hydrogen peroxide), but also because it is a possible intermediate product during aniline polymerization.[22] When aniline is polymerized in the presence of a small amount of aniline dimer, polyaniline growth is accelerated.[23] It would, therefore, be

reasonable to expect that an interfacial oxidative polymerization of aniline dimer should also yield polyaniline. However, in this study, we demonstrate that when aniline dimer is used as the starting material, the interfacial oxidative reactions result in high purity tetra-aniline (TANI) with distinct nanowire/fiber/sheet structures. As the interfacial aniline dimer coupling reaction has not been reported before, we studied the effects of various parameters (such as aniline dimer to oxidizer ratio, oxidizing agent strength, concentration of reactants, and reaction time) on the composition and morphology of the final product. The results of these experiments are discussed below.

2.2.1. Synthetic details

2.2.1.1. Interfacial dimerization of dimer aniline with APS as oxidizer

Tetra-aniline was synthesized using interfacial dimerization between dimer aniline dissolved in an organic solvent that is immiscible with water and APS dissolved in an acidic aqueous solution. To minimize perturbation of the interface, the less dense solution was added slowly to the denser solution. The reaction was allowed to proceed without agitation. Unlike the interfacial polymerization of aniline,[20] the interfacial reaction between dimer aniline and oxidizing agent takes place much faster. At 2 mg/mL dimer concentration, green emeraldine salt precipitates begin to form at the interface within less than a minute. At 5 mg/mL and higher, the precipitates show up almost instantaneously. However, if aniline monomer is used, the precipitates will emerge only after 5 to 10 minutes. This is consistent with the fact that dimer aniline has a lower oxidation potential than monomer aniline and is known to speed up the reaction of aniline going to polyaniline.[21] During the course of the reaction, the interfacial precipitates slowly migrate into the aqueous phase, and the aqueous phase gradually turns from colorless to green. The organic phase turns from light brown to slightly greenish or bluish brown, due to TANI and other oligo-anilines

dissolving in the organic solvent. Typically, the reaction should be complete within a few hours, and an overnight reaction can result in complete depletion of dimer aniline at the interface (based on mass spec data in Figure 2.2). At a high enough dimer aniline concentration, a considerable amount of the products will dissolve into the organic phase due to counter-ion induced solvation of TANI in organic solvents.[24] Therefore, an extended reaction time (more than 24 h) will result in unnecessary loss in yield.

2.2.1.2. Interfacial dimerization of dimer aniline using other oxidizing agents

Compared to aniline, dimer aniline oxidation requires a lower oxidation potential, and therefore a variety of milder oxidizing agents could be used to perform the interfacial reaction with aniline dimer. In this study, hydrogen peroxide (H_2O_2), silver nitrate ($AgNO_3$), and chloroauric acid ($HAuCl_4$) were used as oxidizing agents. Due to the formation of precipitates with silver nitrate and chloride or sulfate ions, nitric acid was used as the doping acid in all reactions. The concentration of aniline dimer in the organic solvent was held constant at 2 mg/mL, and an equivalent amount of oxidizing agent was dissolved in 1.0 M HNO_3. The reactions were initiated by slowing adding the aqueous phase on top of the organic phase without stirring. Similar to the dimer aniline reaction with APS, green precipitates formed quickly after the two phases were combined, although the weaker oxidizing agents do not react quite as fast. As the reaction proceeds, the aqueous phase turns from a clear solution (colorless for H_2O_2 and $AgNO_3$, and yellow for $HAuCl_4$) to a green suspension, and the organic phase turns from light brown to light yellow for $AgNO_3$ and $HAuCl_4$, and to greenish blue for H_2O_2. Similar reactions were also performed with aniline monomer, but no change was observed over a few days. This is likely due to the fact that aniline monomer requires a higher oxidation potential (1.05 V) than those of chloroauric acid (0.93 V) and silver nitrate (0.80 V).

2.2.2 General Spectroscopy Characterizations

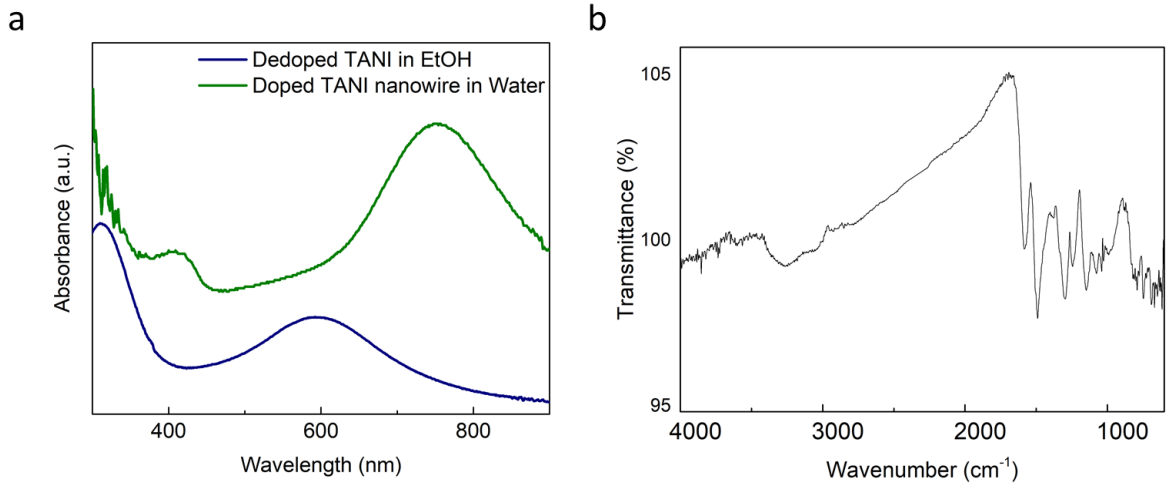

Figure 2.1 (a) UV-Vis spectra of doped and de-doped TANI. (b) FT-IR spectrum of de-doped TANI.

UV-vis spectroscopy was performed on the as-synthesized TANI emeraldine salt dispersed in water and de-doped TANI dissolved in ethanol, as shown in Figure 2.1a. The doped nanowire TANI in water shows peaks at around 300 nm, 420 nm and 760 nm, which can be ascribed to typical TANI emeraldine salt π-π^*, polaron-π^*, and π-polaron band transitions, respectively. The de-doped TANI shows characteristic emeraldine base bands at 310 nm and 590 nm, corresponding to π-π^* and benzenoid to quinonoid excitonic transitions.[15]

FT-IR spectroscopy was performed on de-doped TANI dissolved in ethanol on an attenuated total reflectance device and the spectrum is shown in Figure 2.1b. The broad band from 3200 to 3500 cm^{-1} corresponds to N-H stretching vibrations. The smaller shoulder band from 3000 to 3100 cm^{-1} can be ascribed to aromatic C-H stretches. The sharp peaks at 1580 and 1490 cm^{-1} are associated with C=N and C=C double bond stretching vibrations of the quinonoid and benzenoid rings, respectively. The peaks at 1300 and 1240 cm^{-1} can be ascribed to C-N stretching modes. The peaks at around 1140 cm^{-1} are due to benzenoid-NH^+-quinonoid vibrations.[25,26]

2.2.3. MALDI-TOF Mass Spectroscopy analyses

Interfacial polymerization of aniline has been shown to yield high molecular weight polyaniline,[20,27] and dimer aniline has been proposed to be an intermediate product in the aniline polymerization reactions.[22] Stejskal *et al.*, have reported chemical oxidative polymerization of aniline dimer in single-phase acidic aqueous ethanol solutions, and their process yields polyaniline that has a unimodal molecular weight distribution with weight-average molecular weight of 3700.[28] This is an interesting phenomenon, as polyaniline synthesized in a single phase reaction tends to have lower weight-average molecular weights than interfacially polymerized polyaniline.[23]

It was, therefore, initially expected that an interfacial reaction between aniline dimer and an oxidizing agent would also produce polyaniline. However, the products proved to be soluble in many organic solvents (ethanol, methanol, dichloromethane, *etc.*). Given their solubility in most organic solvents, the products were suspected to be composed of low molecular weight oligomers and MALDI-TOF mass spectroscopy was performed to study the molecular weight distributions. Table S2.1 shows the identities of peaks found in the mass spectra.

2.2.3.1. Effects of reaction time

To understand the effects of reaction time, the interfacial precipitates of the reaction between aniline dimer and APS were extracted with a pipet at set time periods, centrifuged and washed with DI water. The solids were characterized with MALDI-TOF mass spectroscopy without a matrix and the results are shown in Figure 2.2. Note that these samples were not purified extensively via dialysis due to time constraints and small sample quantities, and therefore the mass spectra inevitably show the presence of some impurities. In addition, the thickness of the tetra-aniline precipitate layer at the interface was rather thin at the beginning of the reaction, making

clean extraction extremely difficult to perform. As a result, the 30 min and 2 h samples might show disproportionately high amounts of dimer aniline (mass = 184). As shown in Figure 2.2, the interfacial precipitates slowly transitioned from mostly aniline dimer to mostly tetra-aniline during the first 4 h. The 4 h and 20 h samples show tiny peaks at 548 and 728, corresponding to hexa-aniline and octa-aniline, respectively. After four hours, the spectrum shows no aniline dimer, indicating completion of the reaction. This suggests that a 4 h-reaction time is sufficient for the reaction. Over the next two days, the octa-aniline fraction increased to about 10% after 72 hours. However, we were not able to extend the reaction time to over a week, as the products slowly dissolved into the organic phase. Nonetheless, it is fair to assume that time does not significantly affect the degree of polymerization of the product.

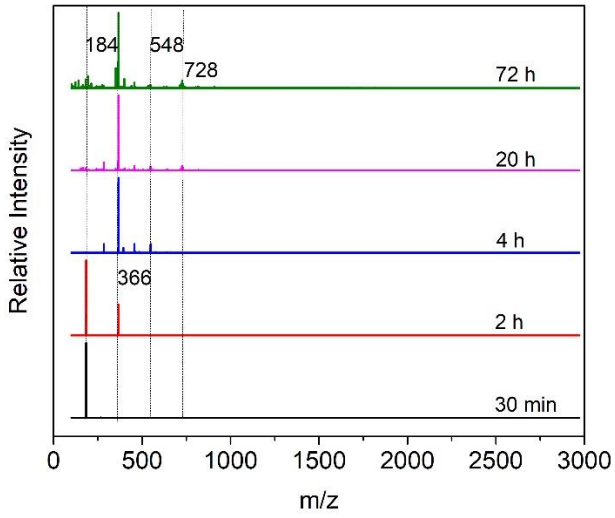

Figure 2.2 MALDI-TOF mass spectra of aniline dimer interfacial reaction products extracted at different time intervals.

2.2.3.2. Effects of APS to dimer ratio

In a traditional tetra-aniline synthesis, the oxidizing agent to dimer aniline ratio is usually maintained at 1:1. To study the effects of oxidizing agent to dimer aniline ratio, interfacial

oligomerization reactions with various APS to dimer ratios were performed and the compositions of the oligomerization products were determined based on MALDI-TOF-MS peak integration. All reactions proceeded for about 4 h, and the MALDI-TOF mass spectra are shown in Figure 2.3a. The composition of each product is estimated based on the area ratio of the mass spectrum peaks, and the semi-quantitative results are shown in Figure 2.3b. Based on limited data, no consistent trend could be observed. However, the majority of the products are TANI and no peaks above 1500 are found. It appears that regardless of the dimer aniline to APS ratio, the reactions tend to stop at the tetramer stage.

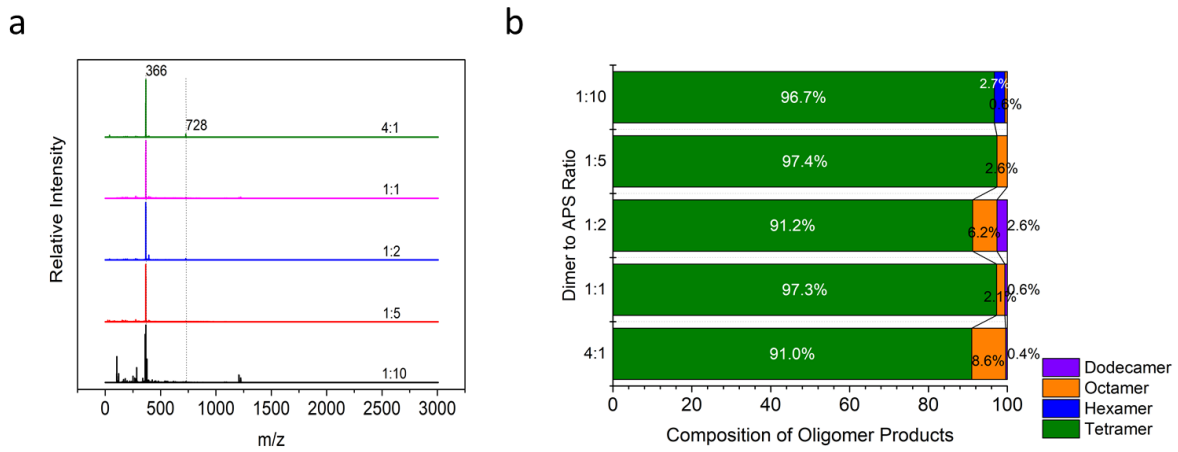

Figure 2.3 (a) MALDI-TOF mass spectra of dimer aniline interfacial reaction products with different aniline dimer to APS ratios. (b) A bar chart showing compositions of the products.

2.2.3.3. Effects of concentrations of reactants

The concentration of the aniline dimer in the organic solution seems to affect not only the reaction rate, but also the molar mass distribution of the products. To study the effects of the concentration of the reactants on the products, different concentrations of aniline dimer in dichloromethane solutions were prepared and reacted with APS/HNO_3 solutions with the same concentrations (1:1 molar ratio reactions). All reactions were stopped at 4 h and the mass spectra

of the products are shown in Figure 2.4. The majority product from all the reactions is TANI (mass = 366). At 1 mg/mL and 2 mg/mL, the products did not contain any higher oligomers, while at higher concentrations of 5 mg/mL and 10 mg/mL, small peaks corresponding to the aniline hexamer (mass = 548) and the aniline octamer (mass = 728) appear in the spectra. High concentration reaction products also show the presence of unreacted aniline dimer (mass = 184), indicating that either longer reaction times or dilution of the reaction mixture is required to achieve completion of the reaction. It is also possible that at higher concentrations, the aniline dimer salt crystals near the interface are sufficiently bulky to prevent the oxidation of interior dimer molecules.

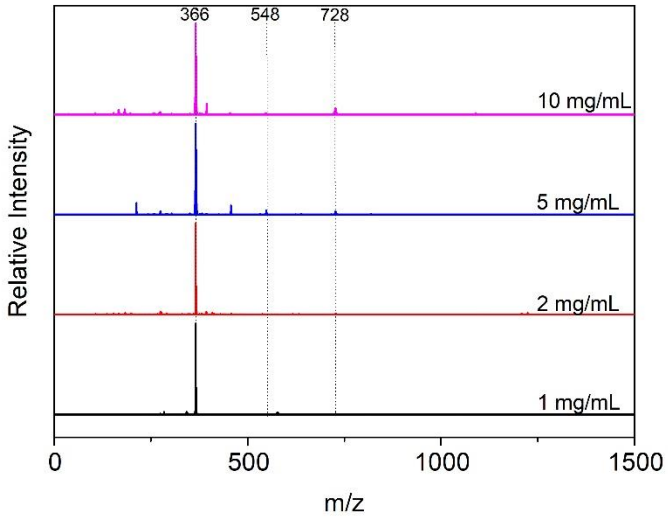

Figure 2.4 MALDI-TOF mass spectra of reaction products from aniline dimer interfacial reactions with different dimer aniline concentrations (1, 2, 5 and 10 mg/ml).

2.2.3.4. Effects of oxidation potential

To study the effects of oxidation potential on the molecular weight of the oligomer products, 3 weaker oxidizing agents were used instead of APS, while the concentration of dimer (2 mg/mL), molar ratio of dimer to oxidizing agents (1 equivalent), and the concentration of dopant acid (1.0

M nitric acid) were held constant. All reactions were stopped after 4 h. In decreasing order of standard oxidation potentials, the oxidizing agents used were: APS (2.01 V), H_2O_2 (1.78 V), $HAuCl_4$ (0.93 V) and $AgNO_3$ (0.80 V). The products of dimerization with different oxidizers exhibited similar molecular weight distributions, as shown in Figure 2.5. All products showed a major peak at 366, corresponding to TANI. $HAuCl_4$ and $AgNO_3$ oxidized products also contained trace amounts of hexa-aniline and octa-aniline, while hydrogen peroxide oxidization products contained almost pure TANI. It seems that as the oxidizing potential is increased from 0.80 V (silver nitrate) to 2.01 V (APS), the final products are still composed of more than 95% tetra-aniline.

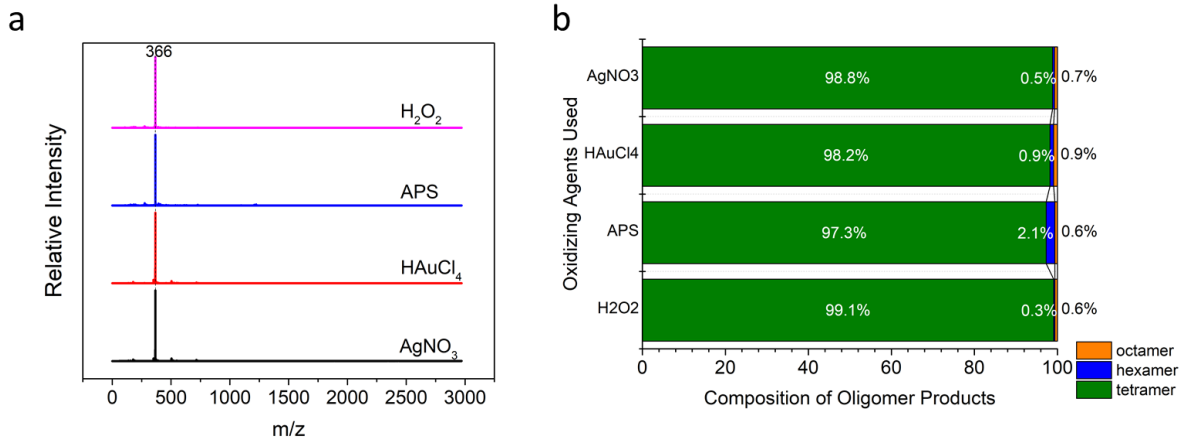

Figure 2.5 (a) MALDI-TOF mass spectra of dimer aniline interfacial reaction products with different oxidizing agents. (b) A bar chart showing compositions of products of interfacial reactions using different oxidants.

In summary, the interfacial dimerization of aniline dimer in the presence of APS is a rather facile and robust method to synthesize TANI. Parameters such as dimer to oxidant ratio, oxidation potential of the oxidants, and the concentration of the reactants have limited effects on the composition of the products. For optimal yield and purity, the reaction should be allowed to proceed for 4 h, and the concentration of the reactants should be limited to no more than 2 mg/mL.

It is also worthwhile to note that hydrogen peroxide tends to yield TANI with very high purity, suggesting a greener synthetic pathway.

2.2.3.5. Mechanism of TANI synthesis

The low degree of polymerization of aniline dimer is an interesting phenomenon. Other research groups have attempted to synthesize higher oligomers of aniline in acidic aqueous media. Wei *et al.* found that the oxidative coupling of TANI to form higher oligomers in an acidic environment seems unlikely.[29] Gao and coworkers synthesized phenyl-capped hexa-aniline by reacting TANI in the pernigraniline oxidation state with aniline dimer under acidic aqueous conditions without any other oxidizing agents.[30] Zhang and coworkers found that octa-aniline and hexadeca-aniline can be synthesized by first reducing TANI to the leucoemeraldine oxidation state and then oxidatively coupling TANI to form aniline octamer and hexadecamer.[19] What these successful synthetic routes share in common is that they each allowed aniline oligomers (or dimers) in the leucoemeraldine state and pernigraniline state to react: Gao *et al.* isolated TANI in the pernigraniline oxidation state and mixed it with aniline dimer in the reduced state; Zhang *et al.* added APS to a suspension of the solid leucoemeraldine form of TANI, which likely resulted in a fraction of the TANI being oxidized to the pernigraniline oxidation state, while the rest remained in the leucoemeraldine state.

Based on these findings, we propose a mechanism of oxidative coupling of aniline oligomers in acidic media, as shown in Figure 2.6: monoprotonated aniline dimer (R = H) (**1**) gets oxidized (2-electron transfer) into a di-imine cation (**2)**, which is attacked by a monoprotonated aniline dimer to form tetra-aniline in the leucoemeraldine oxidation state (**3**). Only the first step involves external oxidizing agents, and the second step is spontaneous in the presence of un-oxidized monoprotonated aniline dimer because of the difference in chemical potentials. When

only oxidized dimer is present, **2** cannot be converted to **3**. The same should also apply to tetramer (R = aniline dimer), although in this case, **2** is TANI in the pernigraniline oxidation state, and it can be attacked either by a monoprotonated aniline dimer or a TANI in the leucoemeraldine salt form. This mechanism is comparable to that proposed for polyaniline chain growth,[29,31] but the low solubility (in aqueous solution) and low oxidation state of aniline dimer/tetramer limits the availability of free un-oxidized aniline dimer/tetramer in the chain growth step of the reaction, thus resulting in a low degree of oxidative polymerization of aniline dimer and tetramer under solid-aqueous reaction conditions.

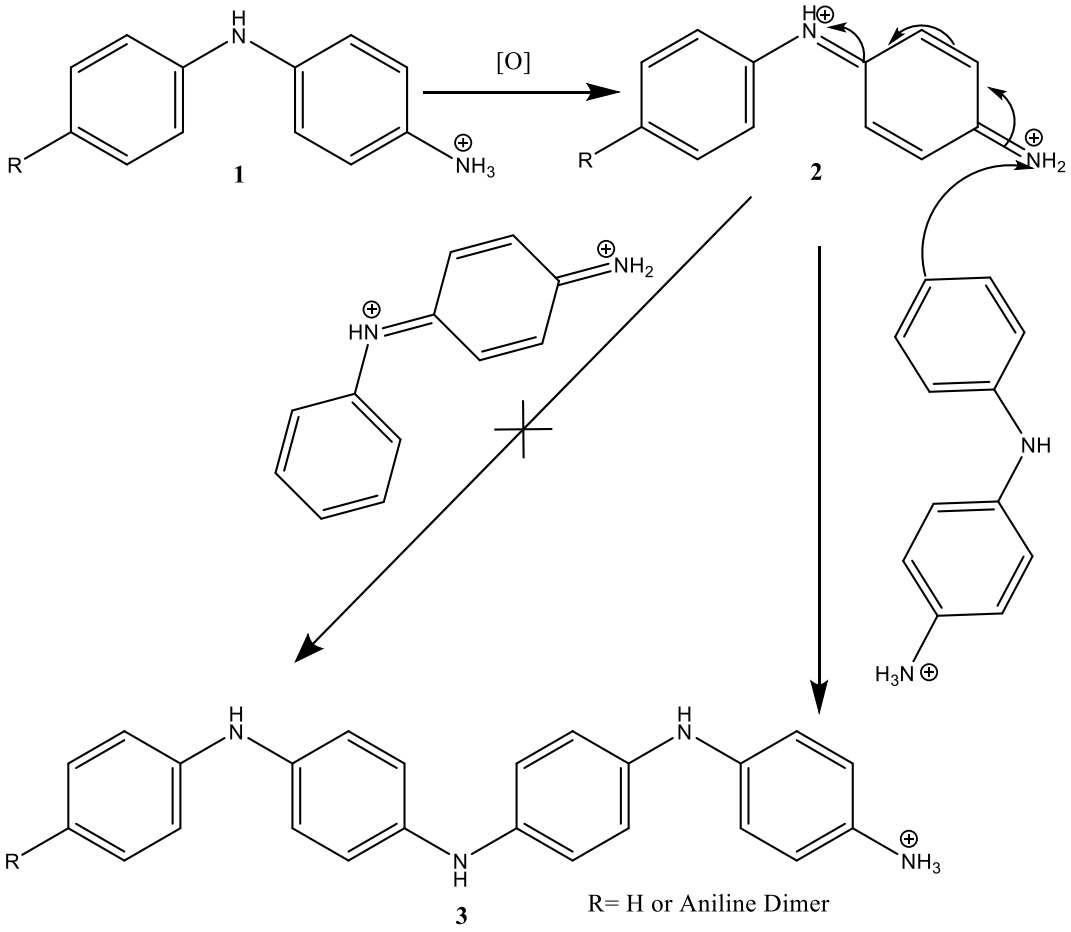

Figure 2.6 Mechanism of oxidative coupling of aniline dimer/tetramer in acidic aqueous media.

2.2.4. Morphology

As with PANI nanowires synthesized using interfacial polymerization methods, TANI as synthesized also possesses some unique nanostructures. The morphology of the de-doped TANI solids were characterized with scanning electron microscopy.

2.2.4.1. Effects of concentration of reactants

As discussed in the synthesis section, the concentration of reactants significantly affects the rate of the interfacial dimerization reaction, although having little effect on the molecular weight distribution of the products. However, in terms of affecting product morphology, reactant concentration plays a critical role. Four dichloromethane solutions of different concentrations of dimer aniline (0.5 mg/mL, 1 mg/mL, 2 mg/mL, and 5 mg/mL) were prepared and reacted with 1 equivalent of APS/1.0 M HNO_3 solutions with the same concentration. All reactions proceeded for 4 h. The SEM images of the de-doped samples are shown in Figure 2.7. At lower concentrations, all TANI products showed distinct interwoven nanowire structures; however, once the concentration was increased to 5 mg/mL, the pure nanowire morphology disappeared, giving way to large coiled sheet-like structures. Similar observations with interfacial PANI synthesis have also been observed.[32]

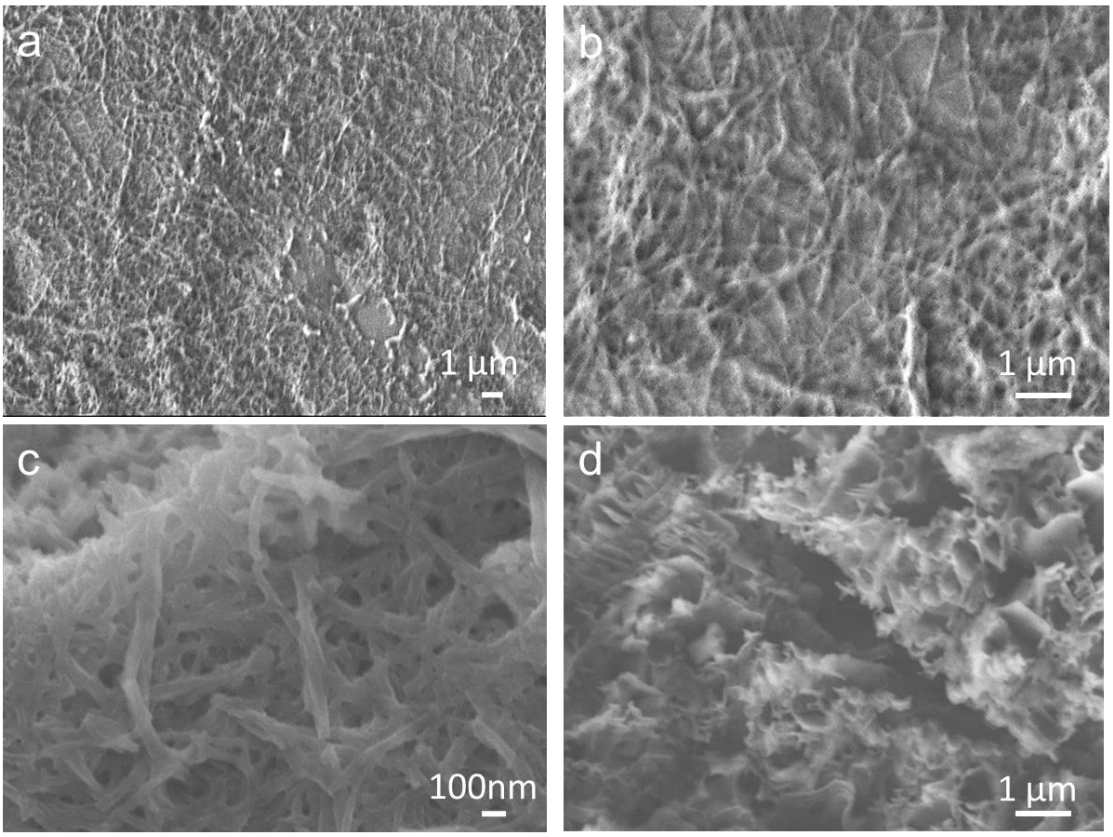

Figure 2.7 Scanning electron microscopy images of TANI synthesized with different aniline dimer and APS concentrations: (a) 0.5 mg/mL, (b) 1 mg/mL, (c) 2 mg/mL and (d) 5 mg/mL.

2.2.4.2. Effects of dopants

In this study, three mineral acids (1.0 M hydrochloric acid, 1.0 M sulfuric acid and 1.0 M nitric acid) were used as dopants during the synthesis, and all reactions used the same concentration of aniline dimer (2 mg/mL) and oxidizing agent (2 mg/mL APS). The resulting TANI products all exhibited distinct nanostructures, with HNO_3-doped TANI showing nanoribbons or nanowires about 200 nm in diameter, H_2SO_4-doped TANI displaying randomly stacked sheets a few microns in size with some nanowires grown on top, and HCl- doped TANI forming clusters of nanowires several tens of microns in length and a few hundred nanometers in diameter, as can be seen in Figure 2.8. One interesting observation is that the H_2SO_4 catalyzed TANI synthesis appears to

have taken place faster than the other two. Similar observations were reported previously where TANI self-assembled into clusters of nanowires in HCl, into clusters of sheets in H_2SO_4, and into clusters of ribbons in HNO_3 over the course of a few days.[16] Therefore, it is deduced that fast reaction rates tend to produce sheet like morphologies.

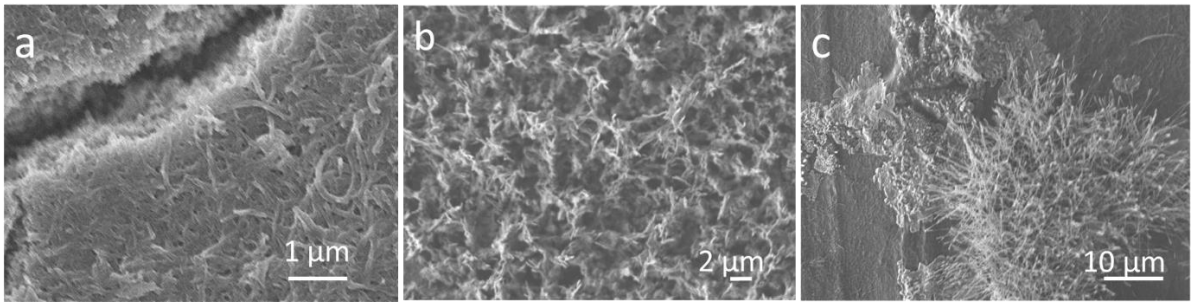

Figure 2.8 Scanning electron microscopy images of TANI synthesized with the following dopants: (a) HNO3, (b) H2SO4, and (c) HCl.

2.2.4.3. Effects of different oxidizing agents

As aniline dimer has a lower oxidation potential than aniline monomer, mild oxidizing agents can be used to synthesize TANI with morphologies that differ only slightly. Four oxidizing agents were used in this study: APS, hydrogen peroxide, chloroauric acid and silver nitrate. The SEM image of the products are presented in Figure 2.9. To eliminate the effects of different dopants, all TANI's were synthesized with 1.0 M HNO_3 as the dopant. All reactions were run for 24 h. TANI synthesized with APS, chloroauric acid and silver nitrate all show distinctive nanowire/nanofiber structures, with diameters ranging from 40 to 100 nm and lengths up to a few tens of micrometers. However, hydrogen peroxide oxidized TANI shows a more complex sheet structure. Upon closer examination, the sheets turned out to be super-structures composed of interwoven nanowires. This more complex morphology might be due to differences in ionic strength of the reaction mixtures. Hydrogen peroxide solution likely has the lowest ionic strength among all four reaction solutions, and lower ionic strength is associated with higher reaction

rates.[33] Hence, the interconnected nanowires quickly grow into 2D plates, as secondary growth could not be prevented.

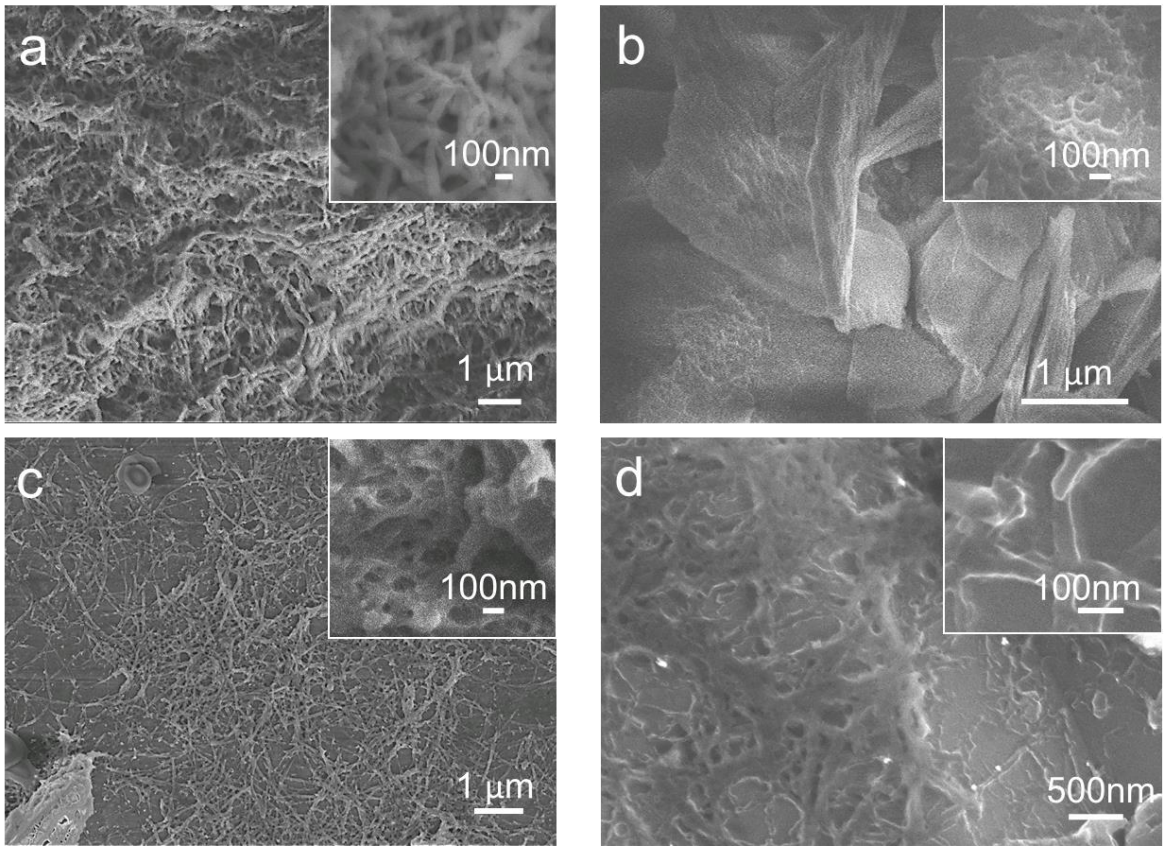

Figure 2.9 Scanning electron microscopy images of TANI synthesized with the following oxidizing agents: (a) APS, (b) H_2O_2, (c) $HAuCl_4$, and (d) $AgNO_3$. The insets show expanded images of the nanofibrillar morphologies.

It is also worth mentioning that when chloroauric acid and silver chloride were used as oxidizing agents, metal particles were initially found on the TANI nanowires (Figure S2.2). However, after 24 h, most metal particles could no longer be seen on SEM samples. A similar phenomenon has been reported previously and is likely due to the fact that TANI functions as an interfacial transfer agent for the metal particles, causing the metal particles to migrate into the organic layer.[14]

2.2.4.4. Self-assembly of dimer aniline across the water/organic solvent interface

One interesting phenomenon was observed during synthesis: when the concentration of oxidant was low, or when a weak oxidizer ($AgNO_3$) was used, it was not uncommon to observe the formation of a white ring around the inside wall of the glass vial at the water-organic solvent interface, before the white ring got oxidized into green tetra-aniline flakes.

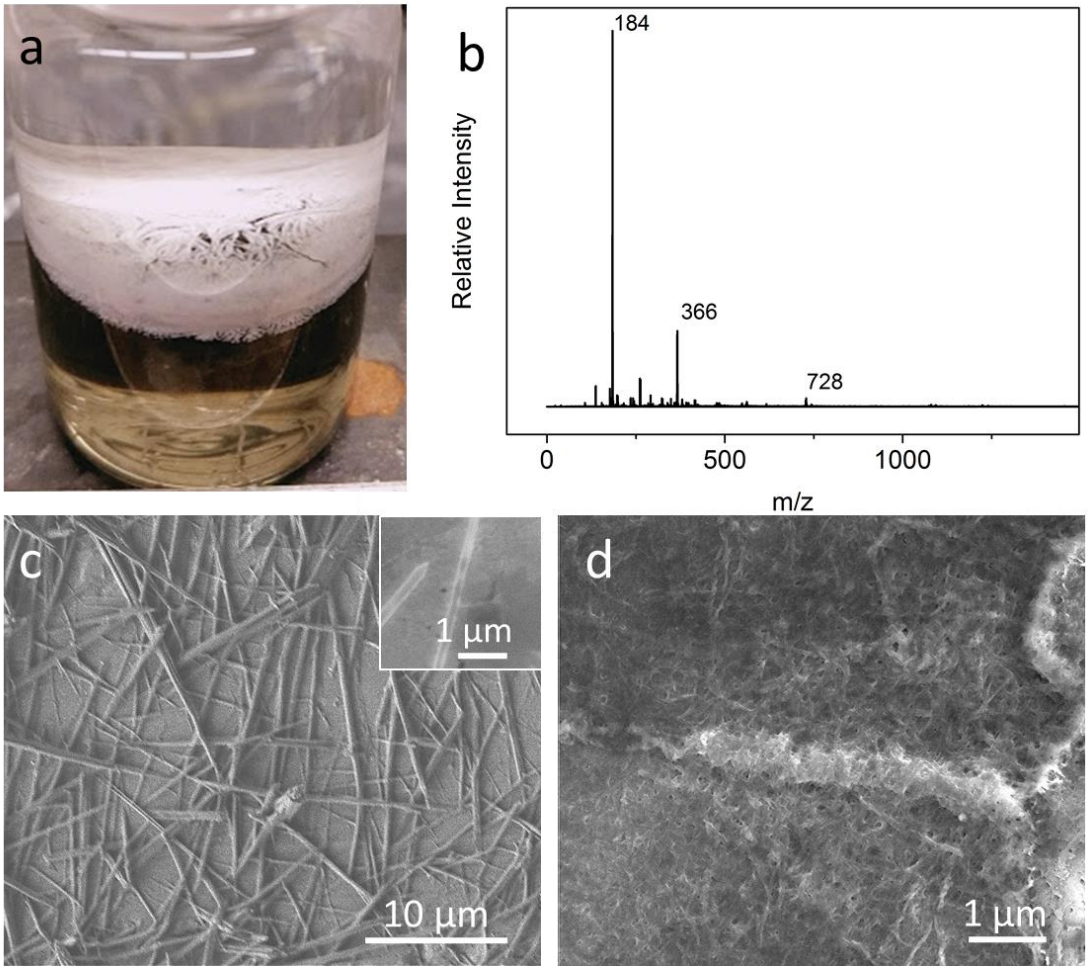

Figure 2.10 (a) A photo of aniline dimer cation self-assembly at the aqueous-organic interface. (b) MALDI-TOF mass spectrum of the white precipitates formed at the interface. (c) SEM images of the white precipitates at the interface. Inset: a zoomed-in image showing the diameter of a thin nanofiber. (d) SEM image of TANI synthesized from the white precipitates.

To prevent oxidation of the white precipitates, an interfacial self-assembly of aniline dimer was performed as described in the experimental section. As expected, the white precipitates still

formed when there was no oxidizer present, as long as the aqueous solution was acidic enough. Therefore, it is speculated that the white solid is likely an insoluble aniline dimer salt (i.e. aniline dimer-HCl). MALDI-TOF mass spectroscopy indeed confirms that the white precipitate consists primarily of aniline dimer (Figure 2.10b). Aniline dimer is originally dissolved in the organic phase; however, upon contact with the acidic aqueous phase, it becomes protonated and migrates to the aqueous phase. The solubility of aniline dimer-HCl in water is low and thus aniline dimer aggregates via π-π stacking, electrostatic interactions and hydrogen bonding. The precipitates are primarily composed of high aspect ratio nanotubes, with diameters ranging from a few tens of nanometers to a few micrometers.

This interesting phenomenon shows that even extremely short chains (only two moieties) can yield surprisingly long nanotubes/nanofibers. The SEM images are shown in Figure 2.10. It is noteworthy that the dimer salt has much more time to self-assemble (30 min) at the interface than it does in the presence of an oxidizing agent (less than a few seconds). Therefore, the bigger "microtubes" were probably grown via Oswald ripening at the expense of the smaller nanotubes. It is highly likely that these small nanotubes, or the precursor to these smaller nanotubes, served as soft templates for TANI/PANI nanowire growth.

To test this hypothesis, the white nanotube/nanowire aniline dimer salt precipitates were added to a solution of APS in 1.0 M HCl and the products were isolated after 4 h. The products proved to be interwoven nanowires, about 70 nm in diameter (of similar dimensions to the smallest aniline dimer salt nanotubes), as shown in Figure 2.10d. These results suggest that a solvent/non-solvent interface is sufficient to produce well-defined nanowire/nanofiber morphologies, while an oxidative environment is not necessary.

Our group has previously reported hierarchical assembly of TANI in organic/aqueous acid co-solvents to yield a myriad of nanostructures.[16] Lyu *et al.* have also studied self-assembly of TANI in organic-acidic media under ultrasonic irradiation.[15] They found that TANI molecules self-assemble into various nanostructures via interplay of π-π interactions, hydrogen bonding, hydrophobic and electrostatic interactions. The same could be true for aniline dimers. More research is currently underway to study the origin of the nanofiber morphology of the aniline dimer salt and how other parameters affect the morphology of self-assembled aniline dimers.

Combining the SEM results, it is apparent that TANI, similar to PANI, intrinsically adopts a nanowire morphology,[34] and this is most likely related to how the dimer salt stacks with each other via electrostatic interactions, π-π stacking and H-bonding. Thus, suppressing the secondary growth of nanowires could yield pure nanowire TANI. However, if the aggregation process takes place too rapidly (due to either high concentration or low ionic strength), secondary growth could result in sheets or a more complicated 3D morphology, and eventually lead to amorphous products. Interfacial conditions are effective in limiting secondary growth in most cases, yielding a majority nanowire/nanotube morphology.

2.2.5. Electrochemical Characterization

Similar to polyaniline, TANI also shows good potential for electrochemical energy storage. The performance of TANI nanowires as electrochemical supercapacitor electrodes were characterized using standard cyclic voltammetry (CV), electrochemical impedance spectroscopy (EIS) and galvanostatic charge-discharge (CC) techniques. The cyclic voltammograms of TANI nanowire electrodes in 1.0 M H_2SO_4 solution from -0.05 to 0.9 V at different scan rates are shown in Figure 2.11a, and the charge-discharge diagrams at different current densities are shown in Figure 2.11b. The EIS was collected in the frequency range from 10 mHz to 1 MHz, at +0.5 V bias

against the reference electrode with a 10 mV amplitude. The applied bias corresponds to the emeraldine to pernigraniline transition potential of TANI. The Nyquist plots are shown in Figure 2.11c.

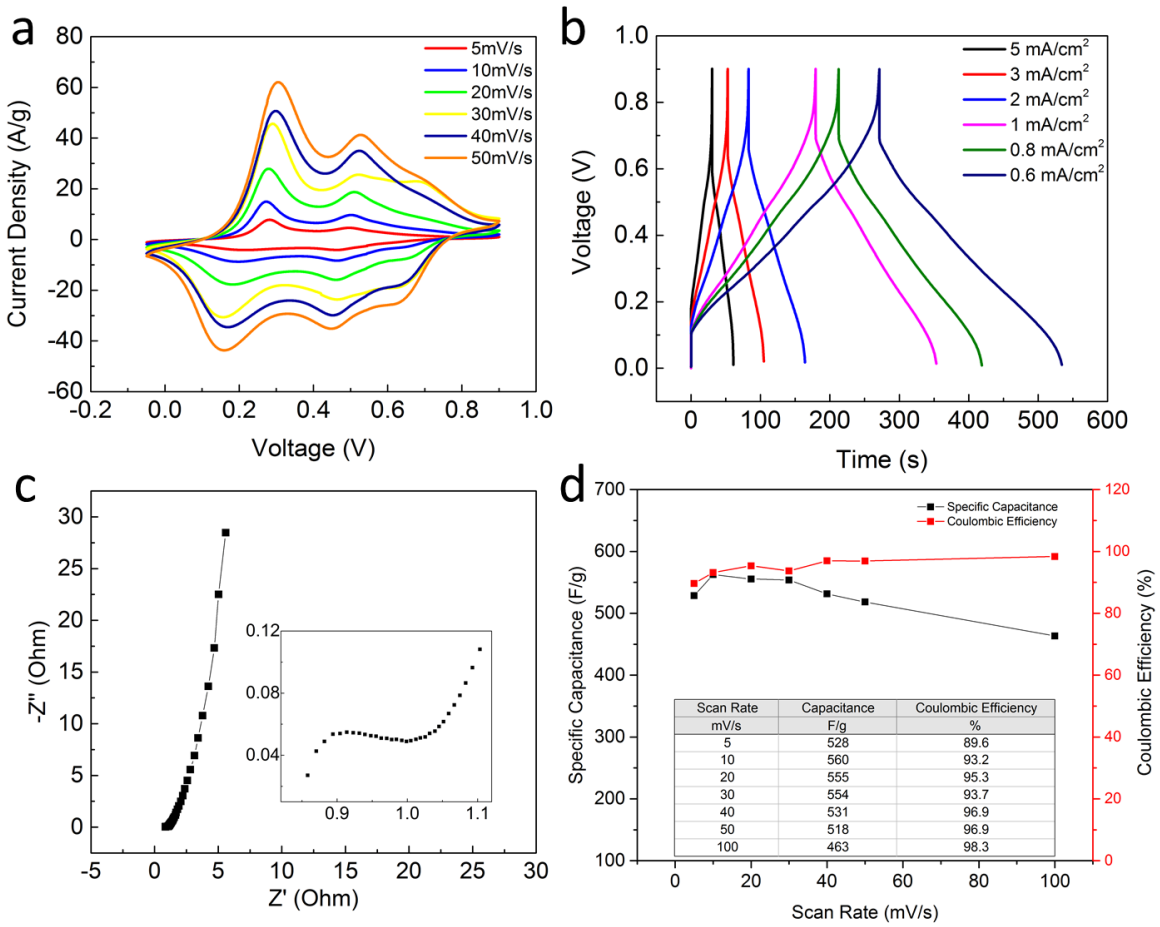

Figure 2.11 Electrochemical performances of a TANI nanowire-electrode in 1.0 M H2SO4: (a) cyclic voltammograms at various scan rates. (b) Galvanostatic charge-discharge curves at various current densities. (c) a Nyquist plot of TANI electrode (0.3 vs. Ag/AgCl). Inset: zoomed-in image showing high frequency range. (d) Specific capacitance and Coulombic efficiency at various scan rates.

The cyclic voltammetry curves show three sets of redox peaks in the first tens of cycles during fast cycling (most prominent in the 30 mV/s, 40 mV/s and 50 mV/s scans), and only two sets of peaks remain in later slow scans. The first set of peaks (0.25~0.3 V vs. Ag/AgCl for the anodic peaks) corresponds to the transition between leucoemeraldine and emeraldine states of

TANI. The second set of peaks (0.45~0.5 V vs. Ag/AgCl for the anodic peaks) corresponds to the transition between emeraldine to pernigraniline states. The third set of peaks (~0.7 V vs. Ag/AgCl for the anodic peaks) are believed to be associated with electrochemical processes of TANI hydrolysis byproducts.[13] The peak height of the anodic peaks are consistently higher than their corresponding cathodic peaks, suggesting that the reactions are not completely reversible. Note that the potential of the first set of peaks correspond very well with reported values for PANI supercapacitors. While the third set of peaks are rarely seen in PANI, given their proposed association with degradation byproducts, it is potentially a great opportunity to understand how PANI electrodes degrade over prolonged cycling.

The specific capacitance and Coulombic efficiency of TANI nanowire electrodes were calculated from CV diagrams based on Equations 2.1 and 2.2, and the results are shown in Figure 2.11d. TANI nanowire electrodes exhibit good specific capacitance and rate capability. However, they suffer from low Coulombic efficiency at slow scan rates, which, in turn, reduces the specific capacitance. This decrease in Faradaic efficiency resulting from leakage currents likely caused the drop in specific capacitance at the 5 mV/s scan rate. Based on the shape of the CV curves (unequal anodic-cathodic peak heights) and Coulombic efficiency data (lower efficiency at slower scan rates), it is likely that there is a chemical process taking place alongside the electrochemical processes (likely an EEC mechanism).[35] One possible process is the hydrolysis of the pernigraniline form of TANI.

The charge-discharge curves show apparent IR drops due to the high final charge voltage/initial discharge voltage (0.9 V), but are otherwise quite close to triangular in shape. Note that the IR drop coincides with the voltage difference between the highest voltage on the CV curve and the potential where the discharge CV curves intersect with the x-axis (I = 0 A). This IR drop

effectively limits the potential window of TANI nanowires to about 0.7 V. When slower scan rates are used, the Coulombic efficiency calculated based on charge-discharge curves range from 90 to 95%.

The Nyquist plot of the TANI nanowire electrodes show good pseudo-capacitor behavior, with a semi-circle in the high frequency range and a steep straight line in the low frequency range. The semi-circle shows a rather small radius, indicating rapid charge transfer kinetics. The plot also shows a very short 45° segment, suggesting fast ion diffusion processes. This can likely be ascribed to the nanowire morphology, as the nanowires exhibit relatively large specific areas and readily accessible ion channels to facilitate ion diffusion. The uncompensated series resistance calculated from the extrapolated intercept of the curve and the x-axis is about 1.0 Ω, further verifying the excellent rate capability of these materials.

2.3. Conclusions

A facile interfacial method has been developed to produce TANI nanowires, nanofibers, or nanosheets in a single step. Various oxidizing agents and dopants can be used to produce high purity TANI nanowires with H_2O_2/HNO_3 yielding the highest purity TANI, and APS/HNO_3 yielding the highest quality nanowires. Other types of morphology can also be obtained by tweaking the concentration of the reactants and the ionic strength of the aqueous solution. TANI nanowire electrodes possess promising supercapacitor performances, with good specific capacitance (560 F/g at a 10 mV/s scan rate and 463 F/g at 100 mV/s) and excellent rate capability.

2.4. Experimental

2.4.1. Preparation of tetra-aniline (TANI) nanowires

Tetra-aniline was synthesized via a modified interfacial polymerization method described in the literature.[20] In a typical synthesis, 20.0 mg of N-phenyl-p-phenylenediamine (dimer aniline) was dissolved in 10 mL dichloromethane. 1 equivalent amount of oxidizing agent (22.0 mg ammonium persulfate, or 20.0 μL 30 v% H_2O_2, or 18.5 mg $AgNO_3$, or 24.0 mg $HAuCl_4$) was dissolved in 10 mL 1.0 M aqueous inorganic acidic solution (HCl, HNO_3, or H_2SO_4). The aqueous phase was added on top of the denser organic phase drop-wise. The interfacial reaction was allowed to react for set time periods (30 min to 24 h) under static conditions. At the end of the reaction, the aqueous phase and the interfacial precipitates were separated from the organic phase and dialyzed (regenerated cellulose dialysis tubing, 12,000-14,000 d, Fisherbrand) against deionized water overnight. Alternatively, the aqueous phase could also be centrifuged and washed with deionized water several times until the supernatant became colorless. The precipitate was then de-doped by dialyzing against 1.0 M NH_4OH overnight, and dried in a conventional oven at 60 $^{\circ}$C overnight. The yield of 4 h APS oxidized TANI was about 92%. The ^{1}H NMR spectrum is shown in Figure S2.3. ^{1}H NMR (400 MHz, DMSO-d_6) δ 7.54 (s, 1H), 7.26-7.20 (t, J = 8.25 Hz, 2H), 7.17-7.09 (t, J = 8.55 Hz, 2H), 7.07-6.76 (m, 12H), 6.74-6.65 (d, J = 8.04 Hz, 2H), 4.94-4.83 (s, 1H). MALDI-TOF MS: m/z 366.

2.4.2. Self-assembly of dimer aniline across a water-dichloromethane interface

About 10 mg of dimer aniline was dissolved in 10 mL dichloromethane. About 2 mL of 1.0 M HCl solution was added on top of the organic solution drop-wise. After 30 minutes, the interfacial precipitates were carefully removed using a plastic spatula, rinsed with a small amount

of de-ionized water, and drop-cast onto a piece of gold-coated PET film for SEM imaging. The precipitates were air-dried at room temperature to prevent oxidation.

2.4.3. General Characterizations

Scanning electron microscopy (SEM) measurements were performed with an FESEM JOEL JSM-6700F FE-SEM at 1 kV to 5 kV. The SEM samples were prepared by drop-casting a sonicated TANI dispersion in deionized water onto aluminum foil; the solvent was allowed to evaporate at room temperature. Matrix Assisted Laser Desorption/Ionization Time of Flight Mass Spectroscopy (MALDI-TOF) measurements were performed with a Bruker Ultra-flex MALDI TOF without a matrix[36] in the range of 0-10,000 d. The MALDI-TOF samples were prepared by dissolving about 1 mg of product in 5 mL of ethanol. About 20 μL of the sample solution was dropped onto the sample holder and the solvent was evaporated at room temperature. Fourier Transform Infrared Spectroscopy by Attenuated Total Reflectance (FT-IR) was performed on a JASCO FT/IR-6300 in the range of 800-4000 cm^{-1} wavenumbers. The dried de-doped TANI solid sample was added directly onto the sample holder. Ultraviolet-visible (UV-vis) spectroscopy was recorded on a Shimadzu UV-3101 PC UV-vis-NIR Scanning Spectrophotometer instrument in the range of 300-1000 nm. The samples were briefly sonicated in a bath ultra-sonicator before being transferred into cuvettes for data collection. The ^{1}H NMR spectroscopy was conducted on a Bruker AV400 NMR spectrometer. The data were collected in DMSO d-6 solution at room temperature.

2.4.4. Electrochemical Characterization

Cyclic voltammetry (CV), galvanostatic charge-discharge (CC) and electrochemical impedance spectroscopy (EIS) analyses were performed on a Biologic VMP3-10 potentiostat. The samples were drop-cast on 1x1 cm^2 graphite paper electrodes, dried in an oven at 50 $^{\circ}C$ overnight and then soaked in 1.0 M sulfuric acid for a few hours before testing. Three-electrode tests were

performed with the TANI sample as the working electrode, platinum foil as the counter electrode and an Ag/AgCl (Sat. KCl) as the reference electrode.

The specific capacitance of the electrode material was calculated from the discharge CV diagrams using the following equation:

$$C_s = \frac{\int_{V_i}^{V_f} idV}{m \times (V_f - V_i) \times v} \tag{2.1}$$

where C_s is the specific capacitance by weight (F/g); i is the discharge current from the CV diagram (A); V_f and V_i denote the final and initial potential (V), respectively; m is the mass of the electrode material (g); and v indicates the scan rate (V/s).

The Coulombic efficiency of the material was calculated from the ratio of the discharge and charge CV area using the following equation:

$$C_E = \frac{\int_{V_i}^{V_f} i_{discharge} dV}{\int_{V_i}^{V_f} i_{charge} dV} \tag{2.2}$$

where $i_{discharge}$ and i_{charge} are discharge and charge current on the CV curves, respectively.

Another way to obtain the Coulombic efficiency of the material is to carry out calculations based on the charge-discharge diagrams using the following equation:

$$C_E = \frac{\Delta t_{discharge}}{\Delta t_{charge}} \tag{2.3}$$

where C_E is the Coulombic efficiency, and $\Delta t_{discharge}$ and Δt_{charge} denote the time it takes to fully discharge and charge the electrode, respectively.

2.5. Supporting information

Table S2.1 Identities of Mass Spec Peaks

Identities of Mass Spec Peaks	
Identity	Peak location
aniline dimer	184
tetra-aniline	366
hexa-aniline	548
octa-aniline	728
dodeca-aniline	1092
hexadeca-aniline	1428

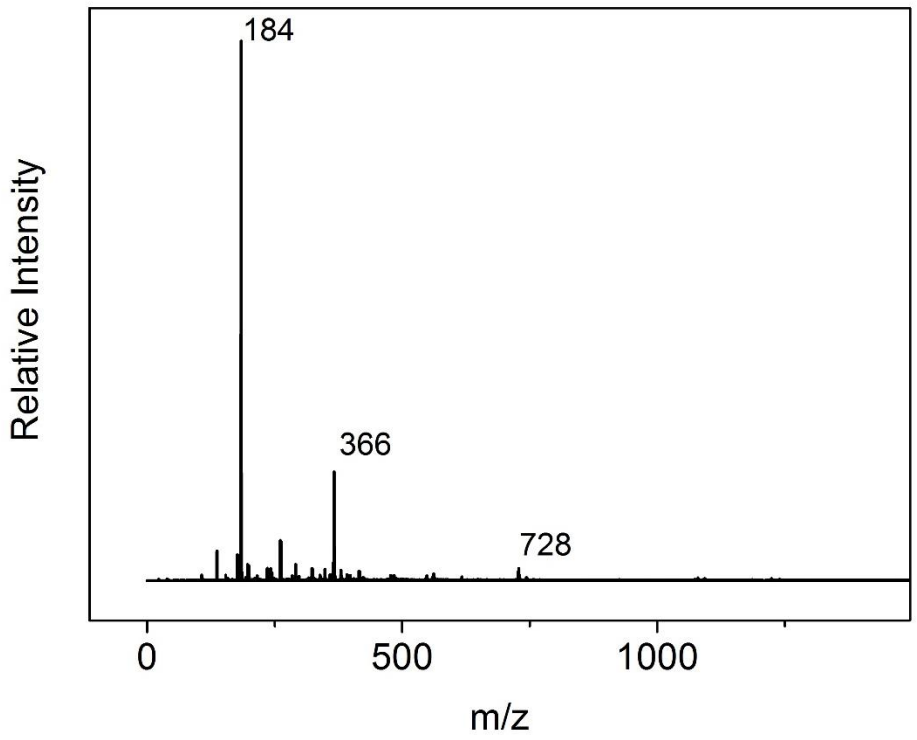

Figure S2.1 MALDI-TOF mass spectrum of dimer interfacial self-assembled precipitates.

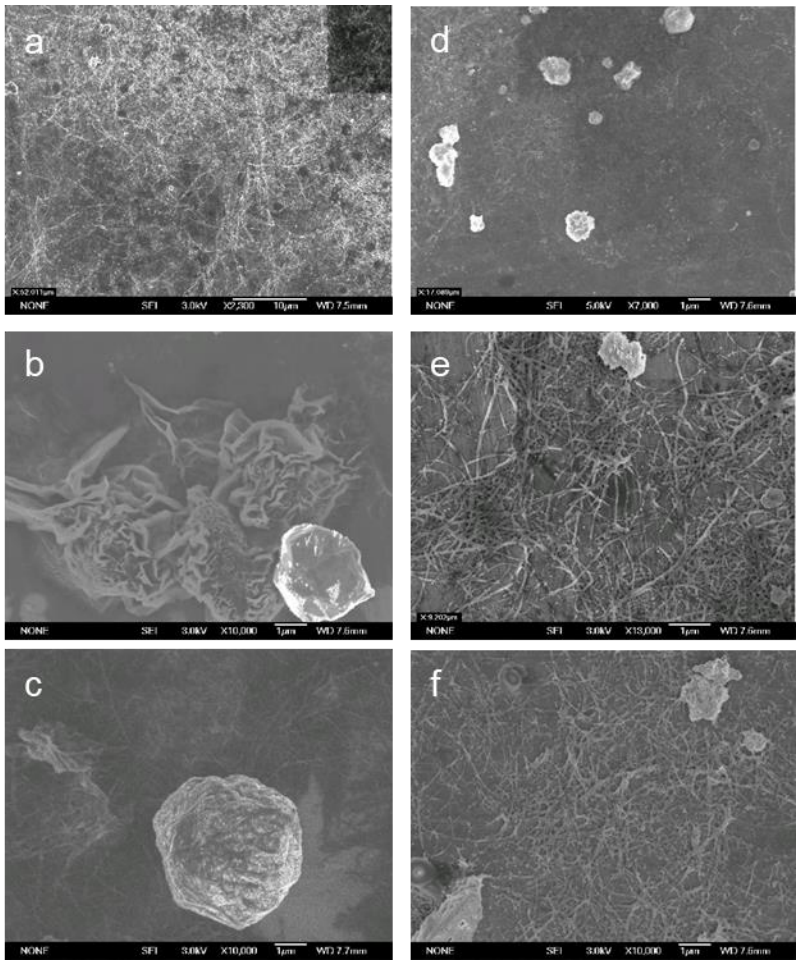

Figure S2.2 SEM images of Ag/Au-TANI reaction mixture extracted at different time intervals: (a) Ag-TANI 1 h, (b) Ag-TANI 2 h, (c) Ag-TANI 4 h, (d) Au-TANI 1 h, (e) Au-TANI 2 h, (f) Au-TANI 4 h.

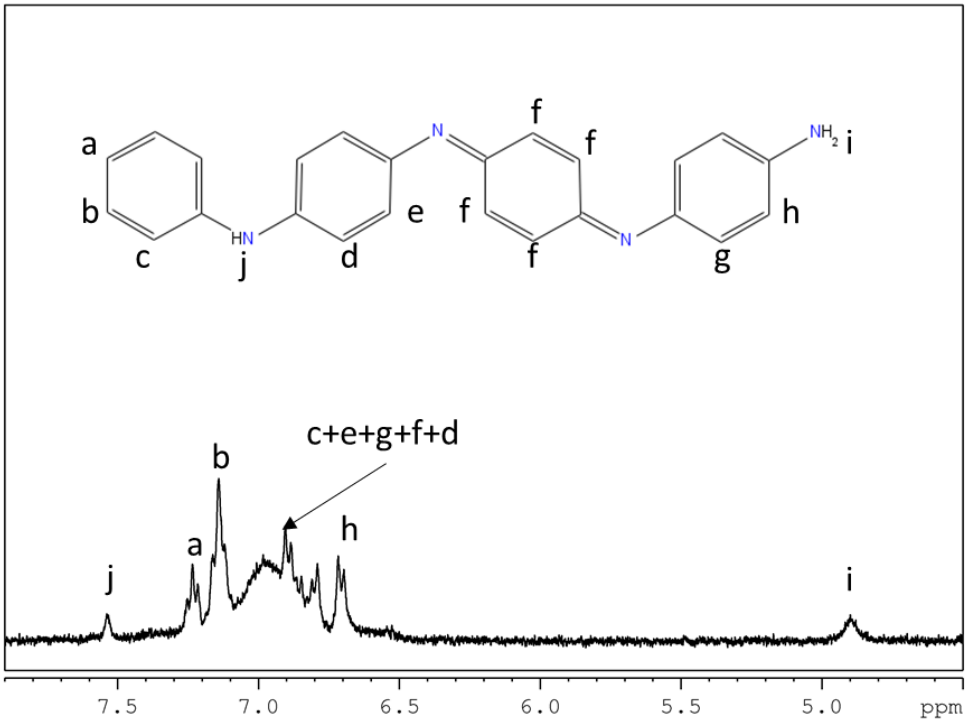

Figure S2.3 ^{1}H NMR of TANI synthesized with APS/1.0 M HNO_3 dissolved in DMSO d-6.

2.6. References

(1) Macdiarmid, A. G.; Chiang, J.-C.; Halpern, M.; Huang, W.-S.; Mu, S.-L.; Nanaxakkara, L. D.; Wu, S. W.; Yaniger, S. I. *Mol. Cryst. Liq. Cryst.* **1985**, *121* (1–4), 173–180.

(2) Huang, J.; Virji, S.; Weiller, B. H.; Kaner, R. B. *J. Am. Chem. Soc.* **2003**, *125* (2), 314–315.

(3) Virji, S.; Kaner, R. B.; Weiller, B. H. *J. Phys. Chem. B* **2006**, *110* (44), 22266–22270.

(4) Al-mashat, L.; Shin, K.; Kalantar-zadeh, K.; Plessis, J. D.; Han, S. H.; Kojima, R. W.; Kaner, R. B.; Li, D.; Gou, X.; Ippolito, S. J.; Wlodarski, W. *J. Phys. Chem. C* **2010**, *114*, 16168–16173.

(5) Baker, C. O.; Shedd, B.; Innis, P. C.; Whitten, P. G.; Spinks, G. M.; Wallace, G. G.; Kaner, R. B. *Adv. Mater.* **2008**, *20* (1), 155–158.

(6) Gu, L.; Liu, S.; Zhao, H.; Yu, H. *RSC Adv.* **2015**, *5* (69), 56011–56019.

(7) Syed, J. A.; Tang, S.; Meng, X. *Sci. Rep.* **2017**, *7* (1), 4403.

(8) Tseng, R. J.; Huang, J.; Ouyang, J.; Kaner, R. B.; Yang, Y. *Nano Lett.* **2005**, *5* (6), 1077–1080.

(9) Mallick, K.; Witcomb, M. J.; Scurrell, M. S. *Gold Bull.* **2006**, *39* (4), 166–174.

(10) Moussa, M.; El-Kady, M. F.; Zhao, Z.; Majewski, P.; Ma, J. *Nanotechnology* **2016**, *27* (44), 442001.

(11) Gu, D.; Ding, C.; Qin, Y.; Jiang, H.; Wang, L.; Shen, L. *Electrochim. Acta* **2017**, *245*, 146–155.

(12) Wang, Y.; Tran, H. D.; Liao, L.; Duan, X.; Kaner, R. B. *J. Am. Chem. Soc.* **2010**, *132* (30), 10365–10373.

(13) Z. C. Sun, L. Kuang, X. B. Jing, X. H. Wang, J. Li, F. S. W. *Chem. J. Chinese Univ.* **2002**, *23* (3), 496–499.

(14) Nirmala Grace, A.; Pandian, K. *J. Phys. Chem. Solids* **2007**, *68* (12), 2278–2285.

(15) Lyu, W.; Feng, J.; Yan, W.; Faul, C. F. J. *J. Mater. Chem. C* **2015**, *3* (45), 11945–11952.

(16) Wang, Y.; Liu, J.; Tran, H. D.; Mecklenburg, M.; Guan, X. N.; Stieg, A. Z.; Regan, B. C.; Martin, D. C.; Kaner, R. B. *J. Am. Chem. Soc.* **2012**, *134* (22), 9251–9262.

(17) Yan, J.; Yang, L.; Cui, M.; Wang, X.; Chee, K. J.; Nguyen, V. C.; Kumar, V.; Sumboja, A.; Wang, M.; Lee, P. S. *Adv. Energy Mater.* **2014**, *4* (18), 1–7.

(18) Li, R. L.; Lin, C. W.; Shao, Y.; Chang, C. W.; Yao, F. K.; Kowal, M. D.; Wang, H.; Yeung, M. T.; Huang, S. C.; Kaner, R. B. *Polymers (Basel).* **2016**, *8* (11).

(19) Zhang, W.; Feng, J.; Macdiarmid, A. G.; Epstein, A. J. **1997**, No. 10, 97–100.

(20) Huang, J.; Kaner, R. B. *J. Am. Chem. Soc.* **2004**, *126* (3), 851–855.

(21) Surwade, S. P.; Agnihotra, S. R.; Dua, V.; Manohar, N.; Jain, S.; Ammu, S.; Manohar, S. K. *J. Am. Chem. Soc.* **2009**, *131* (35), 12528–12529.

(22) Stejskal, J.; Sapurina, I.; Trchová, M. *Prog. Polym. Sci.* **2010**, *35* (12), 1420–1481.

(23) Tran, H. D.; D'Arcy, J. M.; Wang, Y.; Beltramo, P. J.; Strong, V. a.; Kaner, R. B. *J. Mater. Chem.* **2011**, *21* (11), 3534.

(24) Cao, Y.; Smith, P.; Heeger, A. J. *Synth. Met.* **1992**, *48* (1), 91–97.

(25) Navarchian, A. H.; Hasanzadeh, Z.; Joulazadeh, M. *Adv. Polym. Technol.* **2013**, *32* (3).

(26) Abdolahi, A.; Hamzah, E.; Ibrahim, Z.; Hashim, S. *Materials (Basel).* **2012**, *5* (8), 1487–1494.

(27) Huang, J.; Kaner, R. B. **2004**, *126* (3), 851–855.

(28) Ciric-Marjanovic, G.; Trchová, M.; Konyushenko, E. N.; Holler, P.; Stejskal, J. *J. Phys. Chem. B* **2008**, *112* (23), 6976–6987.

(29) Wei, Y.; Tang, X.; Sun, Y.; Focke, W. W. *J. Polym. Sci. Part A Polym. Chem.* **1989**, *27* (7), 2385–2396.

(30) Gao, J.; Li, K.; Sun, H.; Yu, Y.; Wang, C.; Wu, Z.; Zhang, W. *Chem. J. Chinese Univ.* **1999**, *20* (12), 1960–1964.

(31) Sapurina, I. Y.; Shishov, M. A. In *New Polymers for Special Applications*; Gomes, A. D. S., Ed.; InTech: Rijeka, 2012.

(32) Wang, Y.; Jing, X. *J. Phys. Chem. B* **2008**, *112* (4), 1157–1162.

(33) Surwade, S. P.; Manohar, N.; Manohar, S. K. *Macromolecules*. 2009, pp 1792–1795.

(34) Skotheim, T. A.; Reynolds, J. R. *Handbook of Conducting Polymers: Conjugated Polymers Processing and Applications*; 2007.

(35) Heinze, J. *Angew. Chemie Int. Ed. English* **1984**, *23* (11), 831–847.

(36) Ding, Z.; Sanchez, T.; Labouriau, A.; Iyer, S.; Larson, T.; Currier, R.; Zhao, Y.; Yang, D. *J. Phys. Chem. B* **2010**, *114* (32), 10337–10346.

Chapter 3. Electrochemical Deposition of Tetra-Aniline and Its Applications in Supercapacitor Electrodes

Abstract

Electrochemical polymerization of aniline monomer typically results in polyaniline. However, when aniline dimer is used instead of monomer, MALDI-TOF mass spectroscopy shows that the electro-polymerization stops at the oligomer stage. Cyclic voltammetry and pulse chronoamperometry methods can be utilized to deposit nanostructured TANI onto various substrate surfaces. Pulse electrodeposition proves to be a more efficient method than CV at depositing a significant amount of TANI on substrate surfaces. Due to its non-destructive properties, electrochemical deposition is used to grow nanostructured tetra-aniline onto activated carbon (AC) electrodes. The core-shell structure of the TANI-AC composite materials causes synergetic effects between TANI and AC, improving upon the energy density (409 mF/cm^2 vs. 286 mF/cm^2 at 2 mV/s) and the rate capability of AC (76% capacity retention at 100 mV/s compared to 2 mV/s), in addition to the cycle stability of TANI (92% capacity retention after 3000 cycles).

3.1. Introduction

Commercial supercapacitors are typically activated carbon-based electrochemical double layer capacitors (EDLC), storing charge via a physical ion adsorption mechanism. This rapid physical process enables the supercapacitors to demonstrate fast charge-discharge characteristics. However, due to the lack of redox reactions, the energy density of EDLC supercapacitors is much lower than that of batteries. Pseudocapacitors can store charge via fast and reversible redox reactions on the electrode surfaces, vastly increasing the charge storage capacity. Polyaniline

(PANI) is a conducting polymer that can transition through multiple oxidation states, making it a good pseudo-capacitance material. However, PANI-based pseudo-capacitors are usually hindered by low cycle stability that results from physical stresses and chemical degradations during repeated charge-discharge cycles. By combining PANI and activated carbon (AC) into a hybrid composite material, it is possible to simultaneously enhance the energy density of AC and improve the cycle stability of PANI. Compared to other techniques (such as *in situ* polymerization and physical mixing) that make the hybrid materials from ground up, electrochemical deposition is a very simple, yet versatile method, to decorate the surface of existing commercial electrodes.

Electrochemical deposition of polyaniline from aniline monomer in aqueous electrolyte solutions has been studied quite extensively. Several electrochemical deposition methods have been reported to prepare PANI onto various substrates including cyclic voltammetry,[1–3] galvanostatic constant current,[4,5] and chronoamperometry.[6,7] However, almost all previous studies of electrodeposition of PANI used aniline monomer electrolyte solution for deposition, while electrodeposition via pure aniline dimer has not been thoroughly explored. Prior kinetic studies have shown that by adding a small amount of aniline dimer into the aniline monomer solution, the rate of polymerization can be expedited,[8] yet the product of the oxidative polymerization reaction remains long-chain polyaniline. Therefore, the molecular composition of the electrochemical deposition product from aniline dimer should be of interest.

In the previous chapter, interfacial chemical oxidation of N-phenyl-p-phenylenediamine (aniline dimer) has been shown to produce tetra-aniline (TANI) with high purity and nanowire/nanofiber morphologies. The aim of this chapter is to study the electrochemical deposition of PANI/oligoaniline (OANI) using aniline dimer and explore its applications in enhancing supercapacitor performances of AC electrodes. Herein, electrochemical oxidative

polymerization of aniline dimer is shown to produce TANI with relatively high purity. To test the supercapacitor performances, TANI-AC composite materials were prepared by electrodepositing TANI onto activated carbon surfaces via CV or pulse deposition methods. As the TANI was uniformly coated onto the AC surfaces, the composite electrodes benefit from synergetic effects between the conducting oligomer and the carbon substrate, demonstrating much higher energy density than pure AC and much longer cycle life than TANI.

3.2. Results and Discussions

3.2.1. Electrochemical Deposition Processes

Two types of electrochemical processes were employed to deposit oligoaniline onto the working electrode: cyclic voltammetry (CV) and pulse chronoamperometry (pulse deposition). Figure 3.1 shows the current/potential to time response of these two methods. As shown in Figure 3.1a, the CV method applies a cyclic potential sweep in the range of -0.2 to 0.8 V (against the Ag/AgCl reference electrode) at a scan rate of 20 mV/s for 30 cycles. A typical current to time response of this process (a gold plate as the working electrode) is presented in Figure 3.1b. The potential to time and current to time response of a pulse deposition process are shown in Figure 3.1d and 3.1e.

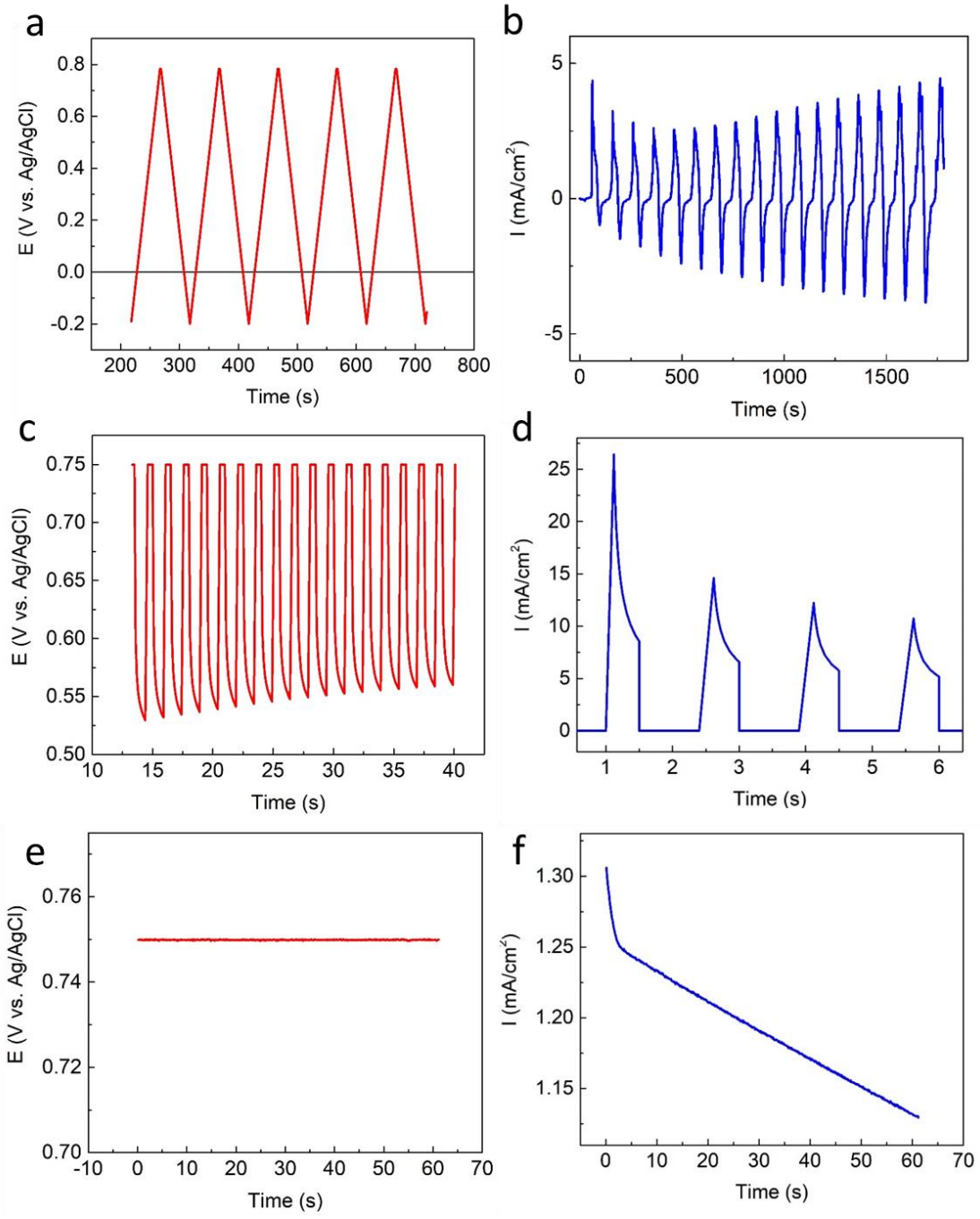

Figure 3.1 The potential to time profiles of a) CV, c) pulse chronoamperometry, and e) non-pulse chronoamperometry, and their corresponding current to time responses: b) CV, d) pulse chronoamperometry and f) non-pulse chronoamperometry.

The pulse chronoamperometry method applies to the working electrode 50 to 500 half-second constant voltage signals of 0.75 V against the reference electrode, each followed by a 1.0 second resting period (0 V vs. the open circuit potential). The applied voltage is determined using

CV data. The aniline dimer oxidation reaction takes place at around 0.6 V, and therefore 0.75 V should be more than enough to induce polymerization/coupling of aniline dimer. Figure 3.1c shows the potential vs. time profile of the working electrode during a typical pulse deposition process. Note that during the resting periods, the working potential does not drop down to 0 V, but instead rests at the open circuit potential of the product. Figure 3.1d displays the current to time response of the first few pulses during a typical pulse deposition process. Within each 0.5-second pulse, the deposition current first spikes up but then gradually decreases over time. This is most likely due to depletion of aniline dimers near the surface of the working electrode. After one second of rest, when the next potential pulse is applied, the deposition current spikes up again, which can be explained by the replenishment of the local aniline dimer concentrations (from bulk solution) during the resting period. This diffusion-controlled phenomenon can be clearly seen in Figure 3.1f, which shows the current-time profile of a 60-second constant voltage electrodeposition process. Note that the current decreases steadily over the entire process without recovery. This diffusion-controlled phenomenon can be circumvented by using a rotating disc electrode. However, this project only utilized stationary working electrodes and hence, a pulse chronoamperometry method is more efficient than a constant voltage method at depositing a significant amount of product onto the working electrode over a relatively short period of time.

Aside from depositing products onto the substrates, the CV method also serves as a powerful tool to study the reaction mechanism(s). Plotting current against potential, the cyclic voltammograms (CV curves) provide a rather informative representation of the CV deposition process. Figure 3.2 shows the CV curves (30 mV/s) of CV electrodepositions of aniline dimer on gold, graphite and activated carbon surfaces. The CV curves of all three substrates appear quite similar in shape, although activated carbon exhibits much higher current density than the others

due to its high specific area. Among the three substrates, gold is the most conductive and therefore its CV is used to analyze the deposition process.

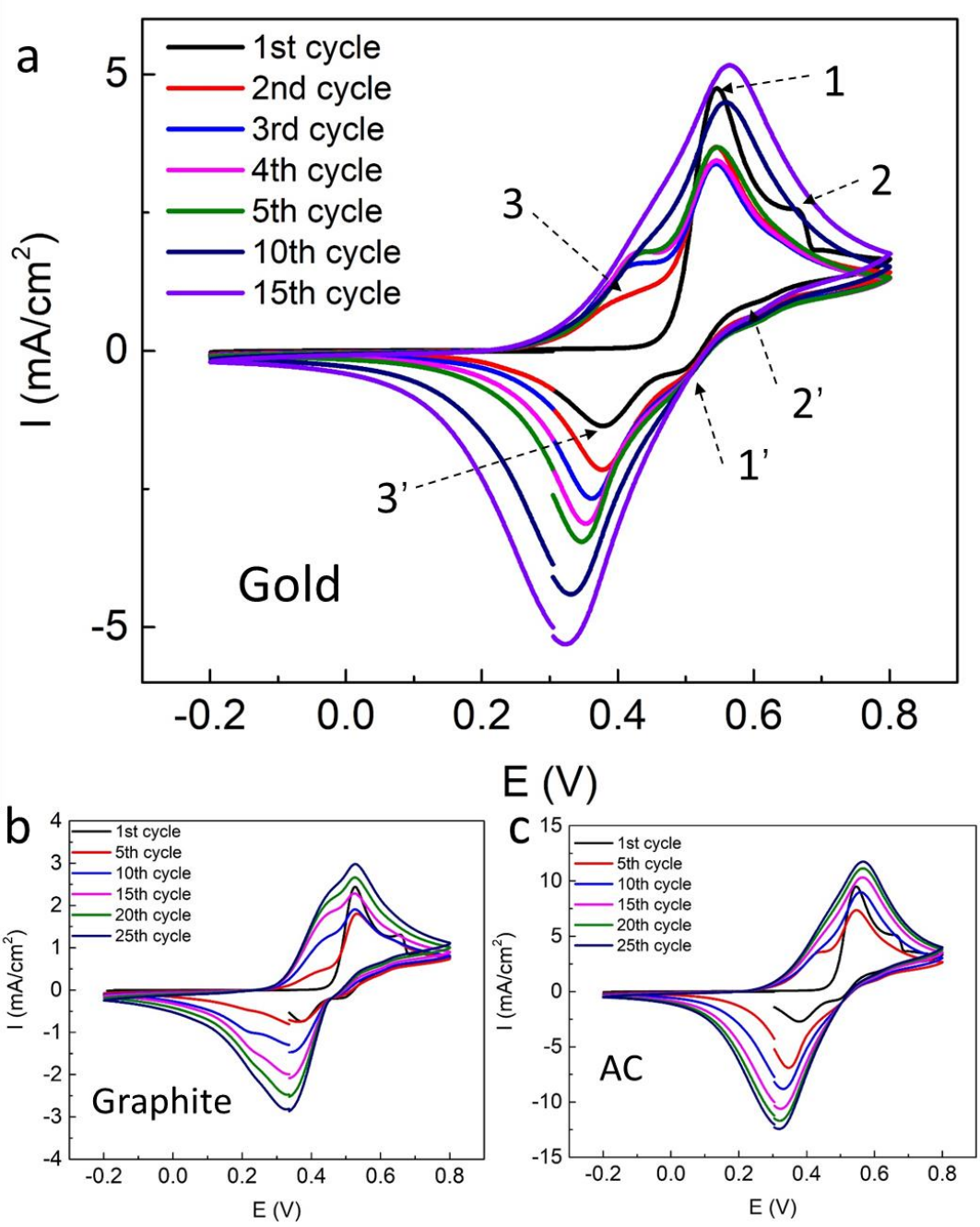

Figure 3.2 The initial cycles of CV deposition of TANI on a) a gold plate, b) a graphite paper electrode, and c) an activated carbon electrode.

As illustrated in Figure 3.2a, the first few cycles of the deposition display 3 sets of redox peaks: 1/1' at 0.543/0.498 V, 2/2' at 0.667/0.613 V and 3/3' at 0.418/0.361 V. The peak separation between the 1 and 1' is about 0.049 V, the separation between 2 and 2' is about 0.054 V and the separation between 3 and 3' is about 0.056 V. Given the peak separation and previously established knowledge of polyaniline/oligoaniline, it is reasonable to assume that all three processes involve a 2-electron transfer. The maximum peak height of 1 is much higher than that of 1', indicating that the electrochemical reaction at 1/1' is reversible, but is followed by a chemical reaction that consumes the oxidation product (i.e., an EC process). Note that oxidation peak 1 decreases in intensity during the first 3 cycles and starts to increase after cycle 4; however, the corresponding reduction peak 1' disappears or merges with peak 3' after the first 2 cycles. The initial decline of peak 1 is likely due to the decrease in local concentration of aniline dimer near the working electrode surface, while the increase in intensity after cycle 3 can be ascribed to the contribution from oligoaniline emeraldine to pernigraniline transition. This is also consistent with the fading of peak 1', as the amount of oxidized aniline dimer species generated decreases each cycle, and is therefore depleted more completely by the follow-up chemical step (thus not accepting electrons from the working electrode to give rise to peak 1'). The electrochemical process corresponding to peak 2/2' only appears in the first 2 cycles and is likely due to the presence of impurities in the aniline dimer solids. Another interesting fact is that reduction peak 3' shows up during the 1st cycle; however, its corresponding oxidation peak first shows up during the 2nd cycle. This implies that the product generated during the electrochemical-chemical process is at a relatively high oxidation state.

Figure S3.1a shows the charge-time profiles of a typical CV deposition vs. pulse deposition (on a gold plate). The amount of product deposited onto the substrate can be calculated based on

the amount of charge (C) passed through the working electrode during the deposition process, using the following equation:

$$\text{mass} = \frac{Q}{F \times n} \times M \tag{3.1}$$

where mass is the weight of the product deposited (g), Q is the amount of charge passed through the working electrode (C), F is the Faraday constant (96,485 C/mol), n is the number of electrons transferred for one molecule of product deposited, and M is the molecular mass of the product (g/mol). One assumption of this calculation is that the Faradaic efficiency of the deposition process is 100%. The CV deposition process is not likely to satisfy this assumption, as a fraction of the aniline dimer that is oxidized during the forward scan gets reduced back to aniline dimer in the reverse scan, without being able to form the final product. In comparison, the pulse deposition process does not go through a reduction phase, and is more likely to satisfy Equation 3.1 (although there is yet another implied assumption: the chemical step is close to 100% efficiency). Nevertheless, based on Figure S3.1a, the pulse deposition is more efficient than the CV deposition at depositing products onto the substrate, because the amount of charge passing through the working electrode per unit time during the pulse deposition is consistently higher than during the CV deposition.

3.2.2. Molecular Weight Analysis

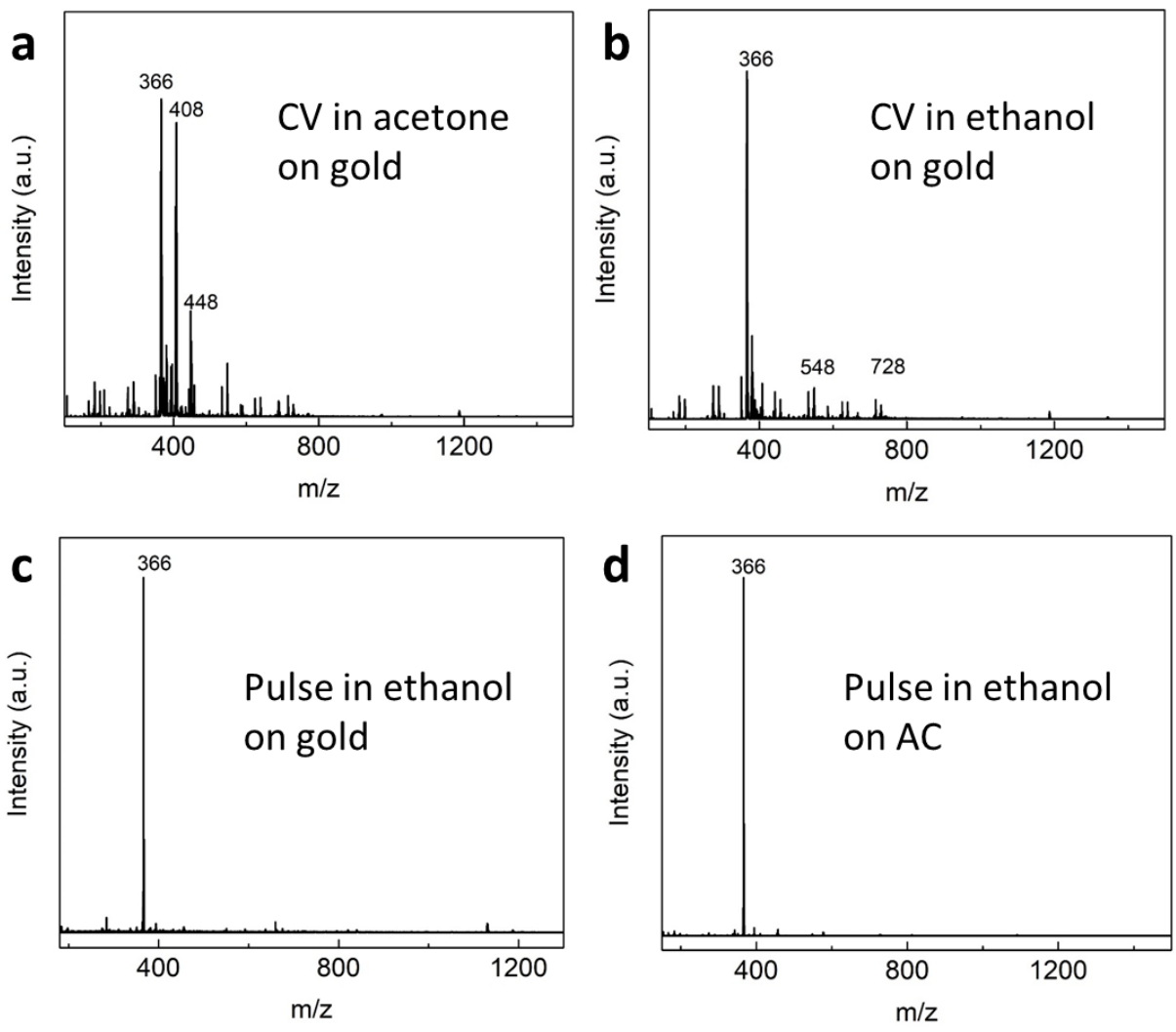

Figure 3.3 MALDI-TOF mass spectra of a) CV deposition products on a gold electrode in an acetone-water electrolyte solution, b) CV deposition products on a gold electrode in an ethanol-water electrolyte solution, c) pulse deposition products on a gold electrode in an ethanol-water electrolyte and d) pulse deposition products on an AC electrode in an ethanol-water electrolyte.

The chemical composition of the electrodeposition products was characterized using MALDI-TOF mass spectroscopy and some mass spectra are shown in Figure 3.3. Even though electrochemical deposition of aniline monomer usually results in the formation of long chain polymers, the electrochemical deposition of aniline dimer seems to produce primarily oligomers. As shown in Figure 3.3a and 3.3b, the mass spectra of the electrodeposition products in acetone and ethanol both show a major peak at 366, corresponding to tetra-aniline (TANI), and some

smaller peaks at 548 and 728, indicating small amounts of aniline hexamer and octamer, respectively. The product in acetone also shows a major peak at 408, which can be credited to the presence of a side reaction between TANI and acetone.[9] As ethanol solution tends to produce purer products, the pulse electrodepositions were only performed in ethanol. Indeed, the molecular weight distribution of the pulse-deposited products appears more monodisperse, as only one major peak can be seen in the mass spectrum in Figure 3.3c.

3.2.3. Electrochemical Deposition Mechanism

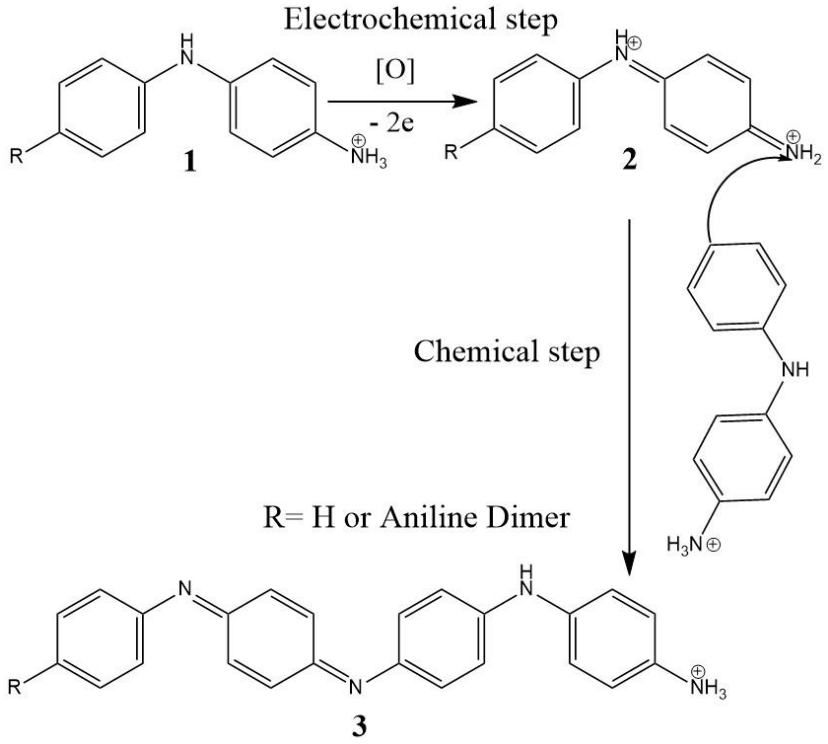

Scheme 3.1 Mechanism of electrochemical-chemical coupling of aniline dimer in acidic media.

Combining CV and MALDI-TOF mass spectroscopy data, a possible 2-step electrochemical-chemical mechanism is proposed for the electrodeposition of aniline dimer in aqueous acidic media, as illustrated in Scheme 3.1. During the first electrochemical step, an aniline dimer **1** is oxidized near the working electrode, losing 2 electrons and becoming the intermediate

radical product **2**. Intermediate **2** then diffuses away from the electrode surface to react with an un-oxidized aniline dimer molecule to form the final product (**3**), which is a molecule of TANI in the emeraldine oxidation state. This chemical step can help to explain the fact that reduction peak 3'(emeraldine to leucoemeraldine transition) is able to show up during the 1st cycle of CV deposition, even though the corresponding oxidation peak 3 can only be seen starting from the 2nd cycle. Alternatively, some intermediate **2** could remain near the surface of the working electrode and, during the backward scan, be reduced back to the initial reactant **1**, giving rise to the reduction peak 1'. As more TANI starts to deposit on the working electrode, the chance of intermediate **2** being reduced back to **1** diminishes and this eventually results in the fading of reduction peak 1'.

3.2.4. Morphology analysis

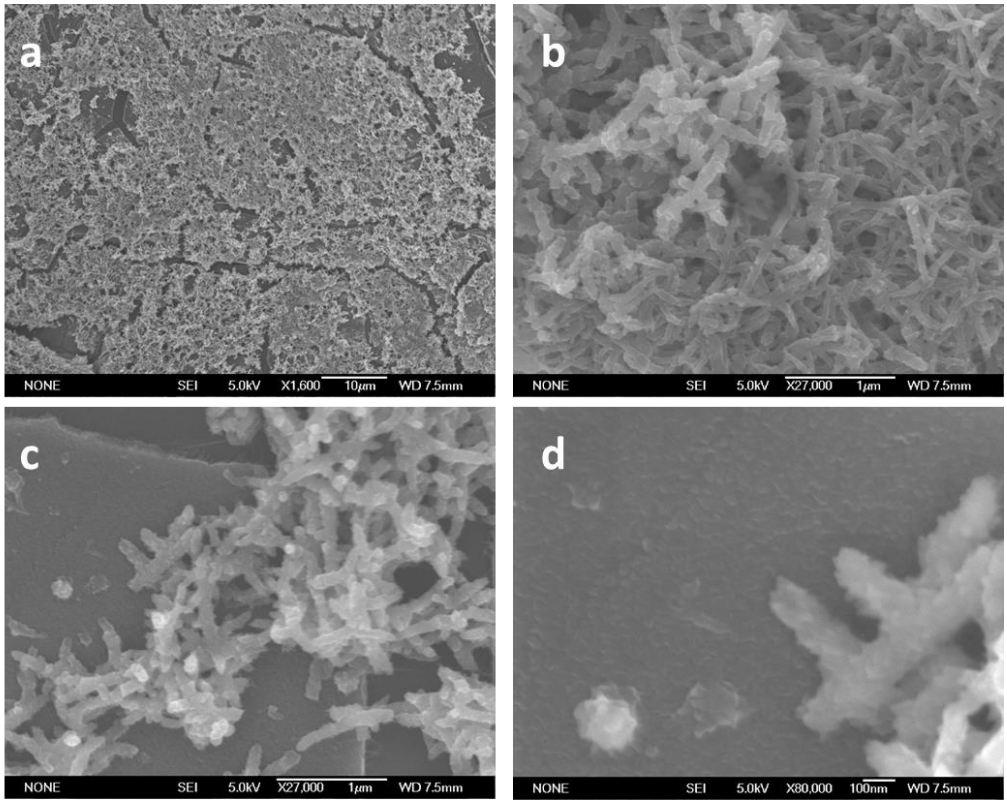

Figure 3.4 SEM images of electrochemically deposited PANI on graphite surfaces at different magnifications.

The methods to electrodeposit PANI nanowire arrays onto various substrates are well established in literature.[2,4,5] A simple galvanostatic constant current deposition can grow PANI nanowire arrays onto most conductive substrates, as demonstrated in Figure 3.4**,** which shows nanowire morphology about 80 nm in diameter and a few microns in length. The graphite substrate is completely covered in nanoscale-like PANI (Figure 3.4c and 3.4d) and on top of the scales some interwoven nanowires are deposited. This observation is in good agreement with a proposed PANI nanowire growth mechanism.[5] During the initial constant current deposition stage, a compact thin film of PANI nuclei (nanoscales) are deposited on the substrate. Once the entire surface of the substrate is covered, new PANI, instead of forming new nuclei, starts to grow along in one

direction on top of the nanoscales (because the concentration of aniline near the electrode surface is diminished), eventually forming nanowires.

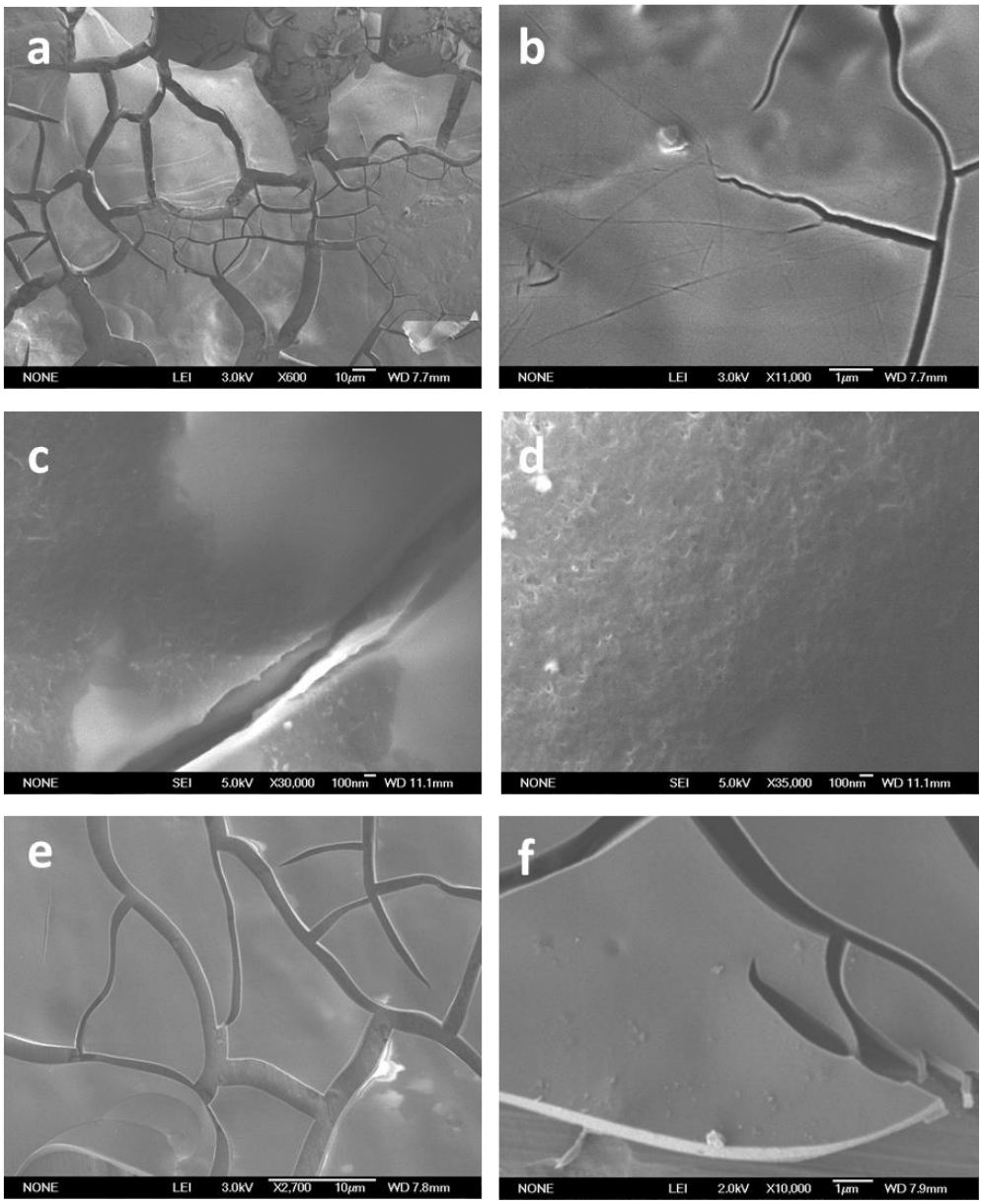

Figure 3.5 SEM images of electrodeposition products on gold using different deposition methods: a) and b) 30 CV cycles, c) and d) 50 short pulses, and e) and f) 500 short pulses.

However, in the case of aniline dimer deposition, the electrolyte solution is a mixture of organic and aqueous solution (because aniline dimer is insoluble in water), rendering the seedling/nuclei growth mechanism likely inapplicable. The morphology of the TANI grown via

different methods onto different substrates was characterized using scanning electron microscopy. Figure 3.5 shows SEM images of TANI deposited on gold surface, while Figure S3.2 presents SEM images of TANI deposited on graphite paper. Comparing the SEM images, the smooth electrode surfaces (gold vs. graphite paper) seem to have similar effects on the morphology of TANI, while CV and pulse deposition produce slightly different nanostructures. 30 cycles of CV deposition on gold surfaces give rise to compact sheet-like structures as shown in Figure 3.5a and 3.5b. On the other hand, 50 short pulses produced TANI with porous nanowire-like structures (Figures 3.5c and 3.5d). However, prolonged pulse deposition eventually resulted in thick TANI sheets found in Figures 5e and 5f**.** TANI growth on graphite exhibits almost identical patterns, even though short pulse deposition initially produces more distinctive nanotube structures (Figures S3.2c and S3.2d). The lack of nanowire/nanotube morphology is most likely due to the relatively high solubility of TANI in the mixed solvents. More often than not, after electrodeposition is complete, a considerable amount of freshly grown TANI is usually found not on the working electrode, but floating nearly the electrode surface. It is likely that the *in situ* grown TANI on the electrode surface might have had nanostructures; however, as more TANI was deposited further away from the electrode surface, the solvent dissolved the TANI on the outer layer. Eventually after all the solvent evaporated, the dissolved TANI self-assembled into a compact thick "clay-like" structure as seen under SEM.

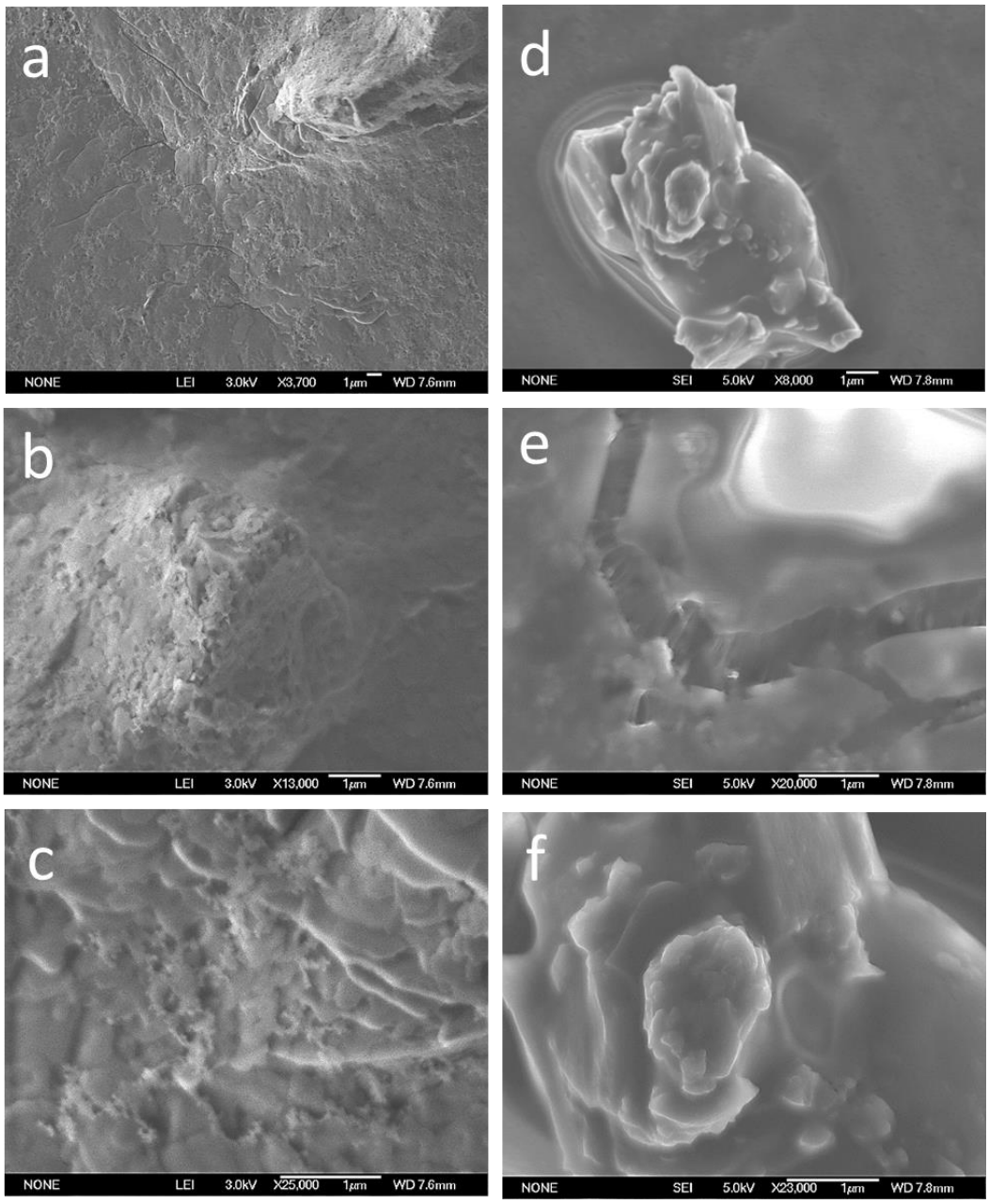

Figure 3.6 SEM images of TANI-AC composites using different deposition methods: a-c) 30 CV cycles, and d-f) 50 short pulses.

As this study aims to utilize TANI for supercapacitor applications, depositing on gold or graphite surfaces, with a large amount of TANI dissolving into solution, is not the best approach. Activated carbon is a common commercial supercapacitor material, with specific high surface area (the morphology of which can be seen in Figure S3.3) for EDLC type of charge storage. However,

activated carbon suffers from a lack of redox/Faradaic processes, limiting its specific capacitance. To further enhance the specific capacitance of AC, TANI was electrodeposited onto activated carbon electrodes (See Figure 3.3d for MS of the product). Interestingly, electrodeposition of TANI onto activated carbon electrodes does induce nanostructure formation. Figure 3.6 shows SEM images of TANI-AC composites prepared by electrochemical deposition methods. Because high surface area of the activated carbon can provide numerous active sites for TANI nucleation, CV deposition produced prominent nanoscale like TANI covering the entire surface of the activated carbon substrate. Pulse deposition seems to have coated a thicker layer of TANI on AC, causing charging-up effects on some SEM images. However, the TANI-AC composite still displays some noticeable nanostructure on AC surface. The presence of nanostructures is likely due to the high concentration of nucleation sites on the carbon substrates and the relatively low concentration of aniline dimer in solution.

3.2.5. Electrochemical supercapacitor characterizations

As a typical EDLC material, activated carbon exhibits lower specific capacitance than pseudo-capacitance materials, such as TANI. Using the short pulse chronoamperometry method, a considerable amount of nanostructured TANI can be evenly deposited on AC surfaces in a matter of minutes, significantly boosting the capacitance of the AC electrodes. In addition to depositing TANI, introducing a redox active electrolyte in the electrolyte solution is also an effective method to increase the capacitance. In this project, a 0.01 M hydroquinone (HQ) in 1.0 M H_2SO_4 solution was prepared to test the TANI-AC electrode performance in redox active electrolyte solutions.

The supercapacitor performances of pulse electrodeposited (50 pulses at 0.75 V, TANI mass = 0.43 mg) TANI-AC electrodes were evaluated using cyclic voltammetry (CV), galvanostatic constant current charge-discharge (CC) and electrochemical impedance

spectroscopy (EIS); the results are shown in Figure 3.7. The mass of TANI deposited was calculated based on the amount of charge that passed through the working electrode as presented in Figure S3.1b, using Equation 3.1. It is worthwhile noting that this calculation overestimates the actual mass deposited on the substrate, as some TANI formed inside the electrolyte solution or dissolved away from the electrode.

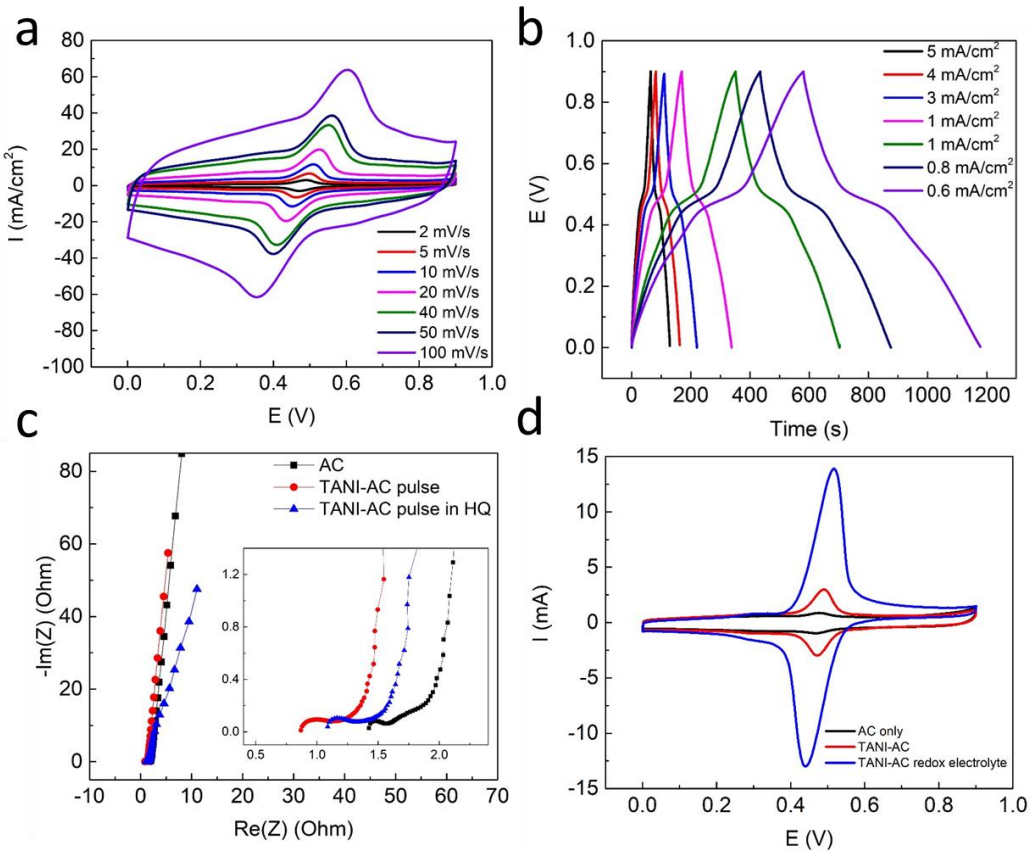

Figure 3.7 a) CV curves of a TANI-AC pulse composite at various scan rates. b) CC curves of a TANI-AC pulse composite at different current densities. c) Nyquist plots of AC, TANI-AC pulse in a 1.0 M sulfuric acid solution and TANI-AC pulse in a redox electrolyte solution. Inset: Nyquist plots in the high frequency range. d) CV curves of AC, TANI-AC pulse and TANI-AC pulse in redox electrolyte solutions. Scan rate = 5 mV/s.

As shown in Figure 3.7, the CV curves of TANI-AC show one prominent pair of redox peaks at around 0.5 V/0.45 V vs. the Ag/AgCl reference electrode, corresponding to TANI

emeraldine to pernigraniline oxidation state transitions. A pair of charging/discharging plateaus that results from the same transition is also seen in the CC curves. Based on CV and CC data, the specific areal capacitance of the composite can be calculated using Equations 3.4 and 3.5. The TANI-AC electrode achieved an areal capacitance of 406 mF/cm^2 at a slow scan rate of 2 mV/s, and retained 76% percent of the capacitance at a faster 100 mV/s scan rate. More CV and CC comparison data are presented in Figures S3.5 and S3.6 and the capacitance results are compiled in Table S3.1.

The good rate capability of TANI-AC is further corroborated by the Nyquist plots in Figure 3.7c. The Nyquist plot of a pseudo-capacitor typically displays a semicircle in the high frequency range, a 45-degree angled slope in the mid frequency range and a steep straight line in the low frequency range. The x-axis intercept of the semicircle and the diameter of the semicircle correspond to uncompensated resistance (of the electrode and solution) and charge transfer resistance, respectively. The Nyquist plot of activated carbon shows an uncompensated resistance of 1.42 Ω and a very small charge transfer resistance of 0.13 Ω (likely due to some oxygen-containing functional groups). By contrast, TANI-AC shows a much smaller uncompensated resistance of 0.72 Ω and a slightly higher charge transfer resistance of 0.67 Ω. This indicates that TANI effectively decreased the electrode resistance of TANI-AC electrode while slightly increasing the charge transfer resistance due to its redox activities. Nonetheless, the overall resistance of TANI-AC is still lower than that of pure activated carbon, indicating better rate capability.

Figure 3.7d shows CV curves (at 5 mV/s) of the activated carbon in sulfuric acid, TANI-AC in sulfuric acid and TANI-AC in the redox electrolyte solution. The TANI-AC curve shows much higher current densities than AC in the redox-active potential range of TANI, enhancing its

areal capacitance by over 40%. The TANI-AC in HQ curve shows even higher current densities, demonstrating that a redox couple (hydroquinone-benzoquinone) in solution can greatly increase the capacitance of TANI based supercapacitors (1.5 to 2 fold increase), yielding high areal capacitances of 677 mF/cm^2 at 2 mV/s and 905 mF/cm^2 at 0.6 mA/cm^2. However, introducing a redox electrolyte into the solution does compromise the overall rate capability. As shown in Figure S3.5, at a high scan rate of 100 mV/s, the peak separation between the cathodic and anodic peaks almost spans the entire potential window, resulting in about 40% capacitance loss compared to its capacitance at 2 mV/s.

To further analyze the rate performance of the TANI-AC composite, the relationship between current and scan rates in the CV characterizations was studied. There typically are two types of charge storage mechanisms in a hybrid supercapacitor like the TANI-AC composite: physical charge/ion adsorptions taking place on or near the surface of the electrode material, and reversible chemical reactions involving the bulk of the redox-active material. The electrostatic ion adsorption process is a rapid surface phenomenon, while the redox reaction is characteristically limited by ion diffusion. This difference in charge storage mechanism is manifested in the measured peak current (i) to CV scan rate (v) dependency, which is characterized by the following equation:

$$i = av^b \tag{3.2}$$

In Equation 3.2, a is an adjustable coefficient and b describes the power law relationship between peak current i and the scan rate v. In a typical surface physical adsorption process, the b-value is close to 1, characteristic of a linear capacitive current to scan rate response. On the other hand, the peak current of a redox/Faradaic process involving bulk materials and ion diffusion

follows the Cottrell equation, with a *b*-value close to 0.5. Therefore, the *b*-values of a material can provide a qualitative description of the charge storage mechanism of a hybrid material.

Another semi-quantitative method that separates the measured current at a specific potential into surface-controlled capacitive currents and diffusion-controlled Faradaic currents is:

$$i = k_1 v + k_2 v^{1/2} \tag{3.3}$$

where i is the measured current at a certain potential, and $k_1 v$ and $k_2 v^{1/2}$ correspond to the surface-controlled and diffusion-controlled current contributions, respectively. Therefore, by plotting the peak currents at specific potentials against scan rates, the surface and diffusion-controlled components can be distinguished.

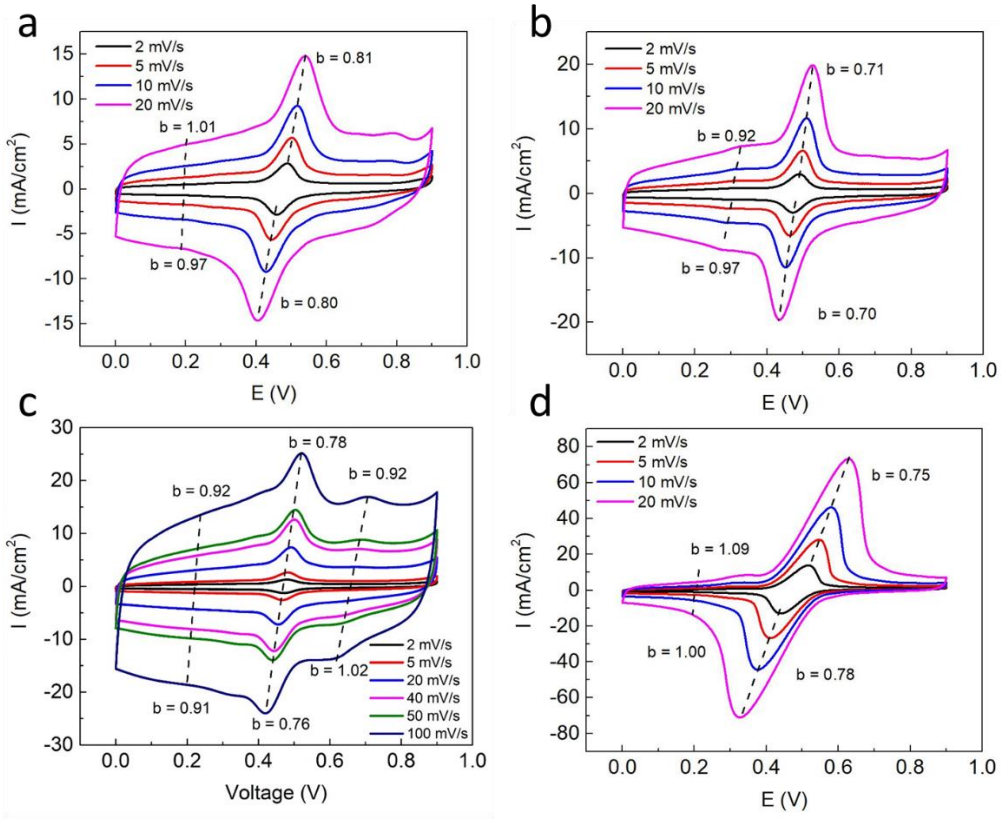

Figure 3.8 CV plots showing b-values of a) a TANI-AC CV composite, b) a TANI-AC pulse composite, c) a TANI-AC physical mixture, and d) a TANI-AC pulse composite in a redox electrolyte solution.

Figure 3.8 shows some *b*-values of TANI-AC composites in 1.0 M sulfuric acid and in the redox electrolyte solution, and more *b* and *k*-value details are tabulated in Table S3.2. From these results, all TANI-AC composites show a b-value close to 1.0 at a non-redox active potential (0.2 V vs. Ag/AgCl) and a *b*-value somewhere in between 1 and 0.5 at a redox active potential (0.5 V vs. Ag/AgCl). This is in good agreement with the shape of the CV curves as the curve is flat at 0.2 V, a typical EDLC-like response, while a prominent peak shows up at 0.5 V, characteristics of a battery-like response. Comparing *k*-value results of TANI-AC composites prepared by different methods (CV deposition, pulse deposition and physical mixing), the TANI-AC pulse sample shows the highest surface-controlled contribution, while the TANI-AC CV and the physical mixture (see Figure S3.4 for SEM images) composites have similar levels of surface vs. diffusion-controlled components. As the surface controlled mechanism is more rapid than the diffusion-controlled mechanism, a higher percentage of surface phenomena indicate better rate performance/power density of the material. For a more practical comparison, Table S3.2 also presents the percentage of the surface-controlled mechanism at 20 mV/s for the composites. At 0.2 V, the anodic peak current of the TANI-AC pulse composite consists of 99% surface contribution and it maintains a good 83% at the emeraldine to pernigraniline redox potential. This indicates that the pulse deposition method can give rise to a synergistic effect between TANI and the carbon substrate, which facilitates the charge transfer and ion diffusion processes, improving the rate capability of the hybrid electrode. In the hydroquinone/benzoquinone redox electrolyte solution, TANI-AC shows slightly sluggish kinetics, because HQ-BQ molecules are in the solution, and their redox processes are inherently more diffusion controlled than that of TANI fixed on the electrode. However, having HQ-BQ in solution also increases the ionic conductivity of the solution and the high concentration of active sites on the electrode surface shortens the diffusion lengths,

offsetting some of the kinetic disadvantages.[10] This effect is also manifested in the *k*-values analysis, where the surface contribution at 0.5 V decreases slightly to 80% at 20 mV/s. It is worthwhile noting that the *k*-values are obtained from the 2 mV/s to 40 mV/s CV data, and the surface contribution will likely decrease if higher scan rate data are analyzed.

The cycling stability of the TANI-AC composites was also evaluated using constant-current charge discharge methods, and the current density used is determined by the capacity of the electrode such that each charge-discharge cycle takes about 30-40 seconds. The cycle stability data of pulse deposited TANI-AC, TANI-AC physical mixture and amorphous TANI electrodes are presented in Figure 3.9. Similar to its polyaniline counterpart, tetra-aniline all by itself suffers from physical stress and chemical degradation during prolonged cycling, losing more than 60% of its initial capacitance in just 900 cycles. A TANI-AC physical mixture exhibits greater cycle stability, maintaining 84% of its initial capacitance after 3000 cycles. Yet, the pulse electrodeposited TANI-AC demonstrates even better cycle life, retaining almost 92% at the end of 3000 cycles. The long cycle life of the TANI-AC pulse composite is also confirmed by the Nyquist plot collected before and after 3000 cycles. As presented in Figure 3.9b, the internal resistance (x-intercept) of the TANI-AC electrode remains unchanged after cycling, while the charge transfer resistance increased very slightly by 0.3 Ω. In contrast, the Nyquist plot of TANI after 900 cycles displays an almost 150 Ω increase in the charge transfer resistance (Figure 3.9c), possibly resulting from severe changes in TANI morphology and chemical properties.

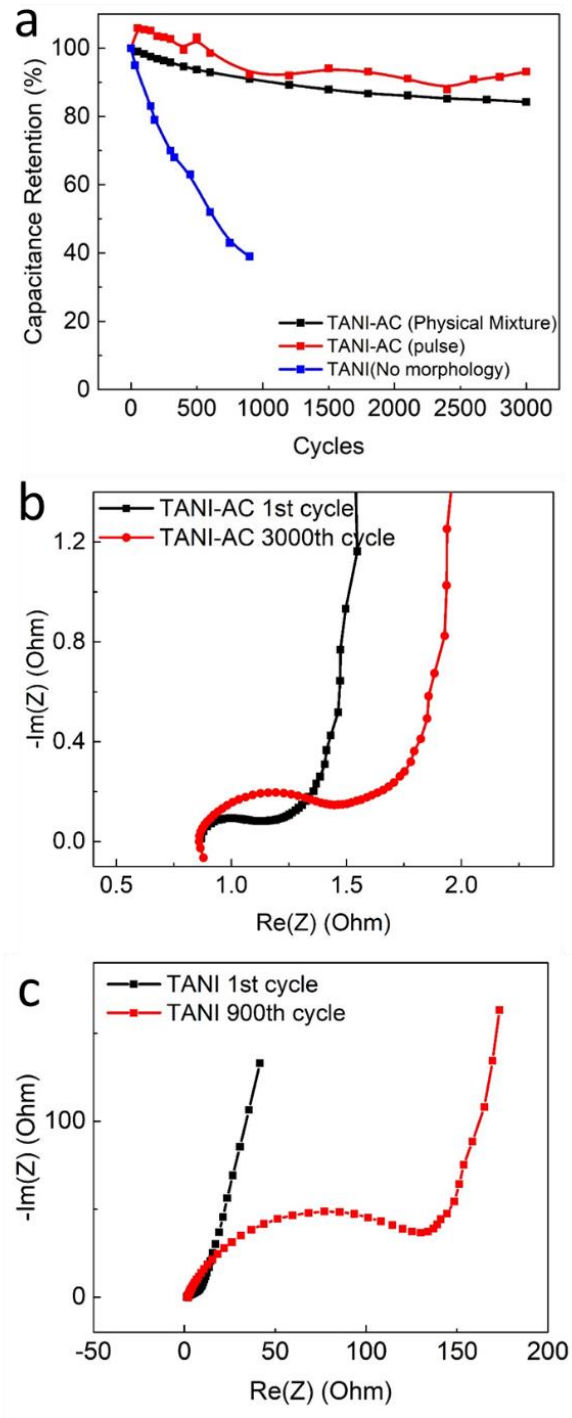

Figure 3.9 a) Cycle stability data of a TANI-AC physical mixture, a TANI-AC pulse composite and amorphous TANI. b) Nyquist plots of TANI-AC before and after 3000 cycles. c) Nyquist plots of a TANI electrode before and after 900 cycles.

The reasoning for the improved cycle stability is likely two-fold. From a physical perspective, activated carbon is a physically robust substrate for the conducting oligomer, thus ameliorating the physical stress TANI experiences during the doping/de-doping process. Additionally, as the pulse deposition process applies an electric potential directly onto the activated carbon, TANI likely grows more uniformly on the AC substrate than it can self-assemble onto AC in a physical mixture. Therefore, TANI-AC pulse composites likely experiences more synergy between TANI and AC than the physical mixture, further enhancing its physical rigidity (as indicated by the small change of charge transfer resistance after cycling). Another interesting observation can be seen in the shape of the CV, as there is only one pair of redox peaks present in the TANI-AC pulse sample, while normal PANI or TANI typically shows two to four sets.[11,12] Mažeikienė and Malinauskas have reported that PANI films degrade faster above 0.7 V vs. Ag/AgCl than they do at below 0.6 V, suggesting that the species formed at higher potentials are less chemically stable.[13] Prior publications suggest that pernigraniline formed at higher chemical potentials tends to go through hydrolysis or other forms of chemical oxidation, thus causing chemical degradation of PANI.[11–14] In the case of TANI-AC, it is not entirely clear why TANI or PANI shows different electrochemical behaviors when composited with carbons. Some suggest that the morphology of the composite could modify the chemical properties of PANI.[15] Nonetheless, the lack of redox peaks at higher than 0.7 V vs. Ag/AgCl indicates the absence of pernigraniline forms of TANI during cycling, and this most likely accounts for the chemical stability of the TANI-AC composites.

3.3. Conclusions

In conclusion, the electrochemical deposition of aniline dimer is a two-step electrochemical-chemical process, producing primarily tetra-aniline and trace amounts of higher

aniline oligomers. Pulse chronoamperometry deposition is a simple and efficient method to grow a thin layer of nanostructured TANI onto activated surfaces, vastly improving the supercapacitor performance of activated carbon electrodes. The hybrid TANI-AC material benefits greatly from the synergy between activated carbon and pulse deposited TANI, demonstrating good areal capacitance (409 mF/cm^2 at 2 mV/s and 399 mF/cm^2 at 0.6 mA/cm^2), superior rate capability (76% retention at 100 mV/s and 90% at 5 mA/cm^2), and great cycle stability (92% after 3000 cycles).

3.4. Experimental

3.4.1. Chemicals

N-phenyl-p-phenylenediamine (aniline dimer), hydroquinone and activated carbon were purchased from VWR. Sulfuric acid and ethanol were obtained from Sigma-Aldrich. Graphite paper (0.070 mm thick) used for current collectors was purchased from Digi-Key Electronics (manufactured by Panasonic Electronic Components, part number: P13689-ND). All reagents were reagent grade and used without further purification.

3.4.2. Characterizations

Scanning electron microscopy (SEM) images were taken with an FESEM JOEL JSM-6700F FE-SEM at 5 to 10 kV. The samples were drop-cast onto aluminum foil substrates and air dried overnight before imaging. The matrix-assisted laser desorption/ionization – time of flight mass spectroscopy (MALDI-TOF MS) of the TANI samples were collected using a Bruker Ultraflex MALDI-TOF in the m/z range of 100 to 3000. The samples were dissolved in ethanol. No matrix was used based on a prior publication.[9] The probe sonicator used for mixing samples was a FS-300N ultrasonic processor, with 300 W (100%) power output, 20 kHz frequency (frequency is auto-tracked by the instrument), and a 2 mm-diameter tip. A typical mixing session

of a 10-20 mL solution lasts 5 min at 50% power output using a 3 s on /1 s off intermittent pulse mode.

Cyclic voltammetry (CV), constant current (galvanostatic) charge-discharge (CC), and electrochemical impedance spectroscopy (EIS) were carried out at room temperature (18-22 °C), on a Bio-Logic VMP3B -10 Potentiostat in a standard 3-electrode setup, with 1.0 M sulfuric acid (or 0.01 M HQ in 1.0 M sulfuric acid) as the electrolyte solution, a 1 x 2 cm^2 platinum foil as the counter electrode, and Ag/AgCl (in saturated KCl) as the reference electrode. The EIS measurements were performed at 0.3 V and 0.5 V relative to the reference electrode, with a 10 mV amplitude in the frequency range of 10.0 kHz to 1.0 mHz. Prior to testing, the working electrodes were soaked in 1.0 M sulfuric acid electrolyte for a few hours. All potentials were recorded relative to the Ag/AgCl (in saturated KCl solution) reference potential.

Calculations of average specific areal capacitance of the electrode material from the discharge CV diagrams are based on the following equation:

$$C_{areal} = \frac{\int_{V_i}^{V_f} i dV}{A \times (V_f - V_i) \times v} \tag{3.4}$$

where C_{areal} is the average specific areal capacitance (mF/cm^2); i is the discharge current from the CV diagram (mA); V_f and V_i denote the final and initial potential (V), respectively; A is the area of the electrode material (cm^2); and v indicates the scan rate (V/s).

Alternatively, the average specific capacitance can be calculated based on CC curves using the following equation:

$$C_{areal} = \frac{I \times \Delta t}{A \times (\Delta V)} \tag{3.5}$$

where C_{areal} is average specific areal capacitance (mF/cm^2), I is the discharge current (mA), Δt is the discharge time (s), A is the area of the electrode material (cm^2) and ΔV is the potential difference in discharge (V).

3.4.3. Preparation of TANI nanowires

Tetra-aniline (TANI) was synthesized via an interfacial polymerization method as described in Chapter 2. In a typical synthesis, 20.0 mg of N-phenyl-p-phenylenediamine (dimer aniline) was dissolved in 10 mL dichloromethane. 1 equivalent amount of (22.0 mg) ammonium persulfate (APS) was dissolved in 10 mL of a 1.0 M aqueous HCl solution. The aqueous phase was added on top of the denser organic phase drop-wise. The interfacial reaction was allowed to react for a set time period: 4 h under static conditions. At the end of the reaction, the aqueous phase and the interfacial precipitates were separated from the organic phase and dialyzed (regenerated cellulose dialysis tubing, 12000-14000 d, Fisherbrand) against deionized water overnight.

3.4.4. Preparation of TANI-AC physical mixture electrodes

10.0 mg of activated carbon (AC) was dispersed in 5.0 mL of DI water under sonication in a scintillation vial. 4.0 mL (0.25% weight concentration) of tetra-aniline (TANI) aqueous dispersion was slowly added under magnetic stirring. The mixture was then probe sonicated at 10 W for 10 min. No binder or conductive additives were added in this process. The TANI-AC dispersions were drop-cast on graphite paper current collectors with an active electrode area of 1x1 cm^2, and the electrodes were dried in a convection oven at 50 ^{o}C overnight. The electrodes were soaked in 1.0 M H_2SO_4 for a few hours before electrochemical testing.

3.4.5. Preparation of activated carbon electrodes for electrochemical deposition

200 mg of activated carbon (AC), 11 mg of carbon black (CB), and 1.1 g of (1.0 weight %) CMC/SBR binder were mixed in 19.0 mL of DI water and probe sonicated for 30 min at 10 W.

The AC to CB to binder ratio is 90% to 5% to 5%. The slurry was drop-cast onto graphite paper current collectors with an active area of 1 cm^2 and then dried in an oven at 50 ^oC overnight.

3.4.6. Electrochemical deposition of PANI nanowires on graphite

PANI nanowires were deposited onto graphite paper substrate via a galvanostatic current procedure reported in the literature.[5] In a typical process, a three-electrode setup was used with a graphite paper electrode (1 × 1 cm^2) as the working electrode, an Ag/AgCl electrode as the reference, and a platinum foil (2 × 1 cm^2) as the counter electrode. The solution was prepared by dissolving 1.17 mL of aniline in 30.0 mL of 1.0 M H_2SO_4 solution under rapid mixing. Electrodeposition was carried out by applying a constant current: 0.01 mA/cm^2 for 30 min.

3.4.7. Electrochemical deposition of tetra-aniline (TANI)

Electrochemical deposition of TANI was performed on a Bio-logic Potentiostat using a three-electrode setup, with a platinum foil counter electrode and saturated Ag/AgCl as the reference electrode. Multiple substrates (gold plate, graphite paper, and activated carbon on graphite paper) were used as the working electrode to study how substrates affect the molecular weight and morphology of the aniline oligomer products. The solutions used for electrodeposition were prepared by mixing 5.0 mL of 10 mmol aniline dimer in an ethanol or acetone solution with 30.0 mL of a 1.0 M sulfuric acid solution. The electrodeposition was performed using either cyclic voltammetry (-0.2 ~ 0.8 V, 20 mV/s for 30 cycles) or pulse chronoamperometry (0.5 s on/1.0 s off, on voltage: 0.75 V, off voltage: 0 V, number of pulses: 50-500).

3.5. Supporting Information

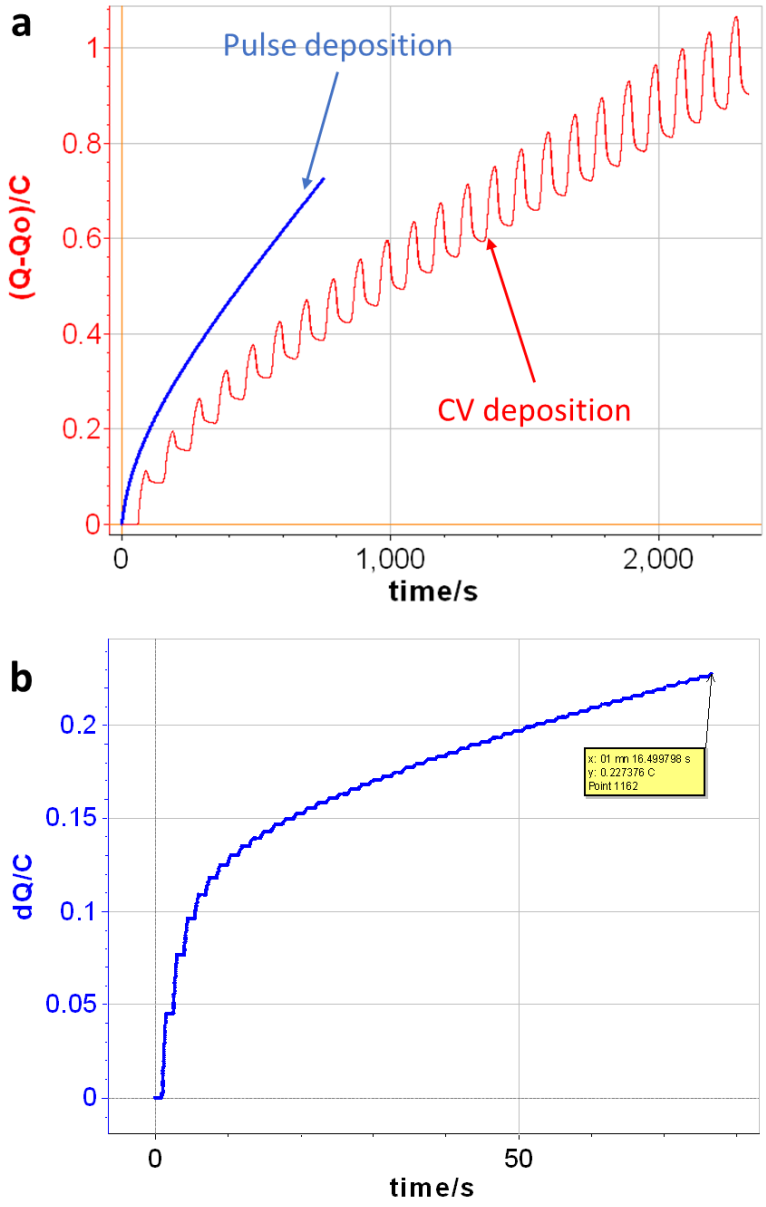

Figure S3.1 Charge-time profile of a) a pulse deposition vs. a CV deposition on gold and b) a 50-pulse deposition on an activated carbon electrode.

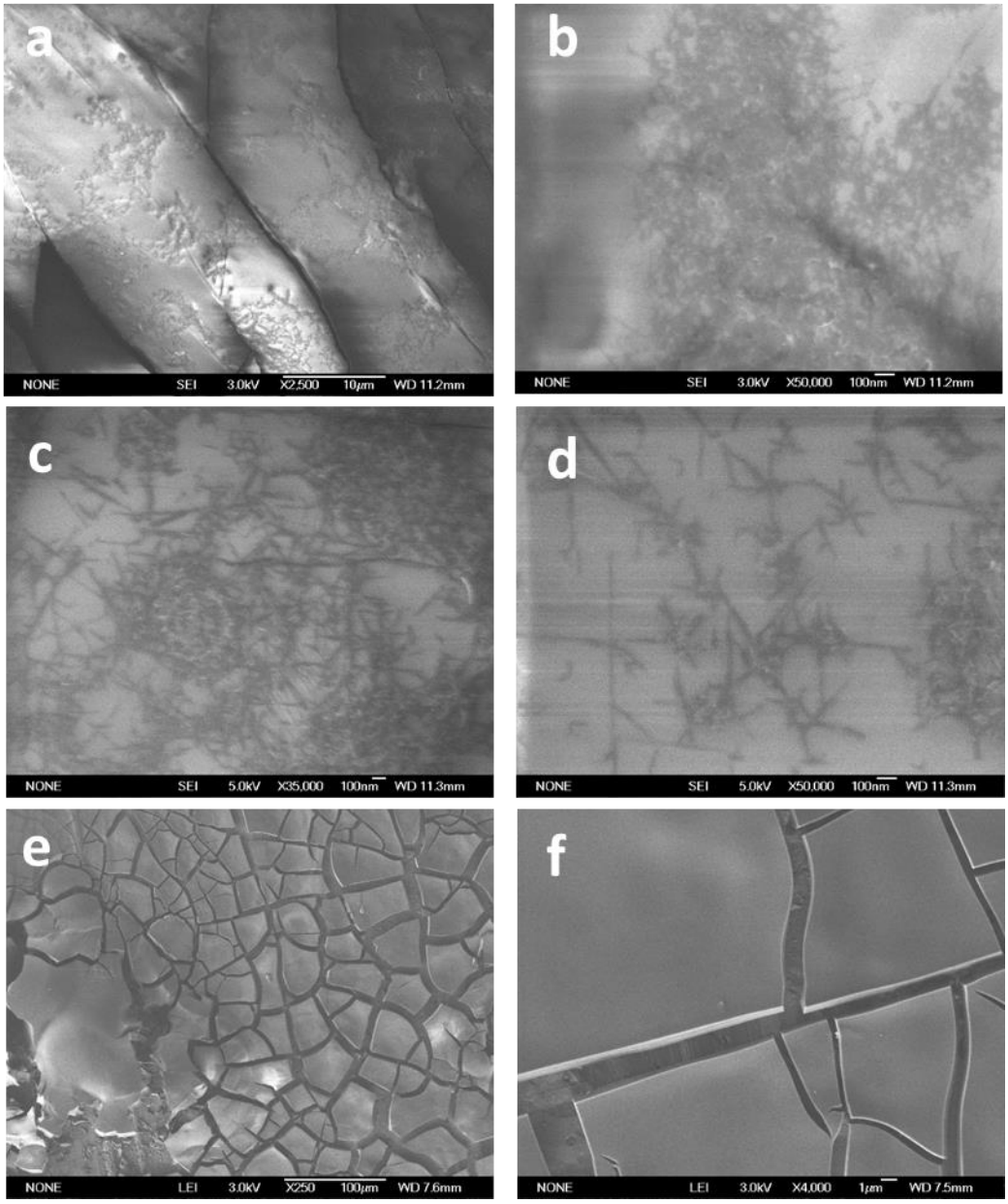

Figure S3.2 SEM images of TANI deposited on a graphite surface using a-b) 30 CV cycles, c-d) 50 short pulses, and e-f) 500 short pulses.

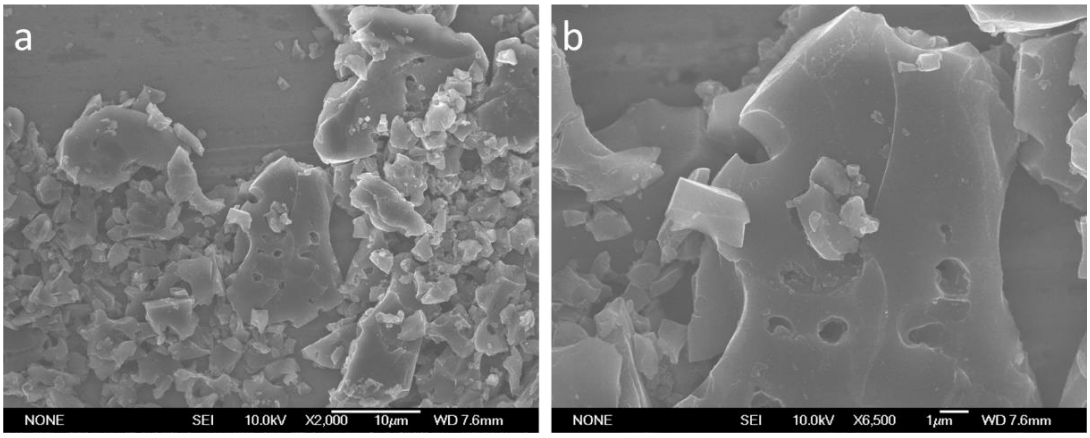

Figure S3.3 SEM images of activated carbon under different magnifications.

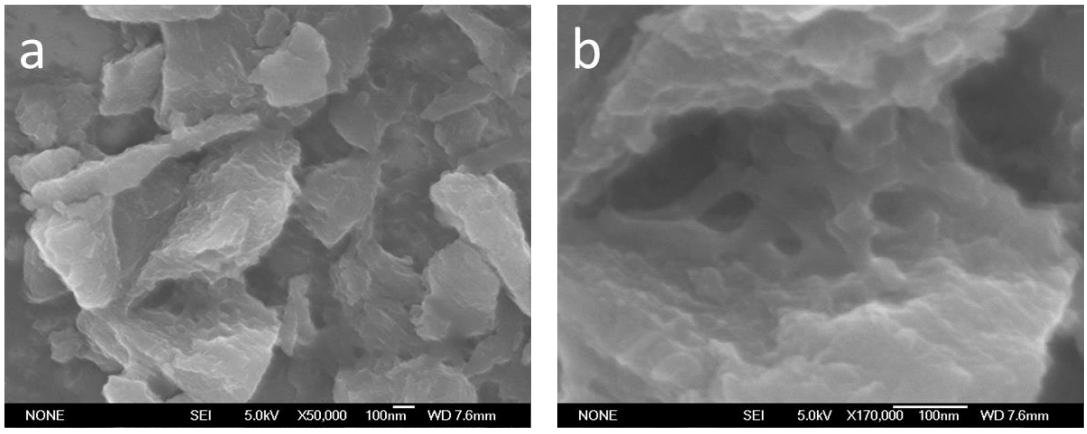

Figure S3.4 SEM images of a TANI-AC physical mixture.

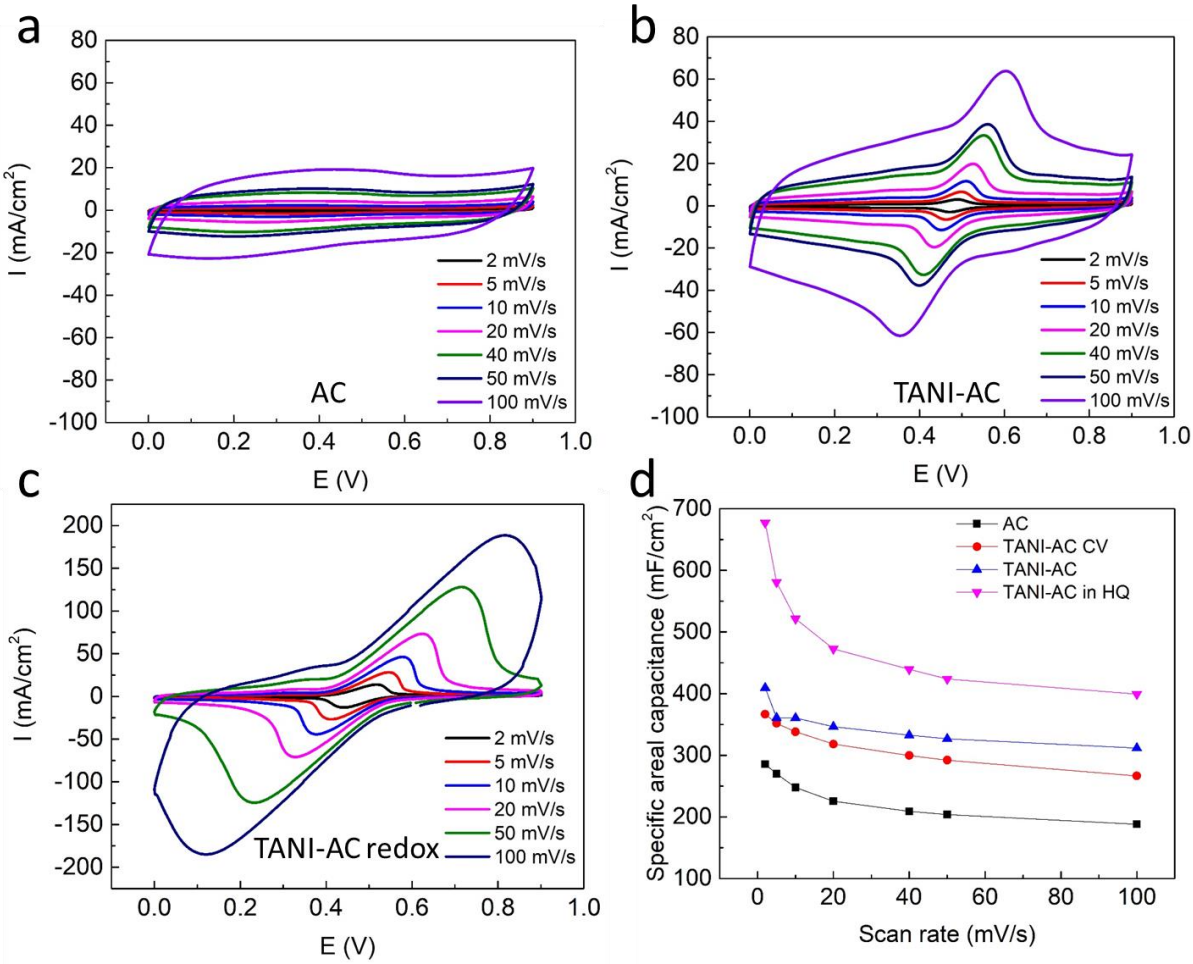

Figure S3.5 CV curves of a) activated carbon, b) a TANI-AC pulse and c) a TANI-AC pulse in a redox electrolyte, and d) the CV rate capability of each of these materials.

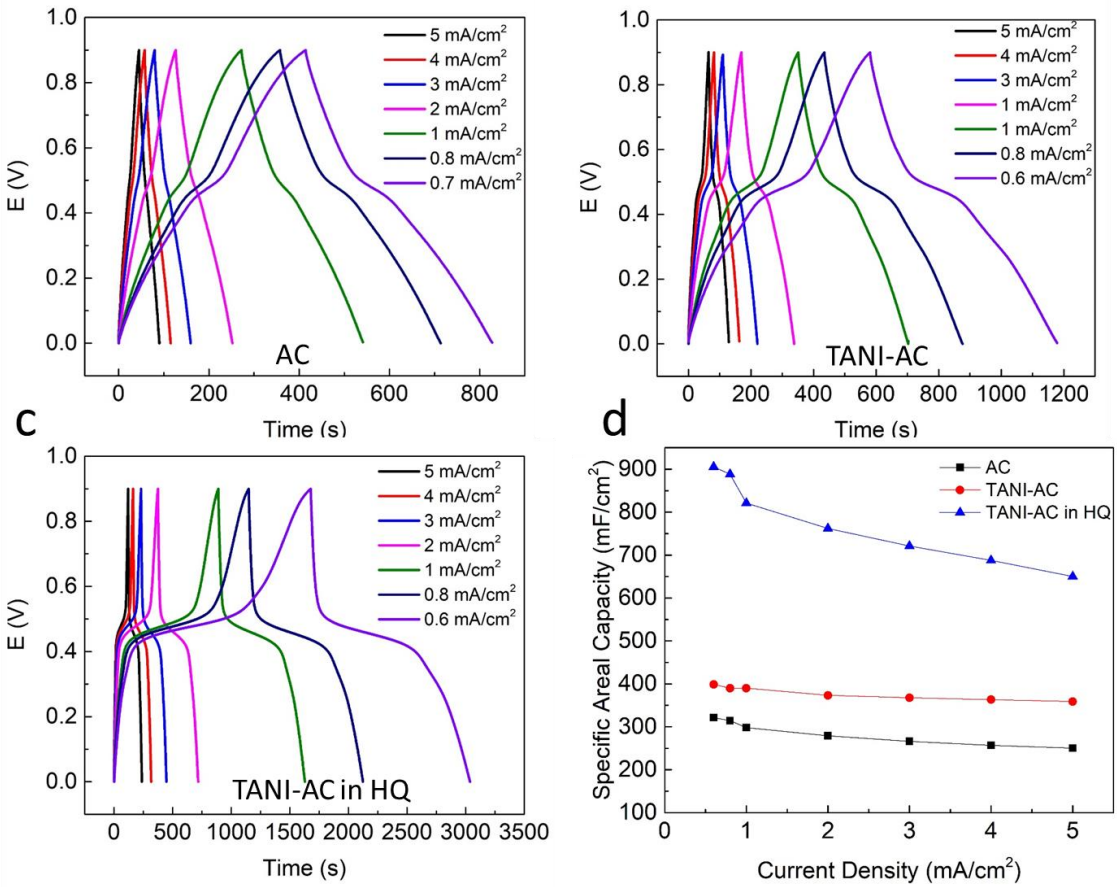

Figure S3.6 CC curves of a) activated carbon, b) a TANI-AC pulse and c) a TANI-AC pulse in a redox electrolyte, and d) the CC rate capability of these materials.

Table S3.1 Specific Areal Capacitance of TANI-AC composites (mF/cm^2)

Specific Areal Capacitance of TANI-AC composites (mF/cm^2)				
	AC	TANI-AC CV	TANI-AC pulse	TANI-AC redox
Scan rate (mV/s)				
2	286	367	409	677
5	270	352	361	581
10	248	338	360	522
20	225	318	346	473
40	209	300	333	439
50	204	292	327	424
100	188	266	312	399
Current density (mA/cm^2)				
0.6	321		399	906
0.8	315		390	888
1	298		390	821
2	279		373	762
3	266		368	721
4	257		363	688
5	251		359	650

Table S 3.2 b and k-Values of TANI-AC Composites (charge/discharge)

***b* and *k*-Values of TANI-AC Composites (charge/discharge)**								
Sample	TANI-AC CV		TANI-AC pulse		TANI-AC mixture		TANI-AC in redox	
Potential	0.2 V	0.5 V	0.2 V	0.5 V	0.2 V	0.5 V	0.2 V	0.5V
b	0.92/0.97	0.71/0.70	1.01/0.97	0.81/0.80	0.92/0.91	0.78/0.76	1.10/1.00	0.749/0.777
k1	0.208/0.335	0.522/0.507	0.175/0.239	0.897/0.870	0.127/0.183	0.269/0.271	0.447/0.9359	3.76/3.11
k2	0.147/0.065	1.31/1.34	0.005/0.0616	0.761/0.817	0.068/0.128	0.524/0.533	0.082/0.146	4.16/4.14
Surface*	86%/96%	64%/63%	99%/95%	84%/83%	89%/86%	70%/69%	96%/97%	80%/77%
Diffusion*	27%/4%	36%/37%	1%/5%	16%/17%	11%/14%	30%/31%	4%/3%	20%/23%

*Surface and diffusion controlled contributions are calculated at 20 mV/s.

3.6. References

(1) Kitani, A.; Izumi, J.; Yano, J.; Hiromoto, Y.; Sasaki, K. *Bulletin of the Chemical Society of Japan*. 1984, pp 2254–2257.

(2) Snook, G. A.; Greaves, T. L.; Best, A. S. *J. Mater. Chem.* **2011**, *21* (21), 7622–7629.

(3) Mohd, Y.; Ibrahim, R.; Zainal, M. F. **2012**, 1301–1306.

(4) Xia, L.; Xia, J.; Wang, Z. *RSC Adv.* **2015**, *5* (113), 93209–93214.

(5) Kai, W.; Haiping, W.; Yuena, M.; Zhixiang, W. *Small* **2013**, *10* (1), 14–31.

(6) Zhao, G. Y.; Li, H. L. *Microporous Mesoporous Mater.* **2008**, *110* (2–3), 590–594.

(7) Gupta, V.; Miura, N. *Electrochem. Solid-State Lett.* **2006**, *8* (12), A630.

(8) Tran, H. D.; D'Arcy, J. M.; Wang, Y.; Beltramo, P. J.; Strong, V. a.; Kaner, R. B. *J. Mater. Chem.* **2011**, *21* (11), 3534.

(9) Z. C. Sun, L. Kuang, X. B. Jing, X. H. Wang, J. Li, F. S. W. *Chem. J. Chinese Univ.* **2002**, *23* (3), 496–499.

(10) Chen, W.; Rakhi, R. B.; Alshareef, H. N. *Nanoscale* **2013**, *5* (10), 4134–4138.

(11) Zhang, A. Q.; Cui, C. Q.; Lee, J. Y. *Synth. Met.* **1995**, *72* (3), 217–223.

(12) Li, R. L.; Lin, C. W.; Shao, Y.; Chang, C. W.; Yao, F. K.; Kowal, M. D.; Wang, H.; Yeung, M. T.; Huang, S. C.; Kaner, R. B. *Polymers.* **2016**, *8* (11).

(13) Mažeikienė, R.; Malinauskas, A. *Synth. Met.* **2001**, *123* (2), 349–354.

(14) Simões, F. R.; Pocrifka, L. A.; Marchesi, L. F. Q. P.; Pereira, E. C. *J. Phys. Chem. B* **2011**, *115* (38), 11092–11097.

(15) Eftekhari, A.; Li, L.; Yang, Y. *J. Power Sources* **2017**, *347*, 86–107.

Chapter 4. Graphene/Oligoaniline Based Supercapacitors: Towards Conducting Polymer Materials with High Rate Charge Storage

Abstract

Carbon-based supercapacitors exhibit great rate capability, power density and cycle life, but suffer from relatively low energy density. Polyaniline provides high specific capacitance, but lacks cycling stability. By combining carbon-based materials with tetraaniline, an oligomer of polyaniline, a hybrid composite is formed that demonstrates improved supercapacitor performance relative to either material alone. In this study, the reduced graphene oxide-oligoaniline composites have been synthesized by a one-step hydrothermal process without the need for adding any oxidizing or reducing agents. FTIR, Raman spectroscopy, XPS, and MALDI-TOF mass spectroscopy indicate the successful reduction of GO to rGO and the formation of aniline oligomers. Unlike most polyaniline nanostructures for which charge storage kinetics are limited by slow diffusion-controlled reactions, the majority of oligoaniline in this composite is exposed to the electrolyte and stores charge through fast surface-controlled reactions. The unique microstructure of the rGO-oligoaniline composites facilitates transport of ions and electrons, leading to greater utilization of the active materials, high specific capacitance (640 F/g or 707 C/g at 0.2 mA/cm^2), great rate capability and good cycle stability (91% retention after 2000 cycles).

4.1. Introduction

Due to its high electrical conductivity, tunable morphology, high theoretical pseudo-capacitance, ease of synthesis, minimal environmental impact and low cost,[1–4] polyaniline (PANI) is considered a promising pseudo-capacitive electrode material for supercapacitors.[5] Oligoanilines, especially phenyl-capped tetra-aniline (TANI), have also been investigated in recent years, as they

also exhibit promising supercapacitor performances.[6,7] However, because of ion doping and de-doping during charge/discharge processes, both PANI and TANI experience a considerable amount of volume change during repeated cycling and degrade rather quickly.[8] As long cycle life is a major advantage that supercapacitors have over batteries, the cycling stability of PANI/TANI presents a great challenge for their practical application as supercapacitor electrodes.

Various groups have attempted to tackle this problem by making composites of PANI/TANI and carbon-based materials, such as carbon nanotubes (CNTs), graphene oxide (GO) and reduced graphene oxide (rGO). These carbon materials are believed to provide good electrical and mechanical support for the conducting polymers, preventing large volume changes and thus the break-down of the conducting polymers. Simotwo and coauthors developed a freestanding PANI-CNT composite material using a single step electrospinning process, and the composite material exhibited good specific capacitance of 385 F/g at 0.5 A/g and 81.4% capacitance retention after 1000 cycles.[9] Liu, *et al*. deposited a carbonaceous shell onto the surface of PANI nanowires and reported excellent cycling stability, but the specific capacitance of the material was likely compromised by the shell.[10] Wang *et al.* reported a nanostructured graphene-PANI composite with high specific capacitance (532 F/g at 2 mV/s) and relatively good cycle life.[11]

Among these carbon materials, rGO demonstrates high electron conductivity, great mechanical strength, a porous structure, large surface area and relatively easy synthesis, making it a particular promising candidate for PANI-carbon composites.[12,13] However, PANI and rGO, once formed, are rather difficult to re-disperse. Therefore, in order to achieve the synergetic effects of a composite material, the precursors to these two materials need to be combined homogeneously and react simultaneously. To combine the materials is relatively easy, as both aniline monomer and GO can be dispersed in aqueous solutions under stirring or sonication. However, growing rGO

and PANI into a uniform composite can be quite difficult: graphene oxide (GO) needs to be reduced (typically by hydrazine, urea, ascorbic acid or another reducing agent) to form rGO, while aniline needs to be oxidized (usually by ammonia persulfate or another strong oxidizing agent) to form PANI. Therefore, *in situ* rGO-PANI composites are usually synthesized in multiple steps. A typical approach is to first oxidatively grow PANI on GO, followed by reduction of the GO to rGO and then re-oxidation of PANI to the conductive emeraldine state to regain its electroactivity.[14] Other groups have utilized the self-assembly of PANI on GO or GO on PANI to make composites, which are later reduced to form rGO-PANI composites.[15,16] However, all these processes are rather time consuming and taxing.

Herein, we report a one-step-one-pot hydrothermal synthesis of reduced graphene oxide-oligoaniline composites (rGO-OANI) without the need for adding either reducing or oxidizing agents as illustrated in Scheme 4.1. Hydrothermal synthesis is a very powerful tool for making rGO[17], PANI[16] and composites.[5,11] N-phenyl-p-phenylenediamine (aniline dimer) has a much lower oxidation potential than aniline monomer and can dimerize under certain conditions to form aniline tetramer (TANI).[4] By starting from GO and aniline dimer, we were able to dimerize/oligomerize aniline dimer and reduce GO simultaneously. Note that no external oxidizing agent (such as APS) or reducing agent (such as hydrazine) was introduced in the process, but environmental oxygen was not purged from the solvents. In addition, aniline dimer and oligomers are shown to be able to reduce GO to a certain extent, such that the composite materials do exhibit excellent supercapacitor behavior. The resulting sheet-like rGO-OANI composite materials show excellent specific capacitance up to 518 F/g (or 570 C/g) at 5 mV/s and 643 F/g (or 707 C/g) at 0.2 mA/cm^2 with good cycling stability. This green, simple and facile process produces

homogeneous composite materials with improved specific capacitance, superior rate capability, and good cycle life.

Scheme 4.1 Illustration of the hydrothermal synthesis of rGO-OANI composites.

4.2. Results and Discussions

4.2.1. Morphology and chemical structural analysis

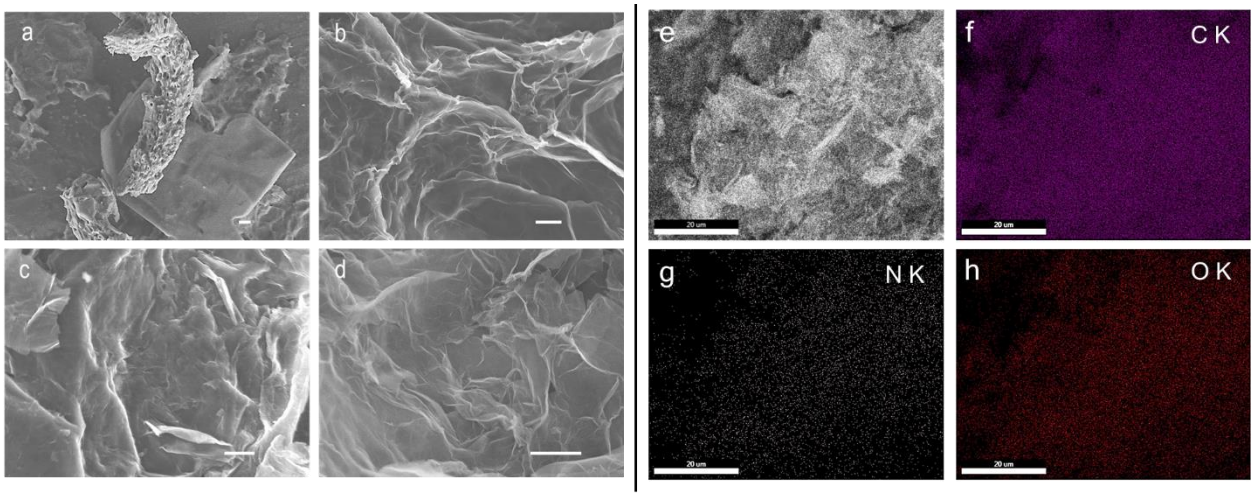

Figure 4.1 SEM images of (a) rGO-OANI 75, (b) rGO-OANI 100, (c) rGO-OANI 140 and (d) rGO 140. Scale bar = 1 µm. (e)- (h) are rGO-OANI 100 SEM images and EDS mapping images showing elemental C, N and O, respectively. Scale bar = 20 µm.

The scanning electron microscopy images of the composites and rGO are shown in Figure 4.1. The morphology of the rGO, rGO-OANI 100 and rGO-OANI 140 composites appear rather similar, although the rGO-OANI 75 does show aggregates of OANI in addition to rGO sheets. The composite materials seem to have thicker edges and appear to be less transparent than pure rGO. It is likely that OANI forms a layer that coats the rGO sheets, as some ridges and valleys are visible on the graphene sheets of the composite materials, while the rGO sheets seem to be mostly flat and clean. Energy dispersive spectra of the composites were also obtained. The elemental mapping images of rGO-OANI 100 are shown in Figure 4.1e-h. The N element mapping image shows that nitrogen is present and uniformly distributed on the rGO sheets, corroborating the previous assumption. It is also worth noting that after being washed in acetone a few times, the composite materials show nearly identical morphology to the rGO sheets (Figure S4.2). This observation suggests that the majority of the conducting polymers are likely composed of oligomers (soluble in organic solvents) adsorbed on the rGO sheets via π-π stacking, H-bonding and other intermolecular interactions. However, SEM alone is not sufficient to rule out the possibility that some oligoaniline are chemically grafted onto the GO sheets. Some additional SEM images can be found in Figure S4.1.

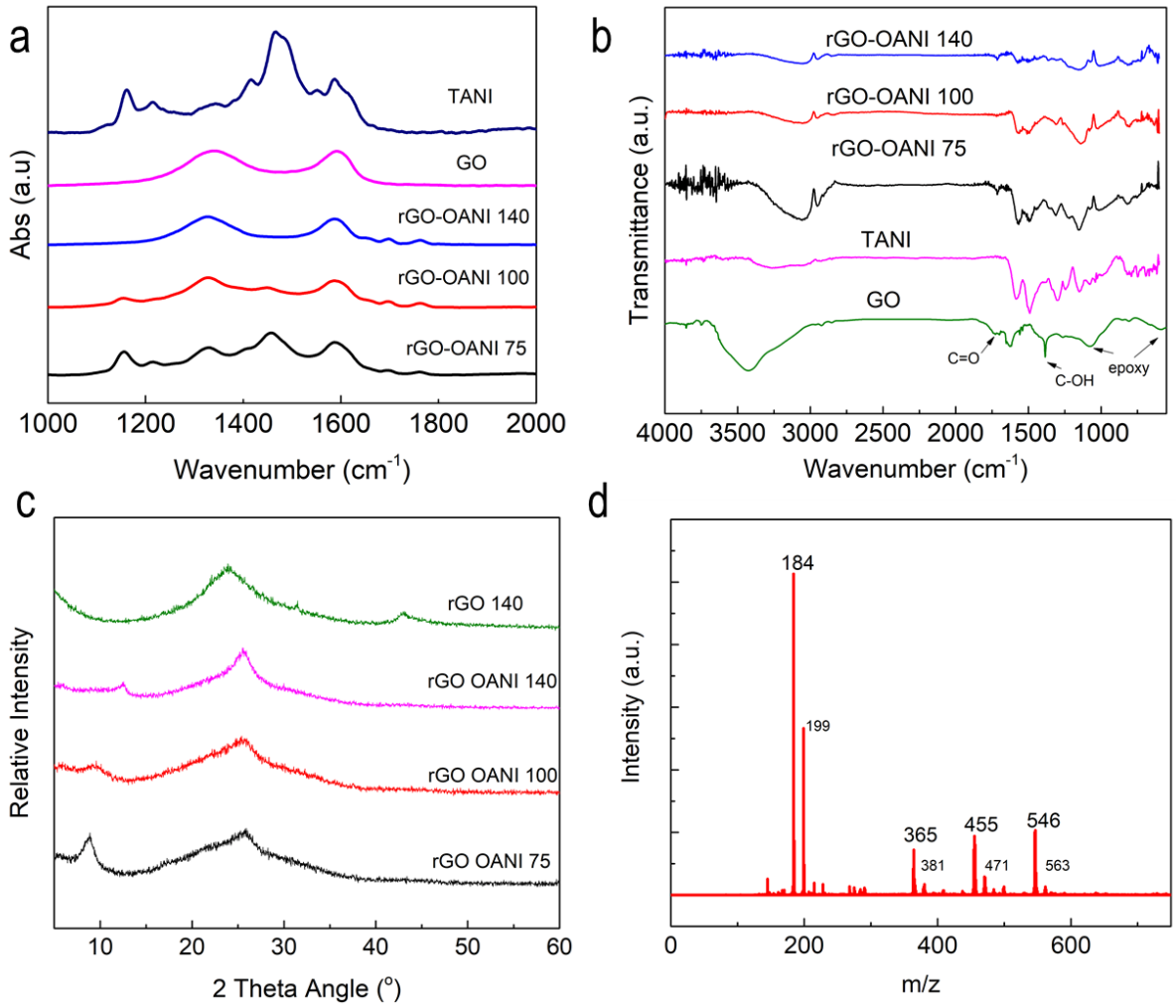

Figure 4.2 (a) Raman spectra of the rGO-OANI composites, GO, and TANI. (b) FTIR spectra of GO, TANI, and the rGO-OANI composites. (c) XRD patterns of the rGO-OANI composites and rGO 140. (d) MALDI-TOF mass spectrum of rGO-OANI 100 in an acetone wash solution.

Raman spectroscopy and FTIR are useful techniques to characterize the chemical structure of the reduced graphene oxide. As shown in Figure 4.2a, the Raman spectra of the composite materials all show characteristic peaks of both reduced graphene oxide and oligoaniline. The peaks ascribed to oligoaniline are: a sharp peak at 1160 cm^{-1} (C-H bending vibration of the semi-quinoid rings), a weak peak at 1215 cm^{-1} (C-N stretching of the quinoid rings), a shoulder peak at 1260 cm^{-1} (shoulder C-N stretching of the benzenoid rings), a weak or shoulder peak at 1400 cm^{-1} (C=C stretching of the phenazine structure), and a strong band at 1455 cm^{-1} (C=N vibrations in the quinoid rings).[18] The two broad bands at 1330 and 1585 cm^{-1} correspond to the characteristic D

band and G bands of rGO, respectively. However, these two peaks also coincide with C-N vibrations of polaron structures and C=C vibrations of the quinoid ring on oligoaniline.[18] Therefore, even though the intensity ratio of the D/G band is usually taken as a measure of the degree of reduction of GO to rGO, the degree of GO reduction cannot be determined conclusively from the Raman spectra. Comparing the composites alone, the D/G intensity ratio increases as the reaction temperature increases from 75 to 140 °C, suggesting that rGO-OANI 140 exhibits the highest degree of reduction. The Raman spectra also show a drastic decrease in the intensity of the OANI peaks (most significantly at 1455 cm^{-1}) as the reaction temperature rises. So, as the degree of GO reduction increases with temperature, the conducting oligomer loading decreases with temperature.

Figure 4.2b shows the FTIR spectra of the rGO-OANI composite materials, pure tetra-aniline (TANI) and graphene oxide (GO). Similar to Raman, the FTIR spectra of the composites show both rGO and TANI/OANI peaks. The broad band from 3200 to 3400 cm^{-1} is associated with N-H stretching of the amine groups on OANI. The peaks at 1580 and 1480 cm^{-1} are ascribed to the stretching vibrations of the C=C bonds on the quinoid and benzenoid rings, respectively. The 1290 and 1245 cm^{-1} are due to aromatic amine C-N stretching of OANI. The 1140 cm^{-1} corresponds to benzenoid-NH-quinoid vibrations, characteristics of delocalization of the electrons in the OANI backbone and an indication of polymerization/oligomerization of aniline dimer.[11] The composite materials show the presence of adsorbed water as indicated by the broad band at around 3600 cm^{-1} (O-H stretching) and the weak peak around 1640 cm^{-1} (scissoring vibration of water[19]). The bands at 2950 and 2890 cm^{-1} are associated with alkane -CH_2 asymmetric and symmetric stretching on GO/rGO/graphite sheets (as a result of impurity and/or defects present in natural graphite[20]). The FTIR spectra indicate the presence of carbonyl groups in the composite materials, as there is a small peak in the 1730-1750 cm^{-1} range. The GO peaks due to epoxy (C-O-C stretching at 1040

cm^{-1}) and hydroxyl groups (C-OH bending at 1380 cm^{-1})[21] disappeared from the composite spectra after the reaction, suggesting a ring-opening reaction of the epoxy groups and the removal of hydroxyl groups during the reduction process.

In conjunction with FTIR and Raman spectroscopy, XPS was utilized to further analyze the chemical structure and composition of the composites. The survey scans of the composites are shown in Figure S4.4a, in which, elements such as oxygen, nitrogen, carbon and trace amounts of sulfur (from sulfuric acid) and silicon (from GO) are identified. From the survey scans, the nitrogen contents of rGO-OANI 75, rGO-OANI 100 and rGO-OANI 140 were determined to be 5.1%, 3.9% and 3.4%, respectively. Since GO is nitrogen-free and the only nitrogen containing species is oligoaniline, the nitrogen contents can be converted to OANI to GO weight ratios: 2/5 for rGO-OANI 75, 1/3 for rGO-OANI 100 and 1/4 for rGO-OANI 140 (see Table S4.1). The conducting polymer loading is inversely related to the reaction temperature (i.e., higher temperatures lead to lower loadings), consistent with the XRD data.

The deconvoluted C1s spectra of the composites are shown in Figure 4.3. The C1s spectrum can be decomposed into six peaks: 284.57 eV (C=C), 285.56 eV (C-N), 286.31 (C-O), 286.7 (C-O-C), 287.1 (C=O), and 288.73 (COOH). Compared with GO, the composites show drastically decreased intensity for peaks corresponding to C=O and C-O-C. rGO-OANI 100 and 140 show more reduction in the COOH peak intensity than does rGO-OANI 75, suggesting that carboxylic acid groups leave as CO_2 at higher temperatures. The N1s spectra are shown in Figure S4.4, and the deconvolution shows peaks for N in three different states: benzenoid amine (399.5 eV), quinoid amine (398.8 eV), and polaronic amine (401.0 eV), further confirming the formation of oligoaniline.[19,22]

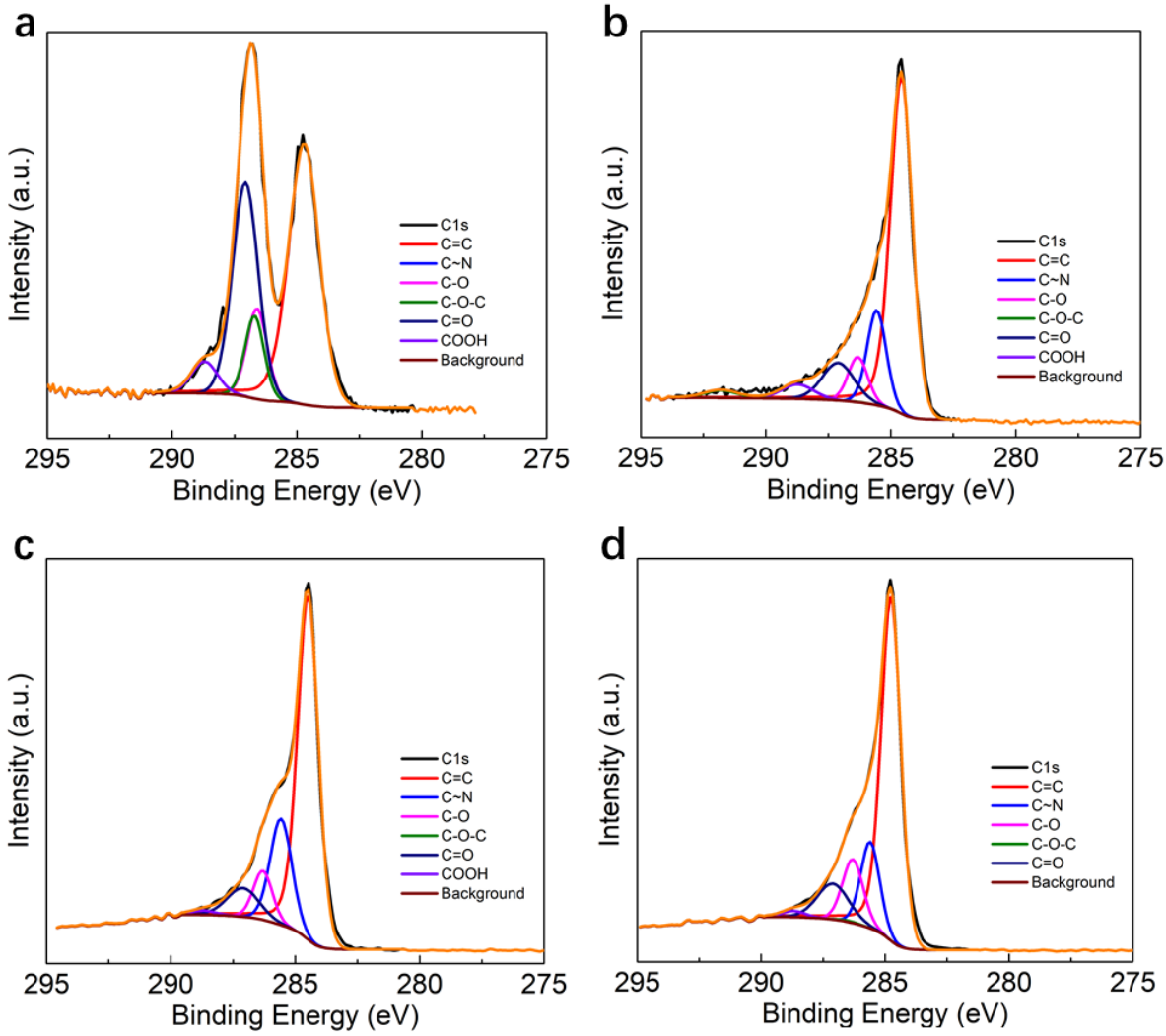

Figure 4.3 X-ray Photoelectron Spectroscopy deconvoluted C1s spectra of (a) GO, (b) rGO-OANI 75, (c) rGO-OANI 100 and (d) rGO-OANI 140.

The structure of the composite materials was further characterized with powder X-ray diffraction (XRD). The XRD patterns of the composite materials synthesized at different temperatures are presented in Figure 4.2c. All composite materials show a very broad peak at around $2\theta = 25.5°$ (interlayer spacing of about 3.49 angstroms), indicative of randomly stacked rGO sheets. A smaller peak can also be found in the 9-12° range that signifies the presence of residual GO. For comparison, the XRD patterns of a composite material, GO, hydrothermally reduced rGOs and PANI nanowire are presented in Figure S4.3. GO shows a sharp graphite (001)

peak at ~13°. rGO 100 also shows a very strong (001) peak at around 11° and a low intensity (002) peak at ~25°, suggesting that graphene oxide cannot be hydrothermally reduced at 100 °C in the absence of a reducing agent. By contrast, rGO 180 shows a broad graphite (002) peak at ~26°, a smaller (100) peak at ~43° but no (001) peak, indicating that, at 180 °C the hydrothermal process is enough to reduce GO even without a reducing agent. However, rGO-OANI 100 shows a much stronger (002) peak compared to rGO 100, but also displays a small (001) peak at ~10°. This indicates that the reduction of rGO in the presence of aniline dimer at 100 °C, is not simply due to thermal reduction. Instead, aniline dimer likely reacts with some oxygen containing functional groups on GO and reduces GO chemically.

The chemical composition of the conducting oligomer resulting from the reaction was analyzed using MALDI-TOF mass spectroscopy. To get an accurate representation of the molecular weight distribution of the oligoaniline after the reaction, about 5 mL of acetone was added into the reaction mixture of one rGO-OANI 100 batch (the initial reaction solution was a mixture of ~2 mL ethanol and ~10 mL water; acetone was added to increase the solubility of oligoaniline in solution), the wash solution/suspension was centrifuged and the supernatant was tested. Shown in Figure 4.2d, the spectrum of the wash solution displays four major peaks at m/z = 184, 365, 455 and 546, and 4 smaller peaks at m/z = 199, 381, 471, and 563. Note that the smaller peaks are all about 16 units higher than the nearest major peaks. The major peaks correspond to aniline dimer, tetramer, pentamer, and hexamer, respectively. The smaller peaks most likely correspond to hydroxylamine byproducts of these oligoanilines reacting with epoxy rings on the GO sheets, via a mechanism similar to that proposed for the reduction of GO using ethylenediamine.[23] It is worth mentioning that since there is an excess of aniline dimer, the amount of aniline dimer added to the reaction is more than enough to react with all the graphene oxide.

However, as shown in other data, the graphene oxide in the rGO-OANI composites was not completely reduced. Therefore, it can be deduced that aniline oligomers can only react with certain types of oxygen containing functional groups (based on XPS data, mainly carbonyl groups and epoxy groups) on the graphene oxide sheets.

To understand the oligomerization of aniline dimer, two control experiments were performed: 1. aniline dimer was dissolved in the same matrix, but in the absence of GO, and heated in an autoclave for 10 hrs; 2. All conditions were identical to control experiment 1, but the solvents were purged with argon gas for 15 minutes before aniline dimer was dissolved. Control experiment 1 yielded a violet solution with some dark violet solid products, while control experiment 2 yielded a greyish-green solution without solid products. The mass spectra of these products are shown in Figure S4.5. In the absence of GO and oxygen, the product shows a typical aniline dimer mass spectrum, with trace amounts of TANI and other impurities. In the presence of oxygen, however, the product shows a slightly higher amount of TANI and trace amounts of higher oligomers, but the overall percentage of oligomer aniline is lower than that of rGO-OANI composites. The results from these control experiments indicate that the dimerization/oligomerization of aniline dimer is likely due to both environmental oxygen and some functional groups on GO. Also interesting is that fact that the peak at m/z = 199 is much smaller in the control spectrum than in the rGO-OANI wash spectrum, corroborating the hypothesis that aniline dimer reacted with GO to form hydroxylamine.

4.2.2. Possible Mechanisms of GO reduction

Based on Mass spec, FTIR, XPS data, and previously presented amine assisted GO reduction mechanisms,[23,24] we speculate that the reduction of GO by aniline dimer involves epoxy

ring-opening followed by de-hydroxylation, thermal de-carboxylation and possibly imine formation.

FTIR data show that the signals from epoxy groups and C-OH groups diminished after the reaction, and this suggests that there is an epoxy ring opening reaction followed by a de-hydroxylation reaction (in agreement with a proposed mechanism from reference [23]). Mass spec data show the presence of hydroxylamines, thus corroborating the above mechanism. Deconvoluted C1s XPS data indicate that C=O and COOH signals also decreased after the reaction, suggesting that COOH leaves as CO_2 at elevated temperatures (100 and 140 °C compared to 75 °C). Even though it is suspected that aniline oligomers could react with C=O to form imines (thus reducing C=O signal intensity), it is not possible to differentiate C=N bonds on the backbone of oligoaniline from those that connect oligoanilines and rGO sheets. Therefore, the formation of imine remains largely speculative.

Based on the above discussion, we propose a de-epoxidation reaction, as shown in Scheme 4.2. The terminal amine group on either aniline dimer or oligomer reacts with an epoxy group on the graphene oxide sheet, opens up a three-membered ring, and grafts onto the GO sheet, forming the intermediate product. The grafted amine group could then further react with an adjacent hydroxyl group on the same side of the GO sheet to perform an elimination reaction that removes the hydroxylamine, forming the final products. It is also possible that some variants of intermediate product, without hydroxyl groups next to the grafted secondary amine, remains unreacted in the final rGO-OANI products. However, based on available data, the presence of the intermediate could not be definitively confirmed.

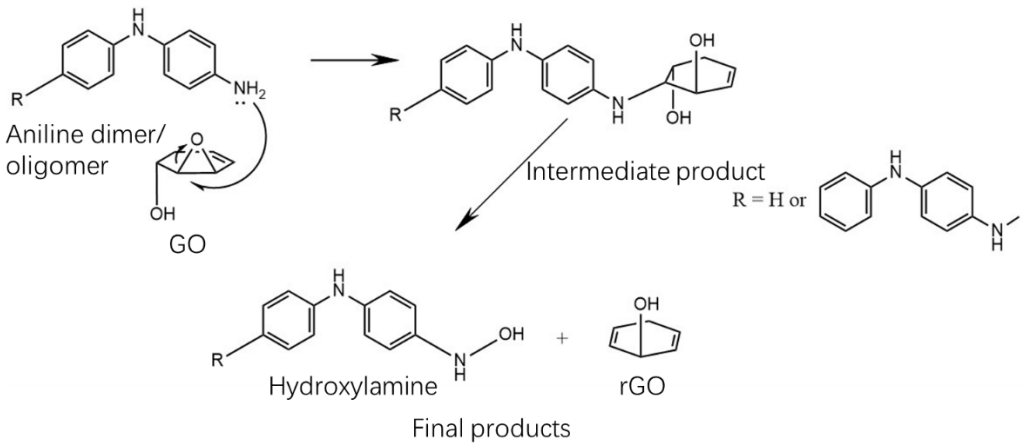

Scheme 4.2 Possible GO de-epoxidation mechanism in the presence of aniline dimer or tetramer.

4.2.3. Electrochemical Characterizations

To investigate the supercapacitor properties of the rGO-OANI composites, cyclic voltammetry (CV), constant current charge discharge (CC), and electrochemical impedance spectroscopy (EIS) measurements were performed using a three-electrode configuration. Figure 4.4a-c show the typical CV diagrams of rGO-OANI 75, rGO-OANI 100 and rGO-OANI 140 electrodes in 1.0 M H_2SO_4 electrolyte solution at various scan rates. All CV curves show two pairs of redox peaks at around 0.25 V and 0.50 V, corresponding to the oligoaniline transitioning from the leucoemeraldine state to the emeraldine state and from emeraldine to pernigraniline, respectively. At higher scan rates (>100 mV/s), both rGO-OANI 75 and rGO-OANI 140 show signs of deviation in the shape of the CV curves, however, rGO-OANI 100 shows little or no such distortion. This suggests superior rate capability and indeed, as shown in Figure 4.4e, rGO-OANI 100 does exhibit an excellent 88.2% capacity retention as the scan rate is increased from 5 to 150 mV/s. It is also worth noting that even though rGO-OANI 75 and rGO-OANI 140 show poorer kinetics, they still retain about ~80% of the 5 mV/s capacity at 150 mV/s. The average specific capacitance and specific capacity values calculated from CV according to Equation 4.4 are shown

in Table S4.2. rGO-140 shows the highest average specific capacitance of 520 F/g (or 570 C/g) at 5 mV/s. However, due to its sluggish kinetics, rGO-OANI 140 falls behind rGO-OANI 100 at very high scan rates (400 F/g vs. 410 F/g).

Figure 4.4f shows a comparison between rGO-100, rGO-180 and rGO-OANI 100 CV curves at 30 mV/s in 1.0 M H_2SO_4. The curve of rGO-100 shows a very low current density compared to the other two, and this is expected as it is mainly comprised of un-reduced graphene oxide. rGO-180 shows a relatively higher current density, indicating that it is indeed reduced graphene oxide. There is a set of redox peaks around 0.4 V that results from the remaining oxygen containing functional groups left on the reduced graphene sheets. The rGO-OANI 100 composite material, by contrast, shows a much higher current density than both rGO samples, not only around the redox active potentials (0.3 V and 0.5 V) but also in the potential ranges dominated by EDLC capacitance (-0.2-0.1 V and 0.7-0.9 V). Due to the *in situ* reaction, the oligoaniline likely has ample opportunities to be adsorbed or grafted onto the reduced graphene sheets, thus, not only providing good electrical contact between the conducting oligomers and the rGO sheets, but also preventing restacking of the sheets. Therefore, the rGO-OANI composites likely benefit from both Faradaic processes and added EDLC capacitance in a synergetic effect, resulting in much higher specific capacitance than rGO alone. The complete CV average specific capacitances/specific capacities of the samples are tabulated in Table S4.2. The instantaneous specific capacitance of the rGO-OANI composites at different potentials and scan rates (derived from CV data using Equation 4.6) are presented in Figure S4.8.

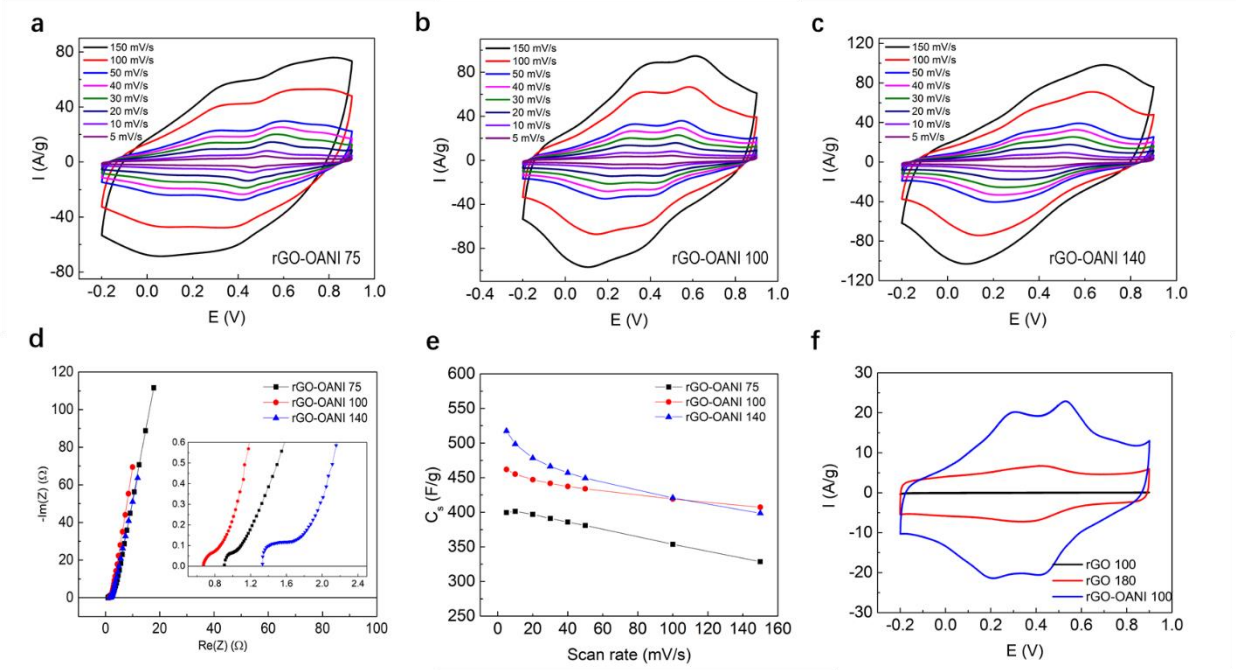

Figure 4.4 Cyclic voltammograms of (a) rGO-OANI 75, (b) CV diagrams o rGO-OANI 100 and (c) rGO-OANI 140 at various scan rates. (d) Nyquist plots of rGO-OANI composites (0.3 V vs ref.). Inset: Zoom-in plot of the high frequency range. (e) Calculated average specific capacitance of rGO-OANI composites at various scan rates. (f) CV diagrams of rGO 100, rGO 180 and rGO-OANI 100 at 30 mV/s.

Figure 4.4d shows the Nyquist plot of the rGO-OANI composites at 0.3 V vs. the reference electrode. All three electrodes exhibit a semicircle in the high frequency range and a straight line in the low frequency range, but rGO-OANI 100 has the smallest x-axis intercept and semicircle radius, corresponding to the uncompensated resistance and charge transfer resistance, respectively. Fitting the EIS data in the frequency range of 1 Hz to 3000 Hz, the uncompensated resistance (of the electrode and bulk solution) and charge transfer resistance of rGO-OANI 100 at 0.3 V vs. the Ag/AgCl reference electrode are calculated to be about 0.675 Ω and 0.080 Ω respectively (see Scheme S4.1 for equivalent circuit and fitting details). In comparison, rGO-OANI 75 shows very similar charge transfer resistance, but slightly higher uncompensated series resistance than rGO-OANI 100. For this reason, its 150 mV/s CV curve displays very clear redox peak separation, but the overall shape appears less rectangular compared to that of rGO-OANI 100. On the other hand,

rGO-OANI 140 suffers from both higher charge transfer resistance and series resistance, which explains the lack of peak separation and rectangular shape on its fast-scan rate CV curves.

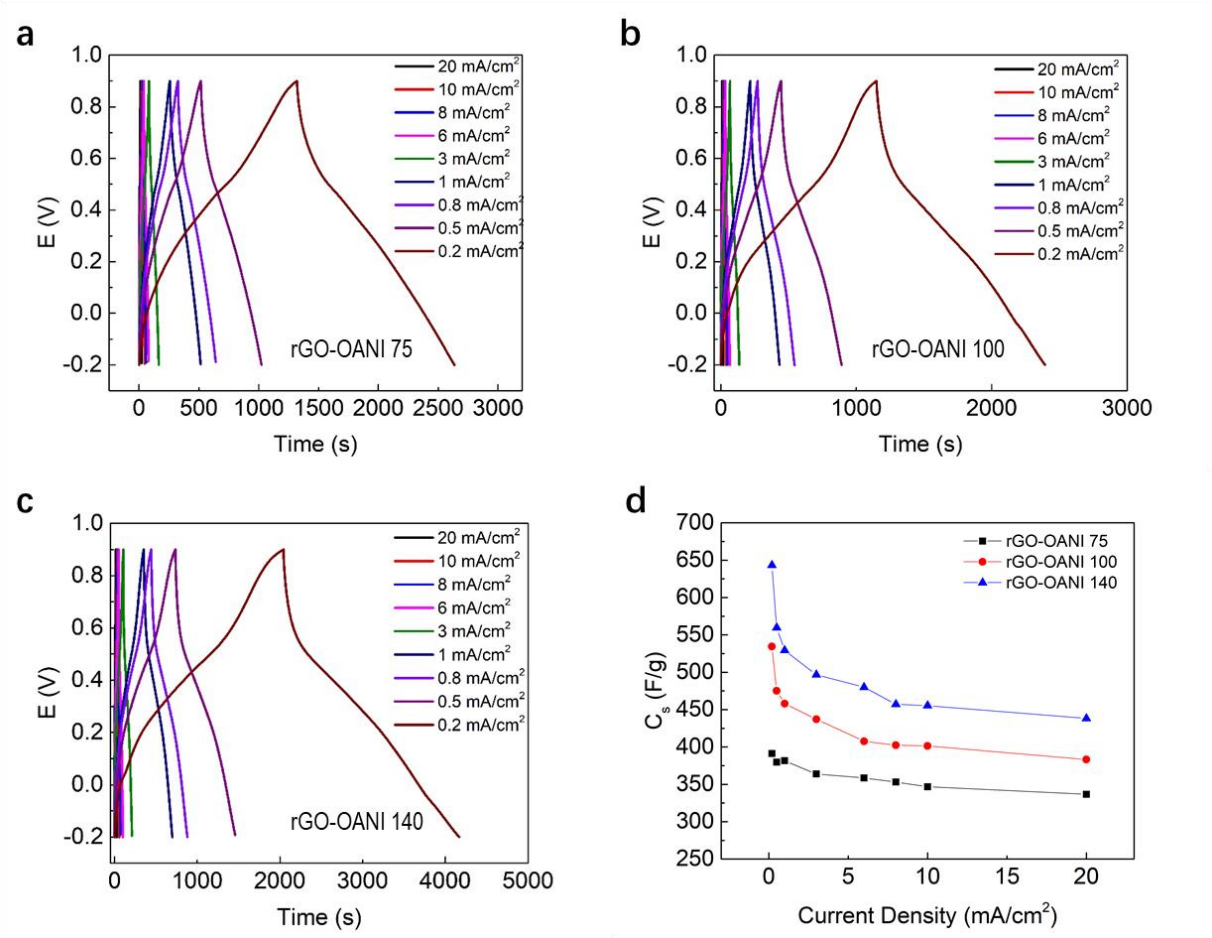

Figure 4.5 Charge-discharge curves of (a) rGO-OANI 75, (b) rGO-OANI 100, and (c) rGO-OANI 140 at various current densities. (d) Calculated average specific capacitances of the rGO-OANI composites.

Figure 4.5 shows the CC curves of the composite materials at different current densities. The slopes of the charge-discharge curves are steeper towards the two ends of the potential window (-0.2-0.1 V and 0.6-0.9 V), and are less steep towards the middle of the potential window (0.1-0.6 V). This variation in the slope of the charge-discharge curves correlates quite well with the CV diagrams, where the redox-active regions (peaks) on the CV curves show up in the middle of the potential window and the EDLC-dominated regions appear towards the two ends. Due to low uncompensated series resistance of these materials, there are no apparent IR drops in the CC curves,

indicating good power output (the resistance calculated from the IR drops can be found in Table S4.4). From the discharge curves, the average specific capacitances (and specific capacities) of the materials are calculated according to Equation 4.5 and the values are reported in Table S4.3. As the current density span of the CC measurements is a bit wider than the scan rate range of the CV measurements (mainly at lower currents/scan rates), the maximum CC specific capacitances observed for the composite materials at 0.2 mA/cm^2 are higher than those of the CV measurements at 5 mV/s. Notably, rGO-OANI 140 exhibits the highest average specific capacitance among all the composites at all current densities: 640 F/g (or 707 C/g) at 0.2 mA/cm^2 (about 0.34 A/g) and 440 F/g (or 480 C/g) at 20 mA/cm^2 (about 33.8 A/g).

Combining the results of CC, CV and XPS data, it is apparent that the specific capacitance of the composite material is inversely correlated with oligoaniline loading. As rGO has a much lower specific capacitance than TANI, this phenomenon could best be explained by the synergetic effects that results from the *in situ* reduction of rGO and the self-assembly of the conducting oligomer on the rGO sheets. It is very likely that the uniform coating of the conducting polymer/oligomers on the porous rGO structures, as seen in rGO-OANI 100 and 140 SEM images, provides both ion channels for mass transport and enhanced utilization ratio of the redox-active material. In contrast, the OANI aggregates shown in the rGO-OANI 75 suffer from a lack of hierarchical porous structures and a higher ratio of inactive core material (dead mass), and thus exhibit lower specific capacitance.

To better understand the charge storage mechanism of the composite materials, the relationship between current and scan rate in the CV experiments were studied. The charge storage process can be separated into two components: the redox reactions of oligoaniline (i.e. diffusion controlled Faradaic processes) and non-redox physical ion adsorption processes (i.e. electrical

double-layer capacitance, or EDLC). These processes can be characterized by analyzing the dependency of the current on the scan rates according to the following equation:

$$i = av^b \tag{4.1}$$

where the measured current *i* follows a power law relationship with the scan rate *v*; where *a* is an adjustable parameter and the *b*-value is indicative of the charge storage mechanism. The *b* value can be obtained by determining the slope from a plot of *log(v)* vs. *log(i)*. For b = 1.0, the storage process is representative of an EDLC-like or a surface dominated mechanism. For b = 0.5, the process is diffusion controlled, characteristic of a Faradaic process.[25,26]

Another analysis of the relationship between scan rate and current at certain potentials can semi-quantitatively separate the diffusion-controlled and capacitive processes using the following equation:

$$i = k_1 v + k_2 v^{1/2} \tag{4.2}$$

In Equation 4.2, i is the measured current at a specific voltage, and $k_1 v$ and $k_2 v^{1/2}$ correpond to surface and diffusion-controlled processes, respectively. Thus, the contribution of different processes can be determined by obtaining the *k*-values. To facilitate the analysis, Equation 4.2 can be rearranged by dividing both sides by $v^{1/2}$, and the equation becomes:

$$i/v^{1/2} = k_1 v^{1/2} + k_2 \tag{4.3}$$

By ploting $v^{1/2}$ against $i/v^{1/2}$, the slope of the plot corresponds to k_1 and the y-intercept corresponds to k_2.[25]

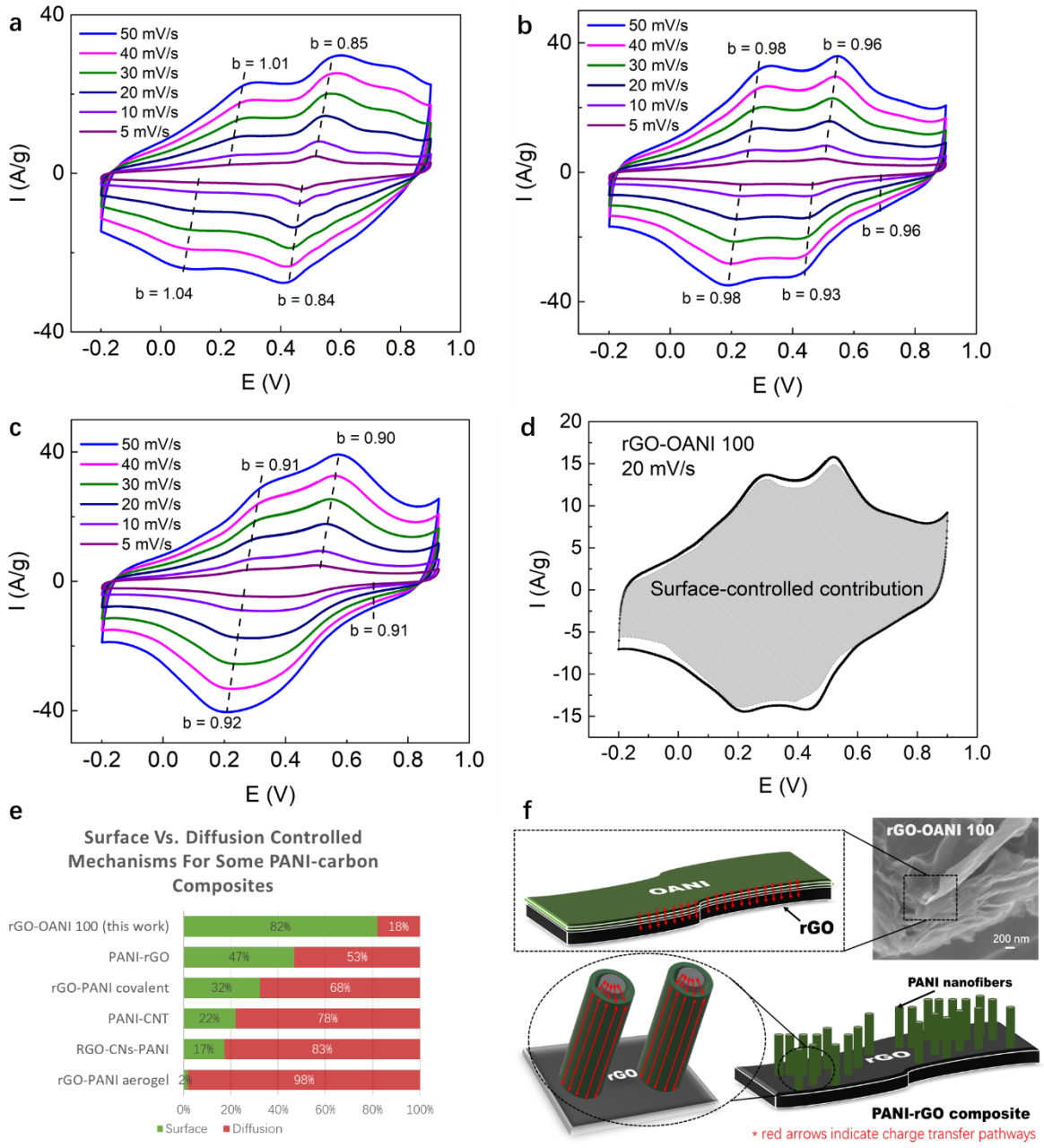

Figure 4.6 Analysis of the charge storage mechanism of (a) rGO-OANI 75, (b) rGO-OANI 100 and (c) rGO-OANI 140 at various potentials. (d) Calculated EDLC-like capacitance contribution in rGO-OANI 100. (e) Surface vs. diffusion-controlled charge storage contribution of some PANI-carbon composites. (f) Illustration of the charge-transfer pathways of rGO-OANI and PANI-nanowire-rGO.

The *b*-values of the composites obtained at various potentials are shown in Figure 4.6, while the actual plots are presented in Figure S4.6 and the detailed results compiled in Table S4.5. For mathematical simplicity, a very slow scan rate of 1 mV/s is applied (unless specified otherwise)

when differentiating different charge storage mechanisms based on *k*-values (Note that the surface-controlled contribution increases with scan rate). The *b*-values for the rGO-OANI composites in the plateau regions (where there are no peaks in the CV curves) are found to be between 0.91 to 1.01, suggesting a surface dominant mechanism. Corroborating the *b*-value analysis, the *k*-value analysis indicates more than 70% surface-controlled contribution. The *b*-value of rGO-OANI 75 obtained at around 0.45 V, the potential corresponding to the emeraldine to pernigraniline transition, is 0.84, indicating that the stroage mechanism is a mixture of surface and diffusion controlled processes. This is in good agreement with the *k*-values, as the surface-controlled contribution falls to about 31%. However, the *b*-values of the rGO-OANI 100 and 140 composites at redox active potentials are found to be close to 1.0, suggesting that the redox/Faradaic processes of OANI thin films/coatings take place primarily on the surface. Indeed, according to the *k*-values, the charge storage mechanism at these peak positions is dominated by more than 67% of surface-controlled contribution. Notably, rGO-OANI 100 shows *b*-values close to 1.0 and very high surface-controlled capacitance contributions in all potential ranges tested (Figure 4.6d and Table S4.7, scan rate = 20 mV/s), corroborating the excellent rate capability demonstrated by the CV and CC results.

In comparison, PANI-carbon composites reported by other groups exhibit *b*-values from about 0.5-0.85 and rapid surface-controlled capacitance of less than 47% at their peak potentials (see Table S4.6),[9,27–29] consequently demonstrating poorer rate capabilities. These composites have polyaniline grown on the carbon substrates, but the polyaniline components show distinct structures and form separate domains on the carbon materials. The illustration in Figure 4.6f shows the difference between rGO-OANI and rGO/PANI nanowires during the charge transfer process. In an ideal senario, where the PANI nanowires do not agglomerate and are all grown vertically

onto the rGO sheets, the redox reactions take place near the surface of the nanowires (leaving a small portion of the core material inactive), and electrons need to travel along the length of the nanowires to get to the rGO and eventually to the current collector. On the other hand, in the rGO-OANI composites, oligoaniline forms uniform thin coatings on the rGO sheets. This very thin oligoaniline layer not only takes advantage of the hierarchical porous structure of the carbon (thus facilitating mass transport), but also increases the utilization of the oligoaniline (less bulk material). In addition, electrons do not need to travel far to get to the rGO sheets. As a result, the redox reactions take place primarily on the surfaces of the composite material, and the redox behavior is more pseudocapacitance-like (or surface-controlled) than battery-like (or diffusion controlled). These results suggest that by uniformly coating conducting oligomers onto the rGO sheets, the composite materials benefit from the synergy between rGO and oligoanilines, and demonstrate even better rate capabilities than nanostructured PANI/carbon composites.

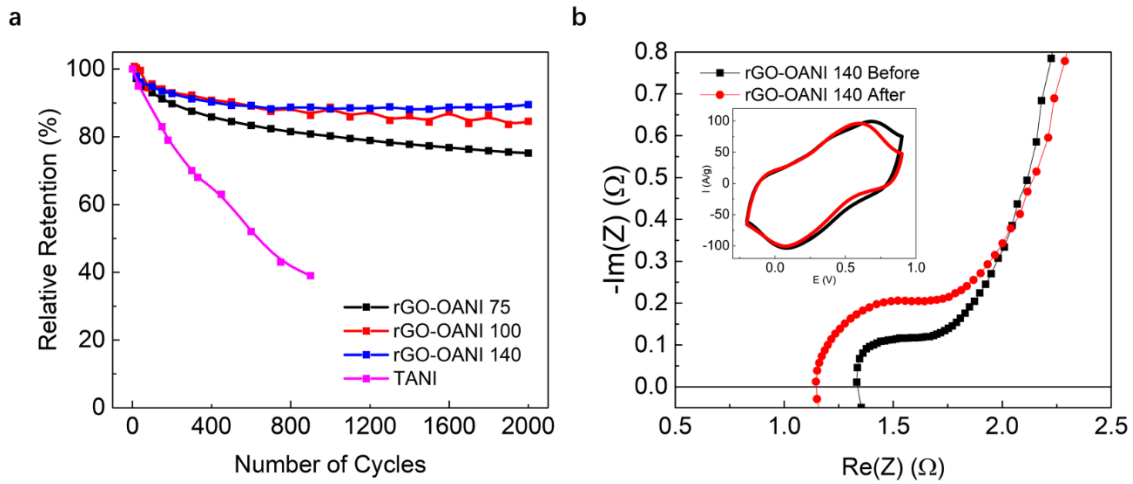

Figure 4.7 (a) Cycling performances of rGO-OANI composites and pure TANI. (b) A Nyquist plot of the rGO-OANI 140 electrode before and after 2000 cycles (0.3 V vs. reference electrode). Inset: CV diagrams of rGO-OANI 140 before and after 2000 cycles at 100 mV/s.

The cycle life of the composite materials was evaluated by CC cycling for 2000 cycles at appropriate current densities, such that each cycle takes about 30-40 seconds to complete. Figure 4.7a shows the relative capacitance retention of rGO-OANI composites and a pure tetra-aniline

sample as a control throughout the cycling tests. Tetra-aniline, similar to PANI, suffers from low cycling stability, as it retains only 40% of its original capacitance after 900 cycles. In contrast, all the composite materials show much improved cycle life: rGO-OANI 75 retains ~80%, rGO-OANI 100 retains ~85% and rGO-OANI 140 retains ~91% of their initial capacitance after 2000 cycles. This is likely because rGO provides a sturdy and flexible framework for sustaining OANI, preventing the polymer's changes in volume during the doping/de-doping processes from degrading the structure. Since the redox reactions take place primarily on the surface of the composite materials, the cycling stability is much improved. Figure 4.7b shows the Nyquist plots (0.3 V vs. the reference) and the CV curves of an rGO-OANI 140 sample before and after 2000 cycles. The area under the curve of the CV decreased slightly after cycling, but the shape of the curve remained essentially the same. The Nyquist plot after cycling shows a slight increase in charge transfer resistance, but also a small decrease in the uncompensated resistance. The decrease in series resistance could be due to activation of rGO or simply a decrease in resistance in the external circuit (the clips and wires were changed after the long cycling test). The source of increase in the charge transfer resistance could be slight changes in the morphology of the conducting oligomers (Figure S4.9), but the increase is relatively minor, thus corroborating the observed good cycling stability of the composite material.

As shown Figure 4.7a, the cycle life of the composites appears to increase with reaction temperature. This could be due to the lower loading of conducting polymers in the higher temperature composites, as the conducting polymers degrade faster than the rGO. Following this trend, a batch of rGO-OANI 180 sample was synthesized and tested. Indeed, it shows better cycle life than rGO-OANI 140 (more than 90% retention after 4000 cycles), but its specific capacitance/capacity is relatively low compared to the other composites (see Tables S4.2 and S4.3).

Some electrochemical properties of the rGO-OANI 180 composite are presented in Figure S4.7. The decrease in specific capacitance could be explained by loss of electroactivity in the conducting polymer due to the high reaction temperature.[11]

4.3. Conclusions

In conclusion, rGO-OANI composite materials were synthesized via an *in situ* redox reaction between aniline dimer and graphene oxide under hydrothermal conditions. Due to the synergy between the *in situ* synthesized OANI and rGO, the composites show excellent specific capacitance, very good rate capability, and good cycle life. The performance of the composites varies depending on the synthesis temperature. The composite synthesized at 140 °C exhibited superior supercapacitive performance, such as great rate capability (77% capacitance retention at 150 mV/s), high specific capacitance (518 F/g or 570 C/g at 5 mV/s and 643 F/g or 707 C/g at 0.2 mA/cm^2) and improved cycle stability (91% capacitance retention after 2000 cycles). The composite materials synthesized at other temperatures also show good performances. Therefore, this one-pot-one-step hydrothermal synthesis is a facile and promising method to produce rGO-OANI composites for supercapacitor applications.

4.4. Experimental

4.4.1. Materials and preparation methods

N-phenyl-p-phenylenediamine (aniline dimer) was purchased from VWR. HCl (37%) and ethanol were obtained from Sigma-Aldrich. Graphite paper (0.070 mm thick) used for current collectors was purchased from Digi-Key Electronics (manufactured by Panasonic Electronic Components, part number: P13689-ND). All reagents were reagent grade and used without further purification.

Preparation of reduced graphene oxide-oligoaniline composites: Graphene oxide was reduced by aniline dimer via a hydrothermal method, while aniline dimer was oxidized and polymerized during the same process. In a typical reaction, 770 mg of GO solution (10 mg net weight) was dispersed in 9.0 mL 0.1 M HCl solution, 30 mg of aniline dimer was dissolved in about 2.0 mL ethanol, and the two solutions were combined and mixed in an ultrasound sonicator bath for 10 minutes. The mixture was then transferred into a 20 mL Teflon-lined autoclave and heated at various temperatures (75, 100 and 140 °C) for 10 hrs. Afterwards, the reaction mixture was dialyzed against deionized water several times and then centrifuged to recover the solid products. The final products were dried in a conventional oven at 60 °C, and named rGO-OANI 75, 100 or 140 (i.e., rGO-OANI 75 indicates that the composite was synthesized at 75 °C). The composites were intended to be used as is, but some of the batches also underwent organic solvent washing in an attempt to remove any physically adsorbed conducting polymer/oligomer. A typical procedure is as follows: 1.5 mL of the dialyzed reaction mixture was centrifuged in a 2.0 mL bullet tube. The solid products on the bottom were then washed and centrifuged with ~2 mL acetone mixture three times (or until the supernatant turned colorless). The solids at the bottom of the tube were next washed 2 more times using ~2 mL of acetone via bath sonication (20 min at room temperature) and centrifuged. All solid composite products for general characterizations were dried in an oven at 60 °C overnight. The products used for electrochemical characterization were left in solution before drop-casting.

Hydrothermal reduction of graphene oxide without addition of aniline dimer: Graphene oxide was reduced via a hydrothermal method in the absence of any added reducing agents. In a typical reaction, 770 mg of GO solution (10 mg dry GO) was dispersed in 9.0 mL 0.1 M HCl and 2.0 mL ethanol solution. The dispersion was bath sonicated for 10 minutes, transferred into a 20

mL Teflon-lined autoclave and heated for 10 hrs at three different temperatures: 100, 140 and 180 °C. The reaction mixtures were washed with DI water and centrifuged a few times to yield the solid products, labelled rGO 100, rGO 140 and rGO 180, respectively. The rGO samples for general characterization were dried in a conventional oven at 60 °C overnight. The samples used for electrochemical characterization were left in solution before drop-casting.

Hydrothermal oligomerization of aniline dimer without additional oxidizing agent: 30 mg of aniline dimer was dissolved in a mixture of 2.0 mL ethanol and 9.0 mL 0.1 M HCl. The solution was bath sonicated for 10 minutes, transferred into a 20 mL Teflon-lined autoclave and heated for 10 hrs at 100 °C. The solution was centrifuged, and the solid product was dialyzed (Fisherbrand cellulose dialysis tube, 12000-14000 Dalton cut-off) against DI water overnight.

Hydrothermal oligomerization of aniline dimer without additional oxidizing agent in the absence of environmental oxygen: The dissolved oxygen molecules in ethanol and 0.1 M HCl solutions were purged by bubbling argon gas into the solutions for 15 minutes. Afterwards, 30 mg of aniline dimer was dissolved in a mixture of 2.0 mL ethanol and 9.0 mL 0.1 M HCl. The reaction mixture was purged with argon gas for 10 minutes, transferred into a 20 mL Teflon-lined autoclave and heated for 10 hrs at 100 °C. The resulting solution (no solid products were found within) was analyzed right after reaction completion.

4.4.2. General characterization

Scanning electron microscopy (SEM) images were taken with an FESEM JOEL JSM-6700F FE-SEM at 5 to 10 kV. Fourier-Transform Infrared Spectroscopy by Attenuated Total Reflectance (FTIR) was performed on a JASCO FT/IR-6300 in the frequency range of 600 – 4000 cm^{-1}. Raman spectra were collected with an inVia (Renishaw) Raman spectrometer with a 633 nm

laser, in the frequency range of 100-4000 cm^{-1}. Powder X-ray diffraction (XRD) was carried out on a Bruker D8 Discover Powder X-ray Diffractometer, in the 2 Theta angle range from 5-90° using a CuKα X-ray beam (λ_{ave} = 1.5418 Å) with a scan speed of 0.1055 °/s, time per step of 0.3 s. XPS measurements were performed using a Kratos Axis Ultra DLD spectrometer with a monochromatic Al K_α X-ray source (λ = 1486.6 eV). The mass spectra of the composites were collected using a Bruker Ultraflex MALDI-TOF in the m/z range of 100 to 3000. The probe sonicator used for mixing samples was a FS-300N ultrasonic processor, with 300 W (100%) power output, 20 kHz frequency (frequency is auto-tracked by the instrument), and a 2 mm-diameter tip.

4.4.3. Electrochemical characterizations

Cyclic voltammetry (CV), constant current (galvanostatic) charge-discharge (CC), and electrochemical impedance spectroscopy (EIS) were carried out, at room temperature (18-22 °C), on a Bio-Logic VMP3B -10 Potentiostat in a standard 3-electrode setup, with 1.0 M sulfuric acid as the electrolyte, a 1 x 2 cm^2 platinum foil as the counter electrode and Ag/AgCl (in saturated KCl) as the reference electrode. The EIS measurements were performed at 0.3 V and 0.5 V relative to the reference electrode (where the CV shows redox peaks), with a 10 mV amplitude and in the frequency range from 1.0 MHz to 1.0 mHz (very high frequency ranges are omitted from the Nyquist plot). The working electrodes were made by drop-casting the probe-sonicated (5 min at 50% power output, pulse mode: 3 sec on/1 sec off) sample solutions (no binder) on 1 x 1 cm^2 graphite paper current collectors, which were then dried in a conventional oven at 60 °C overnight. The mass loading of each electrode was calculated from the weight difference before and after drop-casting (measured by a microbalance ±1 microgram error). Typical loadings of the materials are about 0.4-0.65 mg/cm^2. The working electrodes were soaked in 1.0 M sulfuric acid electrolyte

for a few hours before testing. All potentials were recorded relative to the Ag/AgCl (in saturated KCl solution) reference potential.

Calculations of average specific capacitance of the electrode material from the discharge CV diagrams are based on the following equation:

$$C_s = \frac{\int_{V_i}^{V_f} i dV}{m \times (V_f - V_i) \times v} \tag{4.4}$$

where C_s is the average specific capacitance by weight (F/g); i is the discharge current from the CV diagram (A); V_f and V_i denote the final and initial potential (V), respectively; m is the mass of the electrode material (g); and v indicates the scan rate (V/s).

Alternatively, the average specific capacitance can be calculated based on CC curves using the following equation:

$$C_s = \frac{I \times \Delta t}{m \times (\Delta V)} \tag{4.5}$$

where C_s is average gravimetric specific capacitance (F/g), I is the discharge current (A), Δt is the discharge time (s), m is the mass of the electrode material (g) and $\Delta V$is the potential difference in discharge (V).

The instantaneous specific capacitance can be calculated based on CV data using the following equation:

$$C_s = \frac{I}{m \times v} \tag{4.6}$$

where C_s is instantanous gravimetric specific capacitance (F/g), I is the current (A) read directly from CV data, m is the mass of the electrode material (g) and v is the scan rate (V/s).

4.5. Supporting Information

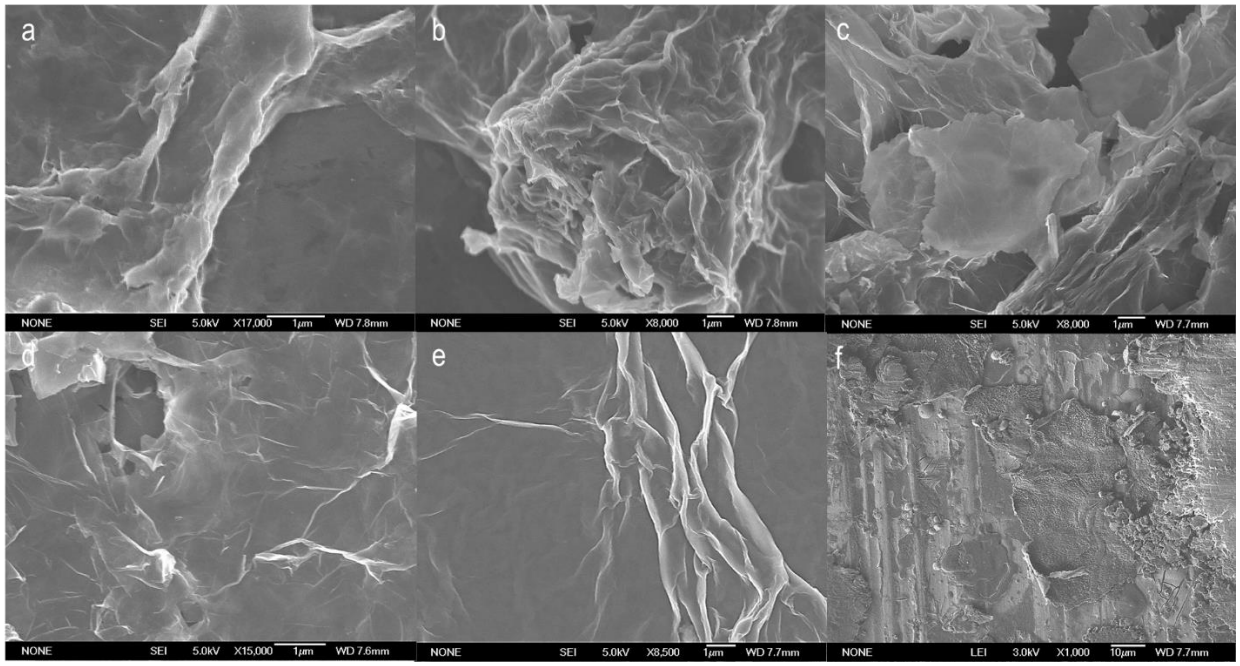

Figure S4.1 Additional SEM images of (a) rGO-OANI 75, (b) rGO-OANI 100, (c) rGO-OANI 140, (d) rGO-OANI 180, (e) GO and (f) hydrothermally synthesized TANI.

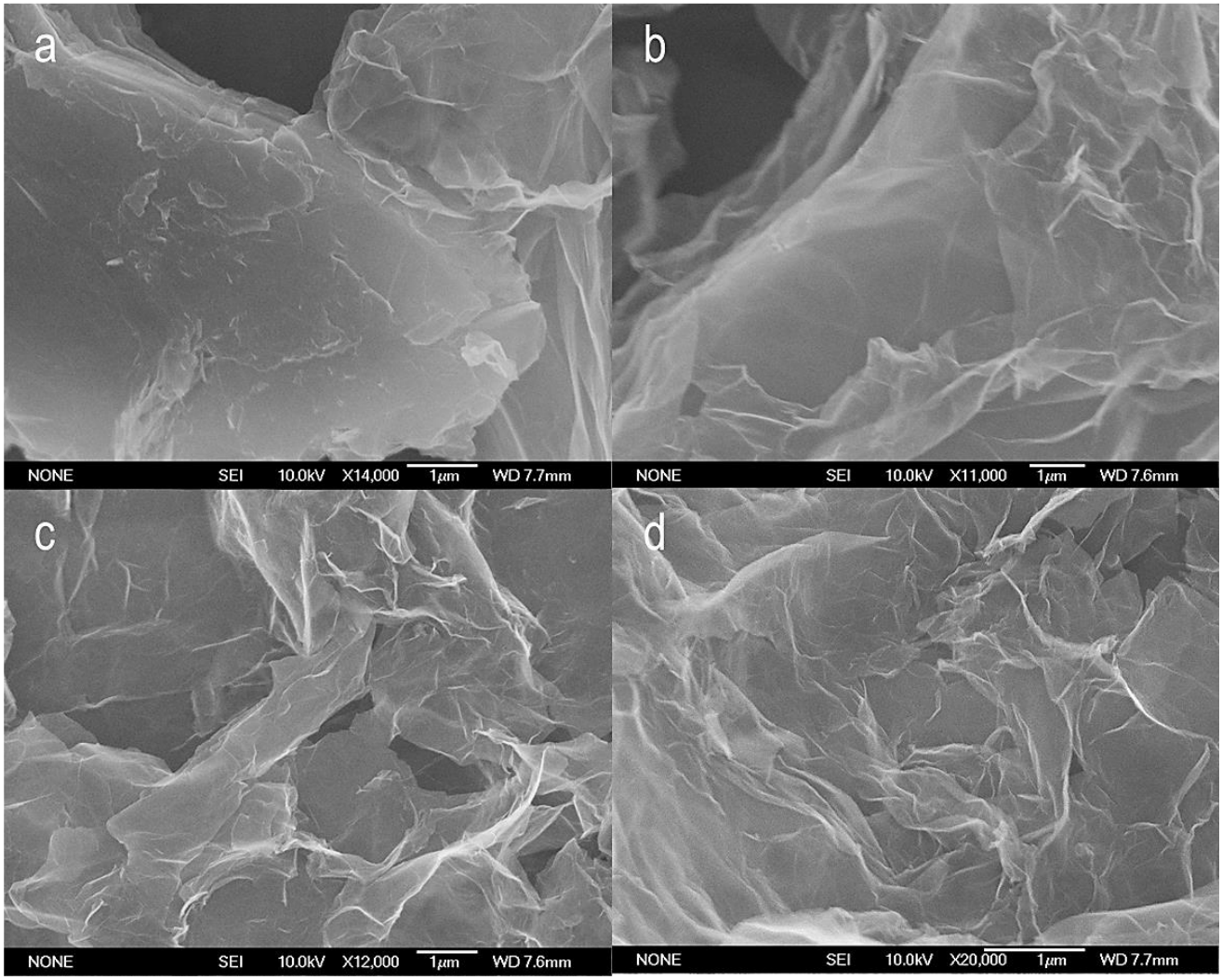

Figure S4.2 SEM images of (a) rGO-OANI 75 after acetone wash, (b) rGO-OANI 100 after acetone wash, (c) rGO-OANI 140 after acetone wash, and (d) rGO 140.

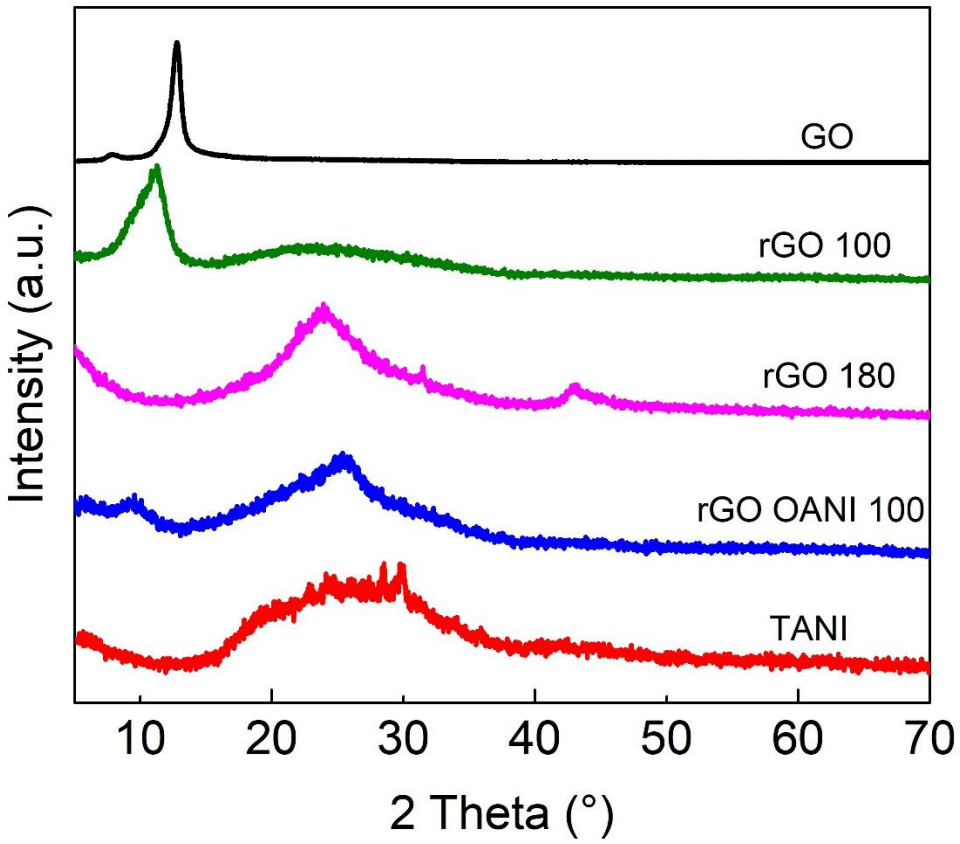

Figure S4.3 XRD patterns of GO, rGO 100, rGO 180, rGO-OANI 100 and TANI.

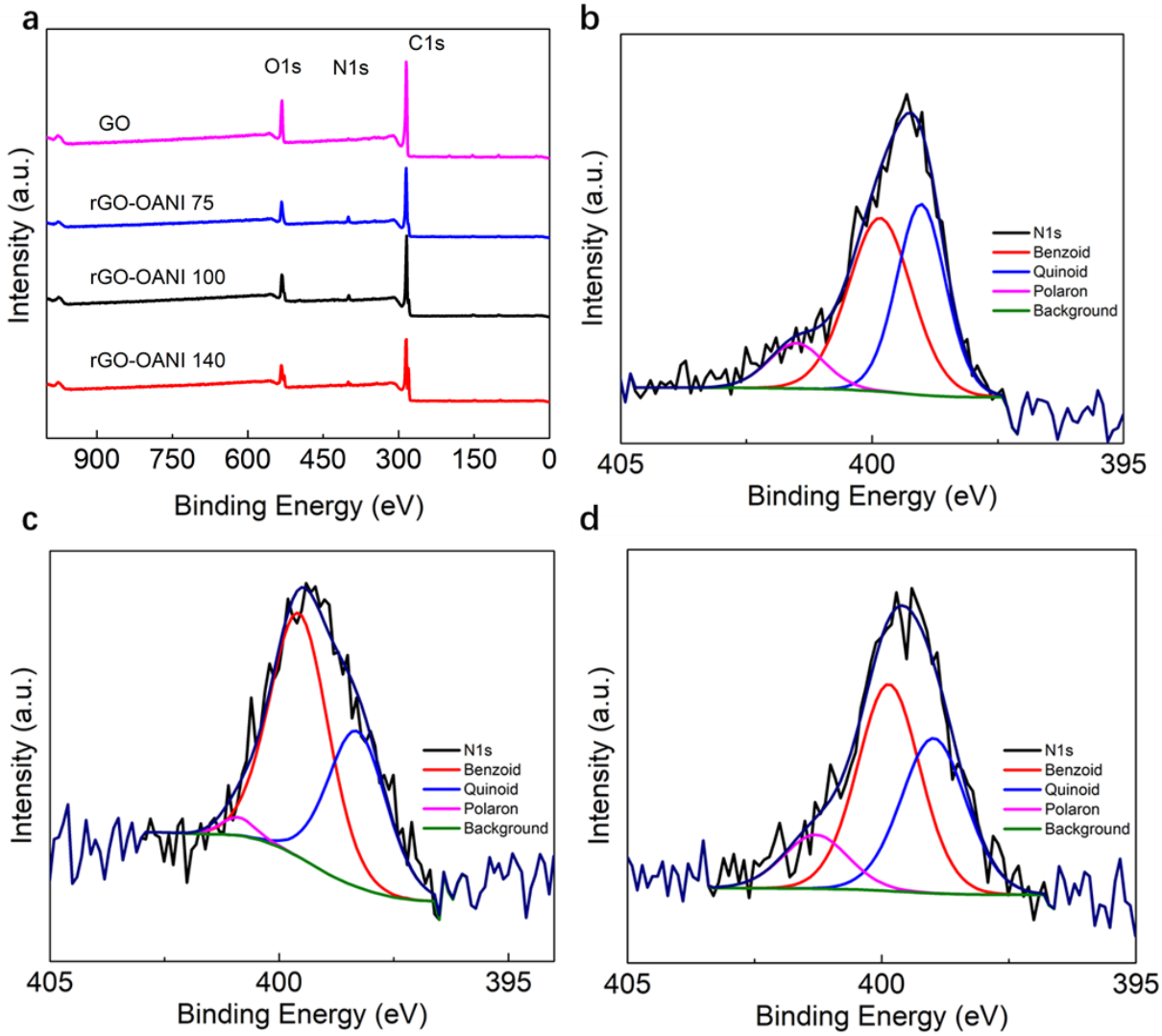

Figure S4.4 (a) Survey scans of GO and rGO-OANI composites. Deconvoluted N 1s peaks of (b) rGO-OANI 75, (c) rGO-OANI 100 and (d) rGO-OANI 140.

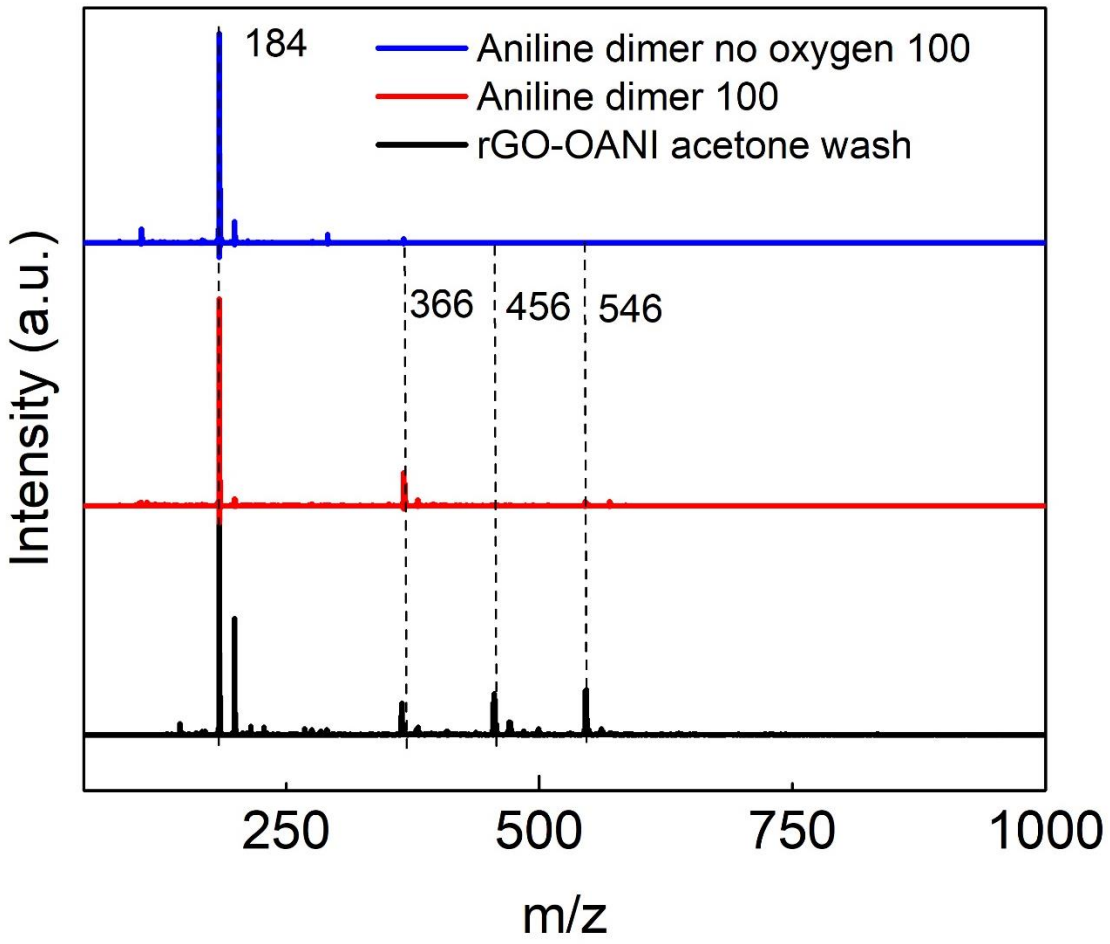

Figure S4.5 MALDI-TOF mass spectra of aniline dimer no oxygen (synthesized in the absence of GO and oxygen), aniline dimer 100 (synthesized in the absence of GO), and the rGO-OANI 100 acetone wash solution.

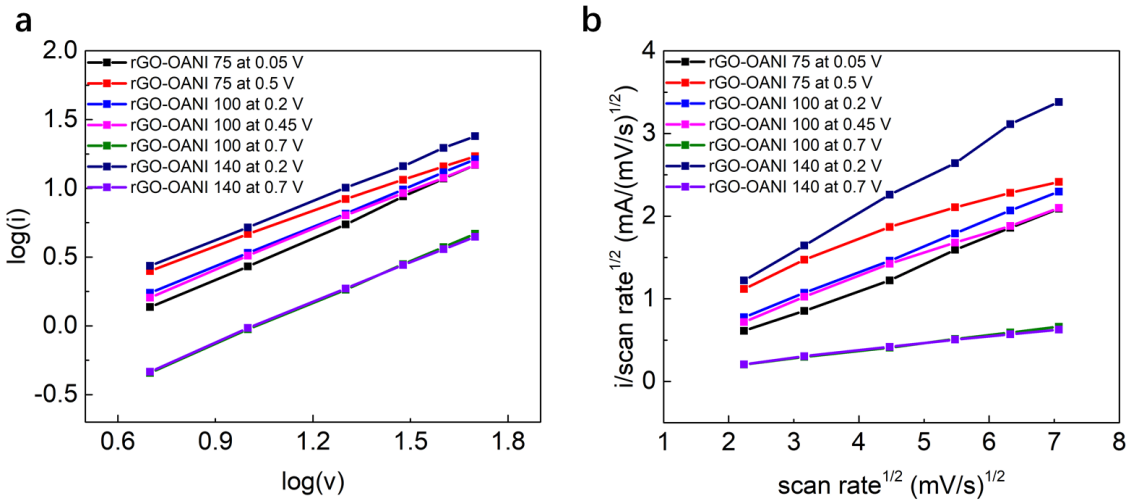

Figure S4.6 (a) b-value analysis plot of the composites. (b) k-values analysis plot of the composites.

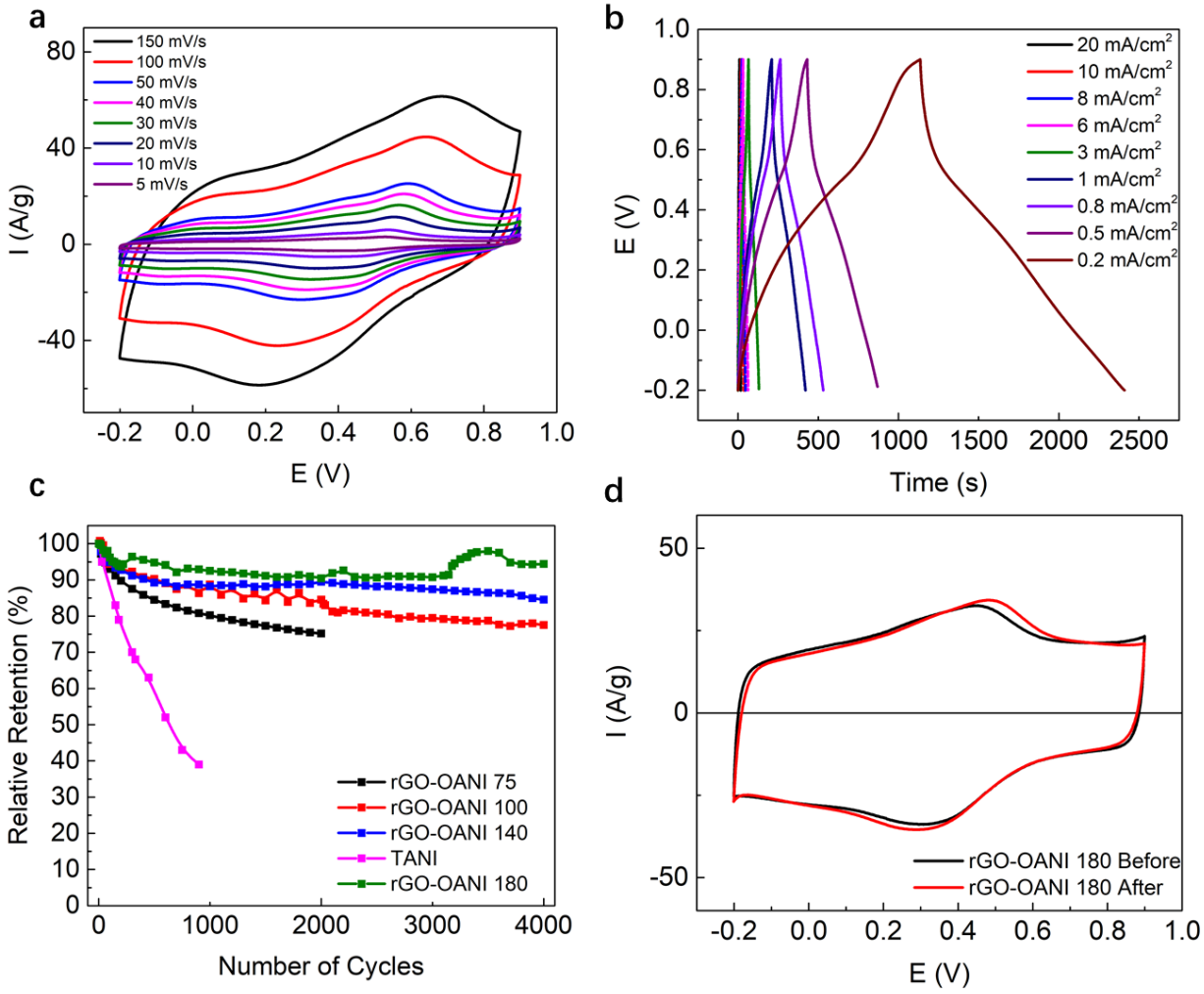

Figure S4.7 (a) CV diagrams of rGO-OANI 180 at various current densities. (b) CC curves of rGO-OANI 180 at different scan rates. (c) Cycling performances of rGO-OANI samples and TANI. (d) CV diagrams of rGO-OANI 180 before and after 4000 cycles.

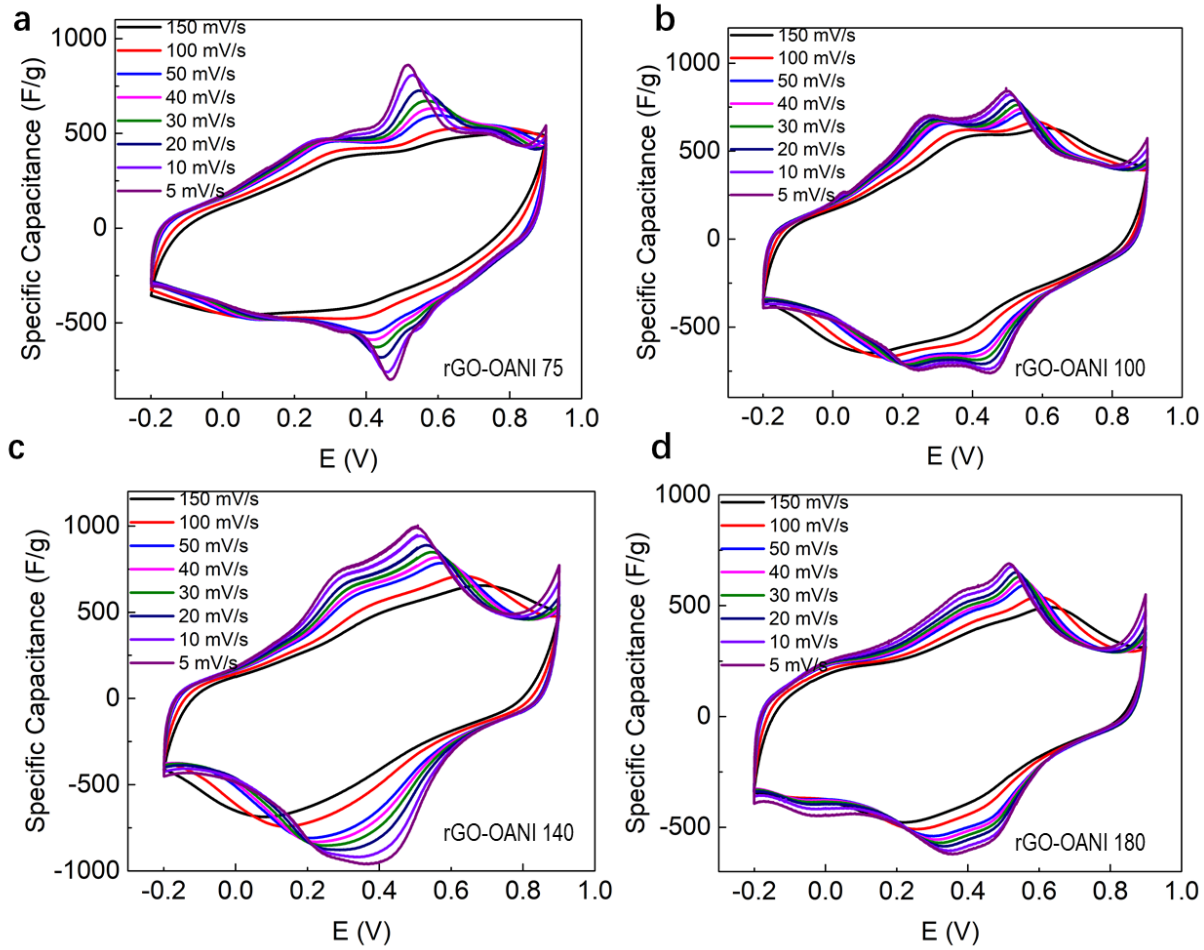

Figure S4.8 Instantaneous specific capacitance of rGO-OANI composites at different scan rates.

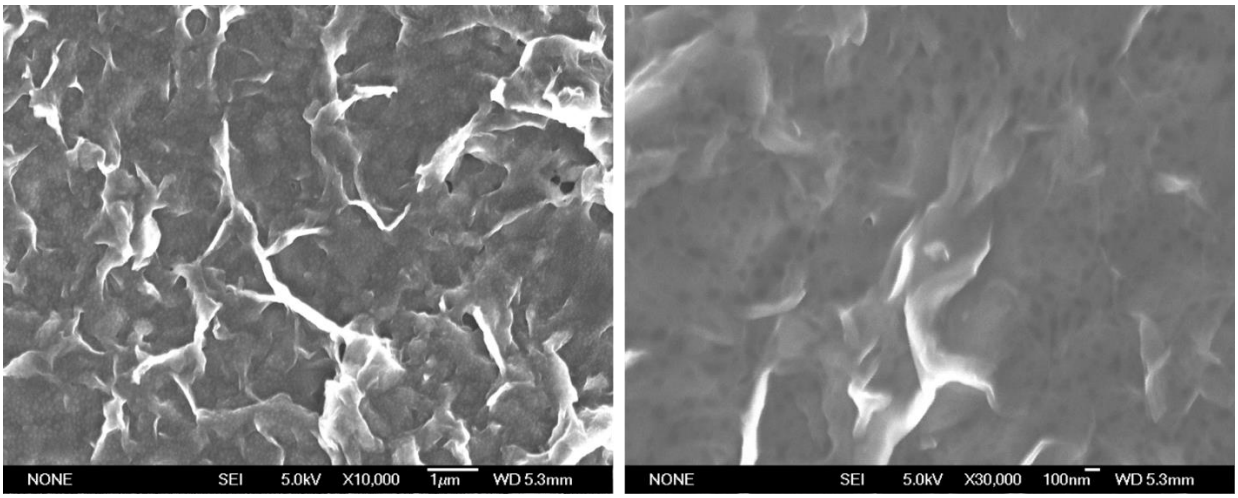

Figure S4.9 Post-mortem SEM images of rGO-OANI 140 electrode materials after 4000 cycles.

Table S4.1 XPS Elemental Analyses

Sample	C 1s %	N 1s %	O 1s %	OANI/GO ratio	C-O	C-O-C	C=O	COOH
GO	65.7	0.0	34.3	0	18.9%	16.3%	56.3%	8.5%
rGO-OANI 75	82.2	5.1	12.6	2/5	34.5%	0.5%	46.9%	18.0%
rGO-OANI 100	81.4	3.9	14.7	1/3	47.9%	0.0%	46.7%	5.4%
rGO-OANI 140	80.1	3.4	16.5	1/4	50.3%	1.0%	43.3%	5.4%

Table S4.2 Average Specific Capacitance/Capacity* Calculated from CV (F/g and C/g)

Scan rate (mV/s)	rGO-OANI 75 (F/g and C/g)		rGO-OANI 100 (F/g and C/g)		rGO-OANI 140 (F/g and C/g)		rGO-OANI 180 (F/g and C/g)		TANI (F/g and C/g)		rGO-180 (F/g and C/g)	
5	400	440	462	508	518	570	390	429	464	418	181	199
10	401	441	455	501	498	548	381	419	488	439	173	190
20	397	437	447	492	479	527	373	410	494	445	169	186
30	391	430	442	486	466	513	368	405	N/a	N/a	166	183
40	386	425	437	481	457	503	364	400	484	436	164	180
50	381	419	434	477	449	494	361	397	486	437	163	179
100	354	389	419	461	421	463	347	382	N/a	N/a	158	174
150	329	362	407	448	399	439	336	370	N/a	N/a	155	171

*Capacity = average capacitance × potential window (1.1 V).

Table S4.3 Average Specific Capacitance/Capacity* Calculated from CC (F/g and C/g)

Current density (mA/cm^2)	rGO-OANI 75 (F/g and C/g)		rGO-OANI 100 (F/g and C/g)		rGO-OANI 140 (F/g and C/g)		rGO-OANI 180 (F/g and C/g)		rGO-180 (F/g and C/g)	
0.2	391	430	513	564	643	707	495	431	195	215
0.5	380	418	412	453	560	616	410	376	181	199
0.8	380	418	395	435	583	641	395	362	175	193
1	382	420	370	407	529	582	389	359	173	190
3	364	400	364	400	497	547	367	332	165	182
6	359	395	347	382	480	528	347	316	161	177
8	353	388	336	370	457	503	341	311	156	172
10	347	382	337	371	455	501	341	308	148	163
20	337	371	319	351	438	482	319	282	148	163

*Capacity = average capacitance × potential window (1.1 V).

Table S4.4 Nyquist Plot Fitting Results of rGO-OANI composites at certain potentials

	rGO-OANI 75 (0.3V)	rGO-OANI 75 (0.5V)	rGO-OANI 100 (0.3V)	rGO-OANI 100 (0.5V)	rGO-OANI 140 (0.3V)	rGO-OANI 140 (0.5V)
R1 (Ω)	0.918	0.918	0.675	0.684	1.364	1.379
C2 (mF)	0.217	0.240	0.471	0.429	0.248	0.239
R2 (Ω)	0.108	0.126	0.080	0.074	0.276	0.296
W2 ($\Omega s^{-1/2}$)	4.04	3.487	2.405	2.684	2.134	2.24
ESR from IR drop(Ω)	1.00		0.63		1.26	

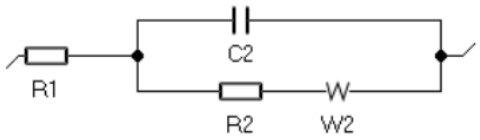

Scheme S4.1 The equivalent circuit used for Z fitting where R1 is the uncompensated resistance, R2 is the charge transfer resistance, C2 is the double layer capacitance and W2 is the Warburg diffusion element.

Table S4.5 b-Value and k-Value Analysis Results (discharge only)

Sample	rGO-OANI 75	rGO-OANI 75	rGO-OANI 100	rGO-OANI 100	rGO-OANI 100	rGO-OANI 140	rGO-OANI 140
Potential	0.05 V	0.5 V	0.2 V	0.45 V	0.7 V	0.2 V	0.7 V
b	1.04	0.84	0.98	0.93	0.96	0.92	0.96
k1	0.3101	0.2661	0.3148	0.2813	0.0944	0.4498	0.0864
k2	0.1141	0.6027	0.0696	0.1235	0.0058	0.2218	0.025
Surface-controlled (at 1 mV/s)	73%	31%	82%	69%	94%	67%	78%
Diffusion-controlled (at 1 mV/s)	27%	69%	18%	31%	6%	33%	22%

Table S4.6 b-Value and k-Value Analysis Results Comparisons

Sample	rGO-PANI aerogel[27]	RGO-CNs-PANI[29]	PANI-CNT[9]	rGO-PANI covalent[28]	PANI-rGO[11]	rGO-OANI 100
Potential	0.55 V	0.05-0.2 V	0.05-0.2 V	0.05-0.2 V	0.05-0.2 V	0.2 V
b	0.48	0.67	0.76	0.84	0.85	0.96
k1	0.0098	0.369	0.0246	1.132	0.037	0.3148
k2	0.6424	1.77	0.087	2.356	0.0425	0.0696
Surface-controlled	2%	17%	22%	32%	47%	82%
Diffusion-controlled	98%	83%	78%	68%	53%	18%

⋆ Surface and diffusion contributions are calculate at 1 mV/s

Table S4.7 b-Value and k-Value Analysis Results of rGO-OANI 100 (charge/discharge) at 20mV/s

Potential	0 V	0.1 V	0.2 V	0.3 V	0.4 V	0.5 V	0.6 V	0.7 V	0.8 V
b	1.1	1.02	0.98	0.98	0.96	0.96	1.01	1.02	0.99
	0.93	0.97	0.98	0.97	0.95	0.93	0.98	0.99	1.09
Surface controlled	89%	98%	95%	96%	93%	93%	98%	97%	98%
	88%	95%	97%	95%	91%	87%	97%	97%	89%
Diffusion controlled	11%	2%	5%	4%	7%	7%	2%	3%	2%
	12%	5%	3%	5%	9%	13%	3%	3%	11%

⋆ Surface and diffusion contributions are calculate at 10 mV/s

4.6. References

(1) Abdolahi, A.; Hamzah, E.; Ibrahim, Z.; Hashim, S. *Materials (Basel).* **2012**, *5* (8), 1487–1494.

(2) Dias, H. V. R.; Wang, X.; Rajapakse, R. M. G.; Elsenbaumer, R. L. *Chem. Commun. (Camb).* **2006**, No. 9, 976–978.

(3) Huang, J.; Kaner, R. B. *Chem. Commun.* **2006**, No. 4, 367–376.

(4) Surwade, S. P.; Agnihotra, S. R.; Dua, V.; Manohar, N.; Jain, S.; Ammu, S.; Manohar, S. K. *J. Am. Chem. Soc.* **2009**, *131* (35), 12528–12529.

(5) Moussa, M.; El-Kady, M. F.; Zhao, Z.; Majewski, P.; Ma, J. *Nanotechnology* **2016**, *27* (44), 442001.

(6) Yan, J.; Yang, L.; Cui, M.; Wang, X.; Chee, K. J.; Nguyen, V. C.; Kumar, V.; Sumboja, A.; Wang, M.; Lee, P. S. *Adv. Energy Mater.* **2014**, *4* (18), 1–7.

(7) Li, R.; Lin, C.-W.; Shao, Y.; Chang, C.; Yao, F.-K.; Kowal, M.; Wang, H.; Yeung, M.; Huang, S.-C.; Kaner, R. *Polymers (Basel).* **2016**, *8* (11), 401.

(8) Li, L.; Song, H.; Zhang, Q.; Yao, J.; Chen, X. *J. Power Sources* **2009**, *187* (1), 268–274.

(9) Simotwo, S. K.; Delre, C.; Kalra, V. *ACS Appl. Mater. Interfaces* **2016**, *8* (33), 21261–21269.

(10) Liu, T.; Finn, L.; Yu, M.; Wang, H.; Zhai, T.; Lu, X.; Tong, Y.; Li, Y. *Nano Lett.* **2014**, *14* (5), 2522–2527.

(11) Wang, R.; Han, M.; Zhao, Q.; Ren, Z.; Guo, X.; Xu, C.; Hu, N.; Lu, L. *Sci. Rep.* **2017**, *7* (174), 44562.

(12) Chua, C. K.; Pumera, M. *Chem. Soc. Rev.* **2014**, *43* (1), 291–312.

(13) Allen, M. *Am. Chem. Soc.* **2009**, 184.

(14) Zhang, K.; Zhang, L. L.; Zhao, X. S.; Wu, J. *Chem. Mater.* **2010**, *22* (4), 1392–1401.

(15) Zhou, S.; Zhang, H.; Zhao, Q.; Wang, X.; Li, J.; Wang, F. *Carbon N. Y.* **2013**, *52*, 440–450.

(16) Zhang, Y.; Xu, W.; Yao, W.; Yu, S. *J. Phys. Chem. C* **2009**, 8588–8594.

(17) Shao, Y.; El-Kady, M. F.; Wang, L. J.; Zhang, Q.; Li, Y.; Wang, H.; Mousavi, M. F.; Kaner, R. B. *Chem. Soc. Rev.* **2015**, *44* (11), 3639–3665.

(18) Trchová, M.; Morávková, Z.; Bláha, M.; Stejskal, J. *Electrochim. Acta* **2014**, *122*, 28–38.

(19) Song, B.; Li, L.; Lin, Z.; Wu, Z. K.; Moon, K. sik; Wong, C. P. *Nano Energy* **2015**, *16*, 470–478.

(20) Monteserín, C.; Blanco, M.; Aranzabe, E.; Aranzabe, A.; Laza, J. M.; Larrañaga-Varga, A.; Vilas, J. L. *Polymers (Basel).* **2017**, *9* (9), 1–16.

(21) Guerrero-Contreras, J.; Caballero-Briones, F. *Mater. Chem. Phys.* **2015**, *153*, 209–220.

(22) Salunkhe, R. R.; Hsu, S. H.; Wu, K. C. W.; Yamauchi, Y. *ChemSusChem* **2014**, *7* (6), 1551–1556.

(23) Che, J.; Shen, L.; Xiao, Y. *J. Mater. Chem.* **2010**, *20* (9), 1722.

(24) Moussa, M.; El-Kady, M. F.; Abdel-Azeim, S.; Kaner, R. B.; Majewski, P.; Ma, J. *Compos. Sci. Technol.* **2018**, *160*, 50–59.

(25) Wang, J.; Polleux, J.; Lim, J.; Dunn, B. *J. Phys. Chem. C* **2007**, *111* (40), 14925–14931.

(26) Cook, J. B.; Kim, H.-S.; Lin, T. C.; Lai, C.-H.; Dunn, B.; Tolbert, S. H. *Adv. Energy Mater.* **2017**, *7* (2), 1601283.

(27) Van Hoa, N.; Quyen, T. T. H.; Van Hieu, N.; Ngoc, T. Q.; Thinh, P. V.; Dat, P. A.; Nguyen, H. T. T. *Synth. Met.* **2017**, *223*, 192–198.

(28) Liu, X.; Shang, P.; Zhang, Y.; Wang, X.; Fan, Z.; Wang, B.; Zheng, Y. *J. Mater. Chem. A*

2014, *2* (37), 15273–15278.

(29) Liu, D.; Wang, H.; Du, P.; Wei, W.; Wang, Q.; Liu, P. *Electrochim. Acta* **2018**, *259*, 161–169.

Chapter 5. Evaluation of nanostructured Tetra-aniline and Tetra-aniline-carbon nanocomposites based supercapacitors

Abstract

Tetra-aniline (TANI), an oligomer of polyaniline, is a promising pseudocapacitance material with good rate capability and relatively high specific capacitance. This chapter presents a detailed evaluation of TANI supercapacitor performances. The performances of TANI supercapacitor electrodes are closely related to the morphology of the electrode materials. Nanostructures within the TANI electrode materials make the electrode behave more pseudocapacitance-like than battery-like, not only improving the rate capability of the electrode, but also extending its working potential range. Additionally, various TANI-carbon composites materials were prepared to study how substrate dimensionality affects performances of the hybrid supercapacitor electrodes. The TANI-carbon nanotubes (1D) electrode demonstrates great rate capability (268 F/g at 200 mV/s compared to 299 F/g at 5 mV/s, an 89% capacitance retention), but the overall specific capacitances are low. The TANI-activated carbon (3D) electrode shows a high specific capacitance of 617 F/g at 0.2 mA/cm^2, but its rate capability is not ideal. The TANI-reduced graphene oxide (2D) electrode demonstrates high specific capacitances of 407 F/g at 0.2 mA/cm^2 and 341 at 20 mA/cm^2, exhibiting excellent rate capability. Both 2D and 3D TANI-carbon composites display great cycle stability (>90% retention after 2000 cycles). With high surface area, interconnected 3D networks and high conductivity, reduced graphene oxide (i.e. graphene) is the most promising carbon substrate to composite with TANI for supercapacitor applications.

5.1. Introduction

As the demand increases for energy storage devices with safe operations, high power ratings and long cycle life, supercapacitors have attracted much attention from both industry and academia. Compared to rechargeable batteries, supercapacitors demonstrate higher rate capabilities and much better cycle stability. They have been widely used in commercial applications that require high current delivery with good storage capabilities.[1] However, most commercial supercapacitors are carbon based, capable of storing only a fraction of the amount of charge that batteries do, limiting their applications to those that need short power bursts, but lower energy storage.[2] To enhance the energy density of supercapacitors, pseudocapacitance materials, such as transition metal oxides/hydroxides and conducting polymers, are introduced.

Polyaniline (PANI) is one of the most studied conducting polymers, thanks to its ease of synthesis, tunable morphology, high conductivity and reversible redox reactions.[3,4] In recent years, PANI has become a good candidate for pseudocapacitance applications, owing largely to its 2000 F/g theoretical specific capacitance.[5] Various research groups have studied numerous parameters to improve the performances of PANI supercapacitors.[6–11] However, PANI-based supercapacitors generally suffer from low cycle stability issues. Tetra-aniline (TANI) is the shortest oligomer of PANI that demonstrates high conductivity and redox activities.[12–16] Furthermore, the short chain length of TANI is believed to improve its resistance to chain breaking during cycling that undermines PANI's cycle stability.[17] However, to the best of our knowledge, there has not been a systematic study on TANI supercapacitors, and therefore, we seek to provide a detailed electrochemical analysis of TANI and TANI-carbon based supercapacitors in this chapter.

Herein, we have made TANI samples with different nanostructures (nanofibrillar, semi-nanotubular and globular) into supercapacitor electrodes and evaluated their performances in

relation to their morphologies. In an attempt to further improve upon the supercapacitor performances of TANI electrodes, TANI was also made into TANI-carbon composite materials with various substrate surface dimensionalities, such as one-dimensional carbon nanotubes, two-dimensional graphene oxide and reduced graphene oxide, and three-dimensional activated carbon. The efficiency of the carbon substrates are assessed based on some key supercapacitor performance metrics of these hybrid materials, such as specific capacitance, rate capability and cycle stability. The two-dimensional reduced graphene oxide is found to be the most suitable carbon substrate for TANI-carbon hybrid composites.

5.2. Results and Discussions

5.2.1. TANI 3-electrode characterizations

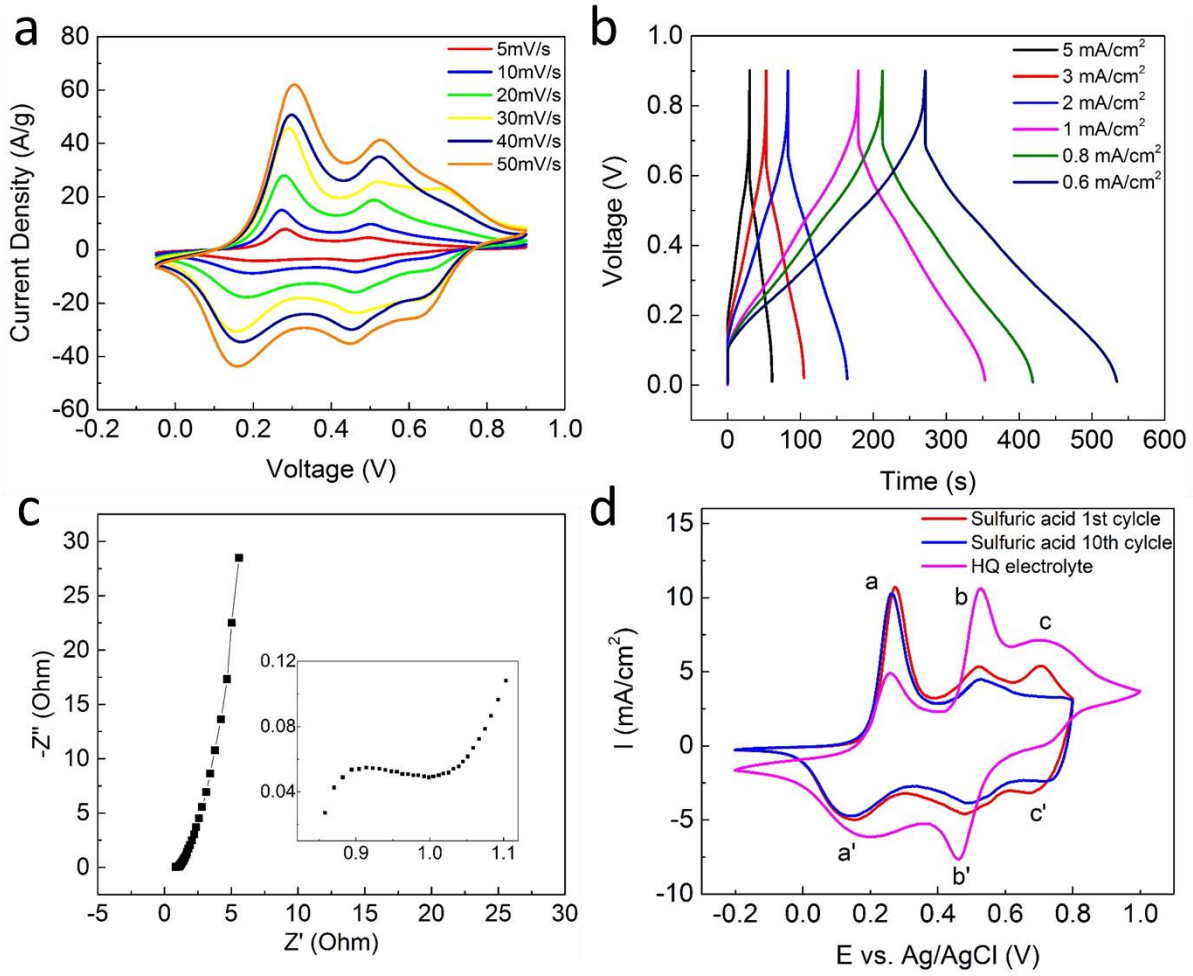

Figure 5.1 Electrochemical performances of a TANI nanowire-electrode in 1.0 M H2SO4: (a) cyclic voltammograms at various scan rates, (b) galvanostatic charge-discharge curves at various current densities, (c) a Nyquist plot of a TANI electrode (0.3 vs. Ag/AgCl, Inset: zoomed-in image showing high frequency range), and (d) CV curves of a TANI-nanowire electrode in sulfuric acid and in 0.01 M hydroquinone (HQ) electrolyte solution.

A detailed discussion of TANI-nanowire single electrode performance is presented in Chapter 2 and the CV, CC and EIS are re-presented in Figure 5.1. The CV curves of a TANI nanowire electrode shows 2 or 3 sets of redox peaks. The redox peak pairs at around 0.2 V (**a**/**a'**) and 0.5 V (**b**/**b'**) vs. the Ag/AgCl reference are assigned to the transitions of TANI

leucoemeraldine (LE) to emeraldine salt (ES) and emeraldine salt to pernigraniline (PN) oxidation states, respectively. A third set of peaks near 0.7 V vs. the reference electrode (**c/c'**) typically shows up during the initial cycling of the electrodes, and is believed to be associated with the hydrolysis byproducts (hydroquinone/benzoquinone) of pernigraniline TANI.[13] Indeed, by adding 0.01 M of hydroquinone (HQ) into the sulfuric acid solution, the peak height of **c/c'** increases (Figure 5.1d), confirming that this redox peak pair does correspond to the HQ/BQ reaction. The galvanostatic charge-discharge (CC) curves of TANI-nanowire electrodes show large apparent IR drops, but are otherwise close to triangular in shape. The apparent IR drop will be discussed later. The Nyquist plot of TANI shows a small semicircle in the high frequency range and a near vertical line in the low frequency range, indicating small charge transfer resistance and good supercapacitance behavior, respectively.

The morphology of a TANI electrode material does affect its supercapacitor performance. Figure 5.2 shows the CV and CC plots of TANI-nanowire and TANI-globular electrodes, while their corresponding SEM images can be seen in Figure 5.3. It is worthwhile noting that globular TANI holds on to atmosphere moisture quite stubbornly and the weight of the electrode materials cannot be accurately measured. As a result, the CV plots (Figure 5.2a) are not normalized to weight and hence, comparing the specific gravimetric capacitance of the two electrodes is not a major concern. There are, however, some other performance metrics of these TANI electrodes that are worth discussing.

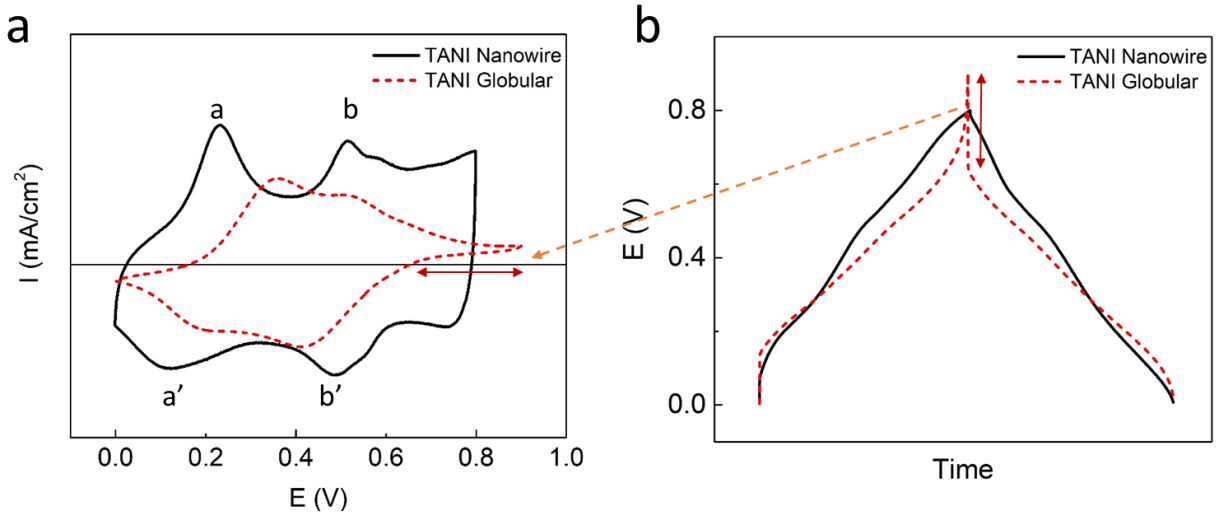

Figure 5.2 (a) CV curves of nanowire TANI and globular TANI (scan rate = 10 mV/s). (b) CC curves of nanowire TANI and globular TANI (current density = 1 mA/cm2).

As shown in Figure 5.2a, the CV curve of the globular TANI electrode intersects with the x-axis at about 0.17 V and 0.63 V (vs. Ag/AgCl), whereas the x-intercepts of the TANI nanowire curve are at 0.05 V and 0.78 V. Two factors likely contribute to the difference in CV shape: the accessibility of redox sites and the surface area of TANI. Due to the nanostructures, nanowire TANI has a higher ratio of surface to bulk material, and thus the TANI molecules are more readily available for rapid surface redox reactions (i.e., pseudocapacitance). However, the globular TANI material lacks hierarchical nanostructures, limiting the percentage of TANI that can participate in surface redox reactions, and its overall charge storage behavior is more battery-like (as indicated by the "duck-shape" at the two ends of the CV curve). Additionally, the nanowire structure increases the specific surface area of the material, providing more surface area for physical ion adsorption (EDLC-like). These two factors increase the background current density of the nanowire TANI electrode, increasing the potential difference between the two zero-current voltages and making the electrode behave more pseudocapacitance-like than battery-like.

The significance of these two zero-current voltages can be explained by the galvanostatic charge-discharge curves shown in Figure 5.2b. Once more, it is worth mentioning that as two different electrodes were compared against each other, their charge-discharge time needs to be normalized and thus the time-axis is unit-less. The most significant difference between the two CC curves is that the globular electrode displays a drastic rise in potential at the start of charging and a similar drop at the onset of discharging, while the potential changes for the nanowire electrode are much subtler. Normally this sudden change in potential is associated with the high resistance of the electrode and is treated as the IR-drop of the electrode. However, in this case, this oversimplified treatment does not stand up to scientific scrutiny, because the IR-drop calculation should only be applied where the electrode CV demonstrates characteristic RC-charging patterns.[18] Comparing the zero-current voltages shown in the CV plot against the potential drop on the CC curves, it is easy to see that the two values are closely related: the drop in potential at the start of the discharge is approximately equal to the difference between the maximum charging potential and the 2nd zero-current potential. On the discharge curve of the globular electrode, the positive currents simply indicate that the electrode is still being oxidized at the given potential even though it is being scanned backwards. As the maximum charging potential (0.9 V vs. reference) for the electrode is set arbitrarily, and there was no rest in between charging and discharging to allow the electrode to relax to its equilibrium potential, a large apparent IR drop is observed on the CC curves as a result of electrode relaxation. Hence, the large IR drop does not indicate that the material is too resistive, but rather that such a potential window is too high for the material. On the other hand, the CV curve of the nanowire TANI shows very characteristic RC-charging patterns at the two terminal potentials, and its corresponding CC curve displays a rather small potential drop (a proper IR-drop) at the start of discharge. The difference in the two zero-current potentials indicates that

the maximum operating voltage of the TANI nanowire electrode can be safely set at least 0.8 V, while the effective maximum potential of the globular electrode should be limited to about 0.6 V. As the energy density of a supercapacitor is proportional to the square of the potential window, the higher working voltage of the nanowire electrode increases the energy density, even without the increased specific areal capacitance.

Another performance metric that is strongly influenced by material morphology is the rate capability, and more specifically the charge storage kinetics. Even though TANI is fixed on the electrode surface, its redox reaction is coupled to a proton transfer process. Therefore, the TANI redox process cannot be treated as a model with all reactants fixed on the electrode, but rather one with redox species dissolved in solution that are subject to diffusion control. To elucidate how morphology affects electrode kinetics, three samples of TANI with varying degrees of nanostructures were made into electrodes. The SEM images, CV and EIS data of the electrodes are presented in Figure 5.3. The first electrode (TANI nanowire) shows very well defined nanowire array structures, the second electrode (TANI mixed morphology) displays a morphology somewhere in between globular and nanotubular, and the third one (TANI globular) is composed of large TANI globular clusters with no distinguishable nanostructures.

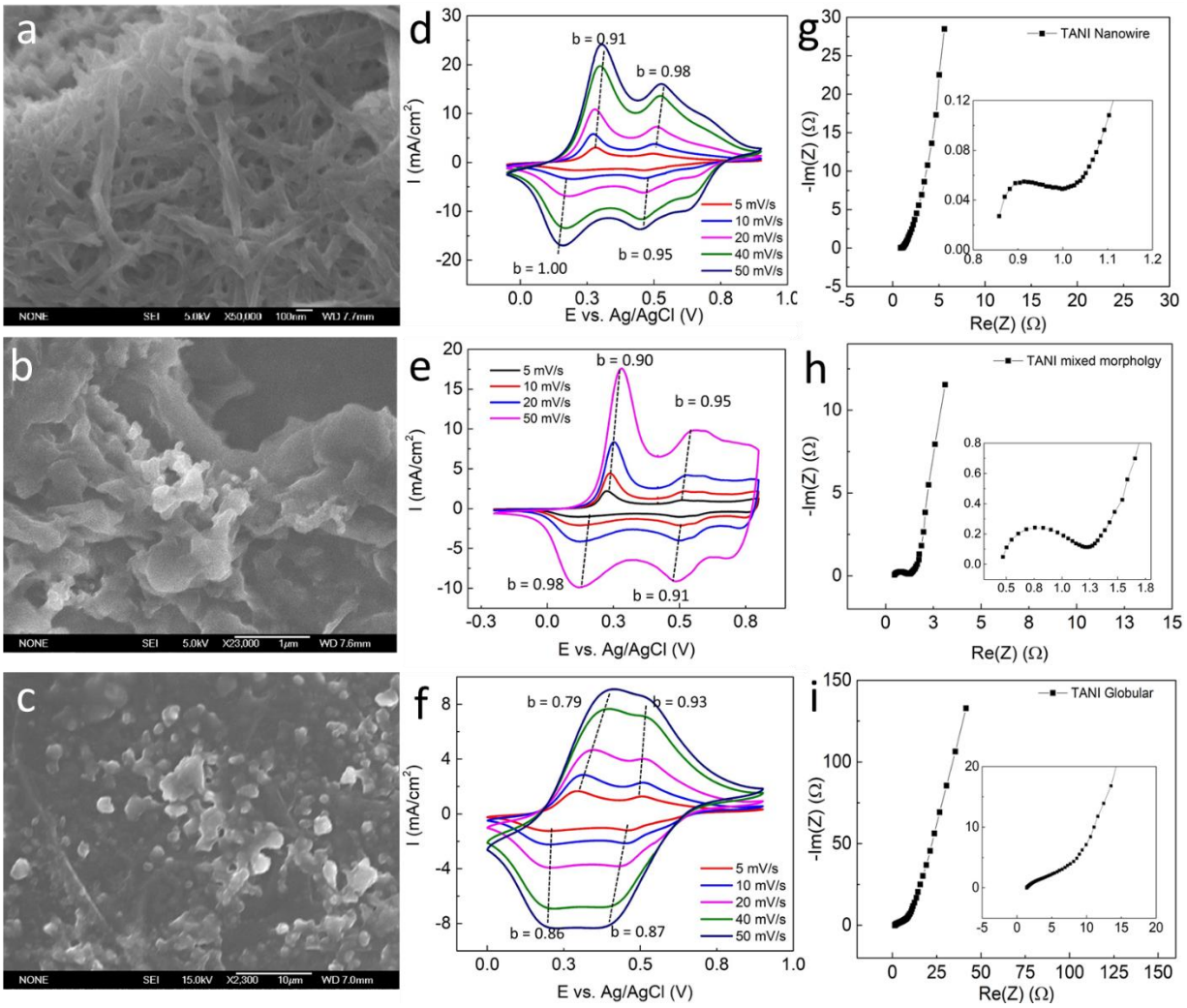

Figure 5.3 SEM images of (a) nanowire TANI, (b) mixed morphology TANI and (c) globular TANI. CV curves with b-values for (d) a TANI-nanowire electrode, (e) a TANI mixed morphology electrode and (f) a TANI-globular electrode. Nyquist plots of (g) a TANI-nanowire electrode, (h) a TANI mixed morphology electrode and (i) a TANI-globular electrode (Insets: high frequency regions of the Nyquist plots.)

The mechanisms of the redox reactions can be categorized by analyzing the rate law dependency of current on scan rates based on CV data at the redox peak locations: **a/a'** and **b/b'** (Figure 5.1d). The detailed mathematical methods used were discussed in the previous chapter (see Chapter 4, Section 4.2.3). In brief, the *b*-value analysis qualitatively characterizes the charge storage mechanism. The current scales linearly with the scan rate (b = 1) for surface dominant processes (EDLC and pseudocapacitance) and the current is proportional to the square root of the

scan rate (b = 0.5) for diffusion-controlled processes (redox reactions involving bulk materials or dissolved species). As both surface and bulk materials can contribute to the overall capacity of the electrode, the *k*-value analysis semi-quantitatively deconvolutes the capacitive current (and thus capacitance) into surface-controlled and diffusion-controlled contributions.

Based on the results of these analyses (Table 5.2), the *b*-values for the nanowire TANI electrode are consistently higher than those for the mixed morphology TANI electrode, which are higher than the ones for the globular TANI electrode. The *k*-value analyses also demonstrate that the redox reactions on the nanowire TANI electrode are more surface-controlled than the globular TANI electrode. For instance, the **b'** peak of the nanowire TANI electrode shows a *b*-value of 1.00 with over 97% surface-controlled (or pseudocapacitance) contributions at 10 mV/s. However, the *b*-value for the same peak of the globular TANI electrode is 0.86 and its pseudocapacitance contribution is only 75%. The kinetic performances of the electrode with mixed morphology are only slightly inferior to the nanowire electrode. To summarize the *b* and *k*-value analysis results, hierarchical nanostructures in the TANI morphology enhance the kinetic performances of the electrode, making the electrode behave more like a pseudocapacitor than a battery.

Another interesting observation is that *b*-values for peak **a** and **b**' are consistently lower than the *b*-values for their respective counterparts (Figure 5.3d and 5.3e), and the overpotential for transition **a** seems to be higher than that of transition **b** (as indicated by the cathode-anode peak separations). One hypothesis is that TANI in the leucoemeraldine state exhibits lower conductivity compared to the emeraldine salt state, and the transition from LE to ES state requires a higher overpotential to compensate for the resistance; therefore, peak **a** shows more peak shifts and a lower *b*-value. Along the same lines, on the reverse scan, the **a'** transition starts from a conductive

ES state and hence, does not require a high overpotential, showing a *b*-value closer to 1. A similar argument can be made for transition **b'**.

To support the CV analysis, EIS characterizations were performed on the three electrodes. Comparing the EIS data of the electrodes at 0.3 V vs. the reference electrode (peak **a/a'**), it can be seen that the nanowire electrode has the smallest semicircle, the electrode with mixed morphology has a slightly bigger semicircle, but both electrodes show very small Warburg impedance elements. The globular electrode shows a half semicircle that is merged with a very long 45° segment, suggesting high ion diffusion resistance. This trend is in good agreement with the morphologies of the electrodes. As the charge transfer process of TANI is coupled to the mass transport of the counter ions, the charge transfer resistance is affected by how fast ions can move in and out of the TANI structure and thus is not a fixed value for the all three electrodes. The nanowire and mixed morphology electrodes both display hierarchical porous structures, providing plenty of space and channels to facilitate ion/mass transport. However, the nanowire array provides more available active sites on the material surface, shortening the average ion diffusion length. As a result, the nanowire electrode demonstrates a smaller charge transfer resistance and Warburg impedance than the mixed morphology electrode. The globular electrode, on the other hand, does not possess mesoporous structures, and hence, its ion diffusion is hindered, resulting in a large ion diffusion resistance.

5.2.2. TANI 2-electrode characterizations

In terms of 2-electrode devices, TANI-based symmetric supercapacitors behave quite a bit differently from carbon-based ones. As the capacitance of TANI electrodes varies with the chemical potential of the material (indicated by its non-square CV curves), the initial open-circuit potential of each electrode in a device can greatly affect the performances of a symmetric TANI

supercapacitor. At the end of the day, the performance of any supercapacitor device depends on how well the positive electrode and the negative electrode are matched. In this section, we demonstrate that for a symmetric TANI supercapacitor, not only mass loading of the electrodes, but also the initial state of charge (chemical potential) of the electrodes can significantly affect the 2-electrode symmetric TANI supercapacitor performance.

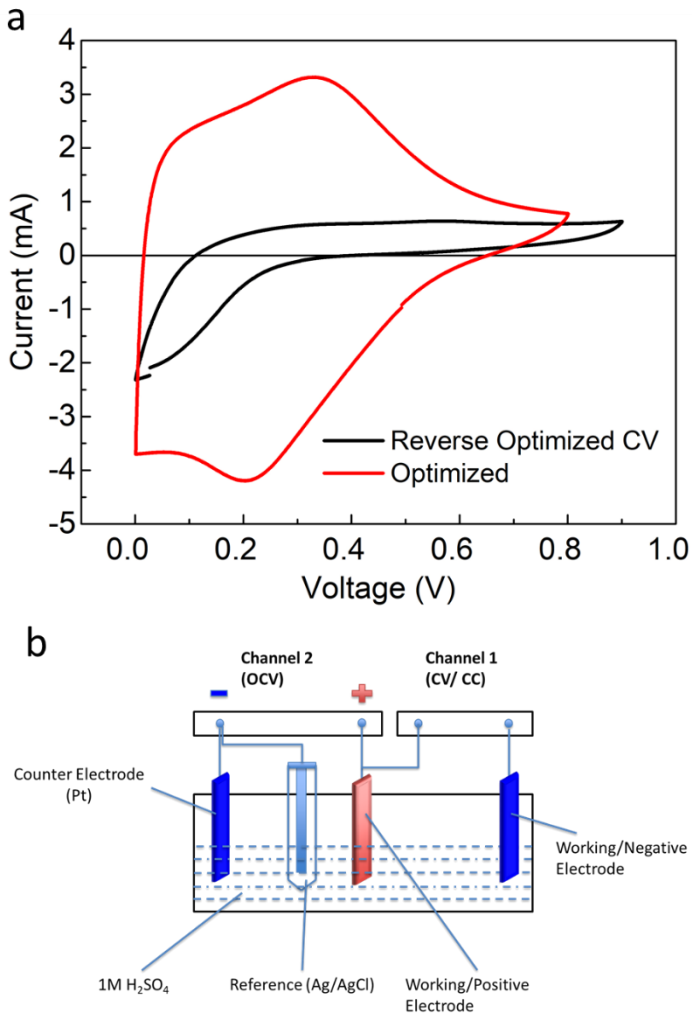

Figure 5.4 (a) CV comparison of a symmetric TANI supercapacitor under two different scenarios. (b) A schematic diagram of the 2-channel-4-electrode setup.

Depending on the initial chemical potential of the electrodes, the CV plot of the same symmetric TANI supercapacitor can vary greatly, as shown in Figure 5.4a. To explain this dramatic difference in performance of the same device, a 2-channel-4-electrode setup was utilized, as illustrated in Figure 5.4b. The Bio-logic VMP3B-10 potentiostat has multiple channels that can be synchronized to collect data simultaneously. In the 2-channel setup-4-electrode setup, Channel 1 is connected to the symmetric supercapacitor in a standard 2-electrode fashion, with the red wire connected to the positive electrode, the blue wire and white wire connected to the negative electrode. This channel runs standard CV, EIS and CC tests on the supercapacitor. Channel 2 uses a standard 3-electrode setup, with the red wire connected to either the positive electrode (shown in the illustration) or the negative electrode of the supercapacitor (depending on which electrode one wishes to monitor), the white wire connected to the reference electrode (Ag/AgCl in saturated KCl solution) and the blue wire connected to a counter electrode (a 1×2 cm^2 platinum foil). This channel runs an open-circuit voltage setting, recording the potential (vs. the reference electrode) of either the positive or the negative electrode (depending on which one is connected) as the supercapacitor is being tested. The merit of this setup is that it shows the chemical potentials of each electrode at any device potential of the supercapacitor, whereas a normal 2-electrode setup can only record the potential difference between the positive and the negative electrode (i.e., the device potential).

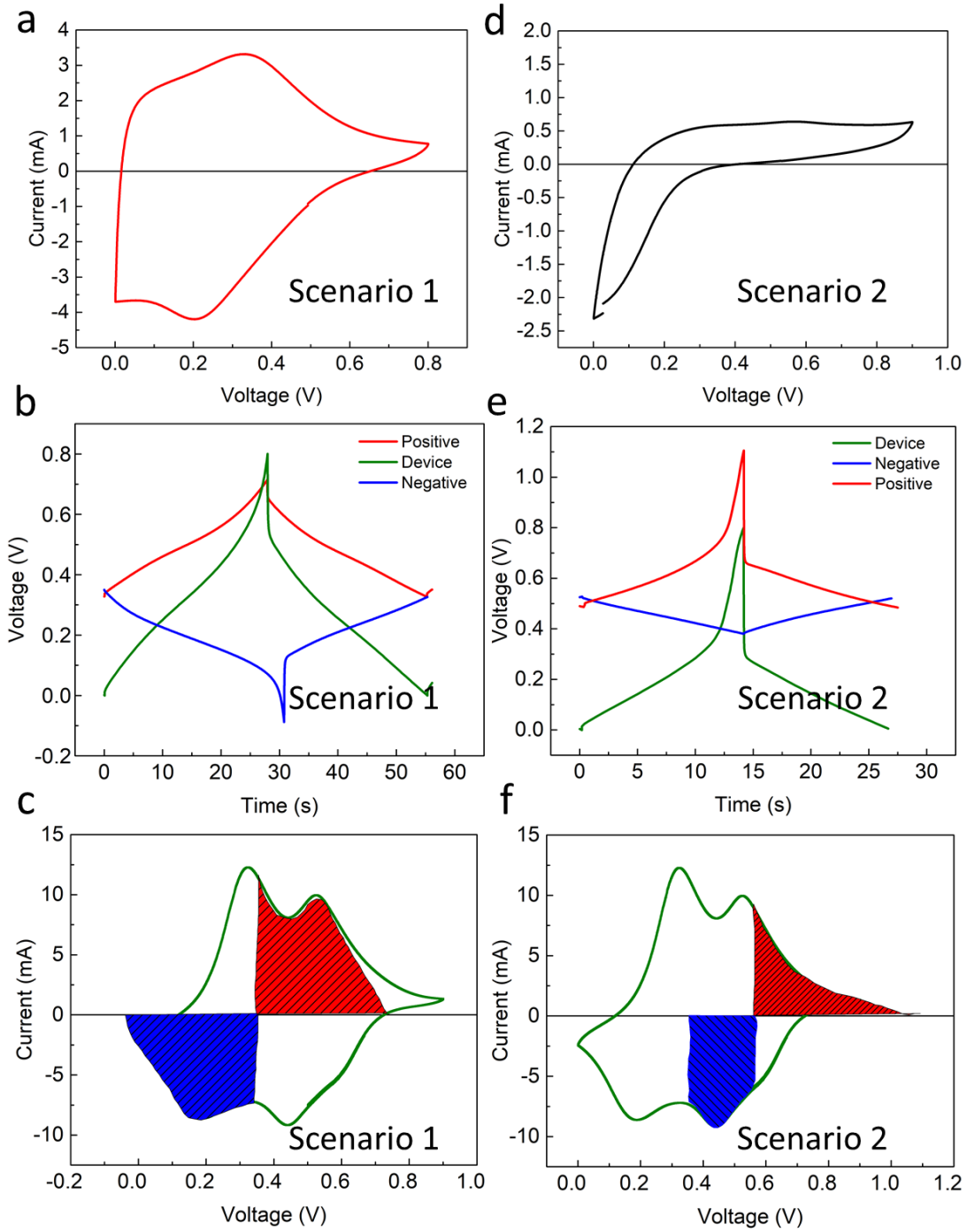

Figure 5.5 Electrochemical results of a TANI symmetric supercapacitor: (a) CV curve (30 mV/s) and (b) CC curves (0.2 mA) and (c) charge capacity matching illustration of Scenario 1, and (d) CV curve and (e) CC curves and (f) charge capacity matching illustration of Scenario 2.

The 4-electrode results of the same symmetric TANI device under two scenarios are shown in Figure 5.5. In Scenario 1, both electrodes were pre-charged to 0.3 V vs. the reference electrode (using a 3-electrode setup), while Scenario 2 has both electrodes charged to 0.5 V. Afterwards, the symmetric device was tested using CV (30 mV/s, 0 - 0.8 V) and CC (2 mA, 0 - 0.8V) methods. Comparing Figure 5.5a-b and 5.5d-e, it is quite obvious that the CV curve in Scenario 1 has overall higher current densities and a wider working potential window. Meanwhile, the device CC curves (in green) indicate that the same device holds more than twice the capacity in Scenario 1 than it does in Scenario 2. This phenomenon can be best explained using the illustrations in Figure 5.5c and 5.5f, which are obtained from the individual electrode potential data shown in Figure 5.5b and 5.5e.

In Scenario 1 (the CC curves shown in Figure 5.5b) the positive electrode went from 0.3 V to 0.7 V, while the negative electrode potential dropped from 0.3 V to -0.1 V, as the 2-electrode device was charged from 0.0 V to 0.8 V. Extrapolating this information onto a CV plot of one of the TANI electrodes used in the device (the two electrodes have near identical CV curves), we can generate Figure 5.5c. The red and blue regions correspond to the areas under the curve over the potential windows traversed by the positive and the negative electrodes during the charging process, respectively. The area of the colored region is directly proportional to the amount of charge held in the electrodes. Notice that the red region and the blue region are of the same area, because all charges that went into the positive electrode came from the negative electrode. This area/charge matching of the electrodes causes the same device to show inferior performances in Scenario 2. As both electrodes start off at 0.5 V, a relatively high chemical potential for TANI, the positive electrode has to travel to a very high chemical potential in order to accommodate the charges provided by the negative electrode. This results in the huge spike in device potential near

12 s and the corresponding precipitous drop at around 15 s. In addition, the area under the curve of the red region for Scenario 2 is much smaller than that in Scenario 1, justifying the substantial difference in charge capacity for the two scenarios. Again, it is worthwhile to point out that the apparent IR drop on the CC plot is the sum of the potential drop of the positive electrode, the potential rise of the negative electrode and the real IR drop. It, therefore, does not symbolize a high resistance of the device, but rather an inappropriate potential window. The effective potential window of the device in Scenario 2 is only 0.25 V, while that of Scenario 1 is about 0.6 V. This also stresses the significance of extending the stable working potential range of TANI electrodes, as discussed in the previous section (nanowire vs. globular morphology).

Comparing the two scenarios, Scenario 1 has both electrodes start from near the midpoint of the working potential window of TANI (-0.1 to 0.9 V) and was therefore able to maximize the area under the CV curve, storing the maximum amount of charge. In Scenario 2, on the other hand, the device is limited by the capacity of the positive electrode, as TANI shows very little capacitance in the potential range from 0.6 V to 1.1 V, showing much reduced capacity. In summary, these two scenarios indicate that when making a symmetric TANI supercapacitor, balancing the mass loading of materials is not sufficient; the starting chemical potential/state-of-charge of the electrodes also need to be optimized for maximizing the capacity and the potential window. Moreover, it can also be inferred that a symmetric TANI device cannot take advantage of the entire working range of TANI (the optimal case in Scenario 1 can only utilize half of the potential window). TANI is best served as the positive electrode material of an asymmetric supercapacitor.

5.2.3. TANI-carbon composite materials

Carbon nanomaterials, such as carbon nanotubes (CNT), graphene oxide (GO), reduced graphene oxide (rGO), and activated carbon (AC), are commonly used in EDLC supercapacitors due to their high surface area. Generally, carbon materials are classified based on their overall nanostructures as one-dimensional (1D), two-dimensional (2D) and three-dimensional (3D) materials. However, as far as interactions with TANI are concerned, the dimensionality of the carbon surface morphology/porosity is more meaningful. Some SEM images of CNT, rGO and AC are presented in Figure 5.6. As shown in the SEM images, even though carbon nanotubes form a connected interwoven 3D network, each nanotube interacts with other materials in a 1D fashion. Similarly, rGO is a 3D material but each individual sheet, while serving as a substrate for TANI, behaves like a 2D sheet. Finally, activated carbon, being treated by some as a zero dimensional material due to lack of an interconnected conductive network, shows three-dimensional surface morphology and hierarchical pore distributions. Therefore, in this section, carbon nanotubes are treated as 1D, reduced graphene oxide and graphene oxide are treated as 2D, and activated carbon is treated as 3D.

In principle, by combining TANI and nanostructured carbon substrates into composite materials, the large surface area of the substrate can increase the number of available surface redox active sites, making TANI behave more pseudocapacitor-like than battery-like. In turn, TANI can also act as a conducting agent to make less conductive carbon substrates, such as activated carbon and graphene oxide, less resistive. In this section, TANI is composited with various forms of carbon substrates via an *in situ* chemical synthesis or a physical self-assembly method, and its supercapacitor performances are evaluated. It is worth mentioning that the specific gravimetric capacitances (presented in Table 5.1) of the TANI-carbon composites are strongly influenced by

TANI loading, which is difficult to control given the differences in the preparation methods and the intrinsic properties of the carbon substrates. As a result, the primary focus of the evaluations will be on the electrochemical behaviors, charge storage kinetics, TANI-carbon synergies and cycle stability.

To briefly describe the composite preparation methods: the *in situ* chemical synthesis first blends an aniline dimer ethanol solution with a carbon substrate in an aqueous dispersion using rapid mixing and probe sonication. Once the aniline dimer molecules are absorbed onto the surfaces and pores of the carbon materials, the oxidizing agent, ammonium persulfate, is slowly added into the reaction mixture during rapid stirring. This *in situ* method aims to uniformly grow TANI on the carbon surfaces, generating synergetic effects between the conducting oligomer and the carbon materials. The physical self-assembly is performed by mixing pre-synthesized TANI nanowires with the pre-dispersed carbon substrate suspension solutions under probe ultrasonication. During the ultrasound mixing, TANI comes into contact with the carbon and becomes attached to its surfaces via intermolecular forces and π-π interactions.

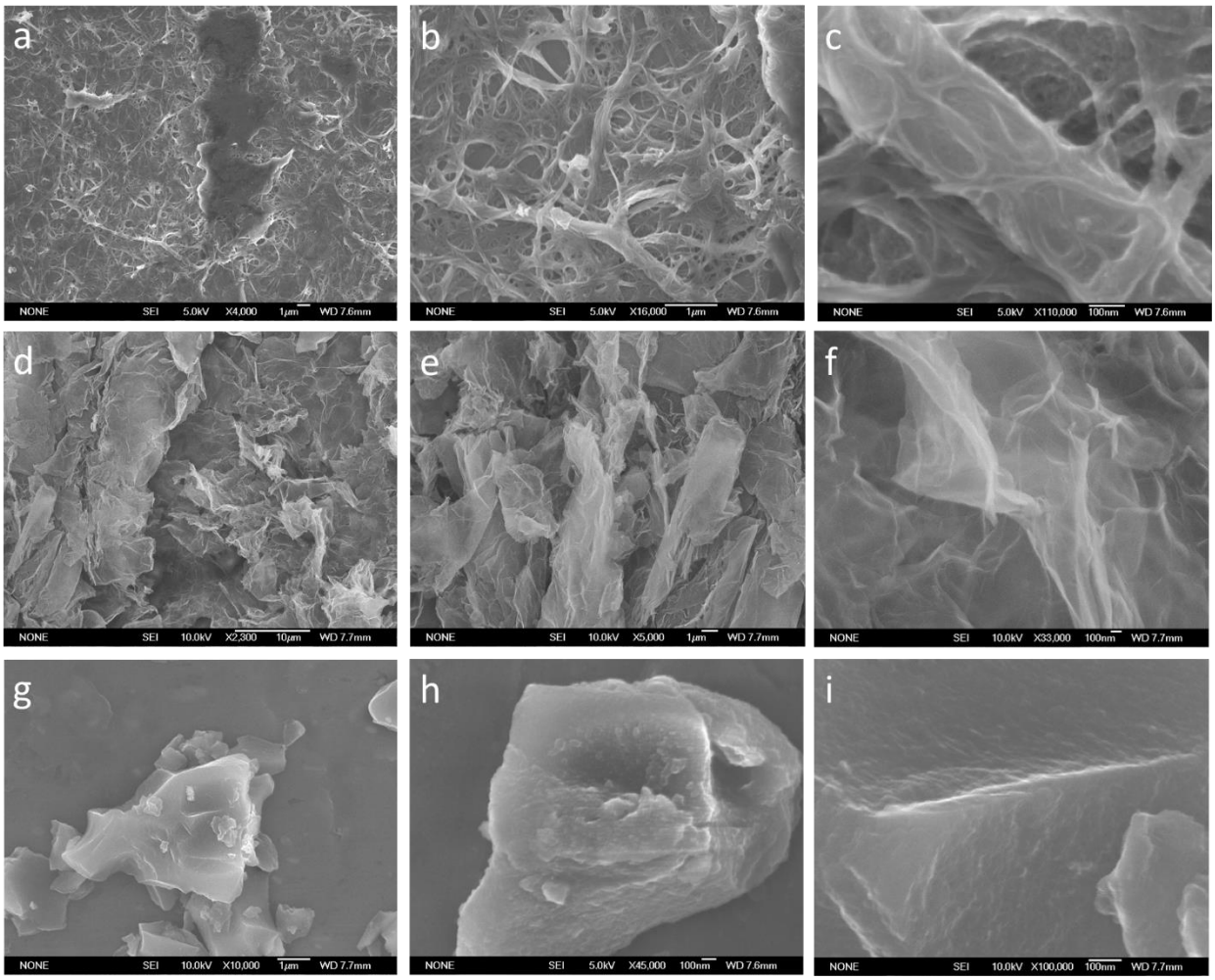

Figure 5.6 SEM images of (a-c) carbon nanotubes, (d-f) reduced graphene oxide, and (g-i) activate carbon at various magnifications.

5.2.3.1. 1D carbon-TANI composites

Carbon nanotubes (CNT) have many attractive properties that make them good supercapacitor materials, such as high conductivity, large surface area and interconnected 3D networks. However, the interwoven nature of the CNTs also make them difficult to disperse (Figure 5.6a). Figure 5.7 shows the SEM images of chemically prepared and physically mixed TANI-CNT composites. The *in situ* chemically prepared composite shows TANI enwrapping the

CNTs and forming an interwoven 3D composite structure, while the physical mixture composite shows distinct nanotubular clusters of TANI in between the CNT networks.

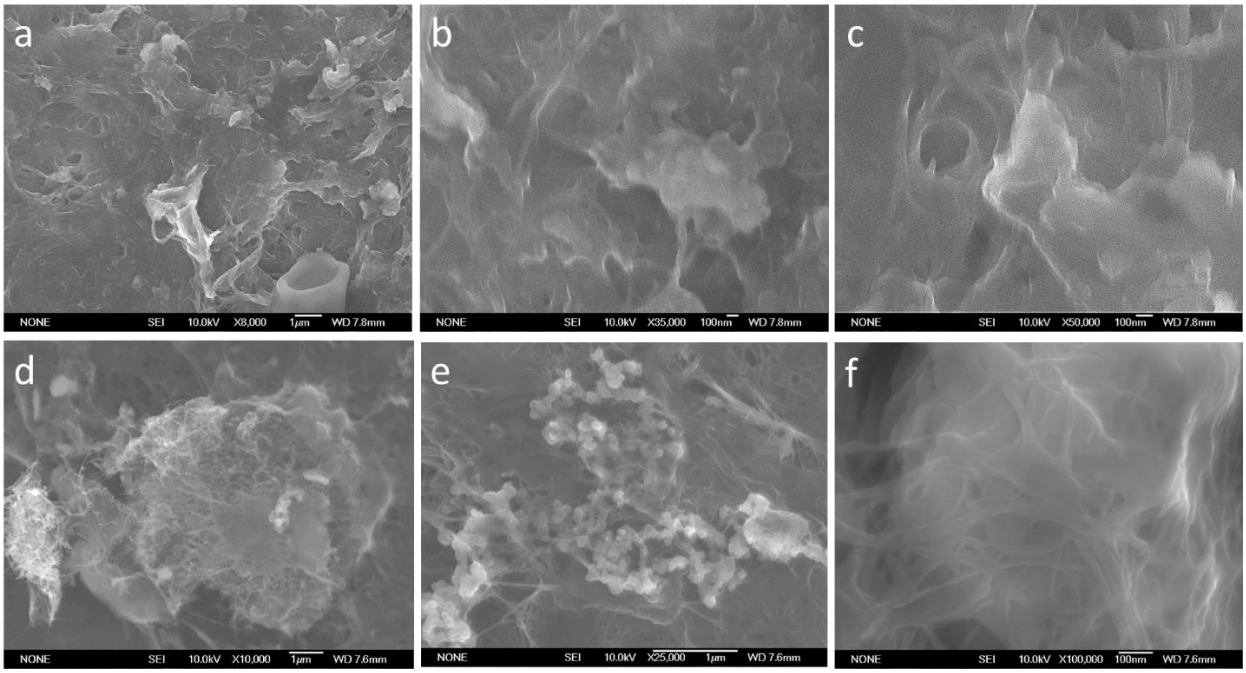

Figure 5.7 SEM images of (a-c) a TANI-CNT in situ composite and (d-f) a TANI-CNT physical mixture composite under different magnifications.

The effects of the composite morphology are clearly manifested in their supercapacitor performances, as shown in Figure 5.8. Both composites show two sets of redox peaks, characteristics of TANI. However, in comparison, the redox peaks of the *in situ* composite appear to be broadened and its CV curves are much more rectangular in shape. The cathode-anode peak separation of the physical mixture composite is also much larger, indicating more prominent diffusion behaviors. In agreement with the CV shapes, the CC curves of the *in situ* composite are also more triangular in shape, characteristic of a pseudocapacitor, while the CC curves of the physical mixture display clear plateaus, representative of a battery-like electrode. This difference in kinetics is also corroborated by the Nyquist plot, as the uncompensated internal resistance of

the physical mixture composite is much higher than the *in situ* composite. Finally, the *b*-values of the two composites also suggest that the redox reactions take place primarily on the surface of the *in situ* composites, while the physical mixture composites show a high percentage of diffusion-controlled redox processes. As a result of the sluggish kinetics, even though the physical mixture composite shows a higher specific capacitance of 355 F/g (vs. 273 F/g for the *in situ* composite) at a slow scan rate of 5 mV/s, its high rate specific capacitance drops down to 212 F/g (vs. 243 F/g at 200 mV/s); more specific capacitances can be found in Table 5.1.

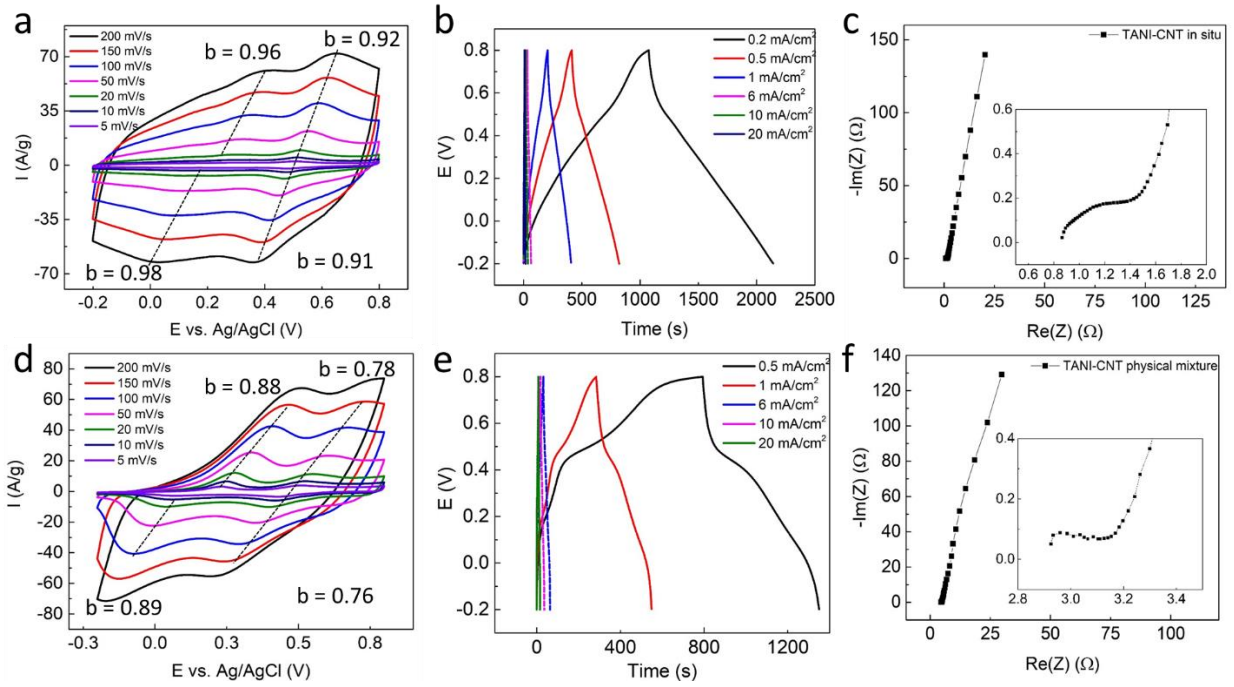

Figure 5.8 Electrochemical performance of two TANI-CNT composites: (a) CV plots, (b) CC curves, and (c) Nyquist plot (inset shows high frequency range data) of a TANI-CNT in situ composite. (d) CV plots, (e) CC curves and (f) Nyquist plot (inset shows high frequency range data) of a TANI-CNT physical mixture composite.

Combining the morphology and the electrochemical performance results from the two composites, the *in situ* composite shows much better rate capability due to synergetic effects from its core-shell structures. The TANI shell increases the percentage of surface TANI molecules, facilitating rapid surface redox charge transfer and counter ion diffusion, while the CNT core helps

distribute the electrons/charges throughout its 3D interconnected networks. The physical mixture, on the other hand, shows separate domains of TANI and CNTs, and the disordered networks of long aspect ratio nanowires and nanofibers result in high charge transfer resistance between the TANI and CNTs. Due to the lack of synergy, the carbon substrate fails to enhance the pseudocapacitance behavior of TANI, resulting in overall inferior supercapacitor performances. Additionally, the interwoven nature of the CNTs make them difficult to disperse and likely contributes to the relatively low specific capacitance of the composites.

5.2.3.2. 2D carbon-TANI composites

Two types of 2D carbon materials are used to make carbon-TANI composites: graphene oxide (GO) and reduced graphene oxide (rGO). Both GO and rGO appear to be wrinkled 2D sheets stacked together to form a 3D network. Compared to rGO, GO tends to have more oxygen containing function groups on the surface, disrupting the sp^2 conducting network, and therefore is lower in conductivity. However, GO is also more hydrophilic and easier to exfoliate in solution.

SEM images of a TANI-GO *in situ* composite and a physical mixture composite are shown in Figure 5.9. The *in situ* composite does not show isolated clusters or aggregates of TANI. The morphology of the composite is very similar to that of GO, except that the sheets seem to have patches of different shades, suggesting that TANI is deposited onto the GO sheets, albeit unevenly. The physical mixture composite, on the other hand, shows semi-globular TANI covering the surfaces of the GO sheets, and some clusters of nanotubular TANI can also be found attached to the edges of the sheets.

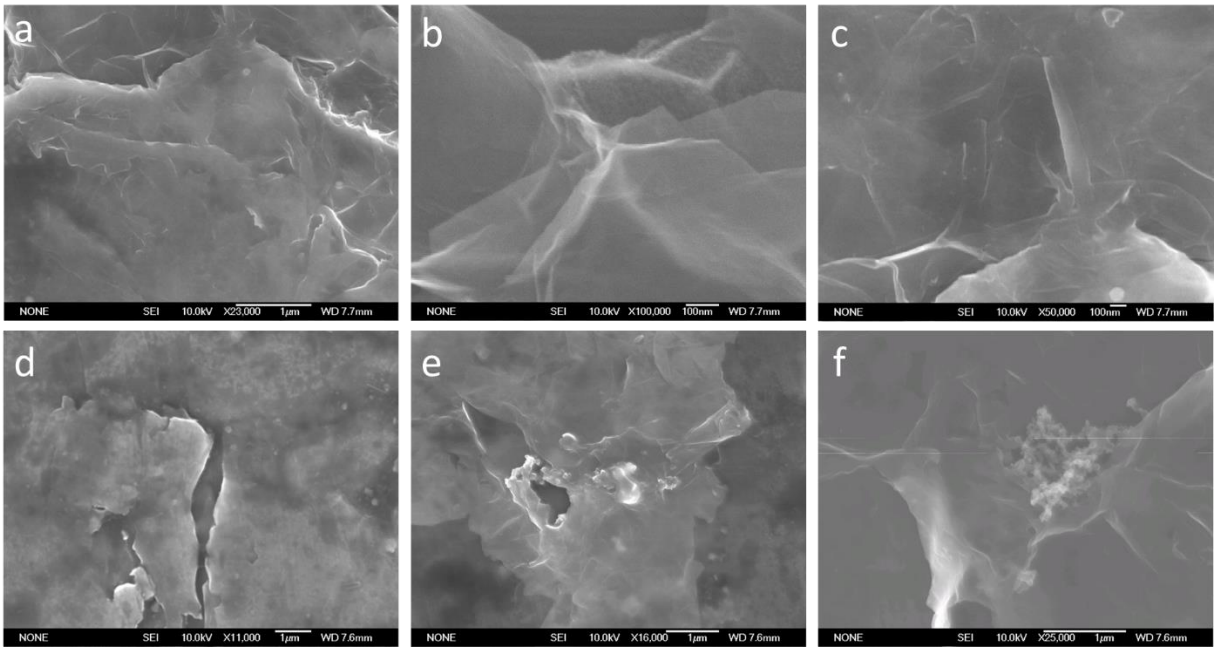

Figure 5.9 SEM images of a TANI-GO in situ composite (a-c) and a TANI-GO physical mixture composite (d-f).

Graphene oxide is inherently low in conductivity, and this property limits the supercapacitor performance (Figure 5.10) of the TANI-GO composites. No sharp redox peaks can be found on the CV curves of either the *in situ* or the physical mixture composite. Instead, the *in situ* composite shows two subtle and broad peaks at the two redox active potentials for TANI. The broadening of the redox peaks reduces the fluctuations of the instant capacitance of the electrode, resulting in nearly linear CC curves. In the case of the TANI-GO physical mixture, the two redox peaks display higher hysteresis and merge into one peak spanning a wide potential range. This broad but prominent peak causes the CC curves to demonstrate asymmetric shapes, with most of the discharge capacity gravitating towards the lower half of the potential window. The high internal resistance is also indicated by the Nyquist plots (0.2 V vs. Ag/AgCl), as both electrodes display a relatively high x-intercept. The *in situ* electrode also shows a relatively long 45° line, suggesting slow diffusion kinetics. This is consistent with the b-values shown on the CV diagrams. However,

it is worth noting that the high resistance of the electrode affects the *b* and *k*-value analysis, as the peak currents are difficult to locate. Nevertheless, both composites demonstrate poor rate capabilities: the *in situ* composite retains about 54% of its 0.5 mA/cm^2 specific capacitance (573 F/g) at 20 mA/cm^2 (311 F/g), and the physical mixture loses about 55% of its 0.5 mA/cm^2 capacitance (408 F/g) at 20 mA/cm^2 (185 F/g). Given the inherently low conductivity of GO, it is difficult to find a coherent correlation between the electrode morphology and supercapacitor performance.

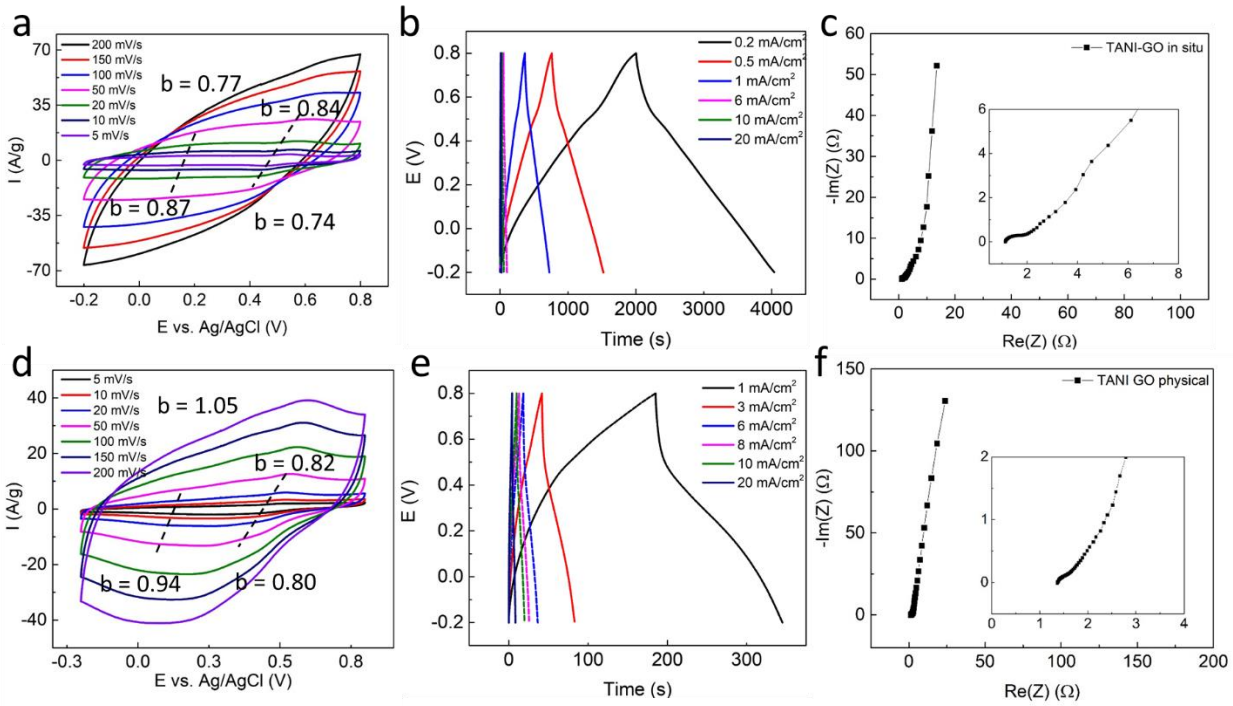

Figure 5.10 Supercapacitor performance of a TANI-GO in situ composite (a) CV curves, (b) CC curves and (c) Nyquist plot (inset shows high frequency data), and a TANI-GO physical mixture composite (d) CV curves, (e) CC curves and (f) Nyquist plot (inset shows high frequency data).

Figure 5.11 shows the SEM images of a TANI-rGO *in situ* composite and a physical mixture composite. The *in situ* composite exhibits rGO-like structures with round edges and rough surfaces, suggesting that TANI growth follows the contour of the rGO surfaces and the composite

is comprised of a TANI shell sheathing the rGO core. In comparison, the physical mixture composite shows clusters of nanotubular TANI structures clinging to the rGO surfaces.

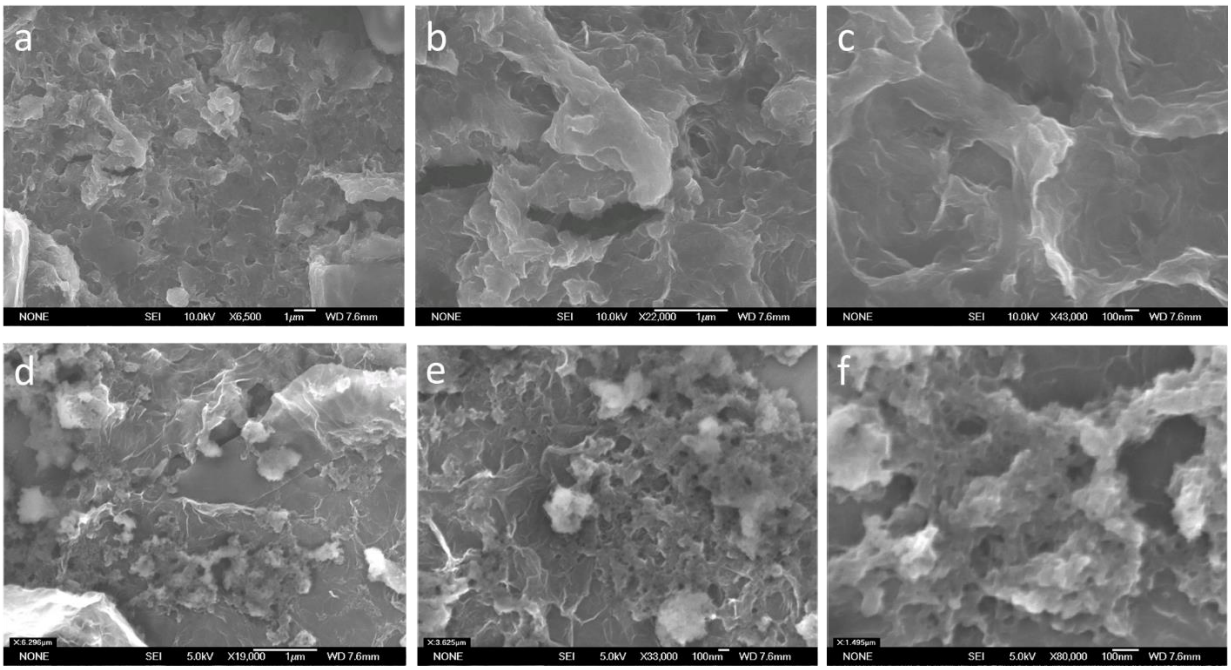

Figure 5.11 SEM images of a TANI-rGO in situ composite (a-c) and a TANI-rGO physical mixture composite (d-f).

Compared to GO, the reduced graphene oxide demonstrates much better conductivity, and this greatly improves the overall supercapacitor performances of the electrodes (Figure 5.12). The CV plots of the *in situ* composites show two sets of redox peaks, while the physical mixture composites shows three pairs. As discussed earlier, the third set of peaks at about 0.65 V vs. Ag/AgCl is associated with the TANI degradation byproducts (HQ/BQ), and it is present in both the pure TANI and the TANI-rGO physical mixture composite CV curves. This suggests that the functional groups on the rGO sheets do slightly alter the chemical properties of TANI in the *in situ* synthesized TANI-rGO composite, while the physical mixture composite retains the original properties of TANI due to lack of synergy. Still, both composite materials demonstrate great rate capabilities. The physical mixture composite retains 75% of its 0.2 mA/cm^2 capacitance (343 F/g)

at 20 mA/cm^2 (258 F/g), and the *in situ* composite only loses 16% at 20 mA/cm^2 capacitance (341 F/g) compared to its 0.2 mA/cm^2 capacitance (407 F/g). The CV curve of the *in situ* composite also maintains a near-rectangular shape at a fast scan rate of 2 V/s (Figure 5.12b).

The high rate capability is confirmed by the EIS data and kinetic analyses. The physical mixture electrode shows a smaller contact resistance (x-intercept) than the *in situ* electrode, but its charge transfer resistance is much higher. While many factors, such as electrolyte resistance, quality of the electrode and external circuit resistance, can contribute to the contact resistance, the large semicircle is definitive evidence that the physical mixture composite experiences higher diffusion control. This is corroborated by the charge storage mechanisms analysis. The *b*-values of the redox peaks on the *in situ* composite are all very close to 1, and the *k*-values suggest that over 94% of the capacitive current are contributed by reversible surface redox reactions (at 10 mV/s). The kinetics of the physical mixture are slightly slower, due to the ion diffusion within the TANI clusters and the charge transfer between TANI and the rGO sheets. However, the physical mixture still exhibits at least an 80% contribution from surface-controlled redox processes (see Table 5.2).

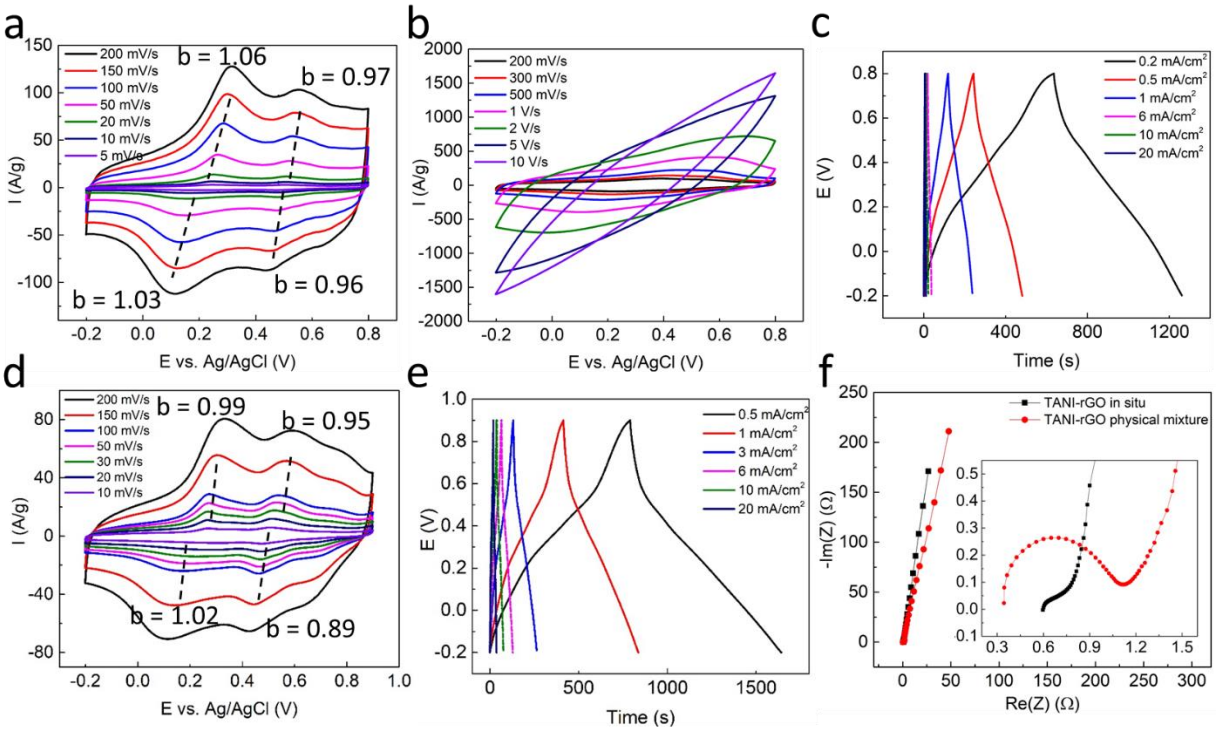

Figure 5.12 Electrochemical performance of a TANI-rGO in situ composite (a) CV at slow scan rates, (b) CV at higher scan rates and (c) CC curves, and a TANI-rGO physical composite (d) CV curves, (e) CC curves and (f) Nyquist plots of the two composite electrodes (inset shows high frequency range data).

5.2.3.3. 3D carbon TANI composites

The SEM images of the TANI-AC composites are presented in Figure 5.13. In the *in situ* composite, TANI is formed on the surface of the activated carbon as a thin and smooth layer, filling in the pores, but not forming interconnected networks. In the physical mixture, however, nanostructured TANI not only covers the entire surface of the activated carbon, but also connects the AC blocks with the interwoven nanowire networks. The difference in morphology is likely due to the preparation methods. The *in situ* synthesis process first allowed the aniline dimer molecules to be absorbed by the activated carbon, and then the oxidizing agent was introduced to oxidatively couple the aniline dimer. As the activated carbon has a very high surface area and a hierarchical distribution of mesopores and nanopores, the majority of the aniline dimer molecules were likely

within the pores of the activated carbon and thus formed TANI directly on the carbon surface. On the other hand, the physical mixing process started with relatively large TANI nanowires (tens of nanometers in diameter and a few microns in length), and even though TANI does disperse to some extent under sonication, the majority of the nanowires could only adhere to the surface of the activated carbon through intermolecular interactions, without going into the carbon mesopores and nanopores.

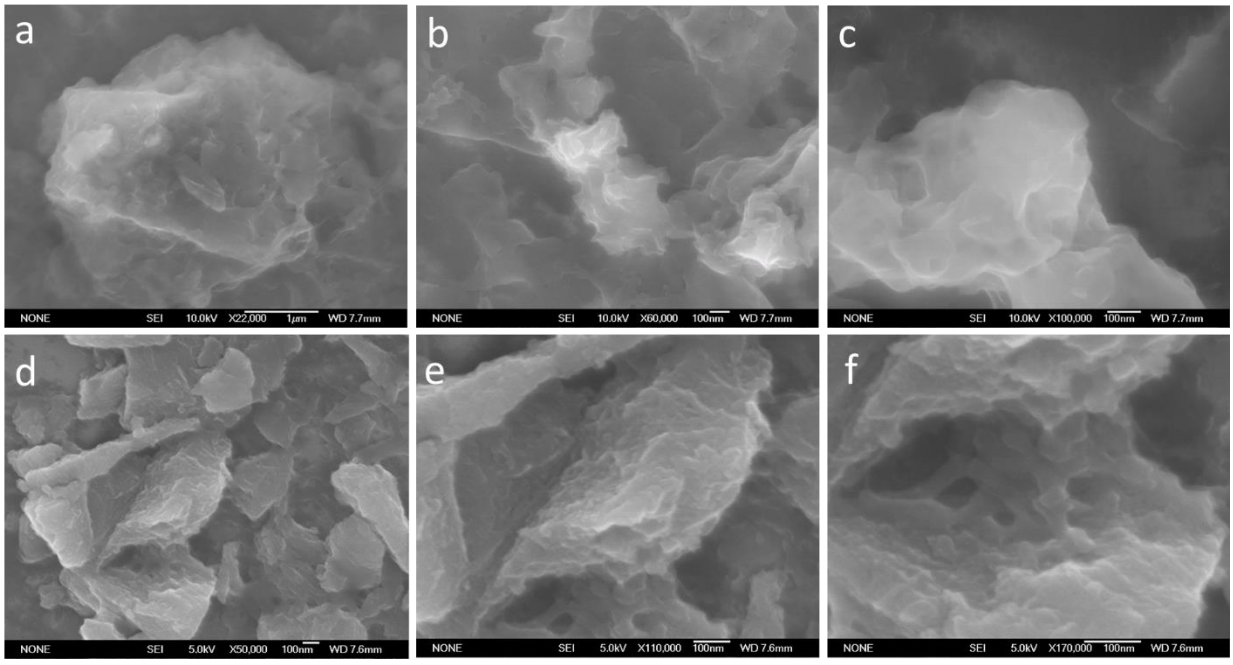

Figure 5.13 SEM images of TANI-AC in situ composites (a-c) and TANI-AC physical mixture composites (d-f) at various magnifications.

Figure 5.14 presents the electrochemical performances of the TANI-AC composite electrodes. Similar to the TANI-rGO composites, the TANI-AC *in situ* composite shows two pairs of broad redox peak on the CV curves, while the physical mixture composite shows three sets. Therefore, a similar argument can be made to explain the different behaviors: the *in situ* composite slightly alters the electrochemical properties of TANI within the synergetic composite, whereas the physical mixture exhibits intrinsic TANI electrochemical behaviors added on top of the carbon

substrate behaviors. The charge storage kinetics from *b* and *k*-value analyses are in agreement with the morphologies of the two composites. The thin layer of TANI on the *in situ* composite shows rapid surface-controlled redox properties, manifested as broad and smooth redox peaks. In contrast, the clustered TANI nanowires on the physical mixture composite experience more diffusion control, giving rise to the sharp redox peaks around 0.45 V. Because of the differences in the redox kinetics, the CC curves of the *in situ* composite appear close to linear, while a plateau shows up at around 0.45 V vs. Ag/AgCl in the physical mixture composite CC. Due to the high surface area of the activated carbon, the *in situ* composite is able to accommodate a significant amount of TANI, resulting in a specific capacitance of 513 F/g at 0.2 mA/cm^2 and 418 F/g at 5 mV/s. However, owing to the lack of conductive TANI networks, the internal resistance of the composite is relatively high as shown in its Nyquist plot (Figure 5.14c). As expected, the rate capability of the composite is mediocre: the TANI-AC *in situ* electrode retains only 54% of its CC specific capacitance at 20 mA/cm^2 (258 F/g) and 66% of its CV specific capacitance at 200 mV/s (276 F/g). Interestingly, the physical mixture composite electrode displays a relatively small internal resistance (Figure 5.14f), largely thanks to the 3D networks of TANI nanowires. Accordingly, the electrode demonstrates good rate capability, retaining 73% of its CC specific capacitance and 91% of its CV specific capacitance. However, there is a possibility that the physical composite lost some of its initial capacitance during the CV testing, resulting in an ostensibly high rate capability (slow scan rates were tested after the fast scan rates).

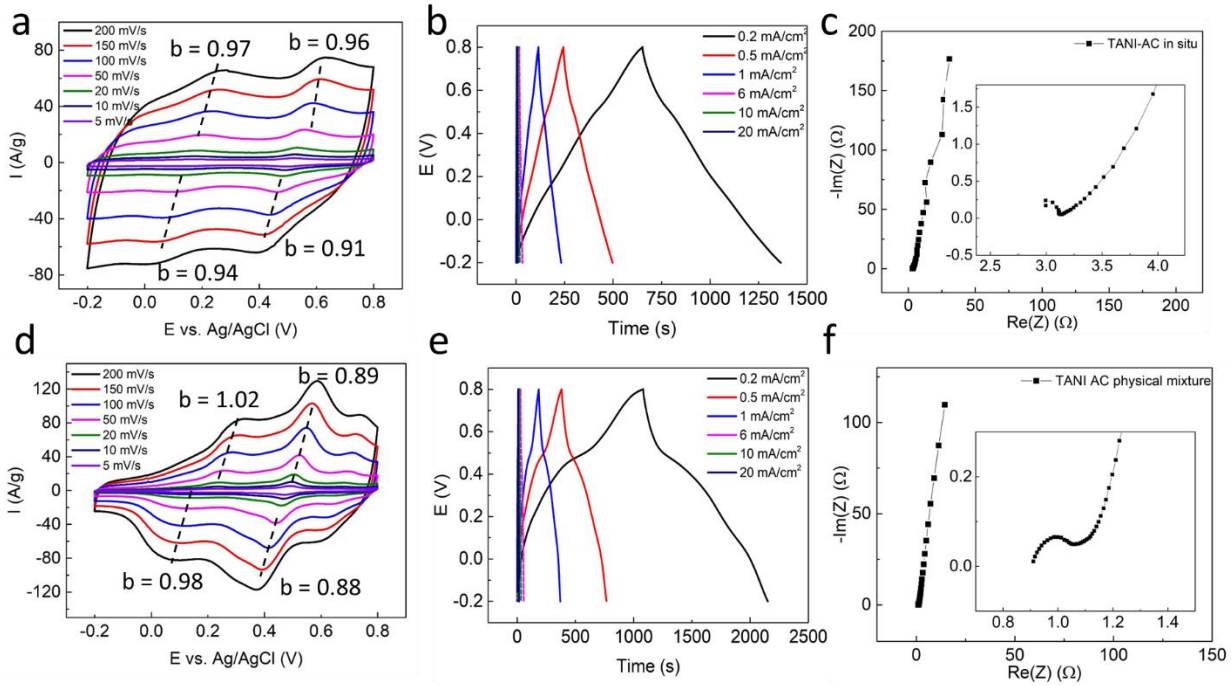

Figure 5.14 Supercapacitor performance evaluation of a TANI-AC in situ composite: (a) CV curves, (b) CC curves and (c) Nyquist plot (inset shows high frequency data), and of a TANI-AC physical mixture composite: (d) CV curves, (e) CC curves and (f) Nyquist plot (inset shows high frequency data).

5.2.3.4. Evaluation of TANI-carbon electrode performances in relation to the carbon surface morphology (1D, 2D and 3D)

As mentioned previously, the electrode performance of the composite materials is strongly influence by the weight percentage of TANI in the composites, which is in turn affected by how the carbon substrate interacts with TANI. However, a systematic study on how to optimize the TANI loading on different carbon materials using various preparation techniques is beyond the scope of this chapter. Nonetheless, given the limited available data, some trends can still be noticed.

The specific gravimetric capacitances of the composites at various scan rates and current densities are listed in Table 5.1. Generally speaking, all *in situ* composites exhibit higher specific capacitances and better rate capabilities compared to their physical mixture counterparts,

indicating the presence of synergy between the carbon substrates and TANI. In terms of the rate capability, the TANI-AC physical composite is an exception because the conductivity of AC is relatively low, compromising the rate capability of the TANI-AC *in situ* composite. As far as the maximum capacitance is concerned, the TANI-GO *in situ* composite shows the highest specific capacitance of 617 F/g at a low current density of 0.2 mA/cm^2. This is likely because GO is the only carbon substrate that is easily dispersible in aqueous solution, and thus has the highest specific surface area to interact with aniline dimer/TANI. Therefore, its composite has the highest TANI loading and hence, the highest specific capacitance. However, due to the low conductivity of GO, the TANI-GO composite displays relatively low specific capacitances at higher scan rates/current densities. Activated carbon also has very high surface area and mesoporous structures, allowing it to absorb a considerable amount of aniline dimer/TANI. Accordingly, the TANI-AC *in situ* composite has the second highest specific capacitance of 513 F/g at 0.2 mA/cm^2; however, it also suffers from the low conductivity of the substrate and retains only 277 F/g at 20 mA/cm^2. Among all the carbon materials, the 1D CNTs have the lowest TANI loading, as suggested by their low specific capacitance. This is likely because the 1D surface morphology of the CNTs is not favorable for aniline dimer adsorption, and therefore the *in situ* dimerization reaction fails to deposit a significant amount of TANI on the CNT networks. Still, the conductive CNT network does greatly improve the rate capability of the composite, showing 87% capacitance retention at 20 mA/cm^2. In comparison, rGO has both high specific surface area and high conductivity, and the TANI-rGO *in situ* composite shows higher specific capacitance than the TANI-CNT and comparable rate capabilities. To summarize the correlation between carbon surface dimensions and electrode performances: the affinity for aniline dimer/TANI and maximum specific capacitance increase with dimensionality (1D < 2D < 1D); however, given the low conductivity of

the 3D activated carbon, the 2D rGO is the most promising carbon substrate for TANI-carbon composites.

Cycle stability is another key performance metric of a supercapacitor electrode. The cycle life of the TANI-carbon electrodes are evaluated by continuous constant current charge-discharge methods, and each cycle takes about 25-30 seconds. The results are presented in Figure 5.15i-k. It is worth mentioning that the cycle life tests were performed on the electrodes after the CV and CC characterizations, and hence, the capacitance retetion is slightly overestimated compared to the initial capacitance of freshly made electrodes.

During charge and discharge, counter ions move in and out of TANI structures, causing drastic volume changes. Over time, the repeated physical stress compromises the physical integrety of the elelctrode material, resulting in loss of capacitance. Additionaly, the pernigraniline form of PANI/TANI is known to under go a hydrolysis reaction, chemically degrading the electrode.[19–22] As a result, TANI experiences both severe physical and chemical degradation during cycling and suffers more than 60% loss of its initial capacitance after 2000 cycles.

As shown in Figure 5.15, all TANI-carbon composite materials demonstrate improved cycle life compared to pure TANI. Notably, the TANI-AC *in situ* composite shows nearly no capacity loss after 2000 cycles, while the *in situ* TANI-GO, TANI-rGO and physical mixture TANI-AC composites all retain more than 90% of their initial capacitance. Upon closer examination, two trends can be found: 1) the *in situ* composites consistantly retain higher capacitance than their physical mixture counter parts; and 2) cycle stability increases with dimensionality of the carbon substrate (3D > 2D > 1D). To understand the trends in cycle stability, cyclic voltammetry was performed on the electrodes after the cycling tests, and the CV curves (at

5 mV/s, except for the TANI-rGO physical mixture, which is at 30 mV/s) before and after cycling are shown in Figure 5.15a-h.

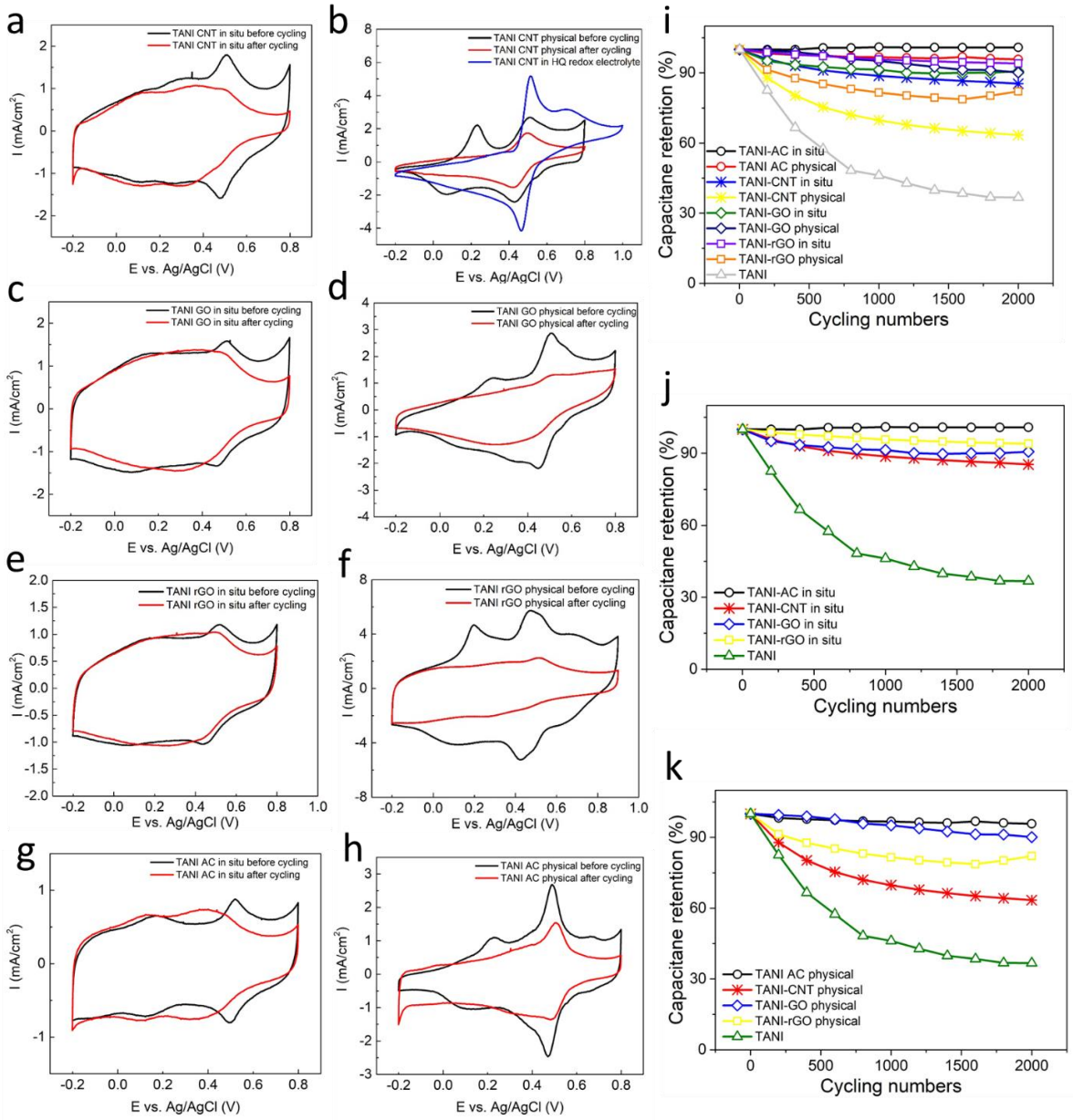

Figure 5.15 Cycle stability performances of the TANI-carbon composites: CV curves before and after cycling for (a) a TANI-CNT in situ electrode, (b) a TANI-CNT physical electrode, (c) TANI-GO in situ electrode, (d) TANI-GO physical electrode, (e) TANI-rGO *in situ* electrode, (f) a TANI-rGO physical electrode, (g) a TANI-AC *in situ* electrode, and (h) a TANI-AC physical electrode. Relative capacitance retention of (i) all the composites, (j) all *in situ* composites, and (k) all physical mixture composites.

As shown in the CV curves, all *in situ* composites retained both redox peak pairs after cycling, although the peak potentials all shifted slightly, suggesting that there is some chemical interactions between TANI and the surface functional groups on carbon. It is highly possible that the *in situ* synthesis and the ensuing electrochemical cycling caused chemical grafting of TANI onto the carbon surfaces. In comparison, the physical mixture electrodes show much reduced redox peak intensities after cycling. This is most likely due to the physical detachment of the TANI aggregates from the composite surfaces (i.e., physical degradation). This type of degradation is most prominent in the case of the TANI-rGO physical mixture, where the SEM images show clusters of TANI deposited on the rGO surfaces. Due to the high conductivity of the rGO, the charge transfer between TANI and rGO is fairly quick and the composite shows characteristic TANI-like CV curves. However, during the 2000 cycles, the physical stress caused the TANI clusters to detach from the rGO, and the electrode after cycling shows typical rGO-like CV curves. A similar phenomenon is also observed in the TANI-GO physical mixture CVs. The TANI-CNT physical mixture shows a CV curve that is akin to a TANI-CNT electrode in a hydroquinone (HQ) redox electrolyte, suggesting that there is a degree of chemical degradation taking place alongside the physical dissolution. Therefore, it is speculated that the physical mixture composites suffer substantial TANI mass loss, due to the weak intermolecular interactions between TANI and the carbon substrates. The *in situ* composites likely benefit from the chemical interactions and synergetic effects between TANI and the carbon, exhibiting better cycle stability.

Correlating the surface dimensionality of the carbon substrates to the cycle life of the composites, the 1D composites show consistently lower cycle stability than the 2D composites, and the 3D composites display the best cycle life among the three. Even the TANI-AC physical mixture retained 96% of its 1st cycle capacitance after 2000 cycles. Two factors likely contribute

to the high stability of the AC composites. First, the AC has a hierarchical pore structure that is very efficient at adsorbing TANI molecules, and even if some of the TANI is detached from one surface of the AC, it is still trapped within the mesoporous structures of the carbon substrate, contributing a portion of its original capacity. Therefore, the physical degradation is partially alleviated. Furthermore, AC is a poor electric conductor and the low conductivity consumes some of the thermodynamic driving force of TANI chemical degradation, driving up the overpotetial required to degrade TANI. Consequently, TANI is more chemically stable within the cycling potential window.

5.3. Conclusions

In conclusion, we have demonstrated that nanostructured TANI shows superior supercapacitor performances compared to globular TANI. The nanowire morphology enhances the specific capacitance and rate capability, makes the electrode behave more pseudocapacitor-like and gives it a higher stable working potential range. The importance of charge balancing the individual electrodes (in terms of both mass loading and state-of-charge) in a symmetric TANI supercapacitor has also been emphasized. We have also evaluated the electrochemical performances of 1D TANI-CNT, 2D TANI-rGO and 3D TANI-AC composites. The hybrid carbon composite materials demonstrate greatly improved cycle stability compared to pure TANI. The results also suggest that the maximum specific capacitance and cycle stability both increases from 1D < 2D < 3D; however, considering the low conductivity of activated carbon, rGO/graphene is the most promising carbon substrate for growing TANI-carbon composites to boost the overall performances of TANI-based supercapacitors.

5.4. Experimental

5.4.1. Synthesis of TANI nanowires

Tetra-aniline nanowires were synthesized via a modified interfacial polymerization method described in the literature.[23] In a typical synthesis, 20.0 mg of N-phenyl-p-phenylenediamine (dimer aniline) was dissolved in 10 mL of dichloromethane. 22.0 mg of ammonium persulfate (APS, 1 equivalent amount) was dissolved in 10 mL of 1.0 M HCl solution. The aqueous phase was added on top of the denser organic phase drop-wise. The interfacial reaction was allowed to react for 4 h unperturbed. At the end of the reaction, the aqueous phase and the interfacial precipitates were separated from the organic phase and dialyzed (regenerated cellulose dialysis tubing, 12,000-14,000 d, Fisherbrand) against deionized (DI) water overnight. The resulting suspension solution was used for drop-casting electrodes without further processing.

5.4.2. Synthesis of TANI with mixed morphology

TANI with mixed morphology was synthesized using a modified interfacial method. 20.0 mg of aniline dimer was dissolved in 10.0 mL of dichloromethane and 22.0 mg of APS was dissolved in 10.0 mL of 1.0 M HCl solution. The two solutions were combined and stirred for 30 min. At the end of the reaction, the aqueous phase was separated from the organic phase and dialyzed against DI water overnight. The resulting suspension solution was used for drop-casting electrodes without further processing.

5.4.3. Synthesis of globular TANI

Globular TANI was synthesized using a traditional one-phase synthesis reported in the literature.[19] In a typical process, 0.80 g of aniline dimer was dispersed in 100 mL of 1.0 M HCl solution chilled in an ice bath. 0.99 g of APS was added into the solution during rapid magnetic mixing and the reaction solution was stirred for another 4 h in the ice bath. At the end of the

reaction, the reaction mixture was centrifuged and the precipitates were washed with 50 mL of DI water 4 times. About 20 mg of the product was dissolved in 10 ml ethanol-water solvent (1:1 volume ratio) and this solution was used for drop-casting electrodes.

5.4.4. Preparation of the TANI-carbon physical mixture composites

20.0 mg carbon substrate (carbon nanotubes, graphene oxide, reduced graphene oxide or activated carbon) was dispersed in 10.0 mL of DI water using probe ultrasonication for 5 min at 50% power (pulse mode 2-second on/ 2-second off). 20.0 mg of TANI nanowires in about 5 mL of DI solution and 440 μL of 1% CMC/SBR binder solution were added to the carbon suspension, and the mixture was probe sonicated for another 10 min. This suspension solution was used for drop-casting electrodes.

5.4.5. Preparation of the TANI-carbon *in situ* composites

20.0 mg of carbon substrate (carbon nanotubes, graphene oxide, reduced graphene oxide or activated carbon) was dispersed in 10.0 mL of DI water using probe ultrasonication for 5 min. 20.0 mg of aniline dimer was dissolved in 2 mL of ethanol and the solution was added into the carbon dispersion. The mixture was mixed via ultrasonication for 10 min. 22.0 mg of APS was dissolved into the prior solution and the mixture was magnetically stirred for 4 h. At the end of the reaction, the reaction mixture was dialyzed against DI water overnight. The resulting solution was used for drop-casting electrodes.

5.4.6. General characterizations

Scanning electron microscopy (SEM) measurements were performed with an FESEM JOEL JSM-6700F FE-SEM at 5 kV to 10 kV. The SEM samples were prepared by drop-casting dilute sample solutions onto aluminum foils and drying in a conventional oven overnight at 50 °C. The probe ultrasound processor used for mixing samples was an FS-300N ultrasonic processor,

with 300 W (100%) power output, 20 kHz frequency (frequency is auto-tracked by the instrument), and a 2 mm-diameter tip.

5.4.7. Electrochemical characterizations

The 3-electrode cyclic voltammetry (CV), constant current charge-discharge (CC), and electrochemical impedance spectroscopy (EIS) were carried out on a Bio-Logic VMP3B-10 potentiostat, with 1.0 M sulfuric acid as the electrolyte, a 1 x 2 cm^2 platinum foil as the counter electrode and Ag/AgCl (in saturated KCl) as the reference electrode. The EIS measurements were performed at 0.2 V and 0.5 V vs. the reference electrode, with a 10 mV amplitude and in the frequency range from 1.0 MHz to 1.0 mHz. The working electrodes were made by drop-casting the probe-sonicated sample solutions on graphite paper current collectors (electrode area = 1 x 1 cm^2), which were then dried in a conventional oven at 60 °C overnight.

The 2-electrode characterizations were performed on the same potentiostat using two synchronized channels. The setup and detailed operations are elaborated in the discussion section. All four electrodes were submerged in 1.0 M sulfuric acid in a beaker, and no separator was used.

5.5. Tables

Table 5.1 Specific Capacitance of the TANI-AC Composites (in F/g)

Specific Capacitance of the TANI-AC Composites (in F/g)								
Current (mA/cm^2)	TANI-CNT in situ	TANI-CNT physical	TANI-GO in situ	TANI-GO physical	TANI-rGO in situ	TANI-rGO physical	TANI-AC in situ	TANI-AC physical
0.2	299	N/a	617	N/a	407	343	513	428
0.5	308	381	573	408	391	303	456	384
0.8	309	377	557	374	384	293	433	371
1	305	382	542	350	384	297	421	371
3	297	306	498	270	370	279	374	347
6	287	276	458	238	362	274	345	333
8	285	265	432	225	357	269	331	329
10	281	257	416	216	356	268	320	325
20	268	230	311	185	341	258	277	312
Retention	87%	60%	50%	45%	84%	75%	54%	73%
Scan rate (mV/s)	TANI-CNT in situ	TANI-CNT physical	TANI-GO in situ	TANI-GO physical	TANI-rGO in situ	TANI-rGO physical	TANI-AC in situ	TANI-AC physical
5	273	355	513	319	367	299	418	352
10	276	329	484	291	383	314	393	354
20	275	303	443	268	387	321	370	354
50	269	273	357	297	387	331	338	342
100	260	248	274	215	378	333	310	331
150	251	229	226	201	373	329	291	325
200	243	212	196	191	368	325	276	320
Retention	89%	60%	38%	60%	100%	98%	66%	91%

Table 5.2 b and k-Value Analysis of TANI and TANI-Carbon Composites (surface/diffusion contribution calculated at 10 mV/s)

Sample:	TANI nanowire				TANI globular			
Potential	0.2 V charge	0.2 V discharge	0.5 V charge	0.5 V discharge	0.2 V charge	0.2 V discharge	0.5 V charge	0.5 V discharge
b value	0.91	1.00	0.98	0.95	0.79	0.86	0.93	0.87
k1	0.42	0.3347	0.3177	0.2643	0.1674	0.1628	0.2094	0.1578
k2	0.439	0.028	0.1376	0.1617	0.334	0.1752	0.084	0.166
Surface	75%	97%	88%	84%	61%	75%	89%	75%
diffusion	25%	3%	12%	16%	39%	25%	11%	25%
Sample:	**TANI-CNT *in situ***				**TANI-CNT physical**			
Potential	0.2 V charge	0.2 V discharge	0.5 V charge	0.5 V discharge	0.2 V charge	0.2 V discharge	0.5 V charge	0.5 V discharge
b value	0.96	0.98	0.92	0.91	0.88	0.89	0.78	0.76
k1	0.1545	0.2298	0.2631	0.2323	0.3815	0.297	0.2569	0.2138
k2	0.1112	0.0461	0.3078	0.2864	0.196	0.2293	0.6432	0.6341
Surface	86%	96%	79%	78%	90%	85%	64%	60%
diffusion	14%	4%	21%	22%	10%	15%	36%	40%
Sample:	**TANI-GO *in situ***				**TANI-GO physical**			
Potential	0.2 V charge	0.2 V discharge	0.5 V charge	0.5 V discharge	0.2 V charge	0.2 V discharge	0.5 V charge	0.5 V discharge
b value	0.77	0.87	0.84	0.75	0.95	0.96	0.82	0.76
k1	0.2442	0.267	0.3658	0.2138	0.2725	0.2757	0.1716	0.1534
k2	0.2564	0.4289	0.3186	0.5533	0.0005	0.0036	0.4044	0.3792
Surface	81%	74%	84%	63%	100%	100%	65%	64%
diffusion	19%	26%	16%	37%	0%	0%	35%	36%
Sample:	**TANI-rGO *in situ***				**TANI-rGO physical**			
Potential	0.2 V charge	0.2 V discharge	0.5 V charge	0.5 V discharge	0.2 V charge	0.2 V discharge	0.5 V charge	0.5 V discharge
b value	1.02	1.02	0.99	1.04	0.99	1.02	0.945	0.894
k1	0.1401	0.1254	0.1534	0.1436	0.7015	0.618	0.6617	0.6012
k2	0.0304	0.0282	0.0137	0.0266	0.101	0.1077	0.4883	0.4704
Surface	94%	93%	97%	94%	96%	95%	81%	80%
diffusion	6%	7%	3%	6%	4%	5%	19%	20%
Sample:	**TANI-AC in situ**				**TANI-AC physical**			
Potential	0.2 V charge	0.2 V discharge	0.5V charge	0.5V discharge	0.2 V charge	0.2 V discharge	0.5V charge	0.5V discharge
b value	0.97	0.96	0.94	0.91	1.02	0.99	0.89	0.88
k1	0.1342	0.1437	0.1489	0.1176	0.2500	0.2018	0.3502	0.3206
k2	0.0805	0.1376	0.1035	0.1844	0.0520	0.0371	0.4645	0.4504
Surface-	88%	82%	87%	74%	96%	96%	77%	76%
diffusion	12%	18%	13%	26%	4%	4%	23%	24%

5.6. References

(1) Miller, J.; Simon, P. *Science* **2008**, *321*, 651–652.

(2) González, A.; Goikolea, E.; Barrena, J. A.; Mysyk, R. *Renew. Sustain. Energy Rev.* **2016**, *58*, 1189–1206.

(3) Snook, G. A.; Kao, P.; Best, A. S. *J. Power Sources* **2011**, *196* (1), 1–12.

(4) Simotwo, S. K.; Delre, C.; Kalra, V. *ACS Appl. Mater. Interfaces* **2016**, *8* (33), 21261–21269.

(5) Peng, C.; Hu, D.; Chen, G. Z. *Chem. Commun.* **2011**, *47* (14), 4105.

(6) Skotheim, T. A.; Reynolds, J. R. *Handbook of Conducting Polymers: Conjugated Polymers Processing and Applications*; 2007.

(7) Zhao, G. Y.; Li, H. L. *Microporous Mesoporous Mater.* **2008**, *110* (2–3), 590–594.

(8) Liu, T.; Finn, L.; Yu, M.; Wang, H.; Zhai, T.; Lu, X.; Tong, Y.; Li, Y. *Nano Lett.* **2014**, *14* (5), 2522–2527.

(9) Gupta, V.; Miura, N. *Electrochem. Solid-State Lett.* **2006**, *8* (12), A630.

(10) Eftekhari, A.; Li, L.; Yang, Y. *J. Power Sources* **2017**, *347*, 86–107.

(11) Moussa, M.; El-Kady, M. F.; Zhao, Z.; Majewski, P.; Ma, J. *Nanotechnology* **2016**, *27* (44), 442001.

(12) Wang, Y.; Tran, H. D.; Liao, L.; Duan, X.; Kaner, R. B. *J. Am. Chem. Soc.* **2010**, *132* (30), 10365–10373.

(13) Z. C. Sun, L. Kuang, X. B. Jing, X. H. Wang, J. Li, F. S. W. *Chem. J. Chinese Univ.* **2002**,

23 (3), 496–499.

(14) Nirmala Grace, A.; Pandian, K. *J. Phys. Chem. Solids* **2007**, *68* (12), 2278–2285.

(15) Lyu, W.; Feng, J.; Yan, W.; Faul, C. F. J. *J. Mater. Chem. C* **2015**, *3* (45), 11945–11952.

(16) Wang, Y.; Liu, J.; Tran, H. D.; Mecklenburg, M.; Guan, X. N.; Stieg, A. Z.; Regan, B. C.; Martin, D. C.; Kaner, R. B. *J. Am. Chem. Soc.* **2012**, *134* (22), 9251–9262.

(17) Yan, J.; Yang, L.; Cui, M.; Wang, X.; Chee, K. J.; Nguyen, V. C.; Kumar, V.; Sumboja, A.; Wang, M.; Lee, P. S. *Adv. Energy Mater.* **2014**, *4* (18), 1–7.

(18) Zhang, S.; Pan, N. *Adv. Energy Mater.* **2015**, *5* (6), 1–19.

(19) Li, R.; Lin, C.-W.; Shao, Y.; Chang, C.; Yao, F.-K.; Kowal, M.; Wang, H.; Yeung, M.; Huang, S.-C.; Kaner, R. *Polymers (Basel).* **2016**, *8* (11), 401.

(20) Zhang, A. Q.; Cui, C. Q.; Lee, J. Y. *Synth. Met.* **1995**, *72* (3), 217–223.

(21) Simões, F. R.; Pocrifka, L. A.; Marchesi, L. F. Q. P.; Pereira, E. C. *J. Phys. Chem. B* **2011**, *115* (38), 11092–11097.

(22) Ahmed, S. M. *Eur. Polym. J.* **2002**, *38* (6), 1151–1158.

(23) Huang, J.; Kaner, R. B. *J. Am. Chem. Soc.* **2004**, *126* (3), 851–855.

Chapter 6. Conclusions and Future work

6.1. Conclusions of the thesis

In conclusion, this thesis has explored the synthesis of tetra-aniline and evaluated the performances of TANI-based supercapacitors. The major discoveries are listed below:

(1) Oxidative polymerization of N-phenyl-p-phenylenediamine (aniline dimer) typically results in the formation of tetra-aniline. Using a simple interfacial method, high purity TANI of varying degrees of nanostructures can be synthesized in a short period of time. Due to the low oxidation potential of aniline dimer, a wide range of oxidants can be employed without significantly affecting the product purity. The TANI nanowires prove to be a promising supercapacitor electrode material with higher specific capacitance, faster rate capability, more surface redox contributions and a wider operating potential window than traditional amorphous TANI. Moreover, the 2-electrode performance of a symmetric TANI supercapacitor is affected by not only the loading, but also the state-of-charge of the individual electrodes. To take full advantage of the pseudo-capacitance of TANI, TANI should be used as the positive electrode material for an asymmetric hybrid supercapacitor.

(2) Electrochemical deposition via aniline dimer also results in TANI formation. The synthesis is a two-step process involving an electrochemical oxidation of aniline dimer cation followed by a chemical coupling of the oxidized dimer radical and a non-oxidized dimer cation. Pulse deposition and CV deposition methods can grow a considerable amount of TANI on the surfaces of the activate carbon (AC) electrode, improving the energy density, and the rate capability of the AC electrode. Due to the synergetic effects between TANI and AC, the TANI-AC composites also demonstrate enhanced cycle stability compared to pure TANI.

(3) Due to its relatively low oxidation potential, aniline dimer can serve as a reducing agent to reduce graphene oxide (GO) while simultaneously being oxidized to form oligoaniline. Utilizing this property, reduced graphene oxide (rGO)-oligoaniline (OANI) composites have been synthesized by a one-step hydrothermal process without the need for adding any oxidizing or reducing agents. FTIR, Raman spectroscopy, XPS, and MALDI-TOF mass spectroscopy indicate the successful reduction of GO to rGO and the formation of aniline oligomers. This unique synthetic route helps to generate synergetic effects between rGO and OANI, and the rGO-OANI composites demonstrate high specific capacitance (640 F/g at 0.2 mA/cm^2), great rate capability and (88% capacitance retention at 150 mV/s compared to 5 mV/s) and good cycle stability (91% capacity retention after 2000 cycles).

(4) Nanostructured TANI pseudo-capacitor electrodes exhibit high specific capacitance and good rate capability, but suffer from low cycle stabilty (40% capacity retention after 2000 cycles). One-dimensional carbon nanotubes (CNTs), two-dimensional graphene oxide (GO) and reduced graphene oxide (rGO), and three-dimensional activated carbon (AC) were composited with TANI in an attempt to study how surface morphology of the carbon substrates influences TANI-carbon hybrid supercapacitor performances. The TANI-carbon composites significantly improve upon the cycle stability of TANI by reducing the physcial stress and impeding chemical degradation during cycling. The specific capacitance and cycle stability of the TANI-carbon composites are shown to increase with the substrate surface dimensions (1D < 2D < 3D). The 1D TANI-CNT composites demonstrate excellent rate capability, but low specific capacity and cycle stability. The 3D TANI-AC composites exhibit great specific capacitance and cycle life, but are limited by their slow rate performances. The 2D TANI-rGO composites have good specific

capacitance, great rate capability and cycle stability, suggesting that 2D graphene is the most suitable substrate for TANI-carbon nanocomposites.

6.2. Elucidating the correlation between the TANI/PANI redox behaviors and the carbon substrate morphology and surface functional groups (Future Work)

Many research groups have made a multitude of various PANI-carbon composites for supercapacitor applications. However, the CV curves of the composites vary wildly. While some composites show three pairs of redox peaks, some only display two or one set of broad peaks; yet, there are other that don't have well-defined redox peaks at all.[1] As we were making different composites of TANI-carbons, similar inconsistencies were also observed, as demonstrated in Figure 6.1.

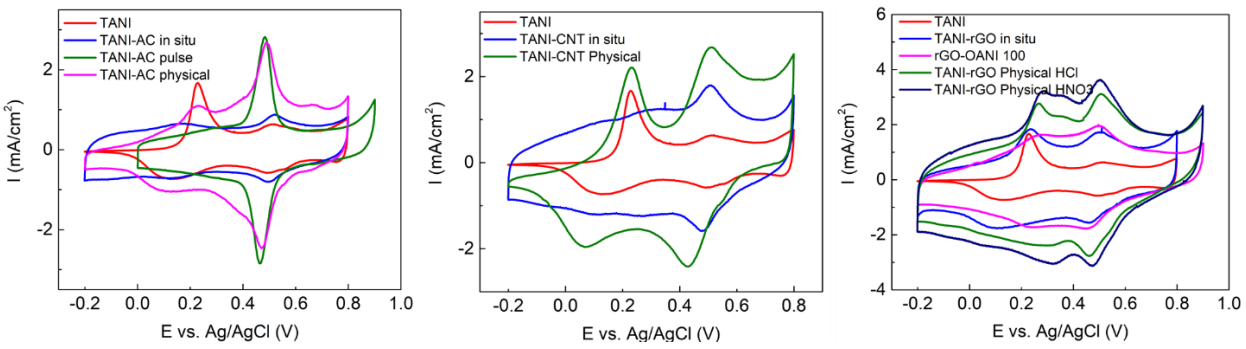

Figure 6.1 CV curves of various TANI-carbon composites showing different redox peak profiles.

The first interesting observation is related to the peak height ratio between the two major TANI redox peaks. In the TANI nanowire electrode CV, the first peak (0.2 V vs. Ag/AgCl) is much higher and sharper than the second peak (0.5 V vs. Ag/AgCl); however, the trend is reversed in most TANI-carbon composite CVs. Additionally, the electrodeposited TANI-AC composite electrode shows only one pair of redox peaks, while the TANI-AC *in situ* composite electrode

displays two and the TANI-AC physical mixture composite electrode has three pairs of redox peaks. The TANI-rGO and TANI-CNT composites also exhibit similar discrepancies. Perhaps the carbon substrate affects the redox properties of TANI not only through their different surface morphologies, but also through the functional groups on the surface?

The reason why this phenomenon is of importance is that the peak profiles of the TANI-carbon composites seemingly affect the cycle stability of the electrodes. Generally speaking, the composites with only one pair of redox peaks are typically more stable than those with two, which show still better cycle life than those with three sets of peaks. In the future, we will analyze different TANI-carbon composites before and after cycling using XPS, Raman, FTIR, UV-vis and SEM characterizations, and seek to understand how the carbon surface functional groups interact with TANI to influence its redox properties and chemical stabilities.

6.3. Graphene-PEDOT-Platinum Tertiary Composite Catalyst for the Hydrogen Evolution Reaction (Future Work)

We have fabricated a Laser Scribed Graphene-PEDOT-platinum (LSG-PEDOT-Pt) tertiary composite material as a Hydrogen Evolution Reaction (HER) catalysis using a three-step synthesis: 1) graphene oxide (GO) films were photo-thermally reduced via a CO_2 laser into laser-scribed graphene (LSG); 2) a layer of PEDOT polymer was grown on the LSG films using vapor-assisted polymerization methods to yield LSG-PEDOT composite films; and 3) platinum nanoparticles were deposited on the LSG-PEDOT composite via pulse chronoamperometry. The PEDOT decorates the surface of the LSG, forming nanoribbon/nanotube-like structures. The pulse chronoamperometry enables platinum to grow vertically on top of the LSG-PEDOT substrate, forming arrays of nanowires. The LSG-PEDOT-Pt composite electrode shows better HER performances than a platinum foil electrode in a 0.5 M H_2SO_4 solution, with a very low Tafel slope of 38 mV/decade, 15 mV (vs. RHE) onset overpotential, and achieves 10 mA/cm^2 current density at a low overpotential of 35 mV (vs. RHE). Even though LSG-PEDOT is an intrinsically poor HER catalyst, its high surface area, high conductivity and low charge transfer resistance make it a good substrate for growing HER catalysts, as demonstrated by the performances of the LSG-PEDOT-Pt. The LSG-PEDOT composite is a promising substrate for developing non-noble metal-based catalysts.

6.2.1. Introduction

Our modern society is heavily dependent upon fossil fuels, because the chemical energy stored in them can be easily extracted by combustion. However, fossil fuels are complicated organic molecules that took millions of years to form under natural conditions, a span so long for human civilization that renders fossil fuels practically non-renewable. Additionally, the

combustion of fossil fuels has led to many problems all over the world, such as global warming and environmental pollution. In recent years, with the development of technologies and infrastructure, the percentage of energy generated from renewable energy sources, such as wind, geothermal and solar powers, has been rising steadily.[2] However, as wind turbines do not rotate all the time and the sun does not shine at night, renewable energy sources like wind power and solar energy contribute to the electric grid intermittently.[3] Thus, there arises an issue of storing the excess energy in order to meet human needs. Electrochemically splitting water into hydrogen and oxygen and storing the excess electric energy as chemical energy is a reasonable and practical approach.[4]

Electrochemical hydrolysis of water involves the following reaction:

$$2\,H_2O\,(\mathrm{l}) \rightarrow 2H_2\,(g) + O_2(g) \quad \left(\Delta \mathrm{G} = 237.1 \frac{\mathrm{kJ}}{\mathrm{mol}} \;\; \mathrm{E} = 1.23\ \mathrm{V}\right) \tag{6.1}$$

The thermodynamic driving force or chemical potential of this reaction is 1.23 V, but the kinetic barriers typically require a much higher overpotential for the hydrolysis reaction to reach a practical rate. In an electrolytic cell, the above reaction can be split into two half-reactions: the hydrogen evolution reaction (HER) on the cathode and the oxygen evolution reaction (OER) on the anode. Of particular interest to us is the hydrogen evolution reaction (HER).

The HER reaction taking place acidic media involves three possible elementary steps: the Volmer step (6.2), the Heyrovsky step (6.3) and the Tafel step (6.4).[5]

$$H_3O^+ + \ e^- + M \leftrightharpoons M - H + H_2O \tag{6.2}$$

$$M - H + H_3O^+ + e^- \leftrightharpoons \ H_2 + H_2O + M \tag{6.3}$$

$$2\mathrm{M} - \mathrm{H} \leftrightharpoons H_2 + 2M \tag{6.4}$$

where M indicates empty surface sites on the catalyst. During the Volmer step, a hydronium ion approaches one vacant site on the catalyst, accepts an electron and transfers a proton to the catalyst, forming a covalent metal-hydride (M-H) bond. From this point, the M-H complex can take two possible steps. It can go through an electrochemical reduction (the Heyrovsky step), accepting one electron from the electrode and another proton from a hydronium ion in water, to produce a hydrogen molecule and a vacant metal site. Alternatively, it can take a chemical approach (the Tafel recombination step), where two adjacent hydrides recombine to form a hydrogen molecule, leaving two empty metal sites. Each one of the three elementary steps can be the rate-determining step.[6]

To evaluate the efficiency of a catalyst, we need to introduce two concepts: the Tafel slope and the exchange current density. The current density on the electrode is directly proportional to the reaction rate, and the current density to the applied overpotential is governed by the Tafel equation.[7]

$$\eta = a + b\log(i) \tag{6.5}$$

where η is the overpotential, i is the current density, a is a parameter related to the exchange current density, and b is the famous Tafel slope. For a generic redox reaction taking place on an electrode surface with redox species dissolved in solution but not experiencing mass transport, similar to the HER reactions, the current density is related to the applied potential according to the Butler-Volmer equation:[8]

$$\mathrm{i} = \mathrm{i}_0\left(\exp\left(\alpha\frac{nF}{RT}\eta\right) - \exp\left(-(1-\alpha)\frac{nF}{RT}\eta\right)\right) \tag{6.6}$$

where i is the current density, i_0 is the exchange current density, α is charge transfer coefficient, n is the number of electrons transferred during the redox reaction, F is Faraday's constant, R is the universal gas constant, T is temperature, and η is the overpotential. Combining Equations 6.5 and 6.6, we can get another expression:[8]

$$\eta = \frac{nF}{RT}\log(i_0) - \frac{nF}{RT}\log(i) \tag{6.7}$$

Notice that the first term of Equation 6.7 corresponds to the a term in Equation 6.5 and when $\eta = 0$, the current density is equal to the exchange current density. However, since we cannot measure zero current, we can plot $\log(\mathrm{i})$ vs. η (i.e., a Tafel plot) instead, and the x-intercept of the reverse extention of the linear part of the plot corresponds to the exchange current density. For a reversible redox reaction at its equilibrium potential, the forward reaction and reverse reaction take place at the same rate, resulting in a net zero current. The rate of the two reactions in equilibrium is referred to as the exchange current density, and therefore, i_0 is a measure of the catalyst's performance. The exchange current density is determined by many factors, but for the HER catalysis, it can be expressed as:[9]

$$i_0 = \frac{RT}{nFR_{ct}} \tag{6.8}$$

where R_{ct} is the charge transfer resistance. This suggests that by reducing the charge resistance of a catalyst (electrode), we can enhance its catalytic activity.

The significance of the exchange current is illustrated in Figure 6.2. The plot on the left exhibits higher exchange current density than the plot of the right. Note that at the same applied overpotential, the measured net current density is also higher for the electrode with higher i_0, suggesting better electrocatalytic performances.

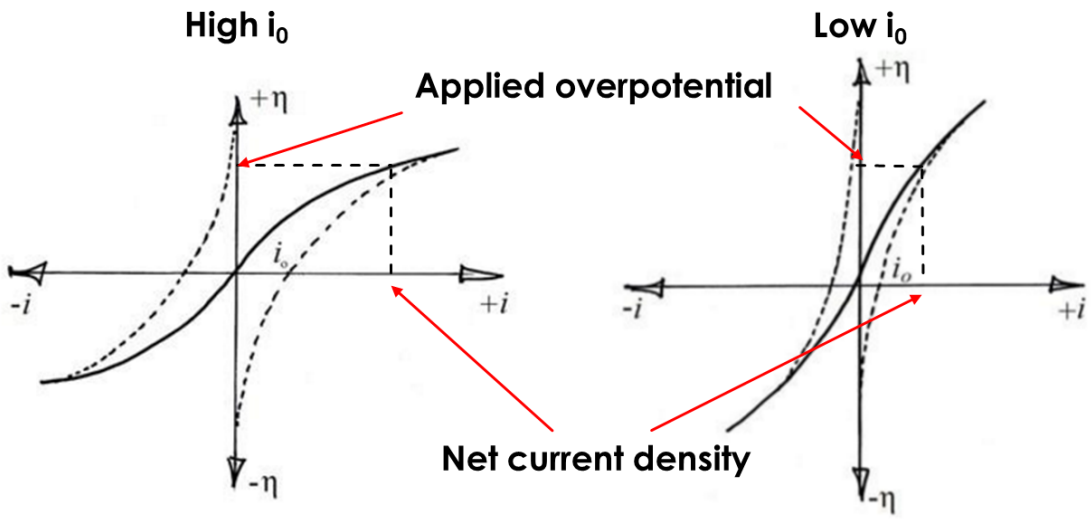

Figure 6.2 Two generic current density vs. overpotential plots with different exchange current densities.

The slope of the Tafel plot is also an important performance metric, as it helps to determine the rate-limiting step of the reaction. Experimental observations and theoretical simulations indicate that if the Volmer step is the rate-determining step, the Tafel slope is 120 mV/dec; if the Heyrovsky step is rate-limiting, the Tafel slope is 40 mV/dec; when the Tafel step determines the reaction rate, the Tafel slope is 30 mV/dec.[5,8]

Given the reaction mechanisms, the general guidelines for finding possible HER catalysts follow the Sabatier principle, which states that the interaction between the catalyst and the substrate cannot be too strong or too weak. If the M-H interaction is too weak, the adsorption will be too slow; however, if the M-H bond is too strong, hydride recombination or desorption will be hindered.[6] Following this principle, the so-called volcano plots for the HER reaction are provided in Figure 6.3. A volcano plot shows the relationship between DFT-calculated hydride adsorption energy, ΔG_{ad}, and the natural log of the exchange current density, i_0. Generally speaking, the higher up a metal is on the plot, the better is its HER catalytic activity.

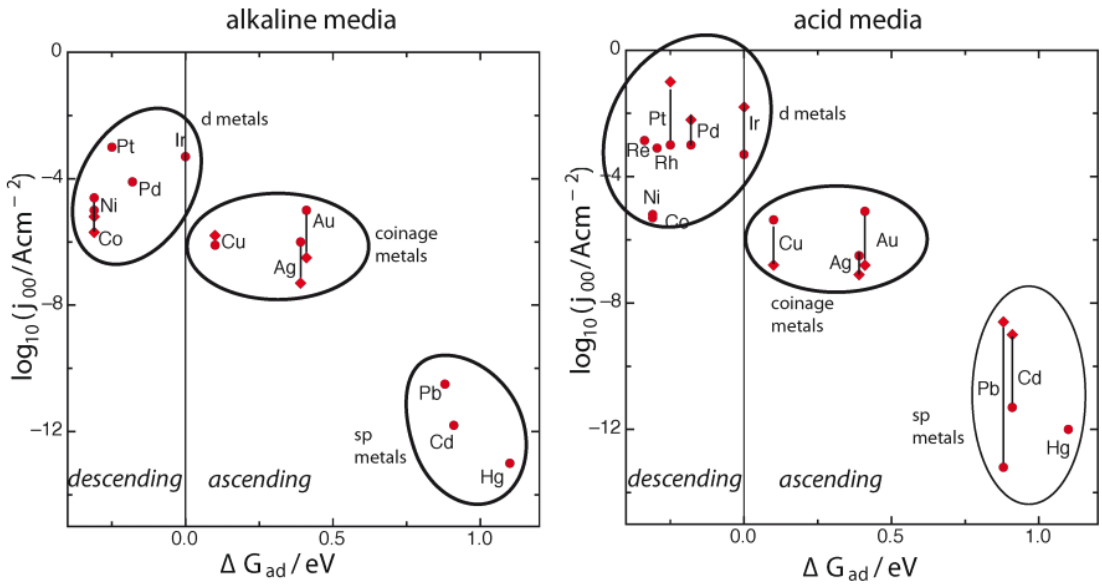

Figure 6.3 Modern volcano plots for hydrogen evolution in acid and alkaline aqueous solutions. (Reproduced with permission.[6] Copyright 2014 Quaino et al.)

Notably, the majority of the metals at the top of the plots are noble metals. Therefore, we are interested in preparing composite materials that can lower the percentage of noble metals, and eventually replace noble metals with earth abundant elements, while still achieving good catalytic performances. In this preliminary work, we demonstrate that laser-scribed graphene (LSG)-PEDOT can serve as a substrate to grow platinum nanowires on, and the resulting tertiary composite is a highly efficient HER catalyst. In future work, a series of non-noble metals, metal oxides and hydroxides will be deposited on this LSG-PEDOT scaffold to achieve similar levels of catalytic activity.

6.2.2. Preliminary results and discussions

The preparation of a tertiary composite material is illustrated in the schematic diagram shown in Figure 6.4. First, graphene oxide was drop-cast onto a graphite paper current collector, forming a dark orange film. The GO film was then reduced with a laser beam, resulting in a black porous

LSG film. An oxidizing agent, iron(III) p-toluenesulfonate or ammonium persulfate in 1-butanol solution, was added onto the LSG film. The partially dried LSG film was then placed into a chamber with a reservoir of liquid 3,4-ethylenedioxythiophene (EDOT), and the chamber was held at 80°C for 4 h. The resulting LSG-PEDOT composite film was then immersed in a potassium hexachloroplatinate (K_2PtCl_6) sulfuric acid solution, and Pt nanoparticles were electrodeposited on the LSG-PEDOT using pulse chronoamperometry.

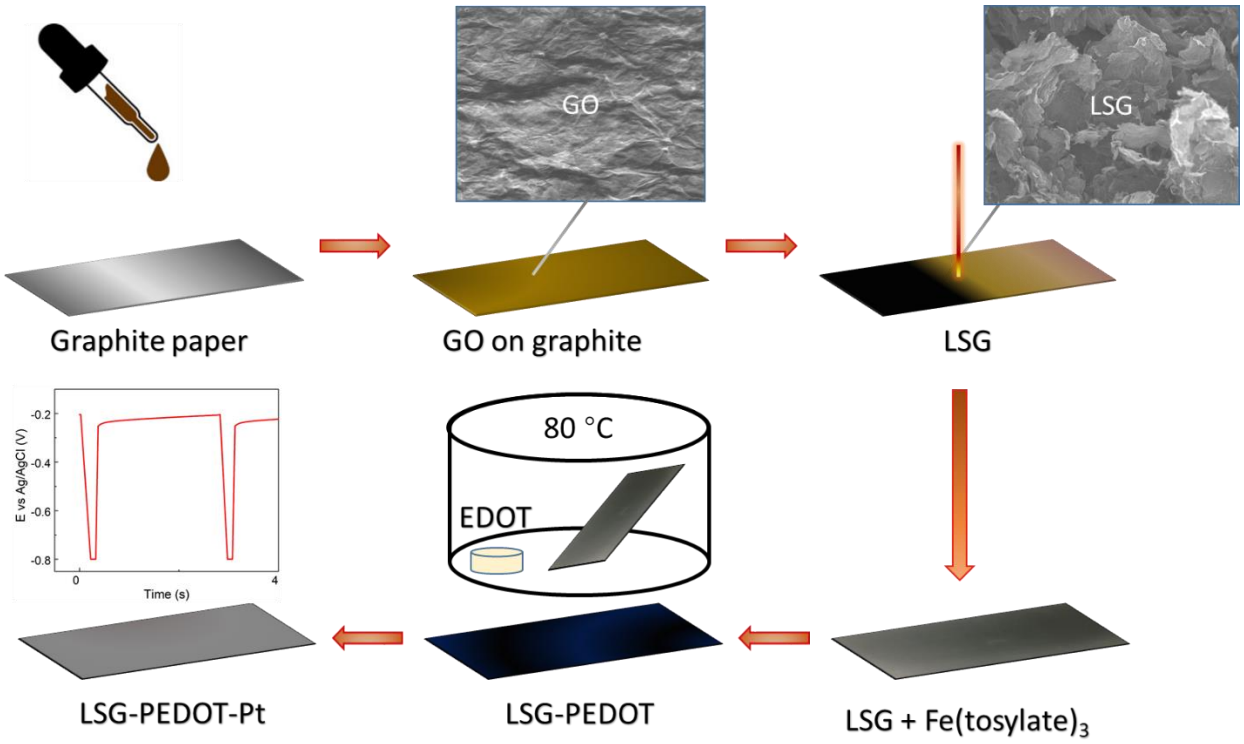

Figure 6.4 A schematic diagram of the LSG-PEDOT-Pt composite preparation process.

Some SEM images of laser-scribed graphene (LSG) samples are presented in Figures 6.5a-c. The LSG samples were prepared by irradiating graphene oxide (GO) films with a CO_2 laser. As the high power laser beam irradiates the graphene oxide film, photothermal reduction of the oxygen containing functional groups on the graphene oxide occurs, causing them to leave in the form of CO_2 gas. As the gas escapes from the GO, it disrupts the stacked layered structure of GO, creating a disordered corrugated morphology. This conversion process significantly increases the

conductivity and the specific surface area of the material, making the LSG an ideal substrate onto which to electrochemically deposit nanostructured platinum for catalyzing the HER.

Initially, the platinum was deposited onto the LSG substrate using a constant voltage method. However, the platinum formed clusters sparsely scattered on the LSG sheets and the loading was relatively low (Figure 6.5d). Realizing that the constant potential method does not allow the local $PtCl_6^{2-}$ concentration to replenish itself, we switched to a pulse chronoamperometry method by repeatedly applying short 0.5 s-pulse potential signals at -0.85 V vs. Ag/AgCl followed by a 1 second 0 V vs. open circuit resting period.[10] Using this method, we were able to deposit a considerable amount of Pt on the LSG surfaces, as shown in Figures 6.5e and 6.4f. The platinum particles initially formed sea urchin-like nanoclusters, likely because the sulfate anions tend to preferentially absorb onto the Pt (111) plane, leading to uneven growth rates in certain directions.[11] After 2000 pulses, the entire surface of the LSG was covered by 3D arrays of Pt nanoplates.

The HER catalysis performance of the LSG-Pt 2000-cycle composite was compared to a 1×1 cm^2 platinum foil, and the results are shown in Figure 6.6. The performance of the LSG-Pt composite was very close to that of a pure platinum foil, but we noticed that its contact resistance was relatively high, suggesting that there is room for improvement. Therefore, we decided to deposit a PEDOT layer on the LSG using a vapor-assisted chemical deposition method described in the literature.[12] We made a batch samples using ammonium persulfate as the oxidizing agent and another batch using iron(III) p-toluenesulfonate ($Fe(OTs)_3$) as the oxidizing agent. The APS-oxidized PEDOT grew along the contours of the LSG, not showing any distinct nanostructures; however, the $Fe(OTs)_3$ oxidized PEDOT shows nanotubular morphology.

We then electrochemically deposited platinum onto the LSG-PEDOT composites using a 400-pulse deposition method. The SEM images of the resulting LSG-PEDOT-Pt composites are

shown in Figures 6.5j-l. It is not quite clear what factors affect the morphology of the composites, as the APS-oxidized LSG-PEDOT-Pt shows nanowire-like Pt structures, while the two $Fe(OTs)_3$-oxidized LSG-PEDOT-Pt composites demonstrate different morphologies.

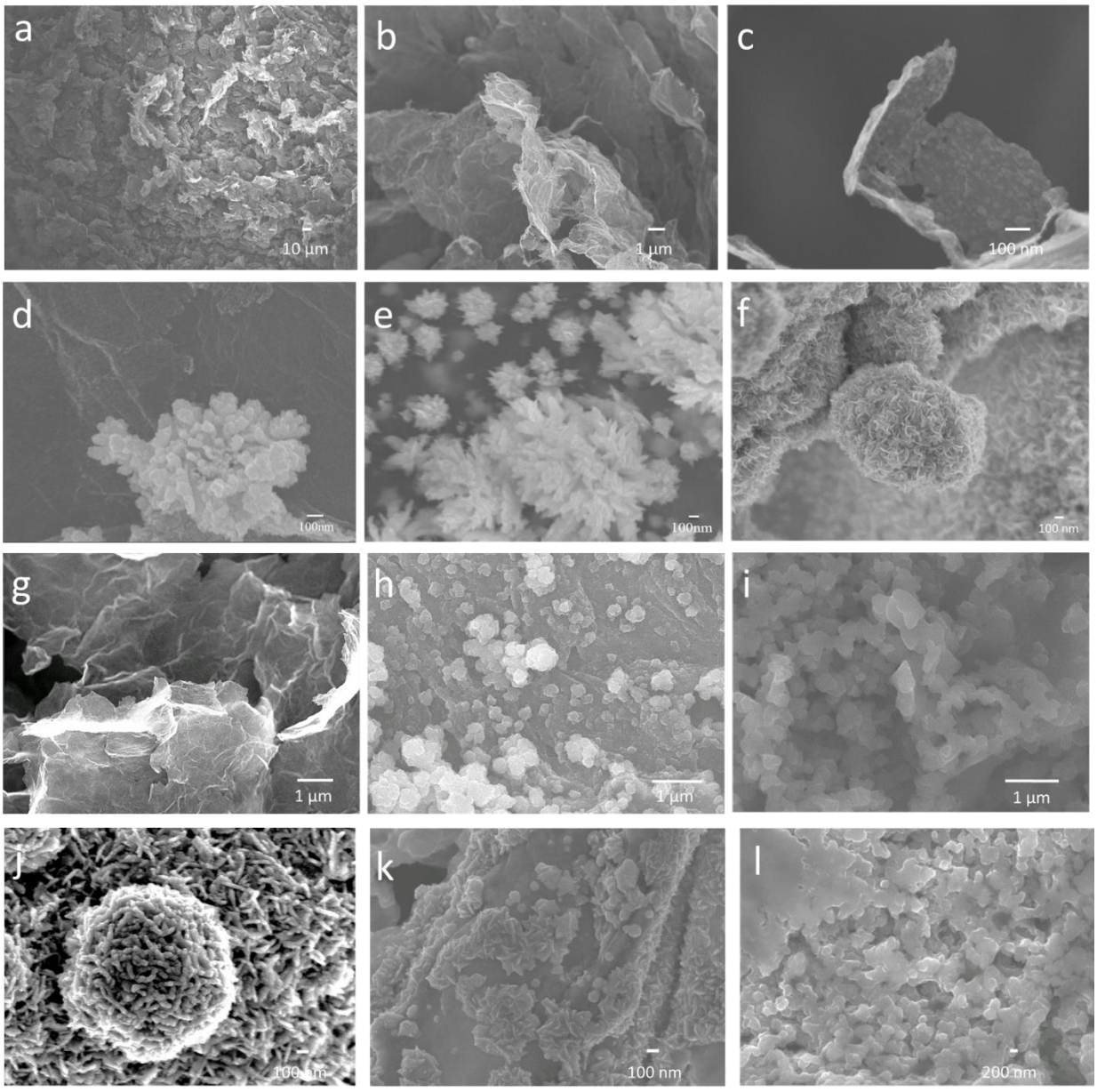

Figure 6.5 SEM images of laser-scribed graphene samples (a-c); LSG-Pt composites deposited using (d) constant voltage, (e) 250-pulse, and (f) 2000-pulse deposition methods; LSG-PEDOT composites oxidized using (a) APS for 30 min, (b) Fe(toslyate)3 for 2 h, and (c) $Fe(toslyate)_3$ for 4 h; LSG-PEDOT-Pt composites after 400-pulse depositions from the above LSG-PEDOT composites.

The HER catalysis performances of the composites and the platinum foil are presented in Figure 6.6. Two essential parameters can be extracted from the linear sweep voltammograms: the HER onset overpotential and the overpotential required to reach 10 mA/cm^2 current density (smaller overpotential indicates better catalytic performance). Based on the onset overpotentials, LSG-Pt is slightly less active than platinum foil, while the LSG-PEDOT-Pt composites are both more active than pure platinum metal. All composites display lower overpotentials required to reach 10 mA/cm^2 current density, with the LSG-PEDOT-Pt APS composite exhibits the lowest overpotential at 35 mV vs. RHE. The Tafel plots of the composites are presented in Figure 6.6b, and the Tafel slopes are taken at around the onset potentials. The Tafel slopes of the platinum foil, the LSG-Pt composite, the LSG-PEDOT-Pt (Fe oxidized) composite and LSG-PEDOT-Pt (APS oxidized) composite are calculated to be 56 mV/dec, 85 mV/dec, 37 mV/dec and 39 mV/dec, respectively. However, the Tafel slope varies drastically with the selected potential range, and the angle of the slope cannot conclusively determine the rate-determining step.[8] However, the exchange current density can still be extracted from the Tafel plots (where the dashed lines intersect with the x-axis), and all composites display higher i_0 than pure Pt foil. This observation is in agreement with the Nyquist plots shown in Figure 6.6c. Even though the platinum foil demonstrates a very small contact resistance, it suffers from the largest charge transfer resistance, as indicated by the large semicircle. The LSG-Pt and the LSG-PEDOT-Pt composites all demonstrate much smaller charge transfer resistances, and according to Equation 6.8, a smaller R_{ct} should lead to a higher i_0.

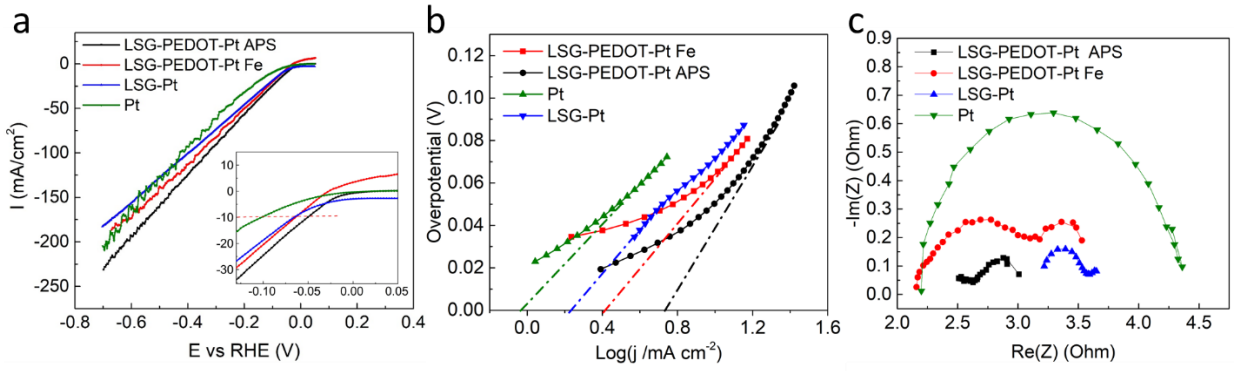

Figure 6.6 Electrocatalytic performances of a platinum foil, a LSG-Pt composite electrode, and two LSG-PEDOT-Pt composite electrodes: (a) the linear sweep voltammograms (5 mV/s), (b) the Tafel plots of the HER reaction (the dashed lines indicate the exchange current densities), and (c) the Nyquist plots of each of the composite electrodes at their respective HER onset potentials.

6.3.2. Experimental

6.3.2.1. Preparation of the LSG substrates

5.0 mL of 1.3 % GO solution was drop-cast on a 5×5 cm^2 graphite paper sheet and was dried in a conventional oven at 50°C overnight. The dried GO film was reduced with a 7-W CO_2 laser (Full Spectrum Laser H-series) at 20% power, 80% raster speed, 5 ms pulse, 1000 dpi resolution with half-tone dithering mode on.

6.3.2.2. Preparation of the LSG-PEDOT composites

1.5 mL of an iron(III) p-toluenesulfonate hexahydrate (1.00 g, 1.48 mmol) and pyridine (59.5 μL, 0.74 mmol) in 1-butanol (10 mL) solution were drop-cast on the LSG substrate. The oxidant loaded film was heated briefly to remove excess butanol such that the solution did not drip off of the film. The film was then put into a chamber with a reservoir (2 mL) of liquid EDOT held at a constant temperature of 80 °C. The reaction was allowed to proceed for various set time periods to obtain composites of different morphologies. At the end of the reaction, the film was removed

from the chamber and rinsed with ethanol. Another batch of LSG-PEDOT composite was made in a similar process, with an ammonium persulfate/pyridine in 1-butanol solution (at the same concentrations) as the oxidizing agent.

6.3.2.3. Electrodeposition of platinum onto various substrates

The electrochemical deposition of platinum was performed on a Bio-Logic VMP3B-10 Potentiostat in a standard 3-electrode setup, with the substrate film (1×2 cm^2 electrode area) as the working electrode, an Ag/AgCl (saturated KCl) as the reference electrode and a platinum foil (2 cm^2) as the counter electrode. The electrolyte solution was a 0.5 M sulfuric acid solution with 0.01 M of potassium hexachloroplatinate (K_2PtCl_6). The electrodeposition was carried out by applying a pulse chronoamperometry method (0.5 s on at -0.85 V vs. Ag/AgCl followed by 1 s off at the open circuit potential, number of pulses varied). After the deposition, the working electrode was rinsed with ethanol and air-dried.

6.3.2.3. Electrochemical catalytic evaluations of the HER catalysts

The electrochemical characterizations of the catalysts were performed on the same potentiostat using a 3-electrode setup. The LSG-Pt electrode, the LSG-PEDOT-Pt electrodes and a platinum foil (1×1 cm^2 effective area) were used as the working electrodes. An Ag/AgCl reference electrode and a platinum foil (1×2 cm^2 on both sides) served as the reference and the counter electrode, respectively. The linear sweep voltammetry was scanned from 0 V to -1.0 V vs. the reference electrode, at a scan rate of 5 mV/s. The electrochemical impedance spectroscopy was performed at 10 mV vs. the HER onset potential of the catalysts, with an amplitude of 5 mV in the frequency range from 1 mHz to 100 kHz.

6.3.3. Summary and future directions

In summary, the LSG-PEDOT-Pt composites demonstrate higher HER catalytic activities than pure platinum metal. The LSG-PEDOT substrate provides high surface area, high conductivity, and low charge transfer resistance for making better HER catalysts. In the future, we will test different synthesis conditions to understand what factors affect the morphology of the PEDOT and the platinum nanoparticles, further improving the performance of the composites. Additionally, we will try to deposit non-noble metal oxides/hydroxides/phosphides or transition metal dichalcogenides onto the LSG-PEDOT substrate and evaluate their electrocatalytic activities.

6.4. References

(1) Eftekhari, A.; Li, L.; Yang, Y. *J. Power Sources* **2017**, *347*, 86–107.

(2) Data world bank. 2011. “Fossil Fuel Energy Consumption (% of Total).” *World Bank*. http://data.worldbank.org/indicator/EG.USE.COMM.FO.ZS.

(3) Vesborg, P. C. K.; Seger, B.; Chorkendorff, I. *J. Phys. Chem. Lett.* **2015**, *6* (6), 951–957.

(4) Parsons, R. *Trans. Faraday Soc.* **1958**.

(5) Strmcnik, D.; Lopes, P. P.; Genorio, B.; Stamenkovic, V. R.; Markovic, N. M. *Nano Energy* **2016**, *29*, 29–36.

(6) Quaino, P.; Juarez, F.; Santos, E.; Schmickler, W. *Beilstein J. Nanotechnol.* **2014**, *5* (1), 846–854.

(7) Bard AJ, Faulkner LR. *Electochemical Methods Fundamentals and Applications*; 2001.

(8) Shinagawa, T.; Garcia-Esparza, A. T.; Takanabe, K. *Sci. Rep.* **2015**, *5* (September), 1–21.

(9) Horvai, G. *Electroanalysis* **1991**, *3* (7), 673–675.

(10) Hsieh, C. Te; Wei, J. M.; Lin, J. S.; Chen, W. Y. *Catal. Commun.* **2011**, *16* (1), 220–224.

(11) Kolics, A.; Wieckowski, A. *J. Phys. Chem. B* **2002**.

(12) Jones, W. E.; Madl, C. M.; Kariuki, P. N.; Gendron, J.; Piper, L. F. J. *Synth. Met.* **2011**, *161* (13–14), 1159–1165.